

# ScholarWorks@GSU

## The Shape of Stellar Convection

Authors	Mary Geer Dethero
Citation	Mary Geer Dethero. "The Shape of Stellar Convection." 2025. Dissertation, Georgia State University. <a href="https://doi.org/10.57709/qg7f-4f86">https://doi.org/10.57709/qg7f-4f86</a>
DOI	<a href="https://doi.org/10.57709/qg7f-4f86">https://doi.org/10.57709/qg7f-4f86</a>
Download date	2026-03-10 06:51:08
Link to Item	<a href="https://hdl.handle.net/20.500.14694/15573">https://hdl.handle.net/20.500.14694/15573</a>

The Shape of Stellar Convection

by

Mary Geer Dethero

Under the Direction of Jane Pratt, Ph.D.

A Dissertation Submitted in Partial Fulfillment of the Requirements for the Degree of

Doctor of Philosophy

in the College of Arts and Sciences

Georgia State University

2025

## ABSTRACT

Recent space missions such as Kepler, TESS, and soon PLATO have provided an abundance of high-quality stellar data, highlighting the need for more accurate models of stellar structure and evolution. A key challenge in this area is understanding how thermal convection contributes to fluid mixing processes in stellar interiors. Thermal convection is fundamentally a multi-dimensional, multi-scale, nonlinear fluid process; evaluating the accuracy of one-dimensional parameterizations of mixing that results from convection is a challenge for stellar structure and evolution. Using the Multi-dimensional Stellar Implicit Code (**MUSIC**), a time-implicit, fully compressible hydrodynamics code designed for global simulations of stars, we study convection in stars that have a wide range of properties. We apply existing diagnostics for evaluating stellar convection, including three versions of a filling factor for convection, and a non-dimensional parameter called the “penetration parameter” based on the convective flux. We also develop two new non-dimensional quantities that we call the plume interaction parameter and the plume merging parameter. We identify a radial shape for the number and the width of convective plumes, and the changing non-local structure of convection as a convection zone deepens. Although the filling factor quantifies the asymmetry of convection, it is not capable of predicting the depth of convective overshooting. Using three different sets of simulations, we confirm that the plume interaction parameter and the plume merging parameter can distinguish between 2D and 3D convection, predict the convective overshooting depth in stars of different masses, and to some extent predict the convective overshooting depth in stars evolving along the red giant branch that have different convection zone sizes.

INDEX WORDS: Stellar convection, Stellar hydrodynamics, Stellar evolution

Copyright by  
Mary Geer Dethero  
2025

The Shape of Stellar Convection

by

Mary Geer Dethero

Committee Chair:

Jane Pratt

Committee:

Russel White

Douglas Gies

Isabelle Baraffe

Electronic Version Approved:

Office of Graduate Services

College of Arts and Sciences

Georgia State University

May 2025

## DEDICATION

In memory of my grandmother, Becky Dethero, a gifted writer and storyteller whose warmth and inclusivity touched everyone she met. Her legacy of creativity and kindness continues to inspire me.

## ACKNOWLEDGMENTS

I am deeply grateful to my dissertation committee members, Dr. Jane Pratt, Dr. Russel White, Dr. Doug Gies, and Dr. Isabelle Baraffe, for their guidance and support throughout this journey. Their expertise, insightful feedback, and encouragement have been instrumental in shaping my research and my growth as a scientist.

I would also like to extend my appreciation to the faculty and graduate students in the Department of Physics and Astronomy at Georgia State University. The collaborative and supportive environment over the past six years has been essential to my development as a Ph.D. candidate. I am thankful for the mentorship, discussions, and friendships that have enriched my experience.

Finally, I am profoundly grateful to my family, Brad, Goode, and Annie Dethero, for their constant encouragement and support. Their belief in me has been a source of strength through every challenge. A special acknowledgment goes to Alexander Grace, who is the light in my life and whose love and support have made this journey all the more meaningful.

The research in Chapters 4 and 5 is part of the Blue Waters sustained-petascale computing project, which is supported by the National Science Foundation (awards OCI-0725070 and ACI-1238993) and the state of Illinois. Blue Waters is a joint effort of the University of Illinois at Urbana-Champaign and its National Center for Supercomputing Applications. This work used the DiRAC Complexity system, operated by the University of Leicester IT Services, which forms part of the STFC DiRAC HPC Facility ([www.dirac.ac.uk](http://www.dirac.ac.uk)). This equip-

ment is funded by BIS National E-Infrastructure capital grant ST/K000373/1 and STFC DiRAC Operations grant ST/K0003259/1. DiRAC is part of the National E-Infrastructure. This work also used the University of Exeter local supercomputer ISCA.

## TABLE OF CONTENTS

ACKNOWLEDGMENTS . . . . .	v
LIST OF TABLES . . . . .	x
LIST OF FIGURES . . . . .	xiii
<b>1 Introduction . . . . .</b>	<b>1</b>
1.1 Stellar modeling plays a foundational role in the field of astronomy	1
1.2 Thermal convection is a complex problem . . . . .	6
<i>1.2.1 Thermal convection in the extreme environment of stellar interiors</i> . . . . .	9
1.3 Multi-dimensional hydrodynamic simulations of stars provide a way forward . . . . .	14
1.4 The goals for this work . . . . .	15
<b>2 Modeling Stellar Convection . . . . .</b>	<b>17</b>
2.1 Stellar structure equations . . . . .	18
<i>2.1.1 Convective Instability</i> . . . . .	20
2.2 Mixing Length Theory . . . . .	25
<i>2.2.1 Deriving MLT</i> . . . . .	26
<i>2.2.2 The mixing length</i> . . . . .	36
2.3 Convective penetration and overshooting . . . . .	38
<i>2.3.1 Convective Overshooting Model</i> . . . . .	43
<i>2.3.2 Choosing a diffusion coefficient</i> . . . . .	44
2.4 The MESA Code . . . . .	46
2.5 Alternative Convection Models . . . . .	50
<b>3 Simulating Stellar Convection . . . . .</b>	<b>51</b>

3.1	The hydrodynamic equations . . . . .	51
3.2	Multi-dimensional Stellar Implicit code (MUSIC) . . . . .	54
	<i>3.2.1 Spatial integration</i> . . . . .	55
	<i>3.2.2 Time integration</i> . . . . .	56
3.3	MUSIC diagnostics for convection . . . . .	59
	<i>3.3.1 Convective overshooting calculations</i> . . . . .	61
4	The filling factor: a single-point diagnostic for stellar convection . . . . .	65
4.1	Simulations . . . . .	68
4.2	Differences between 2D and 3D stellar simulations . . . . .	77
4.3	Filling factor based on volume percentage . . . . .	80
4.4	Filling factor based on mass flux . . . . .	83
4.5	Filling factor based on convective flux . . . . .	86
4.6	Eliminating compressibility as a source of error for the convective flux filling factor . . . . .	91
4.7	Conclusions . . . . .	94
5	Two-point diagnostics for stellar convection . . . . .	96
5.1	The Anders penetration parameter . . . . .	98
5.2	The width of inflows . . . . .	101
5.3	The number of inflows: missing the forest for the trees . . . . .	104
5.4	Differences between convective cores and envelopes . . . . .	106
5.5	The plume interaction parameter . . . . .	109
5.6	The plume merging parameter . . . . .	112
5.7	Conclusions . . . . .	113
6	The mass dependence of properties of convection . . . . .	116
6.1	One-point diagnostics . . . . .	121

6.2	Two-point diagnostics . . . . .	125
6.3	Discussion . . . . .	131
7	Convection in rapidly changing stars along the red giant branch . . . . .	134
7.1	The evolution of convection along the RGB . . . . .	134
7.2	One-point statistics . . . . .	141
7.3	Two-point statistics . . . . .	145
7.4	Discussion . . . . .	149
8	Summary and Conclusions . . . . .	152
8.1	Summary of Results . . . . .	153
	<i>8.1.1 The filling factor</i> . . . . .	153
	<i>8.1.2 Two point diagnostics</i> . . . . .	156
	<i>8.1.3 Width-Number Relation</i> . . . . .	159
	<i>8.1.4 Characterizing the overshooting layer</i> . . . . .	162
	Appendices . . . . .	165
A	Inlists . . . . .	166
	REFERENCES . . . . .	170

## LIST OF TABLES

- Table 4.1 Parameters for compressible hydrodynamic simulations performed with MUSIC. Two different pairs of young sun simulations are included: (1) the *wide2D* and *wide3D* pair have lower radial resolution but the 3D simulation uses a large angle along the equator, while (2) *wm2D* and *wm3D* use a smaller equatorial angle but significantly higher radial resolution. The pair of red giant simulations is *bg2D* and *bg3D*; the pair of current sun simulations is *dcs2D* and *dcs3D*; the pair of convective core simulations is *cc2D* and *cc3D*. The high-resolution 2D simulations are *ccmod2D* and *pms4m2D*. The simulation name, dimensionality, evolutionary state, and stellar mass  $M$  in units of the solar mass  $M_{\odot}$  are provided. The inner radius  $R_i$  of the spherical shell, the radius of the convective boundary  $R_{CB}$  determined by the Schwarzschild criterion, and the outer radius  $R_o$  of the spherical shell for the simulation are given in units of the total radius of each star,  $R$ , as a triplet. The angular extent of the simulation in the polar and equatorial directions is given as  $(\theta, \phi)$ , and the grid spacing in both angular directions is  $(\Delta\theta, \Delta\phi)$ . . . . . 73
- Table 4.2 Time scales for the compressible hydrodynamic simulations performed with MUSIC. The average global convective turnover time  $\tau_{\text{conv}}$  is provided as well as its standard deviation in time, and the total time span for each simulation is given in units of the convective turnover time. . . . . 73
- Table 4.3 The table includes the overshooting depth  $\ell_{\text{ov}}$  in units of the pressure scale height at the convective boundary, the volume-percentage filling factor  $\sigma_{\text{vp,CB}}$ , the mass-flux filling factor  $\sigma_{\text{mf,CB}}$ , and the incompressible convective-flux filling factor  $f_{z,\text{CB}}$ . The subscript CB indicates that the quantity is evaluated at the convective boundary (CB), as defined by the Schwarzschild criterion. 85
- Table 5.1 This table includes several quantities evaluated above or below the convective boundary, as well as two-point diagnostics related to the filling factor for convection. It includes for convective envelopes (convective cores) the average number of inflows (outflows) in the overshooting layer  $N_{\text{OL}}$  and in the convection zone  $N_{\text{CZ}}$ , and the average width of inflows (outflows) in the overshooting layer  $W_{\text{OL}}$  and in the convection zone  $W_{\text{CZ}}$ . The average widths are displayed in units of the percentage of the simulation volume at the given radius. Two-point diagnostics include the Anders penetration parameter  $P_{\text{A}}$ , the plume merging parameter  $\sigma_{\text{merge}}$ , and the plume interaction parameter  $\sigma_{\text{int}}$ . 99

Table 6.1	Parameters of stellar structure models produced with MESA. These models are selected so that the radial position of the convective boundary, as determined by the Schwarzschild criterion, is at $r_{\text{CB}}/R = 0.8$ , and the radius of the star at the photosphere $R$ is provided. The stellar mass $M$ is given in units of the solar mass; the stellar luminosity at the photosphere $L$ is given in units of the solar luminosity. The age, effective temperature at the photosphere, and log of the acceleration of gravity at the photosphere are also provided in the units used by the MESA code. Each MESA has metallicity $z = 0.02$ and helium mass fraction $y = 0.28$ . . . . .	117
Table 6.2	MUSIC simulations for 10 stars using the stellar structures from Table 6.1. All simulations span from the inner radial boundary $R_i/R = 0.4$ to the outer radial boundary $R_o/R = 0.97$ . . . . .	120
Table 6.3	Calculated quantities related to the filling factor for convection for ten pre-main sequence stars. All stars are identical, other than their mass. The table includes the overshooting depth $\ell_{\text{ov}}$ in units of the pressure scale height at the convective boundary and the incompressible convective-flux filling factor at the convective boundary $f_{z,\text{CB}}$ . We include the Anders penetration parameter $P_{\text{A}}$ , the plume interaction parameter $\sigma_{\text{int}}$ , and the plume merging parameter $\sigma_{\text{merge}}$ . It also includes the average number of inflows in the overshooting layer $N_{\text{OL}}$ and in the convection zone $N_{\text{CZ}}$ , and the average width of inflows in the overshooting layer $W_{\text{OL}}$ and in the convection zone $W_{\text{CZ}}$ . The average widths are displayed in units of the percentage of the simulation volume at the given radius. . . . .	125
Table 7.1	Parameters defining model stars produced by MESA. This table describes models along the evolutionary path of a simple 3 solar mass star produced with MESA. Models are along one such evolutionary path that spans a period of 10.61713 million years of evolutionary time. The variable $r_{\text{CB}}$ indicates the radial position interior to the star of the convective boundary, as determined by the Schwarzschild criterion. The metallicity $z = 0.02$ and helium mass fraction $y = 0.2945$ . . . . .	137
Table 7.2	Two-dimensional simulations performed with MUSIC. The table includes the MESA model, the inner radial boundary $r_{\text{in}}/R$ , the outer radial boundary $r_{\text{out}}/R$ , the time span of the simulation in units of convective turnover times $\tau_{\text{conv}}$ , and the resolution, $H_{p,\text{CB}}/\Delta r$ . . . . .	139

Table 7.3 Calculated quantities related to the filling factor for convection for a red giant star at eight points along the first dredge-up point of the red giant branch. The table includes the volume-percentage filling factor  $\sigma_{\text{vp,CB}}$ , the mass-flux filling factor  $\sigma_{\text{mf,CB}}$ , and the incompressible convective-flux filling factor  $f_{\text{z,CB}}$ . The subscript CB indicates that the quantity is evaluated at the convective boundary (CB), as defined by the Schwarzschild criterion. Several additional quantities that are evaluated above or below this convective boundary are also shown. This includes the Anders penetration parameter  $P_{\text{A}}$ , the plume interaction parameter  $\sigma_{\text{int}}$ , and the plume merging parameter  $\sigma_{\text{merge}}$ . It also includes the average number of inflows in the overshooting layer  $N_{\text{OL}}$  and in the convection zone  $N_{\text{CZ}}$ , and the average width of inflows in the overshooting layer  $W_{\text{OL}}$  and in the convection zone  $W_{\text{CZ}}$ . The average widths are displayed in units of the percentage of the simulation volume at the given radius. . . . . 141

Table 7.4 Calculated quantities related to the convective overshooting depth for a red giant star at eight points along the first dredge-up point of the red giant branch. The table includes the overshooting depth  $\ell_{\text{ov}}$  as well as the characteristic lengths from the filling factor profiles  $\ell_{\sigma_{\text{VP}}}$ , and the width profiles  $\ell_{W_{\text{OL}}}$ , in units of the pressure scale height at the convective boundary. . . . . 143

## LIST OF FIGURES

- Figure 1.1 Hertzprung-Russell (HR) diagram including 26 stars whose structures we modeled using the MESA code (Paxton et al. 2010) and then simulated using the MUSIC code (Pratt et al. 2016, e.g.). The stars here represent different masses ( $1 M_{\odot}$  to  $6 M_{\odot}$ ), evolutionary stages from the pre-main sequence to the red giant branch, and metallicities ( $z = 0.0005$  to  $z = 0.02$ ). The color bar represents the size of the convection zone (CZ) in fractional units of the total stellar radius ( $0.2 R_*$  to  $0.825 R_*$ ). The marker size corresponds to the stellar mass. The Sun is plotted for reference. . . . . 4
- Figure 1.2 Temperature (solid purple) and pressure (dashed blue) profiles normalized to their maximum values for a  $3M_{\odot}$  red giant star, produced with the MESA code (Paxton et al. 2010). The maximum values are  $\log_{10} T = 8.05$  in units of Kelvin and  $\log_{10} P = 20.4$  in the cgs unit for pressure, dyne/cm<sup>2</sup>. The horizontal axis is the normalized radius where  $r/R = 1$  is the photosphere, which is the extent of the stellar interior. The vertical black line indicates the radial location of the Schwarzschild convective boundary. . . . . 10
- Figure 1.3 Kippenhahn diagram for a  $3M_{\odot}$  star produced with the MESA code. The pink, shaded regions indicate areas of the star where convection is present. On the pre-main sequence, the star experiences a large convective envelope. The star has a convective core and radiative envelope as it begins to fuse hydrogen on the main sequence. When all the hydrogen fuses into helium in the core, the star moves into the red giant phase, where two convection zones form, one in the envelope and a much smaller one in the helium core. . . . . 12
- Figure 2.1 Temperature gradient for a  $1.365 M_{\odot}$  star with a large convection zone, modeled using the MESA code (Paxton et al. 2010). The temperature gradient  $\nabla = \partial \ln T / \partial \ln P$  profile is shown in dashed blue, the adiabatic gradient  $\nabla_{\text{ad}}$  is shown in solid orange, and the radiative gradient  $\nabla_{\text{rad}}$  is shown in dashed pink. The convective boundary is represented by a solid black line at  $r/R = 0.175$ ; to the left of this line is the radiative zone, and to the right of this line is the convective zone. . . . . 22
- Figure 2.2 (a) Luminosity per mass as a function of stellar radius for a  $6M_{\odot}$  main sequence star with a convective core. (b) Opacity profile for a  $3M_{\odot}$  pre-main sequence star with a convective envelope. The vertical black line represents the convective boundary as defined by the Schwarzschild criterion for each star. 24

Figure 2.3	Evolutionary track for a $3 M_{\odot}$ star with different mixing length coefficients, modeled by MESA. Both models use the Henyey flavor of MLT and metallicity $z = 0.0017$ . . . . .	37
Figure 2.4	Fluxes near the convective boundary in a star, where depth increases to the right. (a) Theoretical sketch of flux as a function of depth with four zones labeled from Zahn (1991). Depth increases to the right, where $z = 0$ is the Schwarzschild boundary and $L_p$ is the convective penetration length. (b) Flux profile for a $3M_{\odot}$ pre-main sequence star simulated with MUSIC. Layer A represents the convection zone, layer B represents the penetration layer, layer C represents the overshooting layer, and layer D represents the radiative zone. The dashed vertical line dividing layers A and B is the Schwarzschild boundary. . . . .	40
Figure 2.5	Modeling convective overshooting in 1D: The step function $\ell_{ov}$ and two diffusion coefficients, $D_{F96}$ and $D_{EVT}$ plotted as a function of depth. The black vertical line represents the bottom of the convective envelope. The blue line represents the step function option for overshooting plumes, while the orange and green lines represent how $D_{F96}$ and $D_{EVT}$ can model the amount of mixing due to overshooting. The black vertical line indicates the Schwarzschild boundary. . . . .	45
Figure 3.1	The global convective turnover time $\tau_{conv}$ over the lifetime of a simulation of a $3M_{\odot}$ pre-main sequence star with a small convective envelope. The black horizontal line represents the average turnover time $\tau_{conv} = 2.5 \times 10^6$ seconds, which is averaged after reaching steady-state, which begins at time $t = 3.4 \times 10^6$ seconds. . . . .	58
Figure 3.2	(a) Pressure scale height profile for MUSIC (pink, solid line) and MESA (blue, dashed line) is identical in structure. (b) Radial root-mean-squared velocity calculated with MUSIC (pink, solid line) and the convective velocity in MLT calculated with MESA (blue dashed line) for a $3M_{\odot}$ pre-main sequence star with a shallow convection zone. The pink-shaded region represents one standard deviation above and below the time-averaged mean. . . . .	59
Figure 3.3	(a) Radial velocity for a pre-main sequence $3M_{\odot}$ star simulated in MUSIC, where pink flows are moving outward and blue flows are moving inward. Black is the zero point. The maximum velocity magnitude is 1.8 km/s. (b) Vorticity magnitude for the same simulation, where dark pink represents zero vorticity, and white represents strong vorticity. . . . .	61

Figure 3.4 Penetration depths as a function of angle  $\theta$  for an arbitrary time frame for (a) core overshooting in a  $6 M_{\odot}$  main sequence star named *ccmod* and (b) envelope overshooting a  $4 M_{\odot}$  pre-main sequence star named *pms4m*. The overshooting depths calculated with EVT are represented by a blue solid line. The dashed line represents the average overshooting depth at this time. . . . . 62

Figure 3.5 Probability density functions for all convective overshooting,  $P(r_o)$ , and the extreme values for overshooting depth  $P(r_{\max})$  or  $P(r_{\min})$ , calculated with the vertical kinetic energy flux. The stars we examine include (a) core overshooting in a  $6 M_{\odot}$  main sequence star, *ccmod*, and (b) envelope overshooting in a  $4 M_{\odot}$  pre-main sequence star, *pms4m*. . . . . 63

Figure 4.1 Visualizations of radial velocity in 2D simulations (first row, left to right: *bg2D*, *wm2D*, *dcs2D*, and *cc2D*, second row, left to right: *ccmod2D*, *pms4m2D*). Outward flows are indicated in pink, while inward flows are in blue; the zero point in velocity is black. The maximum and minimum values of the color scale are defined by a radial velocity magnitude near the maximum for each simulation: *bg2D* ( $\pm 6.5$  km/s), *wm2D* ( $\pm 2.9$  km/s), *dcs2D* ( $\pm 0.63$  km/s), *cc2D* ( $\pm 1.5$  km/s), *ccmod2D* ( $\pm 6.7$  km/s), *pms4m2D* ( $\pm 7.5$  km/s). . . . . 70

Figure 4.2 Visualizations of vorticity in the  $\phi$  direction in 2D simulations (first row, left to right: *bg2D*, *wm2D*, *dcs2D*, and *cc2D*, (second row, left to right: *ccmod2D*, *pms4m2D*). Flows with high vorticity are indicated in white, while zero vorticity is represented in blue. High vorticity identifies eddies in the convection zone and internal gravity waves in the radiative zone. . . . . 71

Figure 4.3 A comparison of radial velocity in the  $3M_{\odot}$  red giant star from (left) 2D simulation *bg2D*, and (right) 3D simulation *bg3D*. The visualization is zoomed in on a small region inside the convection zone to emphasize the differences in the shape of convection between 2D and 3D. Outward flows are indicated in pink, while inward flows are in blue; the zero point in velocity is black. The maximum and minimum values of the color scale are defined by a radial velocity magnitude near the maximum for each simulation: *bg2D* ( $\pm 6.5$  km/s), *bg3D* ( $\pm 2.9$  km/s). . . . . 78

Figure 4.4 The radial profile of (a) the RMS radial velocity  $v_{r,\text{RMS}}$  and (b) the local  $\phi$  enstrophy for 2D and 3D simulations of the  $3M_{\odot}$  red giant star. Figures (c) and (d) are the corresponding plots for the  $20M_{\odot}$  convective core simulations. The lines indicate a time average, taken over the entire simulation time, of the horizontally averaged radial profile. The shaded regions represent one standard deviation above and below the time-averaged line. The radial position of the convective boundary, calculated by the Schwarzschild criterion, is indicated by a vertical black line. The interior radial coordinate of the star  $r$  is normalized by the star's radius  $R$ . . . . . 79

Figure 4.5 Radial profile of the volume-percentage filling factor of (a) the inward moving plumes  $\sigma_{\text{vp},\text{in}}$  for simulations  $bg2D/bg3D$  and (b) the outward moving plumes  $\sigma_{\text{vp},\text{out}}$  for simulations  $cc2D/cc3D$ . The solid and dashed lines indicate time-averaged radial profiles. Shaded areas indicate one standard deviation above and below these averaged lines. A thin vertical line indicates the convective boundary determined by the Schwarzschild criterion. . . . . 83

Figure 4.6 Radial profile of the normalized kinetic energy flux,  $F_k$  for (a) the  $3 M_{\odot}$  red giant star  $bg2D$ , (b) the  $6 M_{\odot}$  main sequence star with a convective core  $ccmod2D$ , and (c) a  $4 M_{\odot}$  pre-main sequence star  $pms4m2D$ . The solid and dashed lines indicate time-averaged radial profiles. Shaded areas indicate one standard deviation above and below these averaged lines. A thin vertical line indicates the convective boundary determined by the Schwarzschild criterion. 84

Figure 4.7 The time-averaged (a) volume-percentage and (b) mass-flux filling factor evaluated at the convective boundary determined by the Schwarzschild criterion,  $\sigma_{\text{CB}}$ , vs the overshooting depth in units of the pressure scale height at the convective boundary  $\ell_{\text{ov}}/H_{p,\text{CB}}$  for all simulations described in Table 4.1. Error bars indicate one standard deviation around the time-averaged value of  $\sigma_{\text{vp},\text{CB}}$ . Error bars obtained in the calculation of the overshooting depth  $\ell_{\text{ov}}$  are smaller than the size of the data points. . . . . 85

Figure 4.8 The radial profile of time-averaged convective flux for (a) the  $3 M_{\odot}$  red giant star  $bg2D$ , (b) the  $6 M_{\odot}$  main sequence star with a convective core  $ccmod2D$ , and (c) a  $4 M_{\odot}$  pre-main sequence star  $pms4m2D$ , normalized to its maximum magnitude value. The shaded region represents one standard deviation in time, above and below the time-averaged line. The radial position of the convective boundary determined by the Schwarzschild criterion is indicated by a vertical black line. . . . . 88

Figure 4.9 Left: The radial profile of the time-averaged filling factor  $f_z$  as defined in eq. (4.10) for 2D and 3D simulations of the  $3M_\odot$  red giant star. The lines indicate a time average, taken over the entire simulation time, of the horizontally averaged radial profile. The shaded regions represent one standard deviation above and below the time-averaged line. The radial position of the convective boundary determined by the Schwarzschild criterion is indicated by a vertical black line. Right: Radial profile of the absolute difference  $|f_z - f_{\text{comp}}|$  between the incompressible convective-flux filling factor and the compressible convective-flux filling factor for 2D and 3D simulations of the  $3M_\odot$  red giant star. The radial position of the convective boundary determined by the Schwarzschild criterion is indicated by a vertical black line. . . . . 92

Figure 5.1 The Anders penetration parameter  $P_A$  vs the overshooting depth in units of the pressure scale height at the convective boundary determined by the Schwarzschild criterion  $\ell_{\text{ov}}/H_{p,CB}$  for all 2D and 3D simulations described in Table 4.1. Error bars consider one standard deviation of the convective flux at each of the two radial points that contribute to this number. A logarithmic scale is applied to the vertical axis because this parameter, as formulated, can be larger than one. . . . . 97

Figure 5.2 Time-averaged profiles of the width of inflows for the young sun simulations (a) in *wide2D/3D*, and (b) in three versions of *bg2D*, each with a different grid size. The radial position of the convective boundary determined by the Schwarzschild criterion is indicated by a vertical black line. . . . . 100

Figure 5.3 Time-averaged profiles of skewness and excess kurtosis of the width of inflows for the red giant simulations (a) in *bg2D*, and (b) *bg3D*. The radial position of the convective boundary determined by the Schwarzschild criterion is indicated by a vertical black line. . . . . 103

Figure 5.4 Time-averaged profiles of skewness and excess kurtosis of the width of inflows for the young sun simulations (a) in *wm2D*, and (b) *wm3D*. The radial position of the convective boundary determined by the Schwarzschild criterion is indicated by a vertical black line. . . . . 103

Figure 5.5 Time-averaged profiles of the number of inflows for the current sun simulations (a) in *dcs2D/3D*, and (b) in three versions of *bg2D*, each with a different grid size. The radial position of the convective boundary determined by the Schwarzschild criterion is indicated by a vertical black line. . . . . 105

Figure 5.6	Number of inflows vs. internal radius for (a) a star with a large convective envelope <i>bg2D</i> , (b) a star with a shallow convective envelope <i>dcs2D</i> , and (c) a star with a small convective core <i>cc2D</i> . The gray box represents the radiative zone, determined by the Schwarzschild criterion. . . . .	107
Figure 5.7	(a) The average number of outflows as a radial profile for a high-resolution convective core, <i>ccmod2D</i> . (b) The average number of inflows as a radial profile for a high-resolution large convective envelope, <i>pms4m2D</i> . The gray boxes represent the radiative zones. The pink and blue shaded regions represent one standard deviation above and below the mean. . . . .	109
Figure 5.8	Nondimensional ratios (a) the plume interaction parameter, and (b) the ratio of average numbers of plumes $N_{CZ}/N_{OL}$ vs the overshooting depth in units of the pressure scale height at the convective boundary determined by the Schwarzschild criterion, $\ell_{ov}/H_{p,CB}$ , for all simulations studied in this work. A logarithmic scale is applied to the vertical axis, which is identical for (a) and (b). The dots represent 3D simulations, and the triangles represent 2D simulations. . . . .	110
Figure 6.1	(a) Evolutionary tracks for 10 pre-main sequence stars with masses ranging from 1.2-6 $M_{\odot}$ modeled with the MESA code. (b) Mass-luminosity relationship for the pre-main sequence stars in this study, where $L/L_{\odot} \sim (M/M_{\odot})^{2.8}$ . . . . .	118
Figure 6.2	Convective velocities for 10 pre-main sequence stars with masses ranging from 1.2-6 $M_{\odot}$ (a) calculated in MESA and (b) calculated in MUSIC simulations. Both (a) and (b) are scaled by the luminosity, such that $v_{conv} \sim (L/L_{\odot})^{1/3}$ . (c) The Mach number calculated in MESA approaches 0.1 in the 6 $M_{\odot}$ star. . . . .	119
Figure 6.3	2D MUSIC visualizations of (a) vorticity and (b) radial velocity for the 3.5 $M_{\odot}$ star, PMS3p5. Dark purple represents zero vorticity, and white represents maximum vorticity. The maximum enstrophy value is $2.5 \times 10^{-8}$ for this snapshot. For the velocity, pink represents outflows and blue represents inflows, where black is the zero point. The maximum velocity magnitude is $\pm 2.6$ km/s. . . . .	122
Figure 6.4	Volume-percentage (a) and mass-flux (b) filling factor profiles for ten pre-main sequence stars with shallow convection zones. The convective boundary for each star is located at $r = 0.8R_*$ , which is represented by a vertical black line. The dashed horizontal line represents a filling factor value of one-half. . . . .	123

Figure 6.5	Distances $\ell_{\sigma_{vp}}$ (purple dots) and $\ell_{W_{OL}}$ (pink triangles) as a function of (a) stellar mass and (b) the overshooting depth. Both plots have a log-log scale. . . . .	124
Figure 6.6	Width (a), and number (b) of inflows for 10 pre-main sequence stars ranging from 1.2 to 6 $M_{\odot}$ . The shaded regions represent one standard deviation above and below the time-averaged mean. The vertical line represents the Schwarzschild boundary, where the convection zone is to the right of this boundary. . . . .	126
Figure 6.7	Plume interaction parameter $\sigma_{int}$ (red dots) and $\sigma_{merge}$ (blue triangles) as a function of (a) stellar mass and (b) convective overshooting depth for 10 pre-main sequence stars ranging from 1.2 to 6 $M_{\odot}$ . A logarithmic scale is applied to both axes. The solid lines are linear fits to the data points. . . .	128
Figure 6.8	The average width of inflows vs. the average number of inflows for all values where the radius is greater than or equal to the radial point where $r = r_{CB} - \ell_{\sigma_{vp}}$ . The bottom right shows the large number of inflows at the photosphere, and the trend increases up to the peak at the top left of the plot as the convection zone deepens. The peak in the top left corresponds to both $N_{CZ}$ and $W_{CZ}$ , which are represented by triangles color-coded to the stellar mass. The width-number relation decreases less steeply as it encounters boundary layer flows, and reaches the final inflection point at the values for $N_{OL}$ and $W_{OL}$ , which are represented by the circles. . . . .	130
Figure 6.9	The Anders penetration parameter as a function of (a) stellar mass and (b) convective overshooting depth. The uncertainty on each point is calculated using the standard deviations of convective flux for the two points used in the calculation. The simulations PMS1p2, PMS1p5, PMS1p7, PMS2p0, PMS2p5, PMS3p0, PMS3p5, PMS4p0, PMS5p0, and PMS6p0 correspond to the colors red, dark orange, light orange, yellow, lime green, green, light blue, blue, indigo, and violet. . . . .	131
Figure 7.1	(a) HR diagram for a 3 $M_{\odot}$ red giant with solar metallicity. The points represent the structures chosen for the eight <b>MUSIC</b> simulations, which are located on the luminosity bump and Hayashi line of the HR diagram. (b) Luminosity bump in a zoomed-in view of the HR diagram. . . . .	135
Figure 7.2	A zoomed-in version of Figure 1.3. Eight vertical lines indicate where the stellar structure was used to produce <b>MUSIC</b> simulations. The colors of the vertical lines correspond to the same color-coded points in Figure 7.1. . .	136

Figure 7.3	(a) The convective velocity for each RG model calculated with the MESA code. (b) The radial root-mean-squared velocity profile for each IN red giant simulation, calculated with MUSIC. . . . .	139
Figure 7.4	(a) Gravity profiles for eight red giant stars. The vertical dashed lines represent the convective boundary, and the dots represent the value for gravity at the convective boundary. (b) Plume interaction parameter calculated with MUSIC scales with the value for gravity at the convective boundary. The models RG1, RG2, RG3, RG4, RG5, RG6, RG7, and RG8 correspond to red, orange, yellow, green, light blue, dark blue, indigo, and violet. . . . .	140
Figure 7.5	Volume-percentage (a) and the mass-flux (b) filling factor profiles for eight $3M_{\odot}$ red giant stars with different ages. The vertical lines represent the Schwarzschild convective boundary for each simulation. The shaded regions represent one standard deviation above and below the time-averaged mean. The dashed line represents a filling factor value of one-half. The red vertical line represents the Schwarzschild boundary for the youngest red giant with the largest convection zone size. The simulations IN1, IN2, IN3, IN4, IN5, IN6, IN7, and IN8 correspond to the red, orange, yellow, green, light blue, dark blue, indigo, and violet lines. . . . .	142
Figure 7.6	(a) The standard deviation in time of the horizontally-averaged volume-percentage filling factor at the convective boundary, $\sigma_{vp,CB}$ , as a function of the size of the convection zone in units of the total stellar radius. (b) The standard deviation in time of the maximum value of the average width of inflows in the convection zone, $W_{CZ}$ . The simulations IN1, IN2, IN3, IN4, IN5, IN6, IN7, and IN8 correspond to the red, orange, yellow, green, light blue, dark blue, indigo, and violet circles. . . . .	143
Figure 7.7	The distances $\ell_{\sigma_{vp}}$ (solid line, diamonds), and $\ell_{W_{ol}}$ (dashed line, triangles) (a) as a function of the size of the convective boundary and (b) as a function of the convective overshooting depth. The simulations IN1, IN2, IN3, IN4, IN5, IN6, IN7, and IN8 correspond to the red, orange, yellow, green, light blue, dark blue, indigo, and violet symbols. . . . .	144
Figure 7.8	The horizontally-averaged (a) width and (b) number of inflows for eight $3M_{\odot}$ red giant stars along the luminosity bump descent. The vertical lines represent the Schwarzschild convective boundary for each simulation. The shaded regions represent one standard deviation above and below the time-averaged mean. The red vertical line represents the Schwarzschild boundary for the youngest red giant with the largest convection zone size. The simulations IN1, IN2, IN3, IN4, IN5, IN6, IN7, and IN8 correspond to the red, orange, yellow, green, light blue, dark blue, indigo, and violet lines. . . . .	145

Figure 7.9	The average width of inflows as a function of the average number of inflows. The triangles represent the characteristic values in the convection zone ( $N_{\text{OL}}$ vs. $W_{\text{OL}}$ ), and the dots represent the characteristic values in the overshooting layer ( $N_{\text{CZ}}$ vs. $W_{\text{CZ}}$ ). . . . .	146
Figure 7.10	The average (a) width and (b) number of inflows as a function of the size of the convection zone, $r_{\text{CZ}}$ . Both $W_{\text{OL}}$ and $N_{\text{OL}}$ exhibit a linear trend until $r_{\text{CZ}} = 0.625$ . The simulations IN1, IN2, IN3, IN4, IN5, IN6, IN7, and IN8 correspond to the red, orange, yellow, green, light blue, dark blue, indigo, and violet circles. . . . .	148
Figure 7.11	Two-point diagnostics $\sigma_{\text{int}}$ (dots) and $\sigma_{\text{merge}}$ (triangles) as a function of (a) convective boundary and (b) convective overshooting depth. The simulations IN1, IN2, IN3, IN4, IN5, IN6, IN7, and IN8 correspond to the red, orange, yellow, green, light blue, dark blue, indigo, and violet circles. . . . .	149
Figure 8.1	The average width of inflows as a function of the average number of inflows for the simulations presented in this work. Two simulations from Dethero et al. (2024), <i>cc2D</i> and <i>dcs2d</i> , are shown in orange, the pre-main sequence stars introduced in Section 6.1 are shown in blue, and the red giants introduced in Section 7.1 are shown in red. A star with a large envelope on the pre-main sequence, <i>pms4m</i> , is shown in green. The triangles represent characteristic points in the convection zone, and the dots represent characteristic points in the overshooting layer. The inset plot is a zoomed-in view of the transition region from numerous, narrow to few, fat inflows, represented by a white square with a black outline. . . . .	159
Figure 8.2	The range of average widths of inflows for the simulations presented in this work. Three main sequence simulations with small convection zones, <i>cc2D</i> , <i>dcs2d</i> , and <i>ccmod2D</i> , are shown in orange, the pre-main sequence stars introduced in Section 6.1 are shown in blue, and the red giants introduced in Section 7.1 are shown in red. Two stars with a large envelope on the pre-main sequence, <i>wide2d</i> and <i>pms4m2D</i> , are shown in green. . . . .	161

## CHAPTER 1

### Introduction

#### 1.1 Stellar modeling plays a foundational role in the field of astronomy

Large space-based surveys, including Kepler (Gilliland et al. 2010), CoRoT (Baglin et al. 2008; Moutou et al. 2013), Gaia (Perryman 2005; Vallenari et al. 2023), and the Transiting Exoplanet Survey Satellite (TESS) mission (Ricker et al. 2015) have produced an enormous amount of data related to stellar populations and clusters. Large-scale stellar surveys enable the assembly of catalogs of stellar distances and magnitudes (Berger et al. 2020b,a), as well as catalogs of binary stars with periods, separations, radius ratios, and eccentricities (Prša et al. 2011; Slawson et al. 2011; Kirk et al. 2016). Combined with Gaia parallaxes and photometries, this observational data can be used to infer stellar mass and luminosity (Justesen & Albrecht 2021). However, only by comparing these parameters to 1D stellar evolution models can the age of a star be estimated (Stassun et al. 2014; Hillenbrand & White 2004). A stellar structure model can then be associated with a star to understand the possible stratification of density, temperature, and pressure and how this is linked to the hydrodynamics of the stellar interior. Applying theoretical modeling of stellar interiors this way is essential for the interpretation of these large data sets.

Stellar models are also an essential tool for understanding galaxies. Stars naturally form clusters, which combine to create galaxies. By observing the combined light from populations of stars in galaxies, astronomers gain crucial insights into the structure and evolution of galaxies (Milone et al. 2011; Milone & Marino 2022; Cantat-Gaudin et al. 2020).

A galaxy’s spectral energy distribution (SED) contains information on its stellar populations: metallicity, age, and amount of star formation present (Conroy 2013). Stellar populations are synthesized based on stellar isochrones using an initial mass function, isochrones, and stellar spectra. Because stellar isochrones are based on connecting stars of the same age, they are fundamentally dependent on stellar structure and evolution calculations. Stellar evolution modeling thus underpins the SED model (Ferraro et al. 2006; Girardi et al. 2000).

One achievement of stellar evolution modeling is its ability to interpret the Hertzsprung-Russell (HR) diagram (see Figure 1.1). Stellar evolution models are able to produce ages and time-relationships between the stars that observers plot on HR diagrams. However, matching observational data and modeled parameters involves some error. For low mass stars (roughly  $0.35\text{--}0.8M_{\odot}$ ) a 10% discrepancy exists between observed and modeled radii (Lacy 1977; Chabrier et al. 2009; Garrido et al. 2019; Kraus et al. 2011; Morrell & Naylor 2019; Torres & Ribas 2002; Chabrier et al. 2007); this is called the ‘radius inflation problem’. For Cepheid variable stars (roughly  $3.0\text{--}9.0M_{\odot}$ ) masses calculated from orbital dynamics of companion stars, or from pulsation modeling, are smaller than those determined from standard stellar evolution models, with the discrepancy being as much as 20% (Guzik et al. 2023; Evans et al. 2018); this is called the “Cepheid mass discrepancy problem.” Models predict that solar-like stars on the main sequence should have higher surface abundances of lithium than observations find (Dumont et al. 2021; Baraffe et al. 2017; Constantino et al. 2021; Binks et al. 2022; Bildsten et al. 1997; Piau & Turck-Chieze 2002). The shallow convective envelopes in these stellar models do not reach depths with temperatures hot

enough to burn lithium, so the amount of lithium in the envelope should not be depleted as much as observations suggest. This is called the “lithium depletion problem.” In addition to the abundance of lithium on the main sequence, Li et al. (2024) investigate the “1% problem,” in which 1% of red giants, mostly in the red clump region of the HR diagram, have an abundance of lithium in their atmospheres. Stellar structure and evolution models would predict that, after the first dredge-up, lithium should be depleted due to the movement of the convective boundary deep into the star. These are just a few of the more prominent examples of errors between observational values and models. However, significant differences between observational data and models play a role in stellar astronomy. For example, the Center for High Angular Resolution Astronomy (CHARA) Array has the capability of identifying fundamental stellar parameters of eclipsing binary stars using long-baseline interferometry (e.g. Lester et al. 2019; Evans et al. 2024). Recently CHARA observations enabled the calculation of stellar mass, radius, and temperature for the eclipsing binary system BW Aquarii; Lester & Gies (2018) produced evolutionary models for these stars using both MESA and YREC, but neither could reproduce their observational data for both systems at the same age within 5% error. Observational astronomers work to improve and expand their measurements; stellar evolution calculations also need to become more sophisticated to meet the need to interpret stellar data.

The one-dimensional parameterization of convection is a likely source of error in stellar evolution models (Kupka & Muthsam 2017; Joyce & Tayar 2023; Salaris & Cassisi 2017; Lovekin 2020). Observations are limited to phenomena that can be observed exterior to

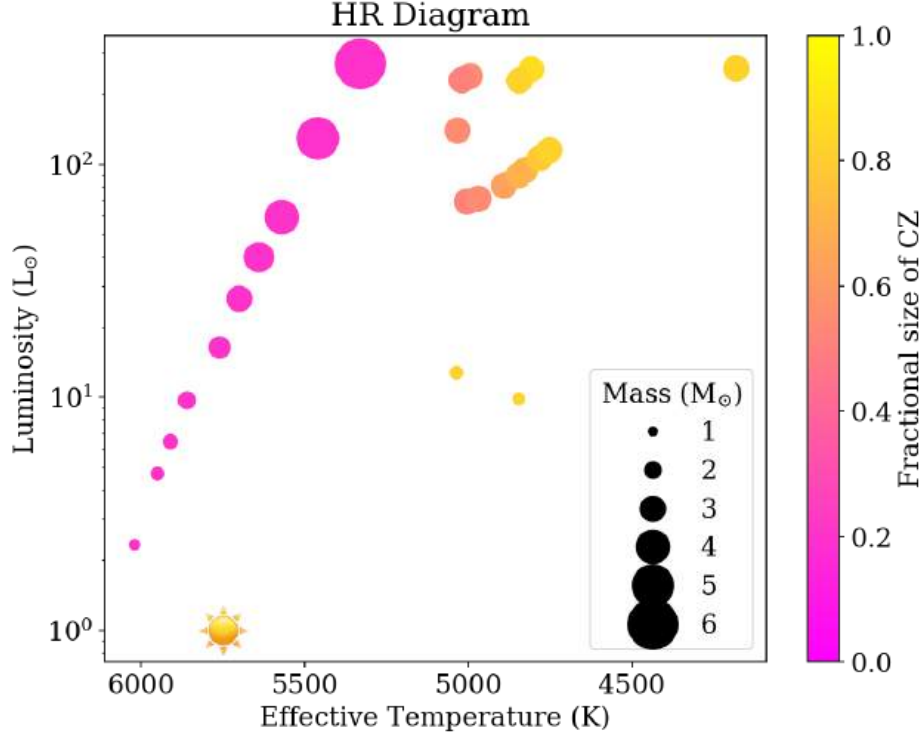


Figure 1.1 Hertzsprung-Russell (HR) diagram including 26 stars whose structures we modeled using the MESA code (Paxton et al. 2010) and then simulated using the MUSIC code (Pratt et al. 2016, e.g.). The stars here represent different masses ( $1 M_{\odot}$  to  $6 M_{\odot}$ ), evolutionary stages from the pre-main sequence to the red giant branch, and metallicities ( $z = 0.0005$  to  $z = 0.02$ ). The color bar represents the size of the convection zone (CZ) in fractional units of the total stellar radius ( $0.2 R_*$  to  $0.825 R_*$ ). The marker size corresponds to the stellar mass. The Sun is plotted for reference.

a star; however, a range of measurements provide indications that stellar convection is a complex and significant process in stellar interiors. The depth of convective envelopes can be estimated using an analysis of the non-radial oscillations in stars (Aerts 2021; Grassitelli et al. 2015), a method developed in the field of asteroseismology. These calculations depend on the quality of stellar structure and evolution models (as discussed by Joyce & Chaboyer 2018; Viani et al. 2018). Convective velocities can be detected just below the stellar surface using spectropolarimetry techniques, where the line-of-sight velocities of infrared iron lines

can be used to constrain convective velocities (Milić et al. 2019). X-ray emissions are linked to magnetic activity on the pre-main sequence, which is attributed to convective dynamos (Preibisch & Feigelson 2005). The activity-rotation relationship suggests that a longer rotation period causes less mixing and shear in the stellar interior, which leads to fewer, weaker X-ray emissions (Schrijver & Zwaan 2008). The surface of the Sun exhibits granules and super granules that are caused by convection (Hirzberger et al. 2008; Rincon & Rieutord 2018; Vieweg et al. 2021). Reconstructions of images obtained with the CHARA Array have revealed plausible evidence of giant convection cells visible on the surface of the massive star  $\rho$  Cassiopeiae (Anugu et al. 2024). Similarly, interferometric imaging has been used to extract convective velocities on the surface of the massive star R Doradus (Vlemmings et al. 2024) and the AGB star CL Lac (Chiavassa et al. 2020). The range and structure of convective flows that observations find in stars point to a fundamental problem in hydrodynamics: that of multi-scale flows.

The properties of stellar convection can be linked to space weather activity and exoplanet habitability. Convection relates to solar atmospheric phenomena and the resulting solar storms and space weather (Schwenn 2006). This activity poses radiation risks to satellites and astronauts operating beyond Earth’s protective magnetosphere (Buzulukova & Tsurutani 2022). In extreme cases, the radiation from solar storms can disrupt terrestrial technology, as exemplified by the Carrington Event of 1859 (Cliver 2006). Predicting these events requires a deeper understanding of the mechanisms driving stellar activity, including stellar convection. Convective flows within the solar interior interact with differential rota-

tion through the dynamo effect to produce a large-scale magnetic field, which allows for flares (Parker 1955; Brandenburg & Subramanian 2005). We observe magnetic activity on other stars through their high-energy spectra. On the main sequence, 11% of M-type stars exhibit strong magnetic activity (Yang et al. 2017). G-type stars like the Sun are generally less likely to be as active than low mass stars, with around 1% exhibiting magnetic activity (Balona 2012). However, the Sun is expected to have been much more magnetically active during the pre-main sequence, which includes the planet-formation phase (Güdel 2020). Astronomers study young stellar objects (YSOs) that resemble the early Sun before life emerged on Earth to understand what stellar events lead to habitable conditions. Superflares, defined as highly energetic X-ray flares exceeding  $5 \times 10^{34}$  ergs (Namekata et al. 2022), have been observed on YSOs such as DS Tuc (Pillitteri et al. 2022; Dethero et al. 2023). This indicates strong magnetic activity, and thus stellar convection, play a role in planet habitability. Understanding stellar convection is essential to understanding our Sun, space weather, and the environment of exoplanets.

## 1.2 Thermal convection is a complex problem

Thermal convection arises in a layer of fluid whenever the temperature gradient across that layer produces a Rayleigh number that is larger than the critical value (e.g. Busse 1978; Ahlers et al. 2009). Because this situation happens in a wide variety of applications, thermal convection is studied across many disciplines, including atmospheric and climate sciences, oceanography, engineering, and mathematics. In fundamental laboratory experiments, ther-

mal convection is often studied in the setting of a thin layer where a temperature gradient is imposed by a heated plate below with temperature  $T_{\text{bot}}$  and a cool plate above the fluid with temperature  $T_{\text{top}}$ . This is called Rayleigh-Bénard convection (RBC), one of the most thoroughly researched problems in fluid dynamics (e.g., Funfschilling et al. 2009; Ahlers et al. 2017; Shi et al. 2012; Scheel & Schumacher 2014). An important parameter of the RBC set-up is the aspect ratio  $\Gamma = L/H$  where  $L$  denotes a characteristic horizontal scale such as the diameter of a convection cell, and  $H$  is the height of the box.

Bénard first conducted experiments on this phenomenon, and Lord Rayleigh later interpreted the results in the early 1900s (Chandrasekhar 1957). Lord Rayleigh established two key findings. First, a critical temperature gradient,  $\beta = (T_{\text{bot}} - T_{\text{top}})/H$ , must be exceeded to trigger convective motion. The onset of convection is determined by the Rayleigh number,

$$\text{Ra} = \frac{\rho\alpha\Delta TH^3g}{\nu\kappa}, \quad (1.1)$$

where  $g$  is gravitational acceleration,  $\nu$  is the kinematic viscosity,  $\kappa$  is the thermal diffusivity,  $\rho$  is the constant density, and  $\alpha$  is the thermal expansion coefficient. A high Rayleigh number ( $\text{Ra} \gg 1$ ) indicates that buoyant forces dominate over viscous or diffusive damping. Convection begins when  $\text{Ra}$  exceeds a critical value,  $\text{Ra}_c \approx 1708$ , though the precise threshold depends on the boundary conditions (Chandrasekhar 1957; Choudhuri 1998). Rayleigh's second finding was that convective motions in RBC form a regular pattern of cells, usually called convection rolls, with each cell being roughly uniform in size. For such experiments, it is typical to examine a small-aspect ratio experiment where  $\Gamma \ll 1$ . The fluid is heated until the critical Rayleigh number is reached, and the convection is maintained at a value

just above the critical Rayleigh number. Experiments of this kind have been used to study pattern formation. The RBC set-up has also been used to explore turbulent convection that is driven at higher Rayleigh numbers. For  $\text{Ra} \gg 2 \times \text{Ra}_c$ , the symmetric convective cells will transition into convective columns and plumes (Guzmán et al. 2021). When RBC becomes turbulent, the turbulent boundary layers at the plates separate from the bulk of the flow, which exhibits large-scale circulation (Chillà & Schumacher 2012; Ahlers et al. 2009; He et al. 2012).

Aside from fundamental experiments like the RBC, thermal convection is frequently found in industrial flow problems where it plays an important role in heat exchangers and solar collectors (Ahlers 2009; Kim et al. 2023), and laser powder bed fusion additive manufacturing (Foteinopoulos et al. 2018; Yan et al. 2018). An understanding of thermal convection in liquid metals is also essential to understanding the blankets of fusion reactors and fission reactors, which transport heat from the reactor to energy generation systems. In these situations the convection is part of a multi-physics system (Smolentsev 2023; Bühler et al. 2024). Liquid metals exist in a different regime from stellar plasmas, as classified by the Prandtl and magnetic Prandtl numbers. These nondimensional numbers correspond to different flow structuring and shape (Van Der Poel et al. 2013; Pratt et al. 2020) as well as different properties of heat transport (e.g., Schmalzl et al. 2002; Ahlers & Xu 2001).

These laboratory fluid dynamics problems typically study the Boussinesq limit, i.e., the limit where the fluid is incompressible (constant density) except for a small buoyancy force (Glatzmaier 2013; Mayeli & Sheard 2021). However, the RBC set-up has also been studied in

the non-Boussinesq regime (e.g., Zhang et al. 1998). The most significant observation from such studies is that the upflows and downflows are asymmetric; they fill different volumes and have different densities. Stellar interiors involve significant changes in density, so that the non-Boussinesq regime is theoretically correct (Spiegel 1971; Glatzmaier 2013). In addition, the visible properties of granules and supergranules on the Sun (Hirzberger et al. 2008; Rincon & Rieutord 2018; Vieweg et al. 2021) exhibit the strong asymmetry between inflows and outflows that corresponds to non-Boussinesq convection.

Non-Boussinesq thermal convection is often seen in natural settings: the oceans, planetary atmospheres, and planetary interiors. Each of these settings involves a combination of physical influences that are distinct from that of stars. Oceanic convection is stratified, and influenced by the salt content of the fluid (Marshall & Schott 1999). Convection in planetary atmospheres is impacted by the moisture levels, the land or water beneath the atmosphere, and day-night cycles (Stevens 2005). Mantle convection consists of liquid metal that forms large-scale convective structures (Ogawa 2008; Trompert & Hansen 1998; Stein & Hansen 2023). Although each of these natural settings is affected by different physics than the convecting plasma in stellar interiors, parameterizing convection for one-dimensional models is a common problem.

### ***1.2.1 Thermal convection in the extreme environment of stellar interiors***

Stellar convection exhibits marked differences from Rayleigh-Bénard convection. In this work, we examine stars with convection zones on the pre-main sequence, main sequence, and red giant branch, which have convection zones that range between shallow and deep.

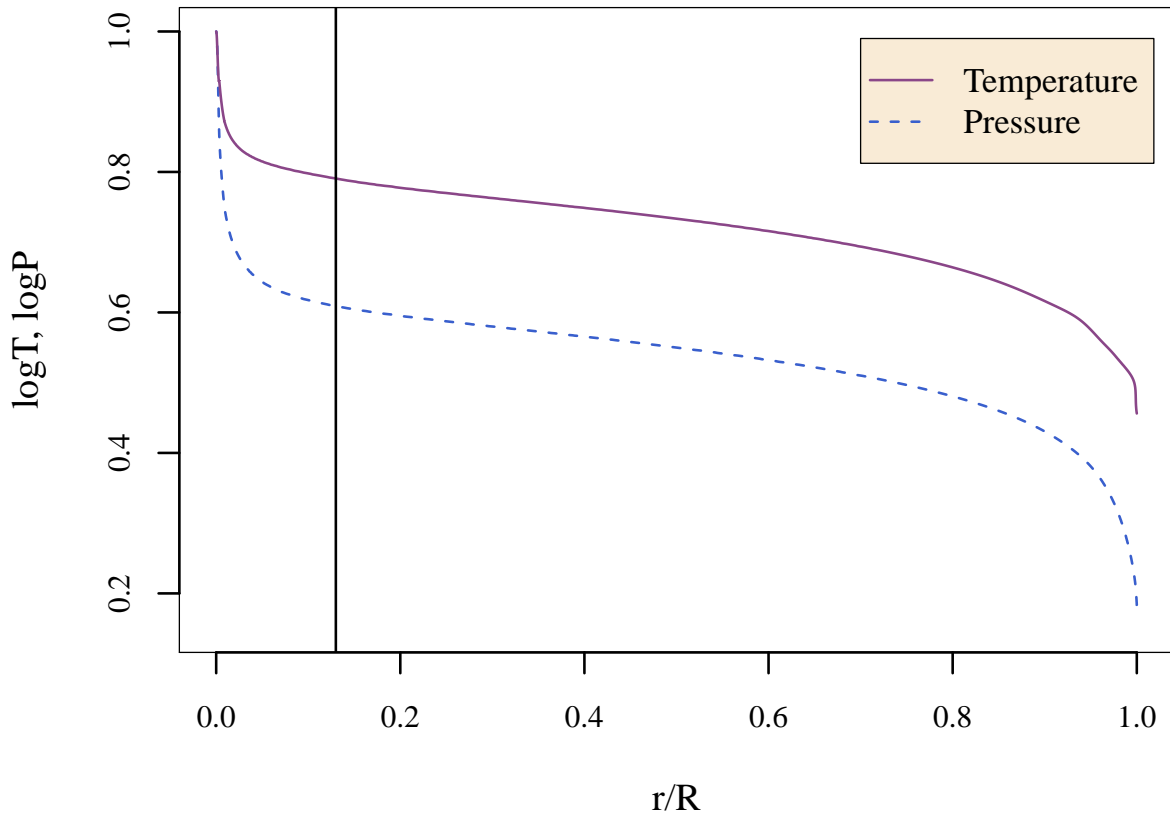


Figure 1.2 Temperature (solid purple) and pressure (dashed blue) profiles normalized to their maximum values for a  $3M_{\odot}$  red giant star, produced with the MESA code (Paxton et al. 2010). The maximum values are  $\log_{10} T = 8.05$  in units of Kelvin and  $\log_{10} P = 20.4$  in the cgs unit for pressure, dyne/cm<sup>2</sup>. The horizontal axis is the normalized radius where  $r/R = 1$  is the photosphere, which is the extent of the stellar interior. The vertical black line indicates the radial location of the Schwarzschild convective boundary.

The temperature and pressure profiles for a stellar structure of a  $3M_{\odot}$  red giant star are shown in Figure 1.2. This model was produced with the open-source, one-dimensional, stellar structure and evolution code, MESA (Paxton et al. 2010), version 10398, using the inlist in Appendix A. This red giant star achieves temperatures of up to  $11.2 \times 10^7$  K in its core. The temperature decreases nonlinearly with increasing radius, reaching  $\approx 4 \times 10^3$

K at the photosphere. The study of matter under extreme densities and pressures is the basis of a field of physics called high energy density science. Stellar convection involves these complicated states of matter, as well as extreme stratification. Stellar convection zones are stratified, with a large density difference between the bottom and the top of the convective layer. For example, in this  $3 M_{\odot}$  red giant star, the density ratio is  $\approx 200$ ; the density ratio across the convection zone in a pre-main sequence star that we study is greater than  $10^5$ . Linked to this is the fact that the temperature gradient across the convective layer is nonlinear; this leads to different regions of a convection zone being more unstable to the convective instability than others, effectively creating a flow that is influenced by a range of driving rates. Convection in highly stratified environments creates multi-scale fluid flows, a grand challenge problem in the field of fluid dynamics.

Convection is a particularly complex fluid phenomenon because it is non-local (e.g., Canuto 2006): the behavior of convection in one region depends sensitively on the behavior of convection in other regions. The consequence is that, for example, changes to models near the photosphere will affect the properties of convection throughout the full radius of a star. As a fluid dynamics phenomenon, convection is non-linear and drives turbulence (Ahlers 2009; Busse 2005). It is often quoted that the Rayleigh number in the solar convection zone is on the order of  $Ra \approx 10^{20}$  (e.g., Ossendrijver 2003). However, stellar convection zones are defined by non-linear temperature gradients (see the solid purple line in Figure 1.2), a non-linear density gradient, and changing viscosity and thermal diffusivities. In general, the Rayleigh number would be expected to have different average values at different values of

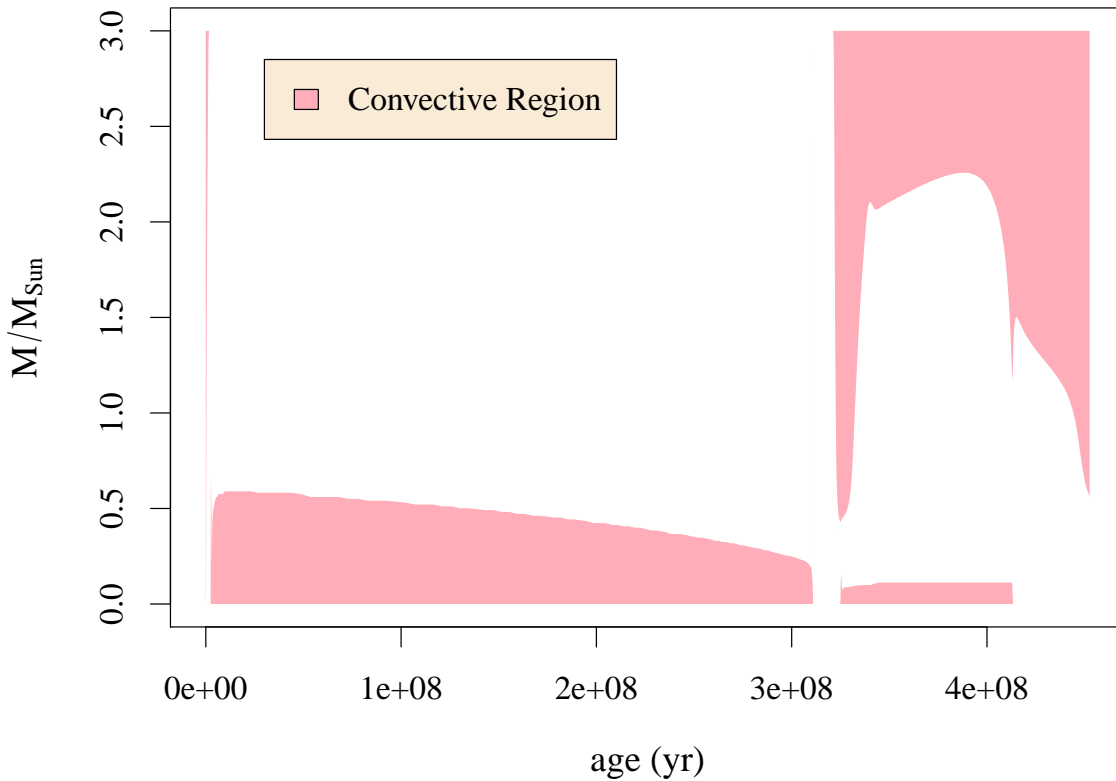


Figure 1.3 Kippenhahn diagram for a  $3M_{\odot}$  star produced with the MESA code. The pink, shaded regions indicate areas of the star where convection is present. On the pre-main sequence, the star experiences a large convective envelope. The star has a convective core and radiative envelope as it begins to fuse hydrogen on the main sequence. When all the hydrogen fuses into helium in the core, the star moves into the red giant phase, where two convection zones form, one in the envelope and a much smaller one in the helium core.

the internal radius of the star. The material that makes up stars – a warm, dense plasma – does not correspond to an ideal gas. The range of parameters in stellar interiors leads to so-called “microphysics” which influences the flow. This consists of a tabulated equation of state (e.g., Oertel et al. 2017; Chabrier & Schatzman 1994; Van Horn 1994) accompanied by tabulated opacities (Farag et al. 2024; Colgan et al. 2016; Rogers & Nayfonov 2002; Iglesias & Rogers 1996) that correspond to the conditions and chemical composition of a star.

The location and extent of convection zones change as a star evolves. Convection zones can occur in the core, in any number of internal shells, or as an outer envelope. For example, in a  $3M_{\odot}$  star, convection occurs in both the core and envelope at different evolutionary stages, as illustrated by the Kippenhahn diagram (Figure 1.3). In this diagram, pink-shaded regions indicate convective zones and white regions represent radiative zones. At the beginning of this star’s evolution, it is fully convective. It develops a radiative core during the pre-main sequence. On the main sequence, it develops a convective core where it spends billions of years fusing hydrogen into helium. Once the hydrogen fuel is exhausted, the star transitions onto the red giant branch (RGB) (Salaris et al. 2002). As the star ascends the RGB, helium fusion occurs in the small convective core, while hydrogen shell-burning takes place in an outer convective envelope (Kippenhahn et al. 2013, Section 31.2). The outer convective envelope deepens until the first dredge-up point. After this point, the outer convective envelope becomes shallower again (Cassisi 2017). Along with these changes in convection zone location and size, stars experience a range of different stratifications in density, pressure, and temperature that can lead to more vigorous convection or contribute to multi-scale flows.

Another interesting problem is how convection zones interact with stable zones, also known as convective boundary mixing. Zahn (1991) describes the process of ‘overshooting’ in which convective plumes ‘overshoot’ from the convection zone into the radiative zone due to high convective velocities. The contribution of overshooting toward the amount of stellar mixing has been characterized by a single length scale, the overshooting length. Convective

overshooting and penetration can influence stellar structure and evolution, but measuring these contributions is challenging.

### **1.3 Multi-dimensional hydrodynamic simulations of stars provide a way forward**

The field of stellar hydrodynamics originated in the 1990s with codes developed to simulate realistic stellar atmospheres using Cartesian grids. The MURaM code (Vögler et al. 2005; Schüssler et al. 2005) and the CO5BOLD code (Steiner et al. 2007; Freytag et al. 2012; Beeck et al. 2012) are two examples that remain in use today. As the capability of supercomputing infrastructure increased, stellar simulations increasingly treated whole spheres. The first efforts used polytropes to create convectively unstable regions within the sphere, and often included only a convection zone (similar to the benchmarking problems described in Jones et al. 2011). Stellar simulations became increasingly realistic in time (Rogers et al. 2006; Browning 2008; Matt et al. 2011; Augustson et al. 2012; Herwig et al. 2014; Woodward et al. 2014; Clarkson et al. 2019; Röpke et al. 2018; Andrassy et al. 2022).

The current state-of-the-art of stellar hydrodynamics employs codes that are an extension of stellar structure and evolution models. These codes use density, temperature, and pressure profiles produced by one-dimensional structure calculations, tabulated equations of state (EOS), and opacities that constitute the accurate microphysics for stellar interiors. While they are not able to follow the evolution of the star over its long lifetime, stellar hydrodynamic codes can provide a window into the large-scale fluid dynamics of stellar interiors.

## 1.4 The goals for this work

Stellar modeling underpins our understanding of galactic, solar, and planetary astronomy. However, the models for stellar structure and evolution do not account for multi-dimensional, multi-scale, and nonlocal effects of convection, or for convective boundary mixing. The convective flux, velocity, and efficiency used in these one-dimensional models lack realistic physics, limiting the predictive power and ability to interpret observations.

The work presented in this dissertation has three main objectives: (1) to examine the utility of available one-dimensional parameterizations of stellar convection, (2) to develop new diagnostics for stellar convection, and (3) to link properties of stellar convection to the extent of convective boundary mixing for a wide range of stars. Our results are based on global simulations produced with the Multi-dimensional Stellar Implicit Code (*MUSIC*), as well as stellar structures calculated with the open-source stellar structure and evolution code *MESA* (Paxton et al. 2010). We survey the current capabilities of 1D convection models in Chapter 2 and multidimensional stellar simulations in Chapter 3. Chapter 4 examines the one-point statistic called the filling factor for stellar convection, which theorists define differently across the literature. Chapter 5 examines two-point statistics that are predictive of convective boundary mixing, including a penetration parameter defined by Anders et al. (2022) and a new parameter introduced in Dethero et al. (2024) that connects the shape of convection to stellar theory, called the plume interaction parameter. Chapters 6 and 7 apply the plume interaction parameter to stars with different ages and masses, assessing its utility to describe convection and predict convective overshooting. Chapter 8 summarizes

the results and implications of this body of work.

## CHAPTER 2

### Modeling Stellar Convection

Because the interior of stars cannot be directly observed, models are needed to provide an understanding of the interior conditions of a star. There are many tools for calculating stellar evolution models, including the Modules for Experiments in Stellar Astrophysics (MESA) (Paxton et al. 2010, 2013), the Lyon stellar evolution code (Baraffe et al. 1998), the Dartmouth Stellar Evolution Program (Dotter et al. 2008), the PAdova and TRieste Stellar Evolution Code (PARSEC) (Nguyen et al. 2022), the Evolution STellaire en Rotation (ESTER) code (Rieutord et al. 2016), the Yale Rotating Stellar Evolution Code (YREC) (Demarque et al. 2008), the Garching Stellar Evolution Code (GARSTEC) (Weiss & Schlattl 2008), the ATON stellar evolution code (Ventura et al. 2008), the binary stellar evolution code BINSTAR (Siess et al. 2013), STAREVOL (Forestini & Charbonnel 1997), the Aarhus Stellar Evolution Code (ASTECC) (Christensen-Dalsgaard 2008), the CESAM code (Morel & Lebreton 2008), and STERN (Brott et al. 2011). This large number of different codes reflects the breadth of different models available for stellar interiors. Although the results of stellar evolution codes have sometimes been compared, e.g., as in the Aarhus red giants challenge (Aguirre et al. 2020), these models have only rarely been compared against one another. Typically a single stellar evolution code is used to generate grids of models which are then compared with observations. This makes it difficult to identify which of the many models for hydrodynamic effects used by these codes is more accurate than others. Here we discuss the basis for all stellar evolution codes and the models used to represent stellar

convection.

## 2.1 Stellar structure equations

Stellar structure and evolution models use a common set of one-dimensional (1D) equations. These equations use Lagrangian coordinates, the mass enclosed  $m(r)$ , rather than the internal radius of the star  $r$ , so that they can efficiently follow the changes in the radius of the star as it expands and contracts over its lifetime (for a complete discussion, see Kippenhahn et al. 2013, Section 10.1). These equations are

$$\frac{\partial r}{\partial m} = \frac{1}{4\pi r^2 \rho}, \quad (2.1)$$

$$\frac{\partial P}{\partial m} = \frac{-Gm}{4\pi r^4}, \quad (2.2)$$

$$\frac{\partial L}{\partial m} = \epsilon_{\text{nuc}} - \epsilon_{\nu, \text{thermal}} - \epsilon_{\text{grav}}, \quad (2.3)$$

$$\frac{\partial T}{\partial m} = \frac{-GmT}{4\pi r^4 P} \nabla, \quad (2.4)$$

$$\frac{\partial X_i}{\partial t} = \frac{m_i}{\rho} \left( \sum_j r_{ji} - \sum_k r_{ik} \right), i = 1, \dots, I. \quad (2.5)$$

Here  $P$  is pressure,  $T$  is temperature,  $m$  is mass,  $\rho$  is density, and  $r$  is the internal radius of the star. Eq. (2.1) is known as the mass continuity equation because it describes how the mass inside a perfect sphere changes with  $r$ . Eq. (2.2) is the equation for hydrostatic equilibrium, which balances gravitational acceleration  $g = -Gm(r)/r^2$  and the gradient of gas pressure  $P$ , where the gravitational constant is  $G = 6.6743 \times 10^{-8} \text{ dyn cm}^2 \text{ g}^{-2}$ . A star is in hydrostatic equilibrium if the only external forces felt by the fluid are the internal gas pressure  $P$  and

the gravity  $g$ , and those forces balance. A star could deviate from hydrostatic equilibrium if, for example, a close companion exerted an additional gravitational force (Kippenhahn et al. 2013, Section 2.1). The energy conservation equation, eq. (2.3), dictates how the luminosity  $L$  varies as a function of the mass coordinate. This rate of energy can be changed by nuclear reactions  $\epsilon_{\text{nuc}}$ , neutrino loss  $\epsilon_{\nu, \text{thermal}}$ , and or changes to gravitational energy  $\epsilon_{\text{grav}}$  because of contraction or expansion. Eq. (2.4) is the energy transport equation, where  $\nabla = \partial \ln T / \partial \ln P$ . The mass fraction evolution equation, eq. (2.5), is the final equation of stellar structure and evolution. It describes the evolution of chemical composition, which can change as the star fuses lighter nuclei  $i$  into heavier nuclei  $j$  with reaction rate  $r_{ji}$ .  $X_i$  is the individual mass fraction of nuclei type  $i$ . The majority of a star's material is hydrogen  $X_H$ , followed by helium  $X_{He}$ . The remaining content is usually described by the metallicity  $Z = 1 - X_H - X_{He}$ , which includes the abundances of all nuclei heavier than hydrogen and helium (Kippenhahn et al. 2013, Section 10.1). This structure can change over time as the mass fraction  $X_i$  changes due to hydrogen or helium fuel becoming exhausted due to the reaction rate  $r_{ji}$  for all nuclei  $i = 1, \dots, I$  (Kippenhahn et al. 2013, Section 10.1). For example, the current abundances measured on the Sun include  $X = X_H = 0.7438$ ,  $Y = X_{He} = 0.2423$ , and  $Z = 0.0139$ , as measured in a solar wind sample (Asplund et al. 2021).

Eqs. (2.1) – (2.5) describe the fundamentals of stellar physics. To be closed, and thus solvable, they also require opacities  $\kappa = \kappa(P, T, X_i)$  and an equation of state  $\rho = \rho(P, T, X_i)$ , which describes the dependence of density on pressure, temperature, and the mass fraction (Salaris & Cassisi 2017). These equations contribute to many stellar evolution codes;

however, each code uses different numerical methods to solve this set of coupled equations. Additional models are employed for rotation, differential rotation, chemical mixing, stellar convection, overshooting, semiconvection, magnetic fields, mass loss, and stellar winds. The contribution of convection to stellar structure and evolution is present in the energy transport equation in the term  $\nabla$ . It can also contribute to the mass fraction evolution equation if material is mixed from the core to the surface, or vice versa, over time. Because our focus is hydrodynamic simulations in stellar structures that are not evolving in time, we now examine the influence of convection on energy transport.

### ***2.1.1 Convective Instability***

The energy transport equation, eq. (2.4), describes the radial transport of energy through the star using a tracer of the temperature gradient  $\nabla = \left(\frac{\partial \ln T}{\partial \ln P}\right)$ . The value of  $\nabla$  used in stellar structure calculations requires a convection model. To determine where convection occurs in a star – whether in a core, shell, or envelope – the most basic criterion compares two quantities: the radiative temperature gradient  $\nabla_{\text{rad}}$ , which describes how temperature decreases with pressure due to radiative transfer, and the adiabatic temperature gradient  $\nabla_{\text{ad}}$ , which describes how temperature decreases as the plasma itself expands. The radiative gradient is defined using two key equations of stellar structure: the equation for hydrostatic equilibrium (eq. (2.2)) and the equation for thermal equilibrium (eq. (2.4)). By combining these equations, the radiative gradient is given by

$$\nabla_{\text{rad}} = \left(\frac{\partial \ln T}{\partial \ln P}\right)_{\text{rad}} = \frac{3}{16\pi acG} \frac{\kappa l P}{m T^4}. \quad (2.6)$$

Here  $a$  is the radiation density constant,  $l$  is the local luminosity,  $G = 6.6743 \times 10^{-8} \text{ cm}^3 \text{ g}^{-1} \text{ s}^{-2}$  is the gravitational constant, and  $c = 2.99 \times 10^{10} \text{ cm/s}$  is the speed of light (Kippenhahn et al. 2013, Section 6.1).  $\nabla_{\text{rad}}$  is the maximum temperature gradient a star can experience at any radial point, and represents how temperature changes in the presence of no convection.

The adiabatic gradient,  $\nabla_{\text{ad}}$ , represents the temperature change when the entropy  $S$  is held constant, implying no heat is lost to radiation when a vertically displaced fluid enters a cooler surrounding environment.  $\nabla_{\text{ad}}$  can be derived from the first law of thermodynamics:  $dq = du + PdV$ , where  $dq$  is the heat change,  $du$  is the change in internal energy, and  $PdV$  is the work done on the surroundings. Using the equation of state (Kippenhahn et al. 2013, Section 4.1), the first law can be written  $dq = c_P dT - \delta dP/\rho$ , where  $c_P$  is the specific heat at constant pressure,  $\delta = -\partial \ln \rho / \partial \ln T$ , and pressure  $P$  and mean molecular weight  $\mu$  are held constant. For the adiabatic case  $dq = 0$ , we therefore find  $(\partial T / \partial P)_S = \delta / c_P \rho$ . Thus, the adiabatic gradient can be expressed

$$\nabla_{\text{ad}} = \left( \frac{\partial \ln T}{\partial \ln P} \right)_{\text{ad}} = \left( \frac{P}{T} \frac{dT}{dP} \right)_S = \left( \frac{P}{T} \frac{\delta}{c_P \rho} \right)_S. \quad (2.7)$$

This gradient equals the true temperature gradient  $\nabla$  at any radial point where extremely efficient adiabatic convection takes place. For example, this is understood to occur in the convective cores of high mass stars.

The comparison of  $\nabla_{\text{rad}}$  and  $\nabla_{\text{ad}}$  at a given radial point determines whether the plasma is stable or unstable to convection at that point. This criterion for convection is known as

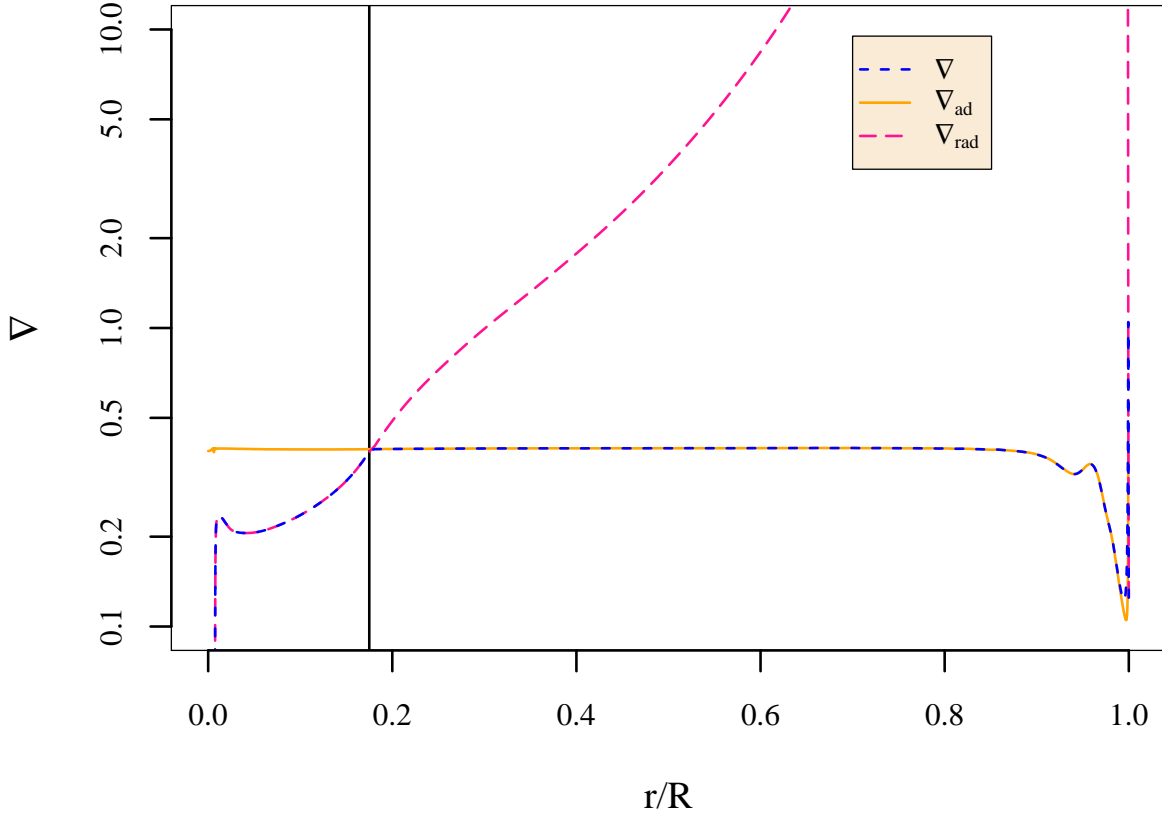


Figure 2.1 Temperature gradient for a  $1.365 M_{\odot}$  star with a large convection zone, modeled using the MESA code (Paxton et al. 2010). The temperature gradient  $\nabla = \partial \ln T / \partial \ln P$  profile is shown in dashed blue, the adiabatic gradient  $\nabla_{\text{ad}}$  is shown in solid orange, and the radiative gradient  $\nabla_{\text{rad}}$  is shown in dashed pink. The convective boundary is represented by a solid black line at  $r/R = 0.175$ ; to the left of this line is the radiative zone, and to the right of this line is the convective zone.

the Schwarzschild criterion, which is expressed as

$$\nabla_{\text{rad}} < \nabla_{\text{ad}} . \quad (2.8)$$

If eq. (2.8) holds, the fluid element is stable to convection. If  $\nabla_{\text{rad}} > \nabla_{\text{ad}}$ , the fluid element becomes unstable to convection. The radial point where the two gradients are equal marks

the location of the Schwarzschild convective boundary, marked in Figure 2.1 by a vertical black line. When  $\nabla_{\text{rad}}$  is smaller, all energy in that radius is transported by radiation, and  $\nabla = \nabla_{\text{rad}}$  (as shown in the radiative zone of the model in Figure 2.1). As  $\nabla_{\text{rad}}$  increases above  $\nabla_{\text{ad}}$ , the rate at which the temperature decreases becomes steeper. A displaced fluid element will expand adiabatically and remain hotter than its surroundings. Convection then becomes the dominant transport process (Kippenhahn et al. 2013, Section 6.1).

If the chemical composition, characterized by the molecular weight  $\mu$  changes within the star, an additional term is included in eq. (2.8). This is called the Ledoux criterion, and is expressed as

$$\nabla_{\text{rad}} < \nabla_{\text{ad}} + \frac{\phi}{\delta} \nabla_{\mu} . \quad (2.9)$$

According to the Ledoux criterion, the vertically displaced fluid can resist adiabatic expansion and remain stable to convection due to a gradient in mean molecular weight,  $\nabla_{\mu}$ . The additional term on the right-hand side involves two partial derivatives, where  $\phi = -\partial \ln \rho / \partial \ln \mu$ , with pressure and temperature held constant, and  $\delta = -\partial \ln \rho / \partial \ln T$ , where pressure and mean molecular weight  $\mu$  are held constant. Differences between the Schwarzschild and Ledoux criteria are observed in evolved stars where heavy elements are produced in the cores (Kippenhahn et al. 2013, Section 6.1)).

Stellar interiors become unstable to convection when either  $\nabla_{\text{rad}}$  is large or  $\nabla_{\text{ad}}$  is small. This leads us to identify two main physical effects that contribute to a convective instability: high rate of energy production and high opacity, caused by a large temperature gradient

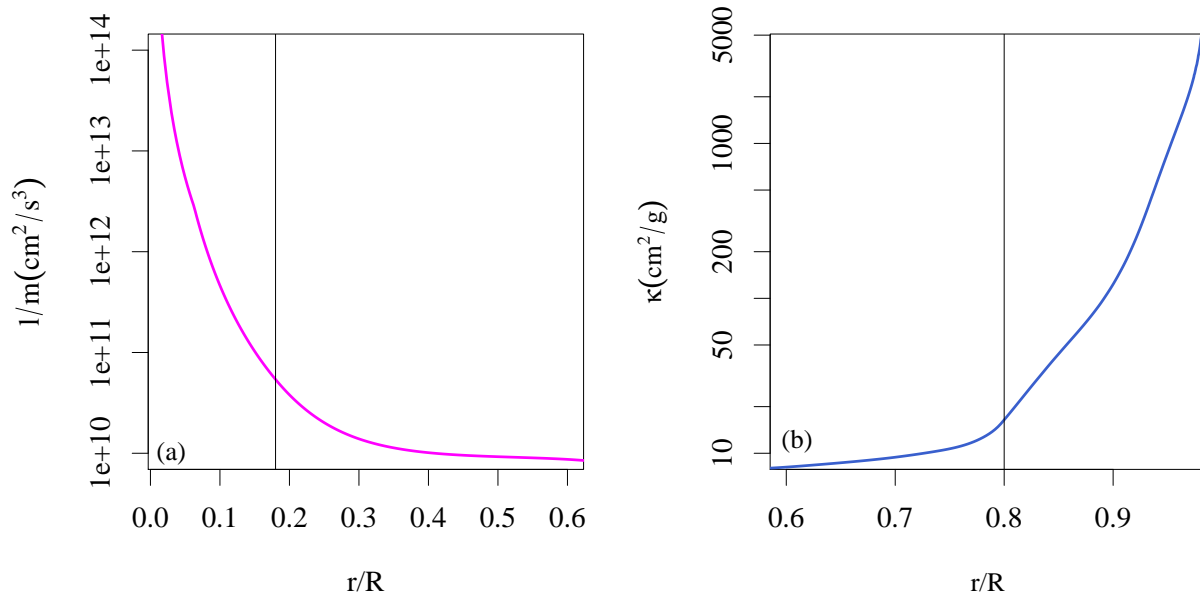


Figure 2.2 (a) Luminosity per mass as a function of stellar radius for a  $6M_{\odot}$  main sequence star with a convective core. (b) Opacity profile for a  $3M_{\odot}$  pre-main sequence star with a convective envelope. The vertical black line represents the convective boundary as defined by the Schwarzschild criterion for each star.

and partial ionization zones near the cooler surface (Salaris & Cassisi 2017). Convective cores in high-mass stars exhibit efficient, adiabatic convection, due to the high rate of energy production. This can be measured by the luminosity divided by the mass as a function of radius, as shown in Figure 2.2(a) for a  $6M_{\odot}$  star with a convective core. Large convective envelopes form on the pre-main sequence due to gravitational core collapse as the star accretes material. The opacity of the material increases while the core temperature increases, creating a large radiative temperature gradient. An opacity profile for a  $3M_{\odot}$  star is shown in Figure 2.2(b). In low-mass main sequence stars like the Sun, shallow convective envelopes develop as a result of partial ionization zones in the cool outer envelope that increase the opacity.

## 2.2 Mixing Length Theory

One-dimensional stellar structure and evolution codes must include a convection model to incorporate contributions from convection in the stellar structure. The most frequent model used is stellar mixing length theory (MLT) (Böhm-Vitense 1958).

The origin of MLT begins with physicist Ludwig Prandtl describing how a mixing length  $\ell_{\text{MLT}}$  could roughly represent both the convective cell and the distance it will travel before dissipating into the surrounding fluid (Prandtl 1925). The theory was later adapted for stars by Biermann (1932) in his Ph.D thesis, in which a mixing length is used to characterize energy transport. MLT originates from a period before computers were available. In the field of computational fluid dynamics (CFD), direct numerical simulations (DNS), large eddy simulations (LES), and Reynolds-Averaged Navier-Stokes (RANS) have superseded MLT, which is now rarely used (Spalart 2006). However, stellar MLT continues to be used today even though hydrodynamic simulations of stellar convection are possible, and convective fluxes and velocities can be calculated and evolved self-consistently (Kupka & Muthsam 2017).

The goal of MLT is to calculate  $\nabla$  so that the energy transport equation, eq. (2.4), can be solved. In the case of a radiative zone where no convection occurs and all energy is released by radiative transport of photons,  $\nabla = \nabla_{\text{rad}}$ . In the case of an efficient, adiabatic convection zone, all energy is transported by convection because no heat is lost to the surroundings, so  $\nabla = \nabla_{\text{ad}}$ . This convection zone is described as *efficient* because all energy is transported via convection, and no energy is lost to radiative diffusion as it travels outward. In the case

of transport due to *inefficient* convection zones, where energy transported by convection is partially lost to radiative diffusion as it travels outward, the gradient  $\nabla$  is calculated using MLT, or another model (Kippenhahn et al. 2013, Section 7.3).

MLT solves five equations for five unknowns in the case of a fluid element becoming displaced in a convectively unstable region, where the transport of energy is a small deviation from pure radiative transport. The five unknowns needed for MLT are: radiative flux  $F_{\text{rad}}$ , convective flux  $F_{\text{conv}}$ , convective velocity  $v_{\text{conv}}$ , the temperature gradient of the fluid surrounding a displaced convective element  $\nabla$ , and the temperature gradient of the displaced convective element  $\nabla_e$  (Kippenhahn et al. 2013, Section 7.1). We derive the five MLT equations needed to solve for these unknowns. These MLT equations have four free parameters, labeled  $b_1$ ,  $b_2$ ,  $b_3$ , and  $\ell_{\text{MLT}}$ . Depending on the values chosen for the first three parameters, MLT can have different ‘flavors.’ One combination of these parameters was detailed by Böhm-Vitense (1958), and is still the most widely used prescription today. The fourth free parameter is the mixing length originally described by Prandtl (1925) and Biermann (1932).

### ***2.2.1 Deriving MLT***

To derive the mixing length theory equations calculated in stellar evolution codes, we begin with a derivation of five equations:  $F_{\text{tot}}$ ,  $F_{\text{rad}}$ ,  $F_{\text{conv}}$ ,  $v_{\text{conv}}$ , and  $\Gamma$ ; using these results, we derive a cubic equation that will allow us to solve for the temperature gradient  $\nabla$ . This derivation is inspired by the following: Hubeny & Mihalas (2014, Section 16.5), Tassoul et al. (1990), Kippenhahn et al. (2013, Section 7.1), and Cox & Giuli (1968).

We begin with a general equation for the total flux in the star,

$$F_{\text{tot}} = L/4\pi r^2, \quad (2.10)$$

where  $L$  is the local luminosity at a radius  $r$  in the star. Using our definition for  $\nabla_{\text{rad}}$  in eq. (2.6), we can rearrange this to form our first equation

$$F_{\text{tot}} = \frac{4acG}{3} \frac{T^4 m}{\kappa P r^2} \nabla_{\text{rad}}. \quad (2.11)$$

However, this would only hold true in the case where all energy is transported by radiation. Assuming some will be transported by convection,  $\nabla < \nabla_{\text{rad}}$ , so the actual contribution from radiative flux is equal to

$$F_{\text{rad}} = \frac{4acG}{3} \frac{T^4 m}{\kappa P r^2} \nabla. \quad (2.12)$$

Equation (2.12) is the second equation needed in our MLT derivation. This allows us to define a relationship between the two, such that

$$F_{\text{rad}} = \frac{F_{\text{tot}}}{\nabla_{\text{rad}}} \nabla. \quad (2.13)$$

Next, we derive the expression for the convective flux in MLT. We imagine a fluid element with length  $d$  is being displaced vertically to some distance  $\Delta r$ . Considering the fluid element moving with an excess temperature  $DT$ , where  $DT$  corresponds with a small deviation from

the surroundings, such that

$$\begin{aligned}
 DT &= \left[ \left( \frac{dT}{dr} \right)_{\text{e}} - \left( \frac{dT}{dr} \right)_{\text{surr}} \right] \Delta r \\
 &= (\nabla - \nabla_{\text{e}}) \Delta r \left( \frac{T}{H_p} \right).
 \end{aligned} \tag{2.14}$$

Given the fluid is moving with a velocity  $v_{\text{conv}}$ , we define convective flux as

$$F_{\text{conv}} = \rho v_{\text{conv}} c_P DT . \tag{2.15}$$

In this scenario, the fluid element can move a maximum distance of  $\ell_{\text{MLT}}$  before dissipating into the surroundings. The choice of the mixing length  $\ell_{\text{MLT}}$  is heavily dependent on a free parameter  $\alpha_{\text{MLT}}$ , such that

$$\ell_{\text{MLT}} = \alpha_{\text{MLT}} H_p, \tag{2.16}$$

and the mixing length is locked to a fraction of the pressure scale height  $H_p$ . Therefore we define  $\Delta r = c_1 \ell_{\text{MLT}}$ . Böhm-Vitense (1958) assumes a value  $c_1 = 1/2$ , meaning that if a fluid element is vertically displaced at some distance ranging from zero to the mixing length, on average,  $\Delta r = (1/2)\ell_{\text{MLT}}$ . We do not assume this approximation so that our derivation is not partial to one flavor; instead, we use a constant  $b_2$  in the manner of Cox & Giuli (1968) and Tassoul et al. (1990). Substituting in the expression for  $DT$  in eq. (2.14), eq. (2.15)

becomes

$$F_{\text{conv}} = b_2 \rho v_{\text{conv}} c_P (\nabla - \nabla_{\mathbf{e}}) \ell_{\text{MLT}} \left( \frac{T}{H_p} \right). \quad (2.17)$$

This is the third equation needed for the MLT calculations.

To derive an equation for the convective velocity, we begin with the radial buoyancy force per unit mass  $F_{r,\text{buoy}}$  where  $D\rho$  is the density difference of the fluid element and its surroundings. Using the relation  $D\rho/\rho = -\delta DT/T$  defined in Kippenhahn et al. (2013, Section 7.1), we define

$$F_{r,\text{buoy}} = g \frac{D\rho}{\rho} = g \frac{\delta DT}{T}. \quad (2.18)$$

Inserting eq. (2.14) into eq.(2.18), we find

$$F_{r,\text{buoy}} = g\delta (\nabla - \nabla_{\mathbf{e}}) \frac{c_1 \ell_{\text{MLT}}}{H_p}. \quad (2.19)$$

The work done by buoyancy on the fluid element is some fraction  $c_2$  of the total work done, such that

$$\begin{aligned} W &= c_2 F_{r,\text{buoy}} \Delta r \\ &= g\delta (\nabla - \nabla_{\mathbf{e}}) \frac{c_1^2 c_2 \ell_{\text{MLT}}^2}{H_p}. \end{aligned} \quad (2.20)$$

Now, we can derive an expression for velocity from the kinetic energy of the fluid element,

where  $KE = v_{\text{conv}}^2/2 = c_3W$ . The square of the convective velocity becomes

$$\begin{aligned} v_{\text{conv}}^2 &= 2c_3W \\ &= 2g\delta (\nabla - \nabla_{\text{e}}) \frac{c_1^2 c_2 c_3 \ell_{\text{MLT}}^2}{H_p}. \end{aligned} \quad (2.21)$$

For the Bohm-Vitense flavor, each of these constants  $c_i = 1/2$ , so that on average, the work done on the fluid element is half of the total work, and half of this work goes into the kinetic energy. The combined coefficient for this equation is  $b_1 = 1/8$ . The general form of eq. (2.21), our fourth MLT equation, is

$$v_{\text{conv}} = \sqrt{b_1 g \delta} (\nabla - \nabla_{\text{e}})^{1/2} \frac{\ell_{\text{MLT}}}{H_p^{1/2}}. \quad (2.22)$$

Finally, to calculate the convective efficiency, we consider the temperature change with depth for the fluid element  $(dT/dr)_{\text{e}}$ , which decreases due to both adiabatic expansion and radiative energy loss to the surroundings. The equation is

$$\left(\frac{dT}{dr}\right)_{\text{e}} = \left(\frac{dT}{dr}\right)_{\text{ad}} + \left(\frac{dT}{dr}\right)_{\text{rad}}. \quad (2.23)$$

According to Kippenhahn et al. (2013, Section 7.1), the second term on the right-hand side can be substituted for an expression in terms of the total energy loss of the volume per unit

time  $\lambda = -\rho V c_P v_{\text{conv}} dT/dt$ , such that

$$\left(\frac{dT}{dr}\right)_e = \left(\frac{dT}{dr}\right)_{\text{ad}} - \frac{\lambda}{\rho V c_P v_{\text{conv}}}, \quad (2.24)$$

where  $V$  is the volume of the fluid element. Multiplying by  $H_p/T$ , we find

$$\nabla_e - \nabla_{\text{ad}} = \frac{\lambda H_p}{\rho V c_P v_{\text{conv}} T}. \quad (2.25)$$

Substituting in an equation for energy loss per time in terms of surface area  $S$  of the fluid,  $\lambda = Sf$ , where the absolute value of the radiative flux  $|\partial T/\partial r| = f/k_{\text{rad}}$  due to the fluid element's excess temperature, we find

$$\begin{aligned} \nabla_e - \nabla_{\text{ad}} &= \frac{H_p}{\rho V c_P v_{\text{conv}} T} (Sf), \\ &= \frac{H_p}{\rho V c_P v_{\text{conv}} T} \left( S k_{\text{rad}} \left| \frac{\partial T}{\partial r} \right| \right). \end{aligned} \quad (2.26)$$

The Bohm-Vitense model assumes  $\partial T/\partial r \sim 2DT/d$  where  $d$  is the diameter of the moving fluid element, but we will replace the 2 with a general constant  $c_4$ . We also use the coefficient of conduction for radiative transport  $k_{\text{rad}} = \frac{16\sigma T^3}{3\kappa\rho}$ , where  $\sigma$  is the Stefan-Boltzmann constant.

Using this relation and eq. (2.14) for the definition of  $DT$ , this equation simplifies to

$$\frac{\nabla_e - \nabla_{\text{ad}}}{\nabla - \nabla_e} = \frac{S \ell_{\text{MLT}}}{Vd} c_1 c_4 \left( \frac{16\sigma T^3}{3\kappa\rho^2 v_{\text{conv}} c_P} \right). \quad (2.27)$$

The first ratio on the right hand side of this equation is described as the ‘form factor’ that

represents the geometry of the displaced fluid element. Böhm-Vitense (1958) uses the value  $S\ell_{\text{MLT}}/Vd = \frac{9/2}{\ell_{\text{MLT}}}$ . By keeping the value general for the form factor, we combine the constants into a single parameter,  $c_5/\ell_{\text{MLT}}$ ; this matches the general equations derived by Cox & Giuli (1968). Inverting this equation gives us an expression for convective efficiency  $\Gamma$ . Replacing the constants  $c_1c_4c_516/3$  with a general constant  $b_3$ , we find our fifth equation,

$$\Gamma = \frac{\nabla - \nabla_{\text{e}}}{\nabla_{\text{e}} - \nabla_{\text{ad}}} = \left( \frac{c_P \rho^2 \kappa v_{\text{conv}} \ell_{\text{MLT}}}{b_3 \sigma T^3} \right). \quad (2.28)$$

The value for constant  $b_3$  in the Bohm-Vitense model is  $b_3 = 1/24$ . Substituting in eq. (2.21) as the convective velocity, we find

$$\frac{\nabla - \nabla_{\text{e}}}{\nabla_{\text{e}} - \nabla_{\text{ad}}} = \left( \frac{c_P \rho^2 \kappa \ell_{\text{MLT}}}{b_3 \sigma T^3} \right) \sqrt{b_1 g \delta} (\nabla - \nabla_{\text{e}})^{1/2} \frac{\ell_{\text{MLT}}}{H_p^{1/2}}. \quad (2.29)$$

We now have expressions for five equations for total, radial, and convective flux, convective velocity, and convective efficiency:

$$F_{\text{tot}} = \frac{4acG}{3} \frac{T^4 m}{\kappa P r^2} \nabla_{\text{rad}}, \quad (2.30)$$

$$F_{\text{rad}} = \frac{4acG}{3} \frac{T^4 m}{\kappa P r^2} \nabla, \quad (2.31)$$

$$F_{\text{conv}} = b_2 \rho v_{\text{conv}} c_P (\nabla - \nabla_{\text{e}}) \ell_{\text{MLT}} \left( \frac{T}{H_p} \right), \quad (2.32)$$

$$v_{\text{conv}} = \sqrt{b_1 g \delta} (\nabla - \nabla_{\text{e}})^{1/2} \frac{\ell_{\text{MLT}}}{H_p^{1/2}}, \quad (2.33)$$

$$\frac{\nabla - \nabla_{\text{e}}}{\nabla_{\text{e}} - \nabla_{\text{ad}}} = \left( \frac{c_P \rho^2 \kappa \ell_{\text{MLT}}}{b_3 \sigma T^3} \right) \sqrt{b_1 g \delta} (\nabla - \nabla_{\text{e}})^{1/2} \frac{\ell_{\text{MLT}}}{H_p^{1/2}}. \quad (2.34)$$

To solve these equations, we still need two variables:  $\nabla$  and  $\nabla_e$ . To sidestep this, we derive a new cubic equation using the variable  $x(\nabla, \nabla_e)$ , where  $x = (\nabla - \nabla_e)^{1/2}$ . Substituting in the equation for convective velocity and the new variable  $x$ , we find

$$F_{\text{tot}} = \frac{4acG}{3} \frac{T^4 m}{\kappa P r^2} \nabla_{\text{rad}}, \quad (2.35)$$

$$F_{\text{rad}} = \frac{4acG}{3} \frac{T^4 m}{\kappa P r^2} \nabla, \quad (2.36)$$

$$F_{\text{conv}} = b_2 \rho c_P \sqrt{b_1 g \delta} \left( \frac{\ell_{\text{MLT}}^2}{H_p^{3/2}} \right) T x^3, \quad (2.37)$$

$$v_{\text{conv}} = \sqrt{b_1 g \delta} x \frac{\ell_{\text{MLT}}}{H_p^{1/2}}, \quad (2.38)$$

$$x = \left( \frac{c_P \rho^2 \kappa \ell_{\text{MLT}}}{b_3 \sigma T^3} \right) \sqrt{b_1 g \delta} (\nabla_e - \nabla_{\text{ad}}) \frac{\ell_{\text{MLT}}}{H_p^{1/2}}. \quad (2.39)$$

Substituting the new expressions for  $F_{\text{conv}}$  and  $F_{\text{tot}}$  into eq. (2.13), we find

$$\frac{F_{\text{tot}}}{\nabla_{\text{rad}}} (\nabla_{\text{rad}} - \nabla) = F_{\text{conv}}, \quad (2.40)$$

$$\frac{4ac}{3} \frac{G T^4 m}{\kappa P r^2} (\nabla_{\text{rad}} - \nabla) = b_2 \rho c_P T \sqrt{b_1 g \delta} \left( \frac{\ell_{\text{MLT}}^2}{H_p^{3/2}} \right) x^3, \quad (2.41)$$

$$(\nabla_{\text{rad}} - \nabla) = A x^3, \quad (2.42)$$

where

$$A = \frac{3\kappa P r^2}{4ac G T^3 m} b_2 \rho c_p \sqrt{b_1 g \delta} \frac{\ell_{\text{MLT}}^2}{H_p^{3/2}}. \quad (2.43)$$

Next, we revisit our equation for convective efficiency to derive an expression for  $\nabla_e$ . We

define

$$B = \frac{c\sigma T^3}{c_p \rho^2 \kappa \ell_{\text{MLT}}^2} \sqrt{\frac{H_P}{b_1 g \delta}}. \quad (2.44)$$

Eq. (2.39) then becomes

$$x = \frac{\nabla_e - \nabla_{\text{ad}}}{B}, \quad (2.45)$$

$$\nabla_e = Bx + \nabla_{\text{ad}}. \quad (2.46)$$

Given that  $x = (\nabla - \nabla_e)^{1/2}$  and utilizing eq. (2.46), we can finally express an equation for

$\nabla$ :

$$\nabla = x^2 + \nabla_e \quad (2.47)$$

$$\nabla = x^2 + Bx + \nabla_{\text{ad}}. \quad (2.48)$$

Now, all that is left to do is solve for  $x$ . We form the final cubic equation by adding

$(\nabla - \nabla_e) + (\nabla_e - \nabla_{\text{ad}})$  to each side of eq. (2.42),

$$(\nabla_{\text{rad}} - \nabla_{\text{ad}}) = Ax^3 + x^2 + Bx. \quad (2.49)$$

This cubic equation is solved in stellar evolution codes. If we assume the solution to this

equation is  $x_0$ , we arrive at MLT solutions for the five variables  $F_{\text{conv}}$ ,  $v_{\text{conv}}$ ,  $F_{\text{rad}}$ ,  $\nabla_e$  and  $\nabla$

solved by stellar evolution codes:

$$F_{\text{conv}} = b_2 \rho c_P T \sqrt{b_1 g \delta} \left( \frac{\ell_{\text{MLT}}^2}{H_p^{3/2}} \right) x_0^3, \quad (2.50)$$

$$v_{\text{conv}} = \sqrt{b_1 g \delta} \left( \frac{\ell_{\text{MLT}}}{H_p^{1/2}} \right) x_0, \quad (2.51)$$

$$F_{\text{rad}} = \frac{4acG}{3} \frac{T^4 m}{\kappa P r^2} (x_0^2 + Bx_0 + \nabla_{\text{ad}}), \quad (2.52)$$

$$\nabla_e = Bx_0 + \nabla_{\text{ad}}, \quad (2.53)$$

$$\nabla = x_0^2 + Bx_0 + \nabla_{\text{ad}}. \quad (2.54)$$

The constants  $b_1$ ,  $b_2$ , and  $b_3$ , are based on the flavor of MLT chosen. The differences in the flavors of Böhm-Vitense (1958), Böhm & Cassinelli (1971), and Tassoul et al. (1990) lie in the convective efficiencies, or how efficient the convection is in transporting the energy without losing heat to the surroundings. However, Salaris & Cassisi (2008) compare two of these flavors and find consistent results between models of low- and intermediate-mass stars. The final free parameter is the constant  $\alpha_{\text{MLT}}$ . After choosing the flavor and value for  $\alpha_{\text{MLT}}$ , the MLT equations can be solved in 1D stellar evolution codes.

To understand the influence of convection on the energy transport equation in the term  $\nabla$ , we calculate eq. (2.54). For convective zones, MLT uses eq. (2.34) to determine the efficiency of convection, which constrains the relationship between  $\nabla$  and  $\nabla_{\text{ad}}$ . The convective efficiency drops when the plasma is optically thin, such as near the stellar atmosphere. Deeper into the star at higher opacities, convection is thought to be more efficient at transporting energy (Hubeny & Mihalas 2014, Section 16.5).

If the efficiency is extremely high, such that the convective efficiency  $\Gamma \gg 1$ , this indicates a small difference between  $\nabla_{\text{ad}}$  and  $\nabla_{\text{e}}$ , so the displaced convective bubble's gradient  $\nabla_{\text{e}}$  assumes  $\nabla_{\text{ad}}$ , and no heat is diffused into the surroundings. In this case, we have  $\nabla = \nabla_{\text{e}} = \nabla_{\text{ad}}$ , so  $x = (\nabla - \nabla_{\text{e}})^{1/2} = 0$ . This approximation reveals that mixing length theory breaks down for extremely efficient convection, providing zeroes for convective flux and convective velocity. Therefore, MLT should be most accurate to model convection under the following ordering of the gradients:  $\nabla_{\text{ad}} < \nabla_{\text{e}} < \nabla < \nabla_{\text{rad}}$ .

### ***2.2.2 The mixing length***

Salaris & Cassisi (2017) describe the assumptions that MLT makes in the derivation above: (1) all convective eddies are the same size, (2) the mixing length is the smallest characteristic length scale in the star, (3) the physical properties of the convective element vary only slightly from the background, and (4) the motion of the element is much smaller than the sound speed.

This first assumption implies that the filling factor, or the amount of fluid moving inward at a given radius, should be constant at all radial points in the star. Because MLT only assigns a 1D length to the eddy, the filling factor should equal one-half at all radial points in the star. The shape of convection throughout the star would rely solely on the choice of the mixing length parameter  $\alpha_{\text{MLT}}$  and the pressure scale height of the star  $H_P$ .

The choice of this mixing length parameter impacts a star's evolutionary path, as shown in Figure 2.3, but that parameter's value is expressed differently across the literature. The value of  $\alpha_{\text{MLT}}$  is often chosen based on which model best matches observations of the Sun

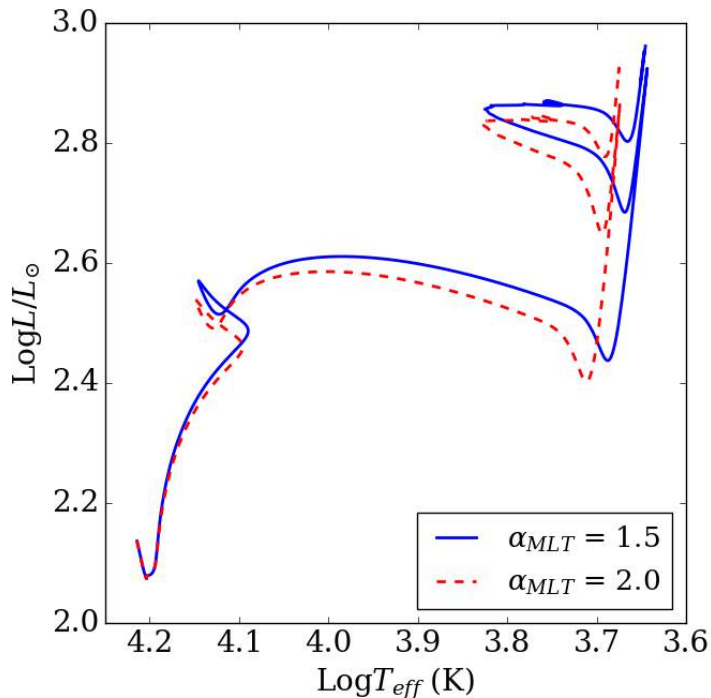


Figure 2.3 Evolutionary track for a  $3 M_{\odot}$  star with different mixing length coefficients, modeled by MESA. Both models use the Henyey flavor of MLT and metallicity  $z = 0.0017$ .

or solar-type stars, at a value of  $\alpha_{\text{MLT}} = 1.931$  (Cinquegrana & Joyce 2022),  $\alpha_{\text{MLT}} = 1.86$  (Ferraro et al. 2006), or  $\alpha_{\text{MLT}} = 1.926$  (Joyce & Chaboyer 2018), but it is not clear that the convection in the Sun is similar to convection in other types of stars with different masses, ages, or compositions (Salaris & Cassisi 2008). Other studies find values of  $\alpha_{\text{MLT}} = 1.4$  for a  $1.2 M_{\odot}$  red giant, using precise red giant observations (Asida 2000), and  $\alpha_{\text{MLT}} = 2.0$  using red giants in globular clusters with various metallicity values (Ferraro et al. 2006). Still other studies experience difficulty with fitting results to one  $\alpha_{\text{MLT}}$ . Cukanovaite et al. (2019) compared evolutionary tracks to simulations of white dwarf convective envelopes and found no  $\alpha_{\text{MLT}}$  that agrees with the simulations, and suggest that boundary mixing is responsible

for this. Joyce & Chaboyer (2018) suggest that  $\alpha_{\text{MLT}}$  should not be a constant, but an adaptive free parameter that can be changed in response to evolution and stellar mass. A wealth of evidence points to the fact that the mixing length, as defined by a fraction of the pressure scale height, is limited in its ability to model convection.

### 2.3 Convective penetration and overshooting

MLT only produces nonzero values for convective flux, velocity, and efficiency in regions where the Schwarzschild or Ledoux criterion is violated, indicating a convective instability. This is because the Schwarzschild criterion was developed with the assumption that acceleration goes to zero at this boundary, but in realistic hydrodynamic simulations, velocities do not vanish in this clean way. In reality, convective penetration or overshooting can occur at any convective-radiative boundary layer (Kippenhahn et al. 2013, Section 30.4).

The Péclet number is the ratio of advection to thermal diffusivity, such that

$$\text{Pe} = v_{\text{RMS}} H_p / \alpha, \quad (2.55)$$

where the thermal diffusivity  $\alpha = \chi / \rho c_P$  and  $\chi$  is the thermal conductivity. Convective penetration occurs when the Péclet number is large ( $\text{Pe} \gg 1$ ). A large Péclet number indicates that convective plumes penetrate the convective boundary with high velocities or a low thermal diffusion coefficient, so a convective plume only dissipates into its surroundings after traveling some length into the stable zone (Zahn 1991; Hurlburt et al. 1984; Renzini 1987). Under the influence of convective penetration, the convective boundary will move, gradually

eroding to extend the size of the convective zone. Several works suggest that the penetration depth is dependent on velocity and the filling factor (Zahn 1991; Brummell et al. 2002). With the assumption of a large Péclet number, Zahn defines the depth of the penetration layer  $L_{\text{pen}}$  as

$$\frac{L_{\text{pen}}}{H_p} = v_{\text{RMS}}^{3/2} (cf)^{1/2} \left[ \frac{3}{2} g Q \alpha \chi_p \nabla_{\text{ad}} \right], \quad (2.56)$$

where  $Q = (-\partial \ln \rho / \partial \ln T)_p$ , the expansion coefficient at constant pressure. The coefficient  $c$  is related to the horizontal flow structure  $\bar{h}$ , and  $f$  represents the filling factor for convection, which indicates asymmetry between inflows and outflows. Calculations of the penetration depth have been reported for hydrodynamic simulations of stellar convection. Rogers et al. (2006) define penetration depth as the length from the convective boundary to the point where the kinetic energy density reaches 5% of its peak value. Brummell et al. (2002) defines the penetration depth a bit deeper, at 1% of its peak value. Pratt et al. (2017) identify the penetration depth at a point where the vertical kinetic flux goes to zero after crossing the convective boundary; this was not an averaged measurement, but calculated from the depth of penetration at each angular position and time. The penetration depths in these studies range from  $0.2H_p$  to  $0.684H_p$ .

Another phenomenon that occurs at the convective boundary in the presence of a low Péclet number is convective overshooting (e.g., Zahn 1991; Anders & Pedersen 2023). In this case, the heat from the plumes at the convective boundary diffuse into the stable zone without altering the temperature gradient, so the Schwarzschild boundary is conserved. The

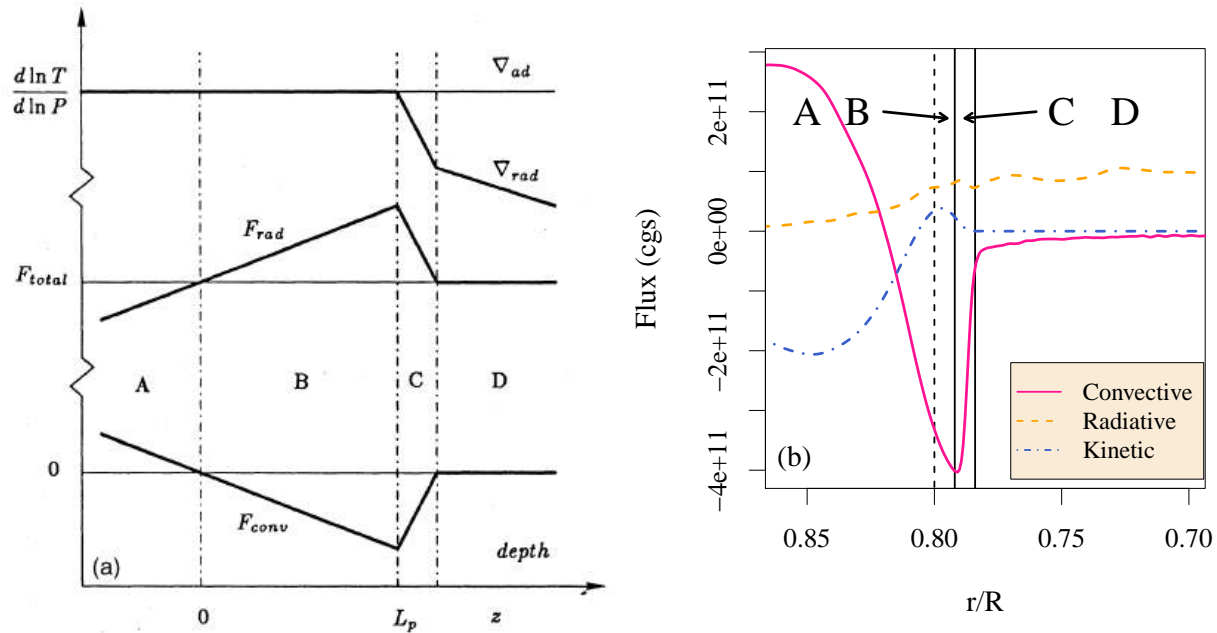


Figure 2.4 Fluxes near the convective boundary in a star, where depth increases to the right. (a) Theoretical sketch of flux as a function of depth with four zones labeled from Zahn (1991). Depth increases to the right, where  $z = 0$  is the Schwarzschild boundary and  $L_p$  is the convective penetration length. (b) Flux profile for a  $3M_\odot$  pre-main sequence star simulated with MUSIC. Layer A represents the convection zone, layer B represents the penetration layer, layer C represents the overshooting layer, and layer D represents the radiative zone. The dashed vertical line dividing layers A and B is the Schwarzschild boundary.

mechanism for overshooting and penetration is the same; the difference between the two is whether there is a high or low Péclet number at the convective boundary.

The Péclet number varies with the interior radius of a star; for a star with different convection zones, convective penetration and convective overshooting can occur at different convective boundaries within the same star. Zahn (1991) defines four distinct layers in stars with a convective envelope: the convective zone (A), the penetration layer (B), the overshooting layer (C), and the radiative zone (D), as shown in Figure 2.4(a). We identify these theoretical layers in a simulation of a  $3M_\odot$  pre-main sequence star produced with MUSIC,

shown in Figure 2.4(b). The boundary between layers A and B is the Schwarzschild boundary and is represented by a dashed vertical line. According to the theoretical picture described by Zahn (1991), the Schwarzschild boundary should be located where the convective flux is zero. In the MUSIC simulation, we observe that  $F_{\text{conv}}$  is still strongly negative at the Schwarzschild boundary due to boundary layer flows. This form for the convective flux is common to the realistic global simulations we produce with MUSIC, and will be discussed in detail along with the results of each simulation. Here it is simply important to note that simulations allow us to understand how the complex, nonlinear interactions of these layers of the star differ from the simple theoretical pictures that have long been used to describe stellar interiors.

Zahn (1991) defines layer B as the penetration layer, in which the fluid is convectively stable and  $\text{Pe} > 1$ , where plumes penetrate this region and erode the convective boundary. The extent of this region is the penetration depth,  $L_p$ , defined in eq. (2.56). According to Zahn (1991), the boundary between layers B and C corresponds to the radial point when  $F_{\text{conv}}$  reaches a minimum value. It is not clear whether this should be the case in the MUSIC simulation, although such a minimum exists. Layer C represents the overshooting layer, which would only be present where  $\text{Pe} < 1$ . The overshooting plumes decelerate due to buoyancy forces and dissipate into the stable zone. In this example, the extent of the overshooting layer is defined as the radial point where  $F_{\text{conv}}$  reaches zero. We draw a similar line in Figure 2.4(b). Finally, we encounter layer D, the stable, radiative zone. Zahn (1991) also defines these boundaries with the radiative flux  $F_{\text{rad}}$ , which reaches inflection

points at the same radial points as the convective flux. In our simulations, we do not see this connection. We also include the kinetic flux,  $F_{\text{kin}}$ , which is represented by the blue dot-dashed line in Figure 2.4.

Considering this example, the convective plumes that cross the Schwarzschild boundary into the stable region contribute to penetration when  $\text{Pe} > 1$  and convective overshooting when  $\text{Pe} < 1$ . The Péclet number in stars is dependent on radius, and for deep convection, this number is reportedly high (Pratt et al. 2016; Meakin & Arnett 2007a; Viallet et al. 2016). We can imagine layer C dissipates into layer D, and we are left with one “convective boundary layer” that encompasses inflows crossing the Schwarzschild boundary. Because we are interested in the amount of mixing in general, we do not distinguish between convective overshooting or penetration in this work; without loss of generality, we use the language “overshooting” to describe the mixing in this convective boundary layer.

The depth of convective overshooting is discussed similarly to the depth of convective penetration. Schmitt et al. (1984) demonstrates that the most important parameters influencing overshooting depth are velocity and a filling factor, such that the overshooting depth  $\ell_{\text{ov}} \sim v^{3/2} f^{1/2}$ . This is the same scaling as the penetration depth defined in eq. (2.56). Other works also emphasize that the shear interaction between inflows and outflows is influential to the overshooting depth (Rempel 2004; Rieutord & Zahn 1995), indicating that the number of plumes could influence overshooting. Other studies have shown evidence of similar layers near a convective boundary. For example, Anders et al. (2022) find a penetration layer analogous to Zahn’s penetration layer. Meakin & Arnett (2007b) find that rather than

convective plumes penetrating a penetration layer, the boundary itself causes shear instabilities that allow the boundary to break up into ‘wisps’ of material that mix into the stable region, which creates a single mixing layer at the boundary. While each of these studies examines different stellar structures, they all show that a sharp transition from unstable to stable is unrealistic. Because overshooting is not accounted for in MLT, additional models are required in stellar evolution codes to represent this mixing.

### ***2.3.1 Convective Overshooting Model***

The simplest way to implement convective boundary mixing into 1D stellar evolution codes is with a step overshoot function, which will extend the Schwarzschild boundary by a multiple of the pressure scale height. The overshooting depth step function is defined as

$$\ell_{\text{ov}} = \alpha_{\text{ov}} H_p . \tag{2.57}$$

In this case, the overshooting depth  $\ell_{\text{ov}}$  is determined by a constant  $\alpha_{\text{ov}}$ . The convective plume will travel a distance  $\ell_{\text{ov}}$  and then immediately diffuse into the surroundings, as shown in Figure 2.5.

The second way to incorporate overshooting is by treating it as a diffusive process according to Freytag et al. (1996); Herwig (2000). Using multi-dimensional hydrodynamic studies, the diffusion coefficient,  $D$ , can be calibrated to model the amount of mixing in the stable

zone due to overshooting plumes.  $D$  is incorporated in the diffusion equation,

$$\frac{\partial A(r, t)}{\partial t} = \frac{1}{r^2} \frac{\partial}{\partial t} D r^2 \frac{\partial A(r, t)}{\partial r}. \quad (2.58)$$

Here  $A$  is any scalar quantity, such as temperature in the case of heat transfer. To date, two different forms have been suggested for the overshooting coefficient  $D$ , including  $D_{\text{F96}}$  defined in Freytag et al. (1996) and  $D_{\text{EVT}}$  defined in Pratt et al. (2017).

### 2.3.2 Choosing a diffusion coefficient

Freytag et al. (1996) use a radiative hydrodynamic (RHD) code to measure the extent of penetration of plumes into the stable zone before diffusing into the surrounding fluid. They examine a small box near the surfaces of a solar model, a main sequence A-star, and a white dwarf. They find that the velocity magnitude of penetrating plumes into the stable region decays exponentially, such that the exponential overshooting diffusion coefficient can be calculated as

$$D_{\text{F96}}(r) = v_{\text{RMS, CB}}^2 t_c \exp - \frac{2(r_{\text{CB}} - r)}{f H_{P, \text{CB}}} \quad (2.59)$$

where  $t_c$  is the characteristic convective timescale,  $r_{\text{CB}}$  is the radius of the convective boundary, and  $f$  is an adjustable parameter that describes the efficiency of convective mixing (Herwig 2000).

As simulations achieve higher resolution and a longer time-series of statistics, more ac-

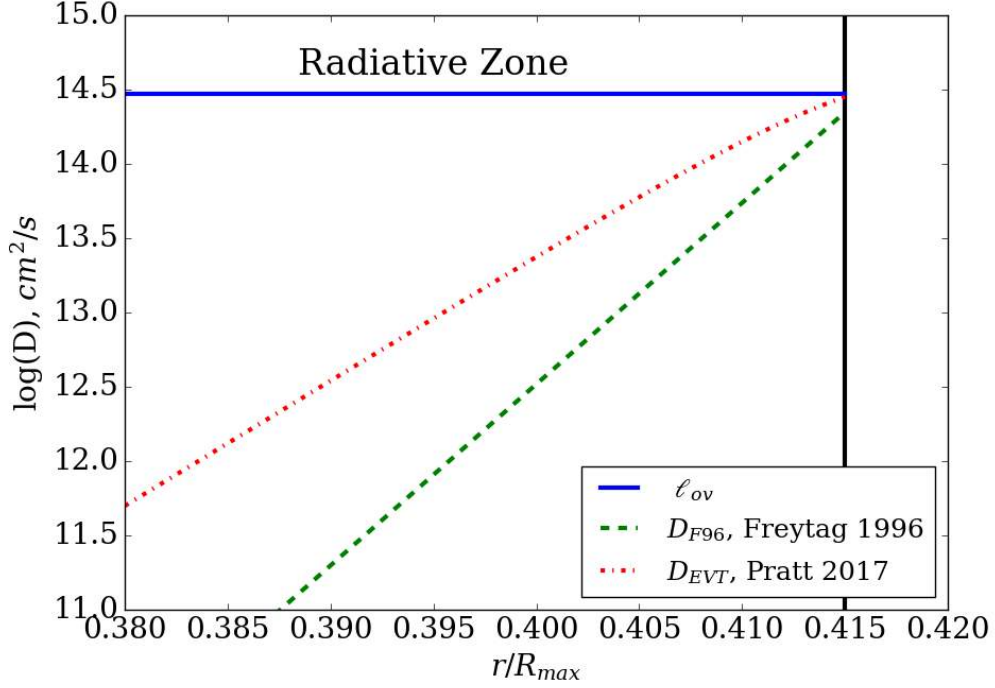


Figure 2.5 Modeling convective overshooting in 1D: The step function  $\ell_{ov}$  and two diffusion coefficients,  $D_{F96}$  and  $D_{EVT}$  plotted as a function of depth. The black vertical line represents the bottom of the convective envelope. The blue line represents the step function option for overshooting plumes, while the orange and green lines represent how  $D_{F96}$  and  $D_{EVT}$  can model the amount of mixing due to overshooting. The black vertical line indicates the Schwarzschild boundary.

curate diffusion coefficients can be calibrated based on simulation data. Pratt et al. (2017) calculate the extent of overshooting based on the thermal and kinetic flux of convective plumes. They show that rather than an exponential decay, the diffusion coefficient for convective overshoot can be more accurately represented by generalized extreme value theory (EVT) and a characteristic Péclet number in the convection zone, such that

$$D_{EVT} = D_0 \text{Pe}_{CB}^{1/2} \left( 1 - \exp \left( - \exp \left( - \frac{(r_{CB} - r)/(R - \mu)}{\lambda} \right) \right) \right). \quad (2.60)$$

The leading factors on the right-hand side of this equation,  $D_0 \text{Pe}_{\text{CB}}^{1/2}$ , represent the documented enhancement of molecular diffusion by convection. The location parameter  $\mu$  and the scale parameter  $\lambda$  are chosen according to the distribution function. The EVT model focuses on describing the tail of the distribution so that the model encapsulates the maximum overshooting lengths that occur in the simulation. Pratt et al. (2017) emphasize that the largest overshooting lengths are important when considering stellar evolution, even if they occur less often.

These two diffusion coefficients and the overshooting step function are plotted in Figure 2.5 to demonstrate how the different models for overshooting behave as a function of depth. The choice of an overshooting model impacts the evolution of the star. For example, isochrone fitting for stellar clusters is heavily dependent on the overshooting depth, and studies that have modeled stellar clusters using the step function are dependent on  $\alpha_{\text{ov}}$  (VandenBerg & Stetson 2004; Maeder & Meynet 1991). Small features on an isochrone such as the ‘hook’ at the end of the main sequence can change shape due to the  $\alpha_{\text{ov}}$  chosen in the model. This small change in shape can alter the predicted age of a cluster by more than a billion years (Kippenhahn et al. 2013).

## 2.4 The MESA Code

To calculate the stellar structure equations informed by MLT and an overshooting model, we use a one-dimensional stellar evolution code. The Modules and Experiments for Stellar Astrophysics (MESA) code (Paxton et al. 2010) is an open-source stellar evolution code that

solves the stellar structure equations and is widely used in the stellar astronomy community. We make use of MESA to create stellar structure models in this work because of its accessibility and broad functionality.

To produce a stellar structure, MESA reads the input file, or `inlist`, to gather information on the star, such as mass and metallicity, and the evolutionary stages to be calculated. There are dozens of other options that the user can specify at this time. Using these initial conditions, MESA uses an ‘`eos`’ module to compute an equation of state, the ‘`kap`’ module to compute opacities, and the ‘`rates`’ module to compute the nuclear reaction network. The equation of state is determined using the OPAL equation of state tables (Rogers & Nayfonov 2002) which relates density and temperature. The OPAL opacity tables provide opacity values for the star based on the core values for temperature and pressure (Iglesias & Rogers 1993). MESA employs the NACRE tables to determine the thermonuclear reactions in the star. There are 86 different reactions for low-energy nuclei in these tables (Angulo et al. 1999).

MESA uses a Newton–Raphson scheme to determine a solution to the stellar structure and evolution equations. Using the Newton method, the nonlinear equations can be approximated by a series of terms utilizing Jacobian matrices. The equations can then be solved iteratively using the Raphson method to converge to a solution (Langtangen 2016; Ypma 1995). The continuous equations shown in Section 2.1 must be discretized to solve

numerically. Eq. (2.1) becomes

$$\rho_k = \frac{dm_k}{(4/3)\pi(r_k^3 - r_{k+1}^3)} \quad (2.61)$$

where  $k$  is the cell index,  $dm$  is the mass element, and  $r_k$  is the radial coordinate of cell  $k$ .

The equation for momentum conservation, eq. (2.2) becomes

$$P_{k-1} - P_k = \overline{dm}_k \left[ \left( \frac{dP}{dm} \right)_{\text{hydrostatic}} + \left( \frac{dP}{dm} \right)_{\text{hydrodynamic}} \right] \quad (2.62)$$

$$= \overline{dm}_k \left[ -\frac{Gm_k}{4\pi r_k^2} - \frac{a_k}{4\pi r_k^2} \right] \quad (2.63)$$

where  $\overline{dm}_k = 0.5(dm_{k-1} + dm_k)$  and  $a$  is the Lagrangian acceleration evaluated by the change in  $v_k$  over timestep  $\delta t$ . The energy transport represented by eq. (2.4) becomes

$$T_{k-1} - T_k = \overline{dm}_k \left[ \nabla_{T,k} \left( \frac{dP}{dm} \right)_{\text{hydrostatic}} \frac{\overline{T}_k}{\overline{P}_k} \right] \quad (2.64)$$

where  $\overline{T}_k = (T_{k-1}dm_k + T_kdm_{k-1})/(dm_k + dm_{k-1})$  is the temperature interpolated by mass at face  $k$ . The temperature gradient  $\nabla_{T,k} = d \ln T / d \ln P$  is computed in a separate module, MLT. This module solves eqs. (2.50) - (2.54). The default prescription is Cox & Giuli (1968), which assumes no radiative losses and high optical depths. MESA incorporates other flavors of MLT such as those described by Böhm-Vitense (1958) and Henyey et al. (1965). The Henyey option allows the convective efficiency  $\Gamma$  to vary with opaqueness, which plays an important role for convective envelopes (Paxton et al. 2010).

Energy conservation in eq. (2.3) becomes

$$L_k - L_{k+1} = dm_k(\epsilon_{\text{nuc}} + \epsilon_{\nu,\text{thermal}} + \epsilon_{\text{grav}}). \quad (2.65)$$

The rates of energy generation can be time-dependent, and are solved at each time step depending on thermonuclear reactions. Finally, the mass fraction evolution equation in (2.5) becomes

$$\begin{aligned} X_{i,k}(t + \delta t) - X_{i,k}(t) &= dX_{\text{burn}} + dX_{\text{mix}} \\ &= \frac{dX_{i,k}}{dt} \delta t + (F_{i,k+1} - F_{i,k}) \frac{\delta t}{dm_k}. \end{aligned} \quad (2.66)$$

The terms  $X_{\text{burn}}$  and  $X_{\text{mix}}$  refer to the change in mass fraction due to nuclear reactions and chemical mixing, respectively. The contribution from mixing is determined by the flux  $F$  of species  $i$  flowing through face  $k$ , where

$$F_{i,k} = (X_{i,k} - X_{i,k-1}) \frac{\sigma_k}{dm_k}. \quad (2.67)$$

The value  $\sigma_k$  is a Lagrangian diffusion coefficient  $\sigma = D(4\pi r^2 \rho)^2$  where  $D$  is the Eulerian diffusion coefficient calculated in the ‘MLT’ module.

To allow for overshooting and penetration in 1D stellar evolution codes, we add an overshooting model on top of MLT. Currently in the MESA code, there are two main options for choosing how much mixing is incorporated at the boundary: 1) a step function  $\ell_{\text{ov}}$  that

extends the Schwarzschild boundary, or 2) a diffusive overshoot parameter  $f_{ov}$  incorporated into a diffusion coefficient in the diffusion equation.

MESA allows for customizing the exponential overshooting depth. The specified parameters include the location of convection (shell, core, or any), the location of the boundary where overshooting occurs (top, bottom, any), and the material burning (hydrogen, helium, metal, no burning, or any). Based on the choices, MESA will choose an overshooting prescription. Alternatively, you can indicate the choice yourself for the step function or diffusive process.

## 2.5 Alternative Convection Models

An alternative to MLT is the Full Spectrum Turbulence (FST) model (Ventura et al. 1998). This treatment of convection allows for the eddies to span a range of sizes, rather than only one size as in MLT. This is more realistic because the large stratification in stars allows for eddies of multiple length scales. The FST model has been expanded and implemented into stellar evolution codes ATON and CESAM (Canuto & Mazzitelli 1991; Canuto et al. 1996; Ventura et al. 1998). Although FST is physically more correct compared to MLT, it is not more realistic in practice. Sonoi et al. (2019) compared MLT and FST to calculations from multi-dimensional simulations with the CO5BOLD code, and they did not find a convection model that agreed with simulation measurements. It is clear that stellar modeling needs improvement and that multidimensional simulations provide a way forward.

## CHAPTER 3

### Simulating Stellar Convection

Simulating stars in two or three dimensions with hydrodynamic codes produces detailed information about the dynamics of stellar interiors that can inform one-dimensional models (Arnett et al. 2015, 2019). This effort is sometimes referred to as the 321D link. In this chapter, we outline the current state of the field of stellar hydrodynamics, which is concerned with simulating and understanding how a dense plasma behaves in the stratified, high pressure and density environment that makes up stellar interiors. We describe the capabilities of the `MUSIC` code developed by a group centered at the University of Exeter in the UK.

#### 3.1 The hydrodynamic equations

The field of stellar hydrodynamics tackles the problem of understanding stellar interiors by solving the hydrodynamic equations in a realistic stellar structure. These equations take many forms, depending on the properties of the fluid, resolution, and domain. However, the ultimate goal is to solve for the density ( $\rho$ ), momentum ( $\rho\vec{u}$ ), and internal energy ( $\rho e$ ).

The compressible hydrodynamics equations are expressed

$$\frac{\partial}{\partial t}\rho = -\nabla \cdot (\rho\vec{u}) , \quad (3.1)$$

$$\frac{\partial}{\partial t}(\rho\vec{u}) = -(\vec{u} \cdot \nabla)\rho\vec{u} - \nabla p + \mu\nabla^2\vec{u} + \rho\vec{g} , \quad (3.2)$$

$$\frac{\partial}{\partial t}(\rho e) = -\rho(\vec{u} \cdot \nabla e) - p\nabla \cdot \vec{u} + \nabla \cdot (\chi\nabla T) . \quad (3.3)$$

Eq. (3.1) represents the mass continuity equation (for a textbook treatment, see Section 4.1

of Choudhuri 1998). The left-hand side represents the change in density at a given point, and the right-hand side represents the divergence of mass, where  $\vec{u}$  is the velocity. This continuity equation is considered compressible because it includes changes in the density field throughout the simulation in both space and time. Compressibility effects common in stellar interiors include internal gravity waves in the radiative zone excited by stellar convection and large fluctuations at the convective boundary (Meakin & Arnett 2007b), and moderate Mach number flows in the envelopes of higher-mass stars, and the influence of density stratification on convection.

The second equation, eq. (3.2), is the momentum equation. The left-hand side represents the change in momentum at a point in time, and the terms on the right-hand side represent forces on the fluid due to pressure  $p$ , viscosity  $\mu$ , and external gravitational forces with a gravitational acceleration  $\vec{g}$ , respectively. The third and final equation, eq. (3.3), represents energy conservation; the left-hand side represents the change in internal energy at a given point. The right-hand side represents changes in momentum and pressure in response to changes in heat due to heat transfer, where  $\chi$  is the thermal conductivity (Kupka & Muthsam 2017).

In the anelastic approximation, eq. (3.1) is simplified using  $\nabla \cdot (\bar{\rho}\vec{u}) = 0$ . The anelastic approximation accounts for the large density stratification in stars, but filters out large perturbations to the density, including sound waves. Therefore, the anelastic approximation cannot accurately treat regions with Mach numbers approaching one, such as in some convective envelopes (Spiegel 1971). Calkins et al. (2015) find that the anelastic approximation

can be inaccurate for fluids with low Prandtl numbers ( $\text{Pr} = \nu_{\text{kin}}/\kappa_{\text{therm}} \ll 1$ ). The Prandtl number in stars is expected to be small compared to other large-scale geophysical fluids. In the Sun,  $\text{Pr} \approx 10^{-7}$  (Käpylä 2011).

The Boussinesq approximation provides an even stronger approximation to the fluid equations, in which the density gradient is assumed to be zero. Eq. (3.1) becomes  $\nabla \cdot \vec{u} = 0$ . This approach is only realistic for stars when the radial extent of the simulation volume is much smaller than the local pressure scale height; the Boussinesq approximation cannot reproduce the large-scale fluid motions present in the interior of stars with any realism (Kupka & Muthsam 2017).

Several multi-dimensional hydrodynamic codes have been used to study convection in stellar interiors, including: *MUSIC* (Goffrey et al. 2017), *PPMSTAR* (Woodward et al. 2014), *PROMPI* (Meakin & Arnett 2007b), *SLH* (Miczek et al. 2015), *Rayleigh* (Featherstone et al. 2022), *CO5BOLD* (Freytag et al. 2012), *ANTARES* (Muthsam et al. 2010), *ASH* (Clune et al. 1999), and *Dedalus* (Burns et al. 2020). These codes use different numerical methods, and solve different approximations to the fluid equations. These codes solve equations for Boussinesq, anelastic, and compressible convection. Some codes are built to study a “box-in-a-star”, with a grid that is a rectangular box, other codes are designed to be a “star-in-a-box”, while still others use a spherical set-up. Additional physics are used in these codes, including magnetic fields, rotations and Coriolis forces, and viscous forces. These codes also span a variety of numerics, including spectral, finite-difference, and finite-volume methods. Solving the compressible fluid equations involves the least amount of approximation. Simulating in

a global geometry, where deep convection zones can be studied over a large physical domain and large stratification, allows for the largest length scales of the flow to be studied. In this work, we use the **MUSIC** code to study simulations of this kind.

### 3.2 Multi-dimensional Stellar Implicit code (MUSIC)

The Multi-dimensional Stellar Implicit code (**MUSIC**) was developed at the University of Exeter to produce data of realistic stellar convection that can contribute to the 321D Link. **MUSIC** uses a spherical shell geometry to capture the largest dynamical scales. The natural consequence of the energy cascade in fluid dynamics is that energy at large scales will influence smaller ones (Miesch et al. 2015). Implicit large-eddy simulations (ILES), like those produced with **MUSIC**, assume that energy dissipation at the smallest scales of the energy cascade can be mimicked by random truncation errors that result from the numerical method; this is an implicit subgrid-scale model.

**MUSIC** solves the compressible hydrodynamic equations in 2D and 3D for density  $\rho$ , momentum  $\rho\vec{u}$ , and internal energy  $\rho e$ :

$$\frac{\partial}{\partial t}\rho = -\nabla \cdot (\rho\vec{u}) , \quad (3.4)$$

$$\frac{\partial}{\partial t}(\rho\vec{u}) = -(\vec{u} \cdot \nabla)\rho\vec{u} - \nabla p + \rho\vec{g} , \quad (3.5)$$

$$\frac{\partial}{\partial t}(\rho e) = -\nabla \cdot (\rho e\vec{u}) - p\nabla \cdot \vec{u} + \nabla \cdot (\chi\nabla T) . \quad (3.6)$$

Eqs. (3.4) – (3.6) are similar to eqs. (3.1) - (3.3), except the explicit viscosity in eq. (3.2) is zero. This set of equations is referred to as the Euler equations (Choudhuri 1998, Section

4.1). **MUSIC** simulations use the same tabulated equation of state and opacity used by the 1D stellar evolution code that produced the stellar structure. In eq. (3.5),  $\vec{g}$  is the gravitational acceleration, a spherically symmetric vector consistent with that used in the stellar evolution calculation.

### ***3.2.1 Spatial integration***

**MUSIC** uses a second-order finite volume method (FVM) to discretize the spatial domain on a staggered grid. The FVM discretizes the equations into cells with individual volumes, such that the flux values can be measured at cell edges as fluid enters and exits the cell. This makes FVM well suited to handle conservation laws (Moukalled et al. 2015). The flux values on the faces are calculated with the Monotone Upwind Scheme for Conservation Laws (MUSCL) method, which is used to approximate the values for conservation laws while preserving monotonicity (Van Leer 1997; Thornber et al. 2008). The term ‘monotone’ indicates that only one numerical solution is found, so the scheme eliminates oscillations or nonphysical solutions. The term ‘upwind’ accounts for the direction of the flow. We use a van Leer limiter to ensure total variation diminishing (as described in Van Leer 1974; Roe 1986; LeVeque et al. 2006), which limits the gradient of the numerical solution from being overly steep by comparing the solution of one cell to the solutions in the neighboring cells. We ensure the function is total variation diminishing so that the solution does not increase, vary, or produce spurious oscillations over time.

The domain of the simulation includes  $r$  and  $\theta$  coordinates; in 3D simulations, the additional  $\phi$  coordinate is also used. We use the quantity  $H_{p,\text{CB}}/\Delta r$  to compare the radial

resolution between different simulations. This measure of resolution indicates how well the number of grid spaces resolves the pressure scale height at the convective boundary. The quantity  $H_{p,\text{CB}}/\Delta r$  is a physically meaningful description of resolution that can be compared with other global stellar simulations, unlike the grid size of the simulation. **MUSIC** allows angles between zero and  $180^\circ$  in  $\theta$ , and between zero and  $360^\circ$  in  $\phi$ . For 2D simulations, **MUSIC** assumes azimuthal symmetry. The spherical grid that is presently available in **MUSIC** has a singularity along the line between the north and south poles; for this reason, the present simulations do not generally include the full  $180^\circ$  angle in  $\theta$ .

### ***3.2.2 Time integration***

Time integration in the **MUSIC** code is fully implicit. The equations are discretized in time using a second-order accurate Crank-Nicholson scheme, which uses a finite difference method (FDM) to approximate the time variable at a midpoint between time steps. The equations are solved implicitly using a Jacobian-free Newton-Krylov (JFNK) solver (Knoll & Keyes 2004). The JFNK solver utilizes several computational techniques, such as the Newton-Raphson iterative root-solving method, the Krylov subspace, and physics-based preconditioners (Viallet et al. 2016; Newman & Knoll 2013; Mousseau et al. 2000; Chen et al. 2014; Holod et al. 2021). These techniques are implemented using three nested loops, working from the inside out. The innermost loop uses Picard linearization to approximate the nonlinear problem as a series of linear problems and determine the physics-based preconditioning matrix. The middle loop uses the physics-based preconditioner to calculate the matrix-vector product in the Krylov subspace. Solving for the matrix-vector product rather than the matrix itself is a low-storage

option, called ‘matrix-free’ or in this case, ‘Jacobian-free.’ Finally, the outermost loop uses the Newton-Raphson method to iteratively converge to a solution.

For simulations that use explicit time integration, the Courant-Friedrichs-Lewy (CFL) condition is a stability criterion; the virtue of implicit time integration is that it can produce a stable solution without satisfying the ‘CFL condition.’ **MUSIC** uses fully implicit time integration. It also takes adaptive time steps that adapt automatically to the physics of the flow based on the CFL number. **MUSIC** calculates three versions of the CFL number related to advection, acoustic waves, and radiative diffusion. The CFL numbers depend on the speed of sound, gravity, thermal conductivity, and opacity. **MUSIC** allows limits on all three versions of the CFL number simultaneously.

In stellar hydrodynamics, we are interested in achieving a long time-series of steady-state data. Before reaching a steady state, the simulation must relax on a timescale that is much longer than the convective turnover time. Pratt et al. (2016) defines a convective turnover time as

$$\tau_{\text{conv}}(t) = \int_{\text{CZ}} dV \frac{H_p}{|v|} / \int_{\text{CZ}} dV . \quad (3.7)$$

In this expression,  $H_p$  is the pressure scale height, and the magnitude of velocity  $|v|$  is calculated in either 2D or 3D, depending on the simulation. The integration covers the convection zone (CZ) and is volume-weighted using volume element  $dV$ . The instantaneous value of  $\tau_{\text{conv}}$  is averaged over time. An example of this calculation is shown in Figure 3.1. To determine the number of turnover times the simulation has experienced in steady-state,

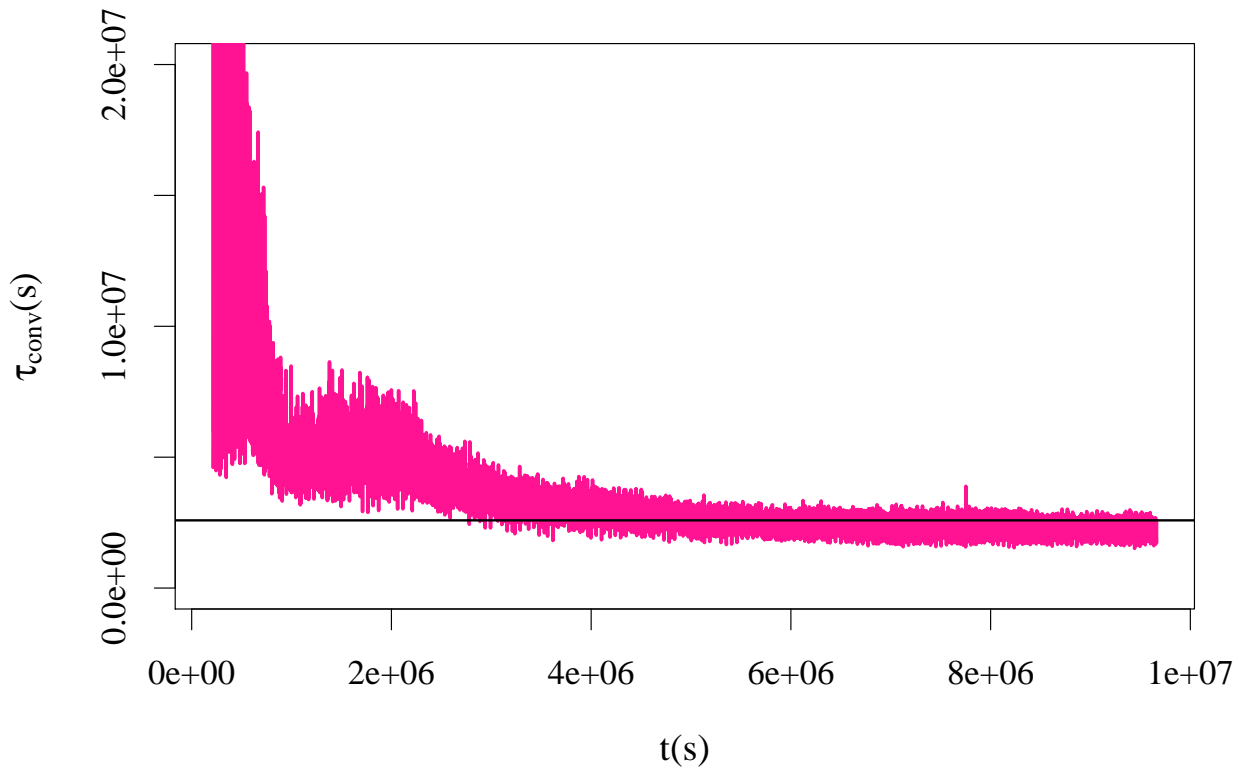


Figure 3.1 The global convective turnover time  $\tau_{\text{conv}}$  over the lifetime of a simulation of a  $3M_{\odot}$  pre-main sequence star with a small convective envelope. The black horizontal line represents the average turnover time  $\tau_{\text{conv}} = 2.5 \times 10^6$  seconds, which is averaged after reaching steady-state, which begins at time  $t = 3.4 \times 10^6$  seconds.

we express the amount of steady-state data in units of average global turnover time. For this simulation, the amount of steady-state data can be expressed as 0.7 turnover times, but we often publish results with more than 100 turnover times of steady-state data (Dethero et al. 2024). The number of turnover times needed for the convergence of a given diagnostic varies.

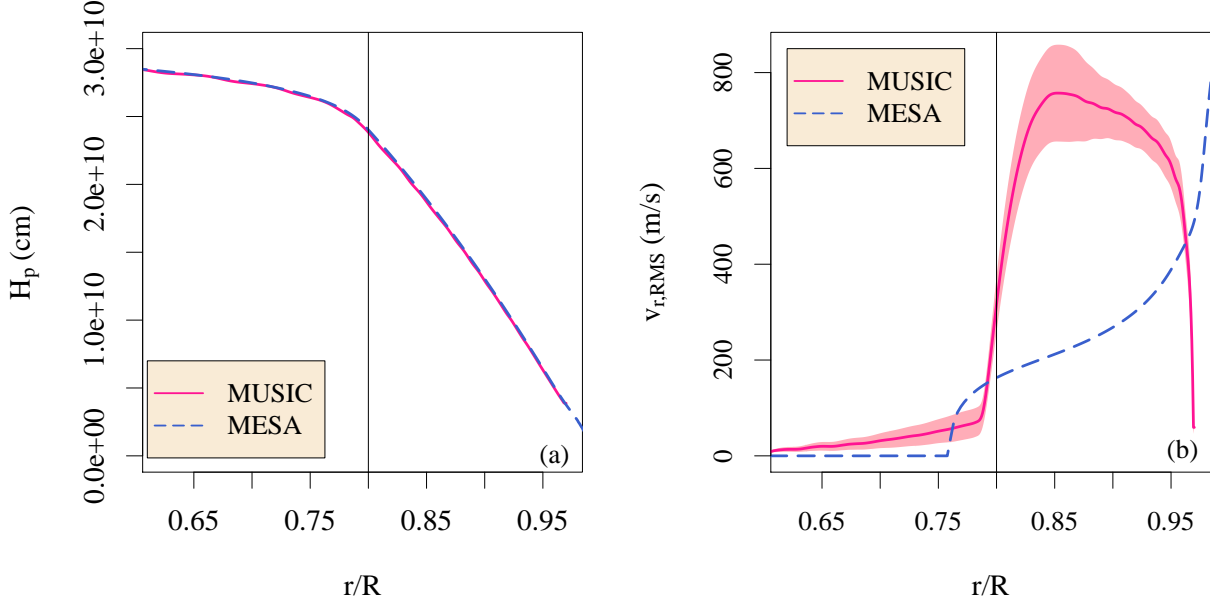


Figure 3.2 (a) Pressure scale height profile for MUSIC (pink, solid line) and MESA (blue, dashed line) is identical in structure. (b) Radial root-mean-squared velocity calculated with MUSIC (pink, solid line) and the convective velocity in MLT calculated with MESA (blue dashed line) for a  $3M_{\odot}$  pre-main sequence star with a shallow convection zone. The pink-shaded region represents one standard deviation above and below the time-averaged mean.

### 3.3 MUSIC diagnostics for convection

MUSIC uses stellar structures produced by either MESA (Paxton et al. 2010) or the Lyon evolutionary code (Baraffe et al. 2002) to calculate the initial state for a stellar simulation. For example, in a  $3 M_{\odot}$  star, we choose a stellar model at an age on the pre-main sequence where the convective envelope covers the outer 20% of the star. We use the stellar profiles from that snapshot to define initial parameters such as temperature, pressure, density, radius, luminosity, mass, and metallicity. We choose the inner radial boundary at radius  $r_i/R = 0.6$  and an outer radial boundary at  $r_i/R = 0.97$ . The grid size of the simulation is  $n_r \times n_{\theta} = 512 \times 201$ , and the resolution of the simulation is  $H_{p,CB}/\Delta r = 105$ . The initial velocities in

the simulation are zero; velocities due to convection grow self-consistently. Once **MUSIC** starts producing steady-state data, we can calculate diagnostics that can be compared to those in 1D convection models. To confirm the stellar structures are identical in both models, we compare the pressure scale height as a profile, as shown in Figure 3.2(a). We compare the convective velocity calculated with 1D MLT (eq. (2.51)) to the root-mean-squared velocities calculated in 2D in **MUSIC**, as shown in Figure 3.2(b). This MESA model incorporates a user-defined overshooting depth of  $\approx 0.18H_{p,\text{CB}}$ , which accounts for the extension of convective flow into the radiative zone. The value of the convective velocity in the **MUSIC** simulation at the convective boundary ( $r_{\text{CB}}/R = 0.8$ ) is twice as high as the MESA model. Figure 3.2(b) emphasizes the need for an improved 1D mixing model. In the **MUSIC** calculation, the uncertainty above and below the velocity profile is based on the standard deviation in time, and it reflects the range of velocities in the convection zone. This is evident when examining the distribution of radial velocities in 2D, which is shown in Figure 3.3(a). The blue flows represent the thin, fast inflows and the pink flows represent the broader, slower outflows. We also show the vorticity magnitude of this simulation in Figure 3.3(b). The  $\phi$  vorticity is represented as  $\omega_\phi = \nabla \times \vec{v}|_\phi$ , and it allows us to visualize the swirling motions in a star in the  $\phi$  direction. This is sometimes represented as the 2D enstrophy, or  $\omega_\phi^2$ , which can be compared easily among simulations, as in Dethero et al. (2024). Another feature of vorticity is that it reveals the internal gravity waves (IGW) in the radiative zone, which are excited by the convective flows hitting the convective boundary, and buoyancy forces restoring these waves (Press 1981).

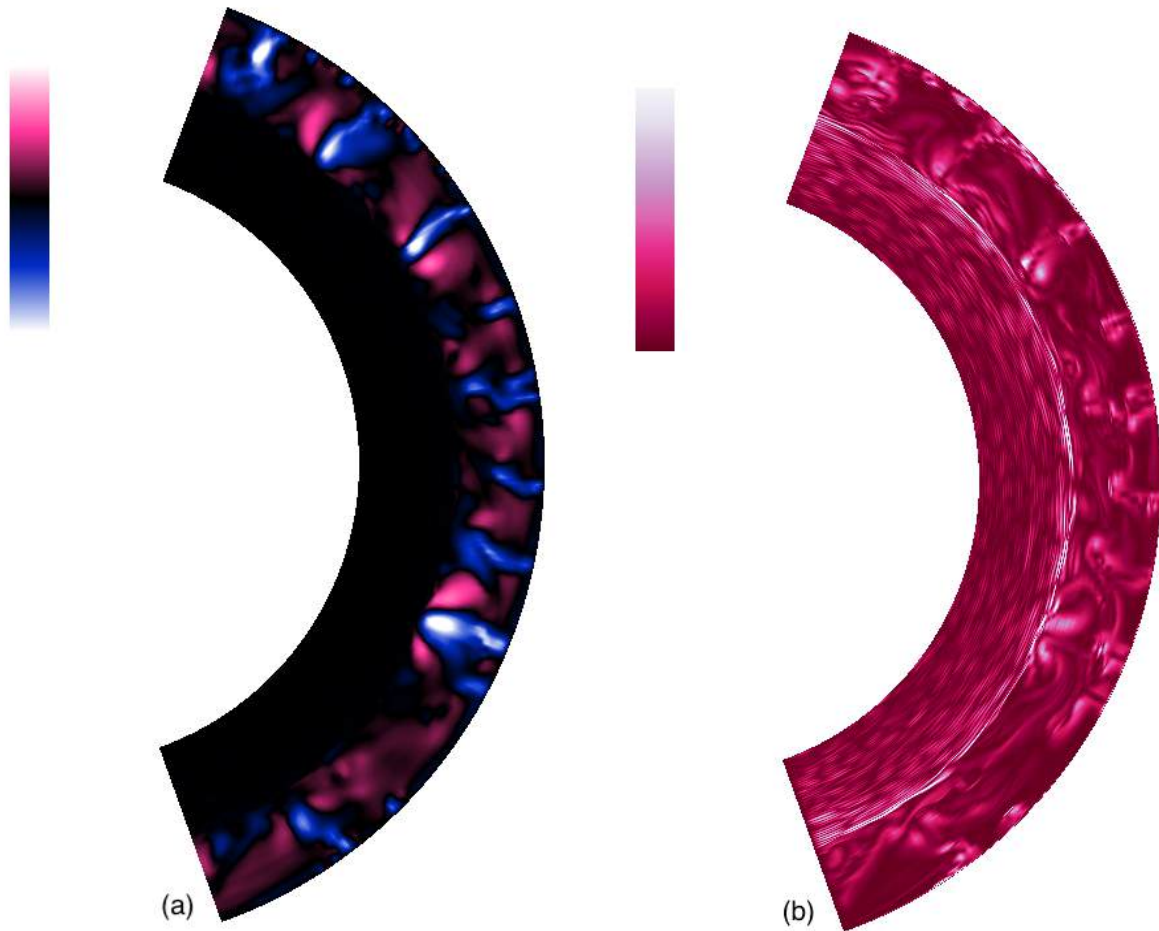


Figure 3.3 (a) Radial velocity for a pre-main sequence  $3M_{\odot}$  star simulated in MUSIC, where pink flows are moving outward and blue flows are moving inward. Black is the zero point. The maximum velocity magnitude is 1.8 km/s. (b) Vorticity magnitude for the same simulation, where dark pink represents zero vorticity, and white represents strong vorticity.

### 3.3.1 Convective overshooting calculations

A useful diagnostic for probing the amount of stellar mixing is the convective overshooting depth  $\ell_{\text{ov}}$ , which quantifies the length that the convective plume travels into the stable region before dissipating. We calculate the convective overshooting depth in MUSIC simulations using two different physical criteria: the vertical kinetic energy flux and the vertical heat

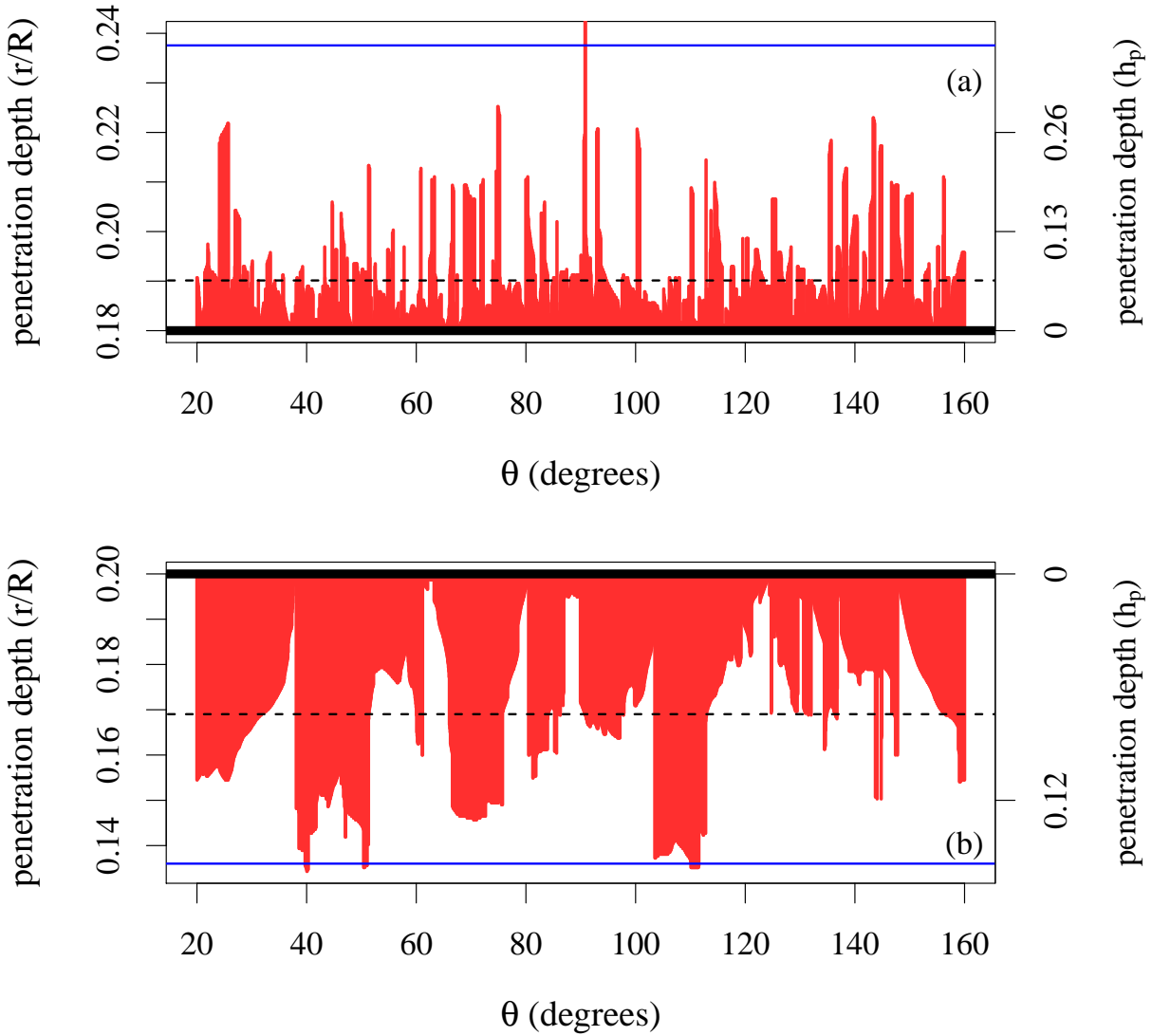


Figure 3.4 Penetration depths as a function of angle  $\theta$  for an arbitrary time frame for (a) core overshooting in a  $6 M_{\odot}$  main sequence star named *ccmod* and (b) envelope overshooting a  $4 M_{\odot}$  pre-main sequence star named *pms4m*. The overshooting depths calculated with EVT are represented by a blue solid line. The dashed line represents the average overshooting depth at this time.

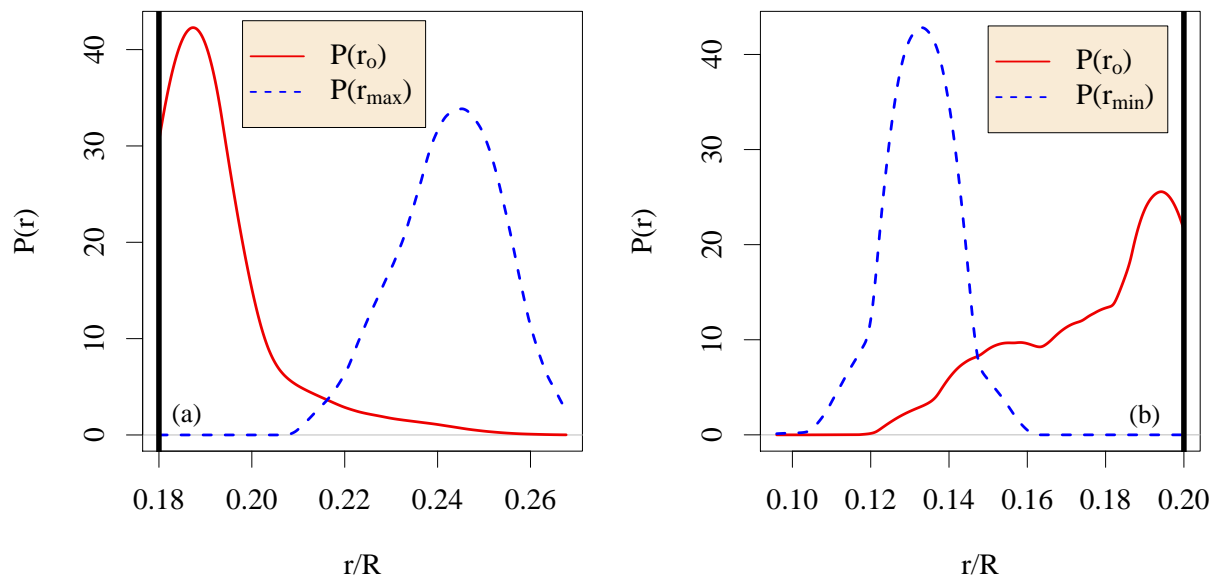


Figure 3.5 Probability density functions for all convective overshooting,  $P(r_o)$ , and the extreme values for overshooting depth  $P(r_{\max})$  or  $P(r_{\min})$ , calculated with the vertical kinetic energy flux. The stars we examine include (a) core overshooting in a  $6 M_{\odot}$  main sequence star, *ccmod*, and (b) envelope overshooting in a  $4 M_{\odot}$  pre-main sequence star, *pms4m*.

flux. The overshooting depth at a given angle is the radial point where the flux changes sign after crossing the convective boundary (Hurlburt et al. 1994; Rogers et al. 2006; Tian et al. 2009; Pratt et al. 2017). Figure 3.4 shows the overshooting depth for both a star with a convective core and a star with a large convective envelope as a function of the angular coordinate  $\theta$ . The left vertical axis identifies the location in the star in units of fractional total radius, and the right vertical axis represents the penetration depth in units of the pressure scale height at the convective boundary. The average penetration depth is expressed by the dashed line. As shown in Figure 3.4(a), one plume travels four times this average. In 1D stellar evolution codes, the quantity for convective overshooting depth is a single number. To calculate the equivalent value from a multi-dimensional hydrodynamic

simulation, the mean value expressed by the dashed line in Figure 3.4 has historically been used. However, the mean is only representative of a Gaussian distribution. The distribution of overshooting plumes is far from Gaussian for two reasons: (1) one side of the distribution is cut-off because overshooting cannot happen inside the convection zone by definition, and (2) convective overshooting is an intermittent processes, so that a heavy wing exists on the half of the distribution that is present (see the red lines in Figure 3.5). For the large convective envelope in Figure 3.5(b), the distribution for  $P(r_o)$  has an especially heavy wing. Pratt et al. (2017) have developed an analysis using extreme value theory (EVT) to determine a depth of convective overshooting,  $\ell_{ov}$ . These values are  $\ell_{ov}/H_p = 0.38$  for the convective core simulation and  $\ell_{ov}/H_p = 0.15$  for the large convective envelope. For both simulations, the overshooting value determined using this EVT analysis is greater than the instantaneous average for the arbitrary snapshot, represented by the solid blue line in Figure 3.4. The question of which stellar properties determine the depth of convective overshooting requires a controlled study, which will be considered in the next chapter.

## CHAPTER 4

### The filling factor: a single-point diagnostic for stellar convection

Predicting the evolution of stars requires a prescription for the amount of mixing caused by convection at different values of the internal radius of the star. This mixing has been widely linked to the concept of a filling factor for the convective inflows (e.g., Schmitt et al. 1984; Stein & Nordlund 1989; Cattaneo et al. 1989; Toomre et al. 1990; Cattaneo et al. 1991; Zahn 1991; Canuto & Dubovikov 1998; Brummell et al. 2002; Rempel 2004; Browning et al. 2004; Rogers et al. 2006; Käpylä et al. 2017; Cai 2020). Conceptually, a filling factor quantifies how much of the star is moving inward at a given radius, where a number less than one-half means that inflows are more concentrated than outflows. Several early works on stellar convection (e.g., Schmitt et al. 1984; Stein & Nordlund 1989; Hurlburt et al. 1984) predict that the large stratification present in stellar convection zones should produce convective motions that have a pronounced asymmetry between inflows and outflows, corresponding to a filling factor less than one-half. Indeed observations of the solar surface find strong, coherent inflows surrounded by weaker, more diffuse outflows (e.g., as discussed in Nordlund et al. 2009). Where present, such an asymmetry would alter the shear interaction between opposing flow structures, and thus change the amount of fluid mixing. The filling factor has been viewed as a fundamental measure of how the stellar convection zone is structured.

Evaluating the filling factor at the boundary of convective instability provides an indication of how much fluid overshoots the convection zone and enters the radiative zone. This provides a link between the structure of convective flows in the convection zone and

the depth of convective overshooting or penetration. Several works (Zahn 1991; Brummell et al. 2002) suggest that a filling factor could play a more significant role in determining the overshooting depth than the radial velocity at the convective boundary. The convective velocities typically differ between 2D and 3D, and the convective flow structures are visually different; the filling factor has been discussed as a plausible source of difference between 2D and 3D stellar simulations (e.g., Schmitt et al. 1984; Cai 2020; Pratt et al. 2020).

The question of how to best define a filling factor remains open because it depends on how to accurately define the edges of structures in a convective flow. Without loss of generality, we call such structures “plumes” in this work. We will also refer to convective flows moving inward toward the core as “inflows” and those moving outward toward the surface as “outflows.” Many works (e.g., Schmitt et al. 1984; Canuto & Dubovikov 1998; Brummell et al. 2002; Andr assy 2015) have defined the filling factor to be the fractional area occupied by inflows at a given radius interior to the star. These works thus define the edges of convective plumes using the radial velocity. We call this definition the *volume-percentage* filling factor. In contrast, Rempel (2004) defines a filling factor as the fraction of the mass flux in the inflows at a given radius; we call this the *mass-flux* filling factor. Zahn (1991) defines a plume based on the convective flux, and uses the fraction of the convective flux carried by inflows to define a filling factor; we call this the *convective-flux* filling factor.

These definitions of the filling factor have been evaluated in ideal box-in-a-star type simulations, which often use a moderate stratification and an ideal gas equation of state. For example, Cai (2020) calculates the filling factor profile for convective cores and links it to the

overshooting depth in a box-in-a-star simulation with an ideal equation of state. Brummell et al. (2002) solve compressible equations for an ideal gas in a box-in-a-star simulation, with a density stratification of  $\sim 50$ , and find filling factors between 0.2 and 0.55. Käpylä (2021) uses the Pencil code to calculate the filling factor profile in a box-in-a-star simulation, using an ideal gas equation of state with density stratification  $\sim 150$ . The filling factor has not been examined in the kinds of global stellar simulations that we perform in this work. Our simulations are performed in a spherical shell that includes a large portion of the stellar radius and uses a density stratification, temperature gradient, equation of state, and opacity tables that are extracted directly from stellar structure models accurate to the current state-of-the-art in stellar modeling. Our simulations also solve the equations for fully compressible convection; no additional assumptions are made that could impact the asymmetry of the convective flow. The field of stellar hydrodynamics includes both realistic and idealized studies; realistic simulations of this kind have not been possible until recently, and push the limits of what can be achieved with modern computational resources.

We evaluate each definition of a filling factor for suitability to use in theoretical models of convection and overshooting based on two criteria, namely whether they: (1) are different for different stellar models and for 2D and 3D simulations, and (2) are correlated with the measured overshooting depth in the simulations. We additionally attempt to resolve whether the filling factor can reveal differences between core convection and envelope convection in stars.

## 4.1 Simulations

In this chapter, we produce and study simulations of stellar convection in six different stellar structures using the MUSIC code. Our simulations are described in Table 4.1. The first four stars were discussed in Dethero et al. (2024); these include a red giant star (simulations *bg2D/3D*), a young sun (simulations *wm2D/3D*, and *wide2D/3D*), a current sun (simulations *dcs2D/3D*), and a large main sequence star with a convective core (simulations *cc2D/3D*). The first star we examine (simulations *bg2D/3D*) is a  $3 M_{\odot}$  star that is ascending the red giant branch, produced with the open-source Modules for Experiments in Stellar Astrophysics (MESA) code (Paxton et al. 2010); this star has a large outer convection zone because it is near the first dredge-up point. The second star that we examine (simulations *wm2D/3D*, and *wide2D/3D*) is a one  $M_{\odot}$  pre-main sequence star, called the young sun, produced with the Lyon stellar evolution code (Baraffe & El Eid 1991; Baraffe et al. 1997, 1998). This model has been described in Pratt et al. (2016, 2017, 2020); the young sun model is approximately three times larger in radius than the current sun, with an age of  $\approx$  one million years, where accreting has stopped and the star is gradually contracting.

The third star (simulations *dcs2D/3D*) is a one  $M_{\odot}$  main-sequence star with a moderate outer convective layer, similar to the current sun, produced with the Lyon stellar evolution code. Similar simulations were studied in Vlaykov et al. (2022) to identify the impact of radial boundary conditions on measurements of convective overshooting in solar simulations. This model has a luminosity of  $L_* = 0.98772L_{\odot}$ , a radius of  $R = 1.0169R_{\odot}$ , and Solar metallicity. The fourth star (simulations *cc2D/3D*) is a  $20 M_{\odot}$  star at the zero-age main

sequence (ZAMS) with a large convective core, produced with the Lyon stellar evolution code. A similar star was studied in Baraffe et al. (2023), in a study of the impact of stellar mass on convective core overshooting, where the star has solar metallicity and a convective core mass of  $8.8 M_{\odot}$ . This model provides an opportunity to explore the filling factor in convective cores, as well as extremely high masses. Two additional stars are examined in this chapter that were not included in Dethero et al. (2024); we have produced higher resolution simulations to highlight similarities and differences between core convection and envelope convection. Of these additional stellar models, the fifth star is a  $6 M_{\odot}$  main sequence star with a small convective core, produced with MESA. The sixth star is a  $4 M_{\odot}$  star on the pre-main sequence with a deeper convective envelope than the young sun, also produced with the MESA code. These stars represent the different stages of evolution where convection occurs: pre-main sequence, main sequence, and evolved stars. They also represent different types of convection zones: outer convective envelopes that range between deep and shallow, as well as convective cores of different sizes. Visualizations of the radial velocities in each of these stars are provided in Figure 4.1. Visualizations of the  $\phi$  vorticity in each star are provided in Figure 4.2.

In each of these simulations, the star is assumed to have a homogeneous chemical composition. We perform four pairs of Implicit Large Eddy Simulations (ILES) (Grinstein et al. 2007; Ritos et al. 2018; Margolin 2019) using the MUlti-dimensional Stellar Implicit Code (MUSIC) in which the first four stellar structures are simulated in 2D and 3D. In these simulation pairs, the simulation volume and grid for the 3D simulation are identical to the 2D

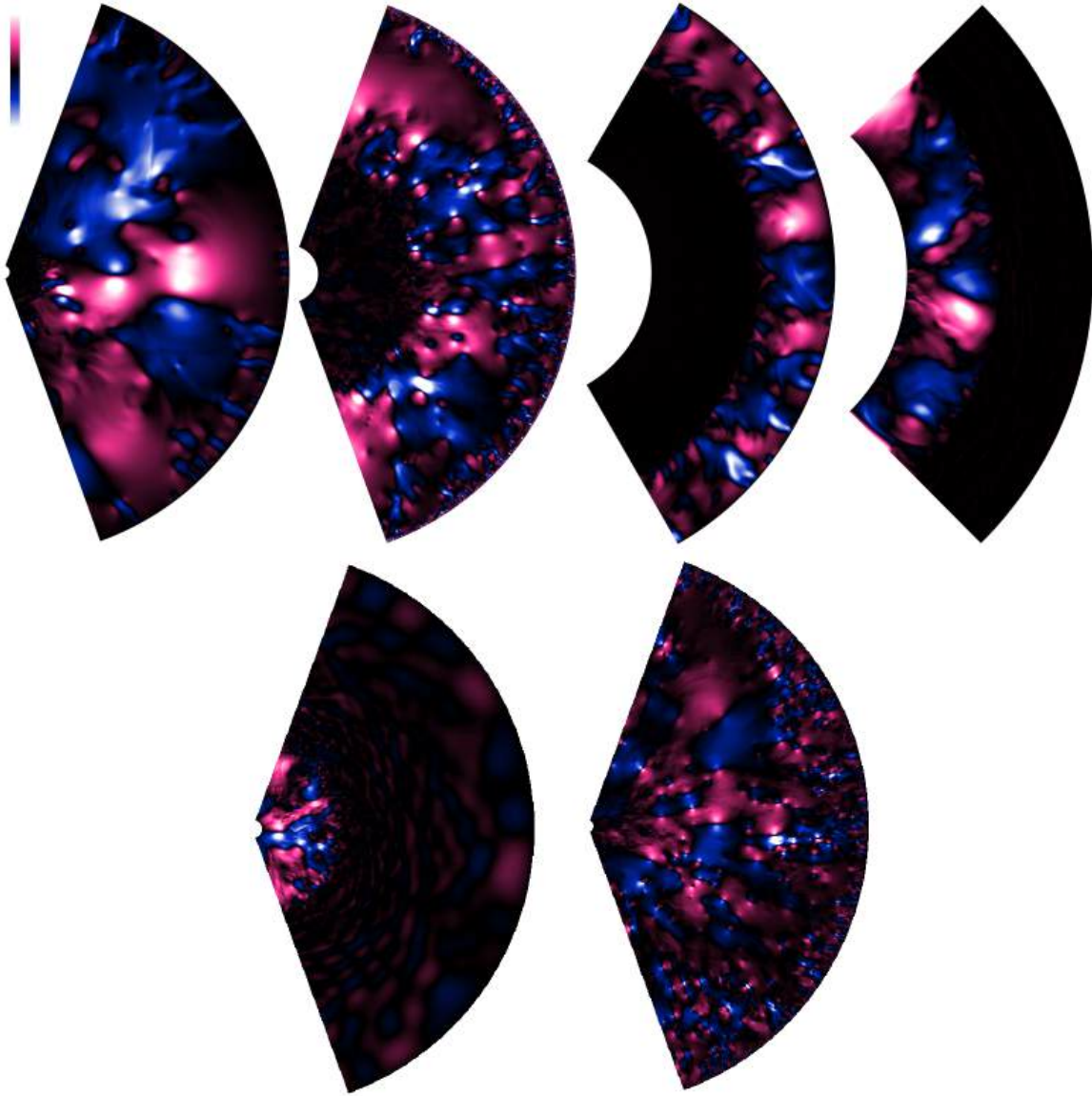


Figure 4.1 Visualizations of radial velocity in 2D simulations (first row, left to right: *bg2D*, *wm2D*, *dcs2D*, and *cc2D*, second row, left to right: *ccm2D*, *pms4m2D*). Outward flows are indicated in pink, while inward flows are in blue; the zero point in velocity is black. The maximum and minimum values of the color scale are defined by a radial velocity magnitude near the maximum for each simulation: *bg2D* ( $\pm 6.5$  km/s), *wm2D* ( $\pm 2.9$  km/s), *dcs2D* ( $\pm 0.63$  km/s), *cc2D* ( $\pm 1.5$  km/s), *ccm2D* ( $\pm 6.7$  km/s), *pms4m2D* ( $\pm 7.5$  km/s).

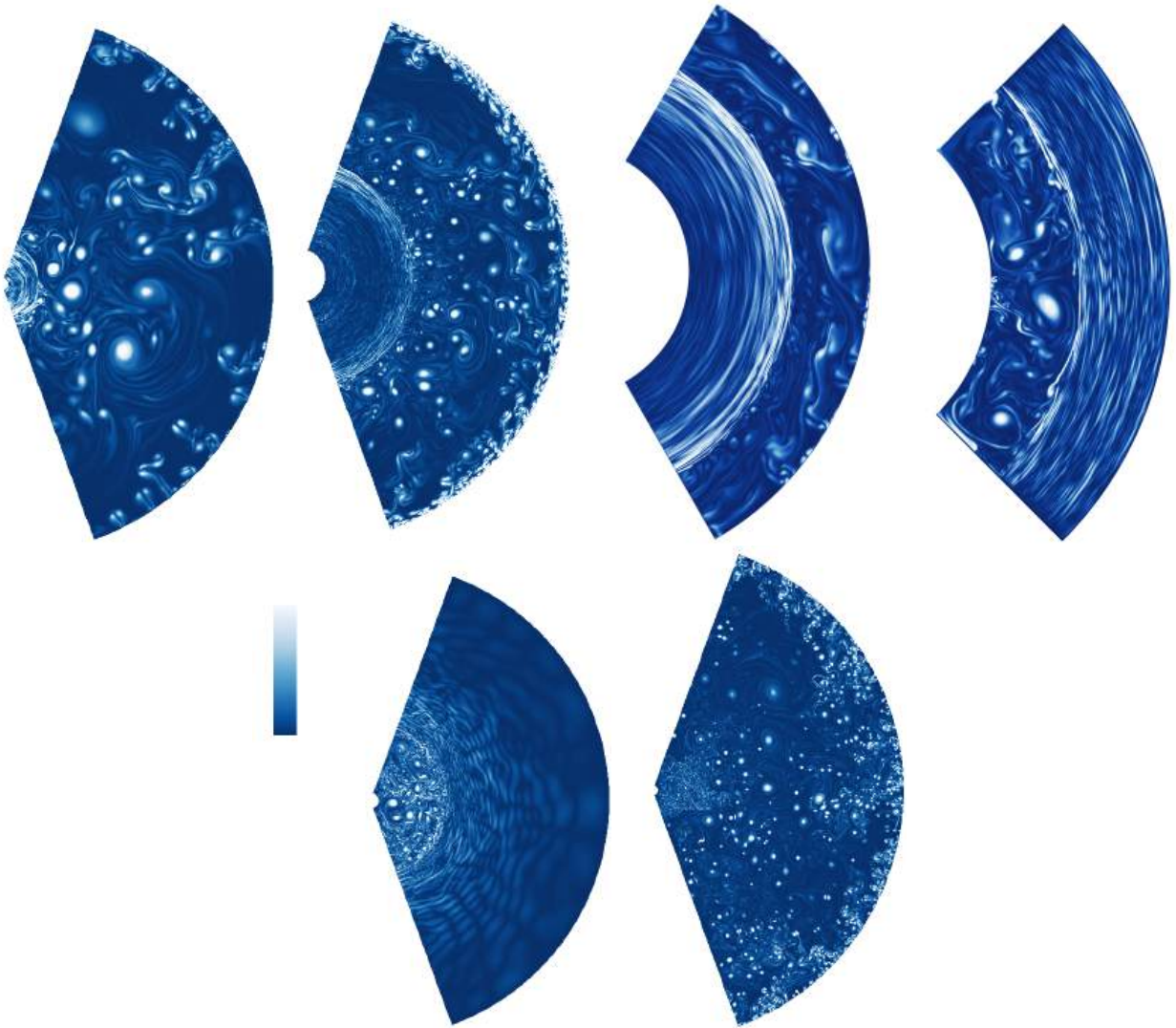


Figure 4.2 Visualizations of vorticity in the  $\phi$  direction in 2D simulations (first row, left to right:) *bg2D*, *wm2D*, *dcs2D*, and *cc2D*, (second row, left to right: *ccm2D*, *pms4m2D*). Flows with high vorticity are indicated in white, while zero vorticity is represented in blue. High vorticity identifies eddies in the convection zone and internal gravity waves in the radiative zone.

simulation except for the dimensionality. The `MUSIC` code uses an adaptive time step, which is constrained identically for each pair of 2D and 3D simulations. The simulation volume and grid in the  $r - \theta$  plane are identical for each pair of simulations.

Three-dimensional simulations are computationally intensive, and this limits the radial resolution that can be used for these 2D/3D simulation pairs. In order to include 2D results with higher radial resolution in this fundamental study of filling factors, we also include the simulations *ccmod2D* and *pms4m2D*. The radial resolution is critically important for accurately measuring convective boundary mixing in stars. Because our goal is generally to use the highest radial resolution possible, we also study convection in spherical shells. The additional high-resolution 2D simulation *ccmod2D* provides a second simulation of core convection to compare with *cc2D*. Similarly the high-resolution 2D simulation *pms4m2D* provides a second example of a star with a deep envelope to support the conclusions we draw from simulations (simulations *wm2D/3D*, and *wide2D/3D*).

In all of our `MUSIC` simulations, the compressible hydrodynamic equations (3.4)-(3.6) are solved in a spherical shell using spherical coordinates: radius  $r$ , and angular variables  $\theta$  and  $\phi$  (in 3D). Our simulations in this work are designed to allow us to study the properties of convection in realistic stellar structures. Other physical effects such as rotation, a tachocline, chemical mixing, and magnetic fields are not included in these simulations. The convective core simulations *cc2D/3D* did allow the gravity to be recalculated, but changes in this gravity term were small (see Baraffe et al. 2023). Gravity was not evolved otherwise.

To allow a clear comparison of the convective turnover time between 2D and 3D simu-

Table 4.1 Parameters for compressible hydrodynamic simulations performed with MUSIC. Two different pairs of young sun simulations are included: (1) the *wide2D* and *wide3D* pair have lower radial resolution but the 3D simulation uses a large angle along the equator, while (2) *wm2D* and *wm3D* use a smaller equatorial angle but significantly higher radial resolution. The pair of red giant simulations is *bg2D* and *bg3D*; the pair of current sun simulations is *dcs2D* and *dcs3D*; the pair of convective core simulations is *cc2D* and *cc3D*. The high-resolution 2D simulations are *ccmod2D* and *pms4m2D*. The simulation name, dimensionality, evolutionary state, and stellar mass  $M$  in units of the solar mass  $M_\odot$  are provided. The inner radius  $R_i$  of the spherical shell, the radius of the convective boundary  $R_{CB}$  determined by the Schwarzschild criterion, and the outer radius  $R_o$  of the spherical shell for the simulation are given in units of the total radius of each star,  $R$ , as a triplet. The angular extent of the simulation in the polar and equatorial directions is given as  $(\theta, \phi)$ , and the grid spacing in both angular directions is  $(\Delta\theta, \Delta\phi)$ .

	dims.	evol.	$M/M_\odot$	$(R_i, R_{CB}, R_o)/R$	$(\theta, \phi)$ ( $^\circ$ )	$(\Delta\theta, \Delta\phi)$ ( $^\circ$ )	$H_{p,CB}/\Delta r$
wide3D	3D	PMS	1	(0.21,0.43, 1.00)	(140, 140)	(0.55,0.55)	63
wide2D	2D	PMS	1	(0.21,0.43, 1.00)	(140,0)	(0.55,-)	63
wm3D	3D	PMS	1	(0.10,0.43, 1.00)	(140,9)	(0.14,0.14)	258
wm2D	2D	PMS	1	(0.10,0.43, 1.00)	(140,0)	(0.14,-)	258
bg3D	3D	RGB	3	(0.02, 0.175,0.90)	(140,19)	(0.30,0.30)	55
bg2D	2D	RGB	3	(0.02, 0.175,0.90)	(140,0)	(0.30,-)	55
cc3D	3D	MS	20	(0.194, 0.287, 0.38)	(90,22)	(0.27,0.52)	140
cc2D	2D	MS	20	(0.194, 0.287, 0.38)	(90,0)	(0.27,-)	140
dcs3D	3D	MS	1	(0.40, 0.72, 0.97)	(120,240)	(0.33, 0.64)	134
dcs2D	2D	MS	1	(0.40, 0.72, 0.97)	(120,0)	(0.33,-)	134
ccmod2D	2D	MS	6	(0.02, 0.18, 0.6)	(140,0)	(0.14,-)	269
pms4m2D	2D	PMS	4	(0.02, 0.2, 0.97)	(140,0)	(0.06,-)	1166

Table 4.2 Time scales for the compressible hydrodynamic simulations performed with MUSIC. The average global convective turnover time  $\tau_{conv}$  is provided as well as its standard deviation in time, and the total time span for each simulation is given in units of the convective turnover time.

	$\tau_{conv}(10^5\text{s})$	time span ( $\tau_{conv}$ )
wide3D	$7.06 \pm 0.3$	3.8
wide2D	$7.9 \pm 0.7$	104
wm3D	$3.91 \pm 0.21$	5.4
wm2D	$3.76 \pm 0.98$	141
bg3D	$6.48 \pm 0.07$	22
bg2D	$10.86 \pm 2.16$	163
cc3D	$92.6 \pm 7.7$	3.77
cc2D	$36.5 \pm 27.5$	35.7
dcs3D	$9.6 \pm 1.0$	3.9
dcs2D	$28.4 \pm 5.5$	84
ccmod2D	$1.4 \pm 0.1$	0.7
pms4m2D	$11.9 \pm 1.1$	11.5

lations, we average the instantaneous value of eq. (3.7) over time for each simulation. The magnitude of velocity in the denominator is calculated in either 2D or 3D, depending on the simulation. The values are recorded in Table 4.2. Our highest resolution simulation pair is *wm2D/wm3D*, as defined by the number of grid spaces that resolve the pressure scale height at the convective boundary,  $H_{p,\text{CB}}/\Delta r$ . The resolution for each simulation is recorded in Table 4.1. Simulation *wm3D* has a grid of  $r \times \theta \times \phi = 1312 \times 1024 \times 64$ ; as a comparison, simulation *pms4m2D* has a grid of  $r \times \theta = 2256 \times 2256$ , which translates to more than 4 times the radial resolution at the bottom of the convection zone. Our simulations all have sufficient radial resolution to produce a characteristic radial profile for velocity in 2D.

All simulations in this work are ILES, and convergence is not expected in the absolute sense that direct numerical simulations (DNS) converge. A universal shape of the velocity profiles can be observed with sufficiently small grid spacing, and the increase in the velocities becomes less as the grid spacing is progressively decreased (see also the discussion of ILES and convergence by Andrassy, R. et al. 2024). A study of the effect of grid spacing was examined systematically for the young sun by Pratt et al. (2016) and for the current sun by Vlaykov et al. (2022). The main sequence core convection simulation was studied by Baraffe et al. (2023). Similar results are obtained for the red giant simulations. Because of the complications presented by ILES for convergence, we find the use of resolution criteria based on  $H_{p,\text{CB}}/\Delta r$  to be more useful for convective overshooting than the traditional DNS-style convergence studies. As noted in Pratt et al. (2020), another reason grid spacing is particularly important for ILES is that it is directly related to the effective numerical

viscosity, which will influence the stellar mixing. Such resolution criteria allow for clear comparisons between simulations of different stars that use different grids. All data studied here are produced during steady-state convection, a period where the time-averaged value of the total kinetic energy is well-defined and not evolving in time. Each 3D simulation includes at least 3 convective turnover times of data taken during steady-state convection; for each 2D simulation, the time span is more than  $30 \tau_{\text{conv}}$ , except for *ccmod2D*, which has not yet reached a convective turnover time. The uncertainties in the calculation of the average convective turnover time have a larger standard deviation for the 2D simulation than the 3D simulation; this is clearly impacted by the longer time series of data available for the 2D simulations (e.g., also observed by Pratt et al. 2020).

We examine simulations with two variations on energy boundary conditions that maintain the original radial profiles of density and temperature of the 1D stellar evolution model. For the *wide2D/wide3D* and *wm2D/wm3D* simulations, which include the full stellar radius up to the photosphere, the surface radiates energy with the local surface temperature. In this case, the energy flux varies as  $\sigma T_s^4$ , where  $\sigma$  is the Stefan-Boltzmann constant and  $T_s(\theta, t)$  is the temperature along the surface. This boundary condition can only be effectively used when the near-surface layers are included in the simulation volume and the temperature gradient near the surface is sufficiently resolved; otherwise, it results in artificially high cooling rates. The young sun simulations have more than one grid space per pressure scale height in this region. For the *bg2D/bg3D*, *cc2D/cc3D*, *dcs2D/dcs3D*, *ccmod2D*, and *pms4m2D* simulations, which do not include the full stellar radius, we hold the energy flux and luminosity constant

on the outer radial boundary, at values established by the stellar structure. Pratt et al. (2016) and Vlaykov et al. (2022) examine the effects of boundary conditions on convective properties for the young sun and current sun, respectively. In both studies, they find including the near-surface layers increases velocity amplitudes and thus extends the overshooting layer.

In all of the simulations studied here, we use the luminosity profiles accurate to the stellar structure models; we do not employ the tactic of luminosity boosting to shorten the convective turnover time and bring the thermal time scale of the star closer to the convective turnover time. Luminosity boosting leads to a substantial reduction in computational costs and makes reaching thermal equilibrium feasible when a large enough boost factor is used. However, it can also distort the original background stratification of the star. Even if this is avoided, as discussed in Baraffe et al. (2021), luminosity boosting increases the overshooting depth, the local heating in the overshooting layer, and the shape of the spectrum of waves excited (Lecoanet et al. 2019; Le Saux et al. 2022). Our choice to use luminosities that have not been artificially boosted is motivated by the need to measure an overshooting depth for a specific star. The simulations that we study in this work are far from thermal equilibrium. However the temperature gradient is not evolving during these simulations, and the statistics that we produce are meaningful.

For the velocity, we impose non-penetrative and stress-free boundary conditions in the radial directions for all simulations. The energy flux and luminosity are held constant at the inner radial boundary, at the value of the energy flux at that radius in the one-dimensional stellar evolution calculation. On the inner radial boundary of the spherical shell, we impose

a constant radial derivative on the density for all simulations. At the outer radial boundary, we apply different boundary conditions that suit the local derivatives in density best. For simulations *bg2D/bg3D*, *ccmod2D*, *wide2D/wide3D*, and *wm2D/wm3D* this is a hydrostatic equilibrium boundary condition on the density that maintains hydrostatic equilibrium by assuming constant internal energy and constant radial acceleration due to gravity in the boundary cells (Grimm-Strele et al. 2015). For simulations *dcs2D/dcs3D* and *cc2D/cc3D* the outer radial boundary has a constant radial derivative imposed on the density. For simulations *bg2D/bg3D*, *wide2d/wide3d*, *wm2D/wm3D*, *dcs2D/dcs3D*, *ccmod2D*, and *pms4m2D* we impose periodicity on all physical quantities at the boundaries in  $\theta$  and  $\phi$ . For simulation *cc2D* the angular direction is treated with reflective boundary conditions; for simulation *cc3D* both angular directions are treated with periodic boundary conditions.

## 4.2 Differences between 2D and 3D stellar simulations

For each of the pairs of simulations that we study, the root-mean-square (RMS) radial velocity profile in the 2D simulation is larger than in the 3D simulation (see for example Figure 4.4). This is a common result for stellar convection also noted in Muthsam et al. (1995) and Pratt et al. (2020); the extent to which the 2D velocities are larger appears to be dependent on the stellar model examined. In addition, the radial velocities in 2D and 3D simulations look different; 3D simulations appear to be “rougher,” i.e., more small-scale structure is present. This is particularly visible at points where inflows and outflows interact (see Figure 4.3).

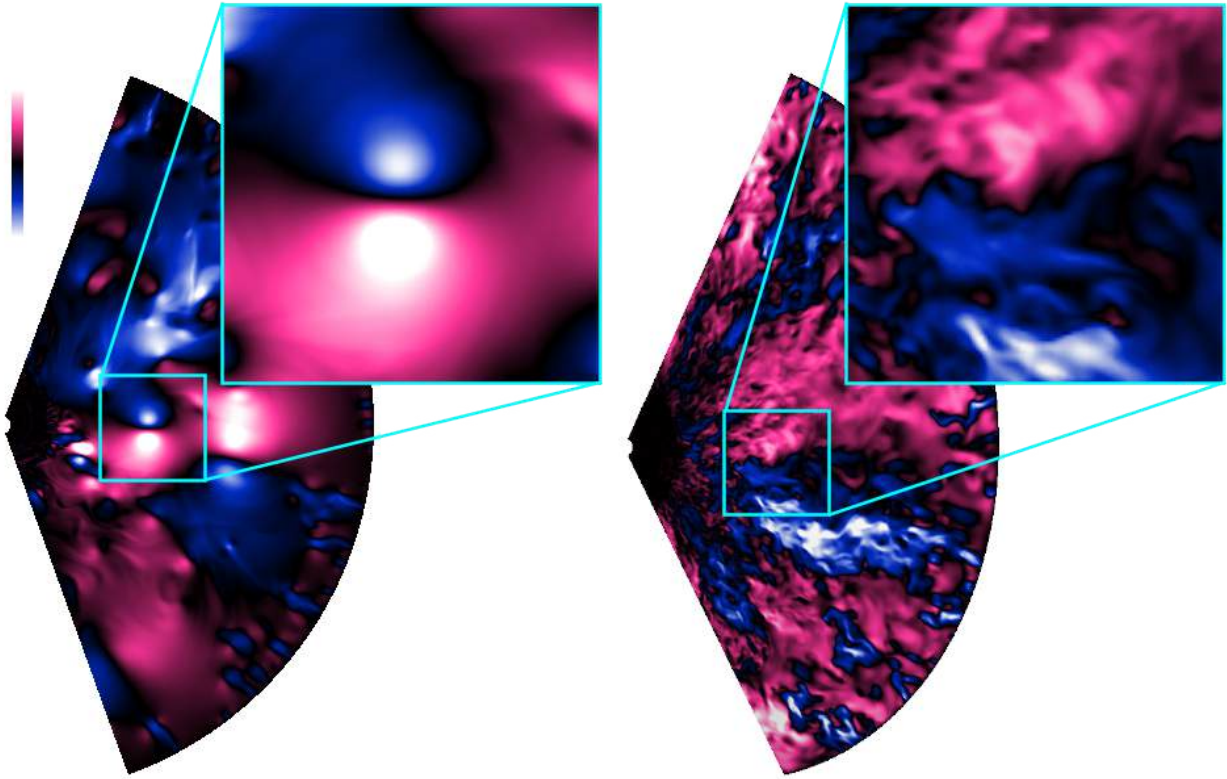


Figure 4.3 A comparison of radial velocity in the  $3M_{\odot}$  red giant star from (left) 2D simulation *bg2D*, and (right) 3D simulation *bg3D*. The visualization is zoomed in on a small region inside the convection zone to emphasize the differences in the shape of convection between 2D and 3D. Outward flows are indicated in pink, while inward flows are in blue; the zero point in velocity is black. The maximum and minimum values of the color scale are defined by a radial velocity magnitude near the maximum for each simulation: *bg2D* ( $\pm 6.5$  km/s), *bg3D* ( $\pm 2.9$  km/s).

The differences between 2D and 3D simulations also reach beyond velocity amplitudes into the structure of the flow. We examine the radial profile of the local enstrophy in the  $\phi$ -direction, defined as the square of the  $\phi$  component of the vorticity  $\omega_{\phi} = \nabla \times \vec{v}|_{\phi}$ . The local  $\phi$  enstrophy is larger in 2D than in 3D, with the largest differences occurring at, or near, the convective boundary (see Figure 4.4). These plots reveal a different shape and

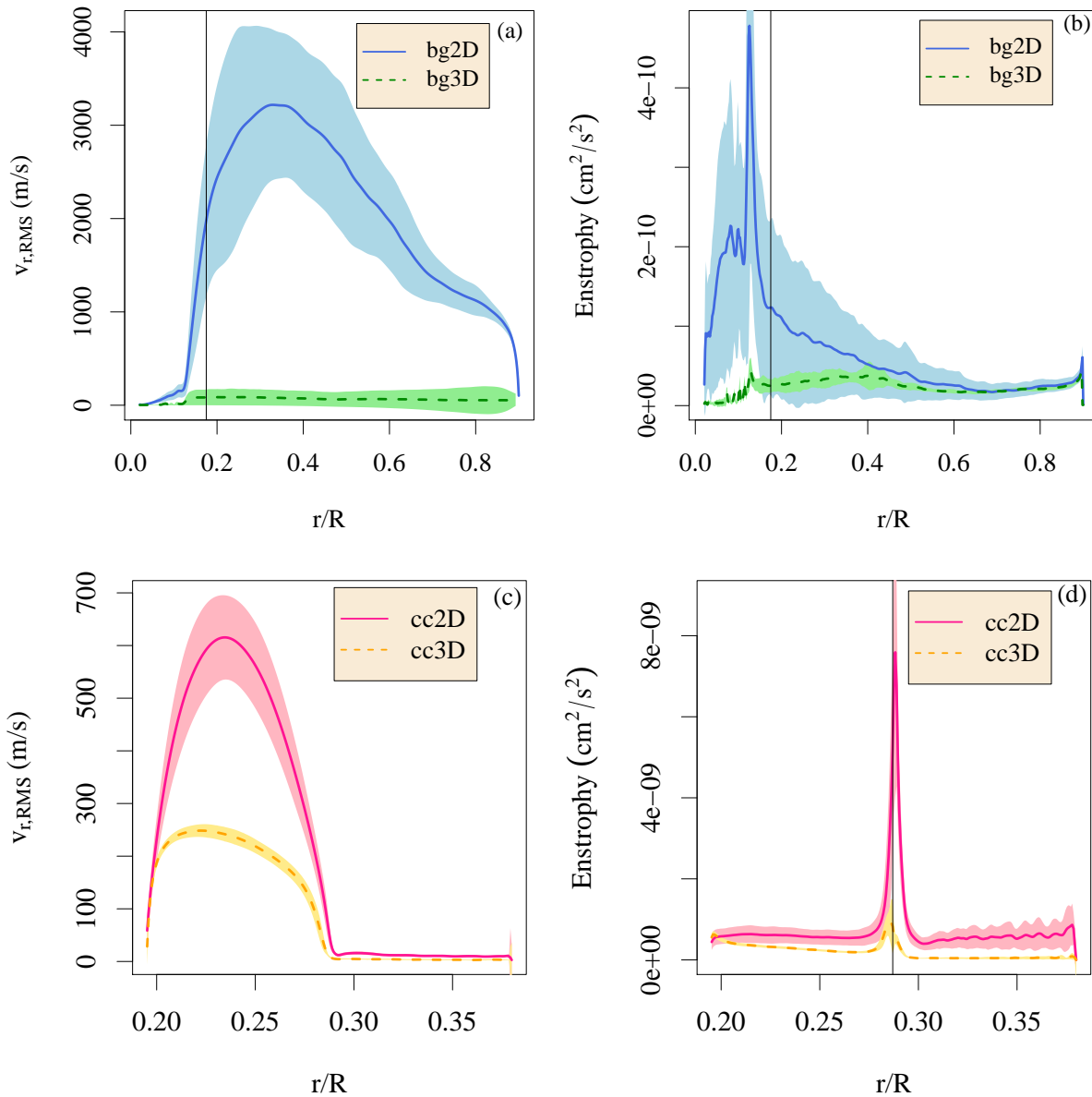


Figure 4.4 The radial profile of (a) the RMS radial velocity  $v_{r,RMS}$  and (b) the local  $\phi$  entrophy for 2D and 3D simulations of the  $3M_{\odot}$  red giant star. Figures (c) and (d) are the corresponding plots for the  $20M_{\odot}$  convective core simulations. The lines indicate a time average, taken over the entire simulation time, of the horizontally averaged radial profile. The shaded regions represent one standard deviation above and below the time-averaged line. The radial position of the convective boundary, calculated by the Schwarzschild criterion, is indicated by a vertical black line. The interior radial coordinate of the star  $r$  is normalized by the star's radius  $R$ .

structuring in the flow that occurs near convective boundaries based on the dimensionality.

We calculate the overshooting depth  $\ell_{ov}$  by fitting the distribution of overshooting plumes calculated using the vertical kinetic energy flux with a generalized extreme value distribution, as described in Pratt et al. (2017). We adopt the location parameter from this fit as the overshooting depth  $\ell_{ov}$ . The values of  $\ell_{ov}$  are provided in Table 4.3 for all of our simulations. For the simulation pairs *wm2d/wm3D*, *bg2D/bg3D*, and *cc2D/cc3D* these numbers are extremely close. For the simulation pair *dcs2D/dcs3D*, the 2D simulation has somewhat deeper overshooting, while for the simulation pair *wide2D/wide3D*, the 3D simulation has somewhat deeper overshooting. Given the limited amount of data for the 3D simulations, it is not clear whether these differences between the 2D and 3D simulations are statistically significant.

### 4.3 Filling factor based on volume percentage

We define a volume-percentage filling factor to be the fractional volume occupied by either the inflows  $\sigma_{vp,in}$  or the outflows  $\sigma_{vp,out}$ :

$$\sigma_{vp,in} = \frac{V^{in}(r, t)}{V^{in}(r, t) + V^{out}(r, t)}, \quad (4.1)$$

$$\sigma_{vp,out} = \frac{V^{out}(r, t)}{V^{in}(r, t) + V^{out}(r, t)}. \quad (4.2)$$

Here  $V^{in}$  indicates the total volume of grid cells at a given radius that has an inward velocity, while  $V^{out}$  indicates the total volume of grid cells that have an outward velocity. The natural consequence is that the sum of the filling factors of inflows and outflows must be

one,  $\sigma_{\text{vp},\text{in}} + \sigma_{\text{vp},\text{out}} = 1$ . Because of this relation, we will generally use the notation  $\sigma_{\text{vp}}$  to indicate the filling factor for the plumes moving toward the convective boundary, dropping the “in” and “out” labels. Conceptually, the volume-percentage filling factor is equating the situation where there are many small plumes with an equivalent single large inflow and single large outflow. Many works (Schmitt et al. 1984; Brummell et al. 2002; Andr assy 2015; K apyl a 2024) have used this kind of definition for a filling factor. Some have chosen to evaluate the area at the cell surfaces rather than the volume of the cell to calculate this filling factor. These two alternatives converge toward the same value as the cell size is decreased; using the volume to calculate this filling factor is convenient because MUSIC is a finite-volume code. In the work of Zahn (1991), the implication is that the filling factor is a single number, independent of radius. However other authors, including Schmitt et al. (1984), Cai (2020), Canuto & Dubovikov (1998), and K apyl a (2024), formulate a filling factor that is a function of the radial depth in the star; doing so allows us to examine ideas about non-local convection throughout the stellar radius. Based on ideas acquired from early simulations of solar convection, Canuto & Dubovikov (1998) expect a highly asymmetric convection pattern with fast, concentrated inflows and slow, broad outflows. Based on observational data at the solar surface and the idea of a stratified star, they thus assert that the filling factor for inflows is always less than half:  $\sigma_{\text{vp},\text{in}} < 1/2$ .

A calculation of  $\sigma_{\text{vp}}$  in our simulation pair *bg2D/bg3D* is shown in Figure 4.5. Both of these simulations evidence a  $\sigma_{\text{vp}}$  close to a third near the surface of the star, in rough agreement with observations of solar surface convection (e.g., Nordlund et al. 2009). The

similarity between our simulations and observations of the solar surface is striking, given that the resolution of near-surface dynamics is challenging for simulations of the stellar interior. As we examine  $\sigma_{vp}$  deeper in the convective envelope, we find that it grows to approximately one-half, indicating that the convection becomes highly symmetric at the point that plumes are overshooting the bottom of the convection zone. This result is interesting when considered in conjunction with the kinetic energy flux (see Figure 4.6). The kinetic energy flux in all of our simulations is negative in the upper and middle parts of the convection zone. It becomes positive near the convective boundary, a result not seen in early works (e.g., Hurlburt et al. 1984). These combined results indicate that flows in the convection zone are more complex than the simple picture of thin, fast-moving inward plumes. In the highly stratified deep interior, inward moving plumes can be both faster and wider than plumes in the near-surface layers.

We calculate the value of the volume-percentage filling factor for plumes moving toward the convective boundary in each simulation. We then extract the value at the convective boundary,  $\sigma_{vp,CB}$ , for each of our simulations; these can be found in Table 4.3. Across all simulations, the mean value of  $\sigma_{vp,CB}$  is 0.499 and the median value is 0.50. For each simulation, the value of 0.5 is within one standard deviation of the time-averaged value. We find no clear difference between the values of  $\sigma_{vp,CB}$  calculated from 2D and 3D simulations. The distributions of these values, calculated over the period of steady state convection, strongly overlap; for some simulations, the time-averaged 2D value is slightly larger, and for others, the time-averaged 3D value is slightly larger. Given the wide range in overshooting

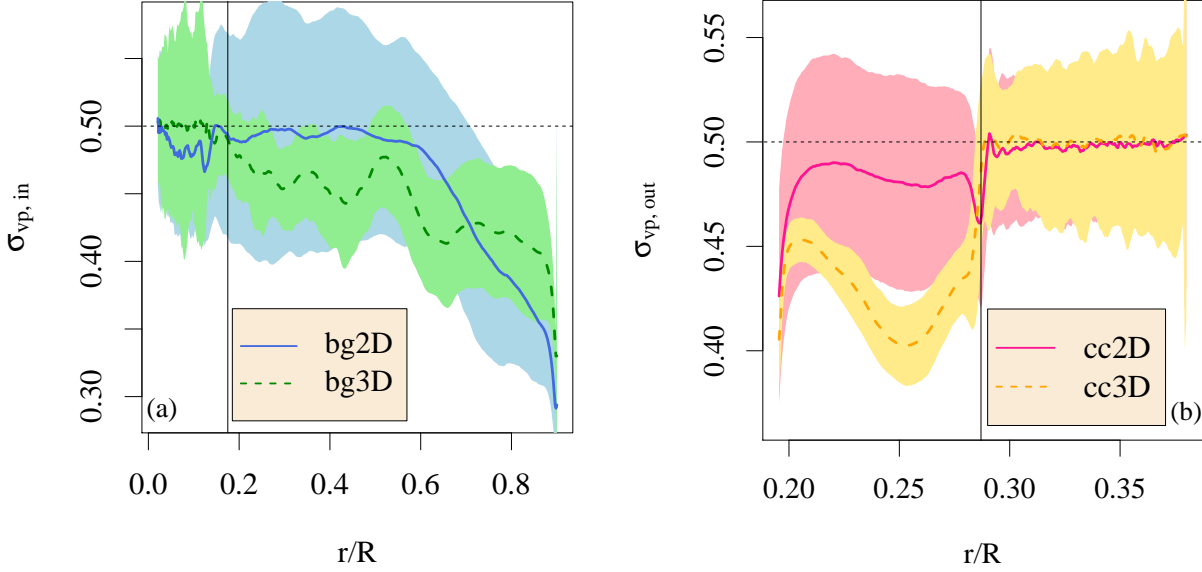


Figure 4.5 Radial profile of the volume-percentage filling factor of (a) the inward moving plumes  $\sigma_{vp,in}$  for simulations *bg2D/bg3D* and (b) the outward moving plumes  $\sigma_{vp,out}$  for simulations *cc2D/cc3D*. The solid and dashed lines indicate time-averaged radial profiles. Shaded areas indicate one standard deviation above and below these averaged lines. A thin vertical line indicates the convective boundary determined by the Schwarzschild criterion.

depths that we calculate for the four different pairs of 2D/3D simulations that we examine, we find no clear correlation between the volume-percentage filling factor at the convective boundary and the overshooting length (see Figure 4.7).

#### 4.4 Filling factor based on mass flux

We define filling factors based on the vertical mass flux  $F_{\text{mass}} = \rho v_r$  so that

$$\sigma_{mf,in} = \frac{|F_{\text{mass}}^{\text{inflows}}|}{|F_{\text{mass}}^{\text{inflows}}| + |F_{\text{mass}}^{\text{outflows}}|}, \quad (4.3)$$

$$\sigma_{mf,out} = \frac{|F_{\text{mass}}^{\text{outflows}}|}{|F_{\text{mass}}^{\text{inflows}}| + |F_{\text{mass}}^{\text{outflows}}|}. \quad (4.4)$$

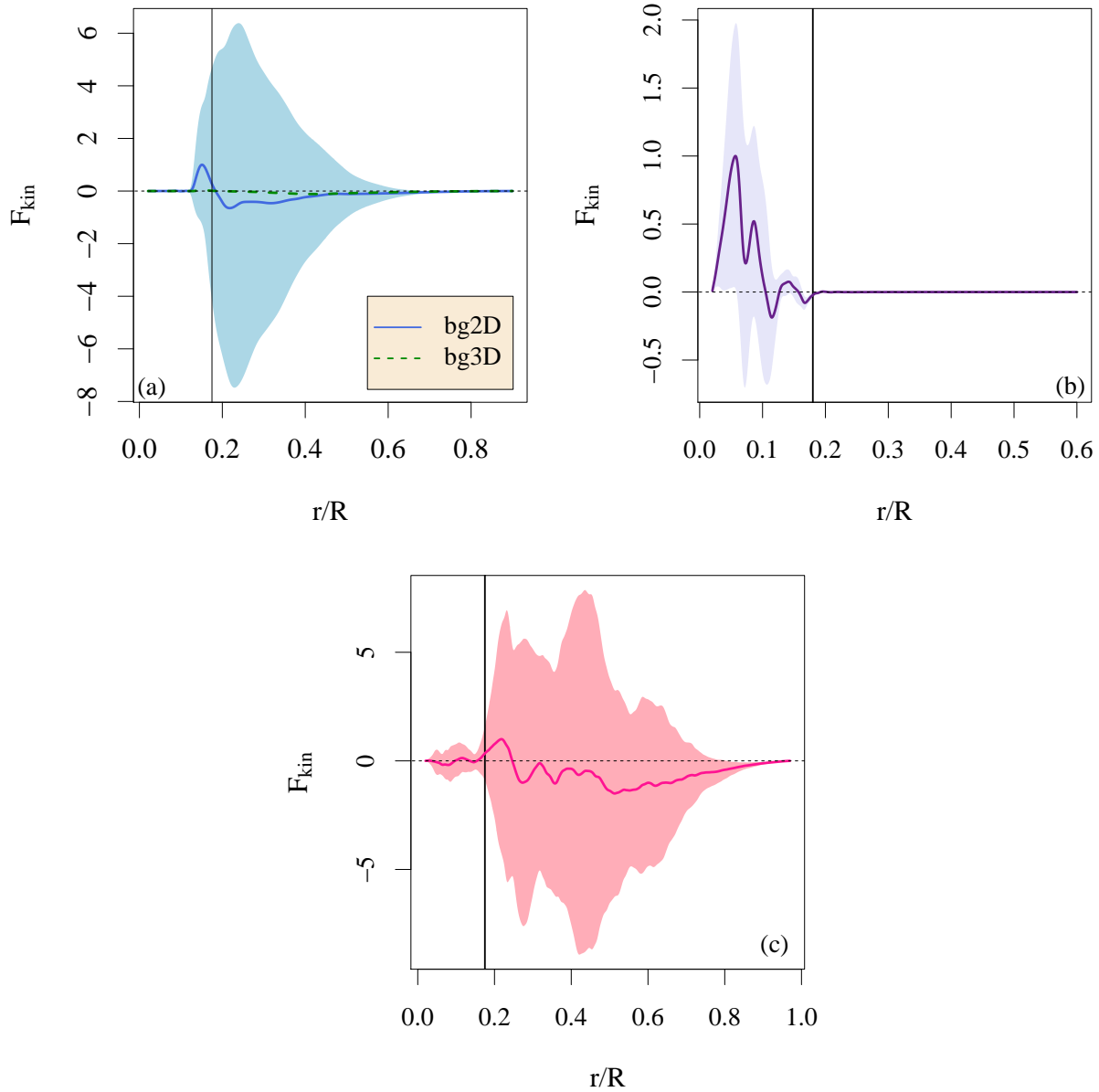


Figure 4.6 Radial profile of the normalized kinetic energy flux,  $F_k$  for (a) the  $3 M_{\odot}$  red giant star *bg2D*, (b) the  $6 M_{\odot}$  main sequence star with a convective core *ccmod2D*, and (c) a  $4 M_{\odot}$  pre-main sequence star *pms4m2D*. The solid and dashed lines indicate time-averaged radial profiles. Shaded areas indicate one standard deviation above and below these averaged lines. A thin vertical line indicates the convective boundary determined by the Schwarzschild criterion.

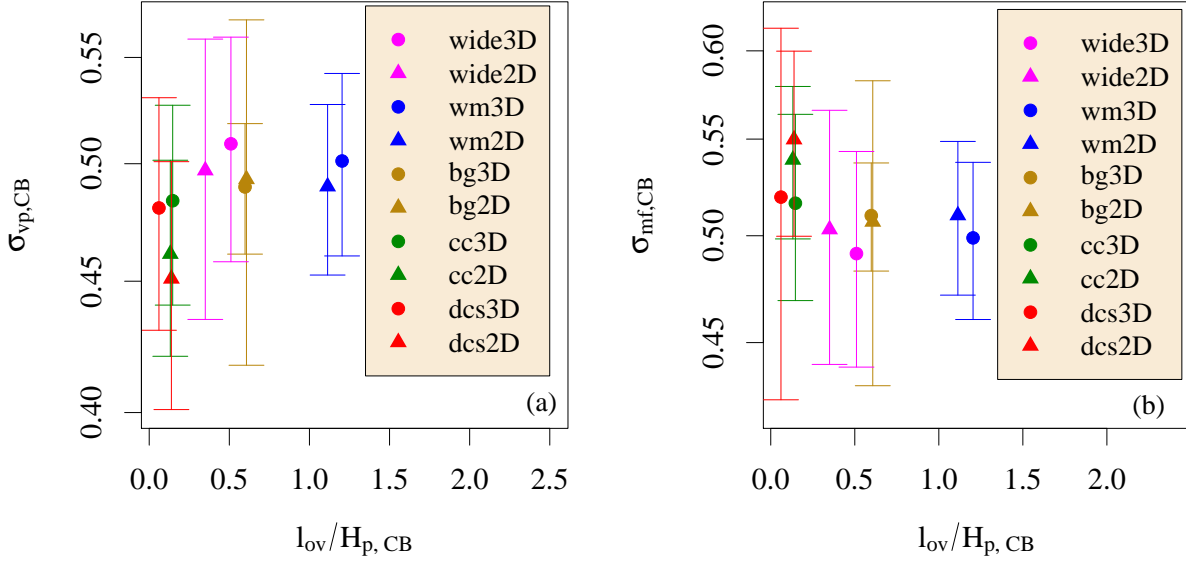


Figure 4.7 The time-averaged (a) volume-percentage and (b) mass-flux filling factor evaluated at the convective boundary determined by the Schwarzschild criterion,  $\sigma_{CB}$ , vs the overshooting depth in units of the pressure scale height at the convective boundary  $l_{ov}/H_{p,CB}$  for all simulations described in Table 4.1. Error bars indicate one standard deviation around the time-averaged value of  $\sigma_{vp,CB}$ . Error bars obtained in the calculation of the overshooting depth  $l_{ov}$  are smaller than the size of the data points.

Table 4.3 The table includes the overshooting depth  $l_{ov}$  in units of the pressure scale height at the convective boundary, the volume-percentage filling factor  $\sigma_{vp,CB}$ , the mass-flux filling factor  $\sigma_{mf,CB}$ , and the incompressible convective-flux filling factor  $f_{z,CB}$ . The subscript CB indicates that the quantity is evaluated at the convective boundary (CB), as defined by the Schwarzschild criterion.

	$l_{ov,k}/H_{p,CB}$	$\sigma_{vp,CB}$	$\sigma_{mf,CB}$	$f_{z,CB}$
wide3D	0.51	0.51	0.49	-0.11
wide2D	0.35	0.50	0.50	-0.10
wm3D	1.20	0.50	0.50	0.00
wm2D	1.11	0.49	0.51	-0.02
bg3D	0.60	0.49	0.51	0.00
bg2D	0.61	0.49	0.51	-0.04
cc3D	0.15	0.48	0.52	0.00
cc2D	0.13	0.46	0.54	-0.07
dcs3D	0.06	0.48	0.52	0.00
dcs2D	0.14	0.45	0.55	-0.02
ccmod2D	0.38	0.49	0.51	-0.02
pms4m2D	0.15	0.49	0.51	-0.03

The use of absolute values in the denominator of these ratios is necessary because, due to mass conservation, the direct sum of these fluxes is small at any point in time. We note that  $\sigma_{\text{mf,in}} + \sigma_{\text{mf,out}} = 1$ , and we will generally use the notation  $\sigma_{\text{mf}}$  to indicate the filling factor for the plumes moving toward the convective boundary. This definition of a mass-flux filling factor represents a mass-weighted rather than volume-weighted version of the filling factor.

Table 4.3 includes values of the mass-flux filling factor at the convective boundary,  $\sigma_{\text{mf,CB}}$ , for each of our simulations. Like the volume-percentage filling factor, the mass-flux filling factor is close to one-half at this point. Figure 4.7 (b) demonstrates that, like the volume-percentage filling factor, there is no clear trend between 2D and 3D results, with strongly overlapping distributions from 2D and 3D simulations. There is also no clear correlation between the mass-flux filling factor and the overshooting length. For the selection of stars that we study in this work, the mass-flux filling factor provides similar information to the volume-percentage filling factor.

Canuto & Dubovikov (1998) defined a filling factor based purely on the velocity (see eq. (49a) of that work). For the simulations examined in this work, this velocity-based filling factor produces results similar to the mass-flux filling factor.

#### 4.5 Filling factor based on convective flux

The analytical work of Zahn (1991) is based on the radial profile of the convective flux

$$\overline{F}_{\text{conv}}(r, t) = -c_p(r, t)\rho(r, t)\overline{u_r(r, \theta, t)T_1(r, \theta, t)}. \quad (4.5)$$

The bar on the right-hand side of this equation indicates an average over the horizontal directions, here indicated by  $\theta$ . The temperature fluctuation  $T_1$  is the difference between the local temperature field  $T$  and the average temperature at a given radius, angle, and time. We conveniently measure this temperature fluctuation as a deviation from an initial radial profile, because the radial profile of the temperature does not evolve during our simulations. This formulation of the convective flux neglects any changes in the density and specific heat that could be dependent on an angle.

Examining the convective flux in eq. (4.5), we find that the difference between this flux in the inflows and outflows is large around the convective boundary, resulting in a characteristic negative trough when the total convective flux is calculated (see Figure 4.8). This is consistent with earlier works; both Brun et al. (2011) and Browning et al. (2004) define the top of the overshooting layer as the point where the time average of the convective flux first changes sign. They then define the bottom of the overshooting layer as the radius in the radiative zone where the convective flux becomes small. As is clear in the figure, using this definition of an overshooting layer along with our fully compressible simulations would mean defining a sizable portion of the convection zone as part of the overshooting layer. This shape of the convective flux is not the result of changes in the temperature gradient of the star; the average temperature profile has not evolved during the course of our simulations. The large extent of the shaded area in the figure also demonstrates that the time-variation in the convective flux is substantial. These characteristics are universally present for the different kinds of stars we have simulated.

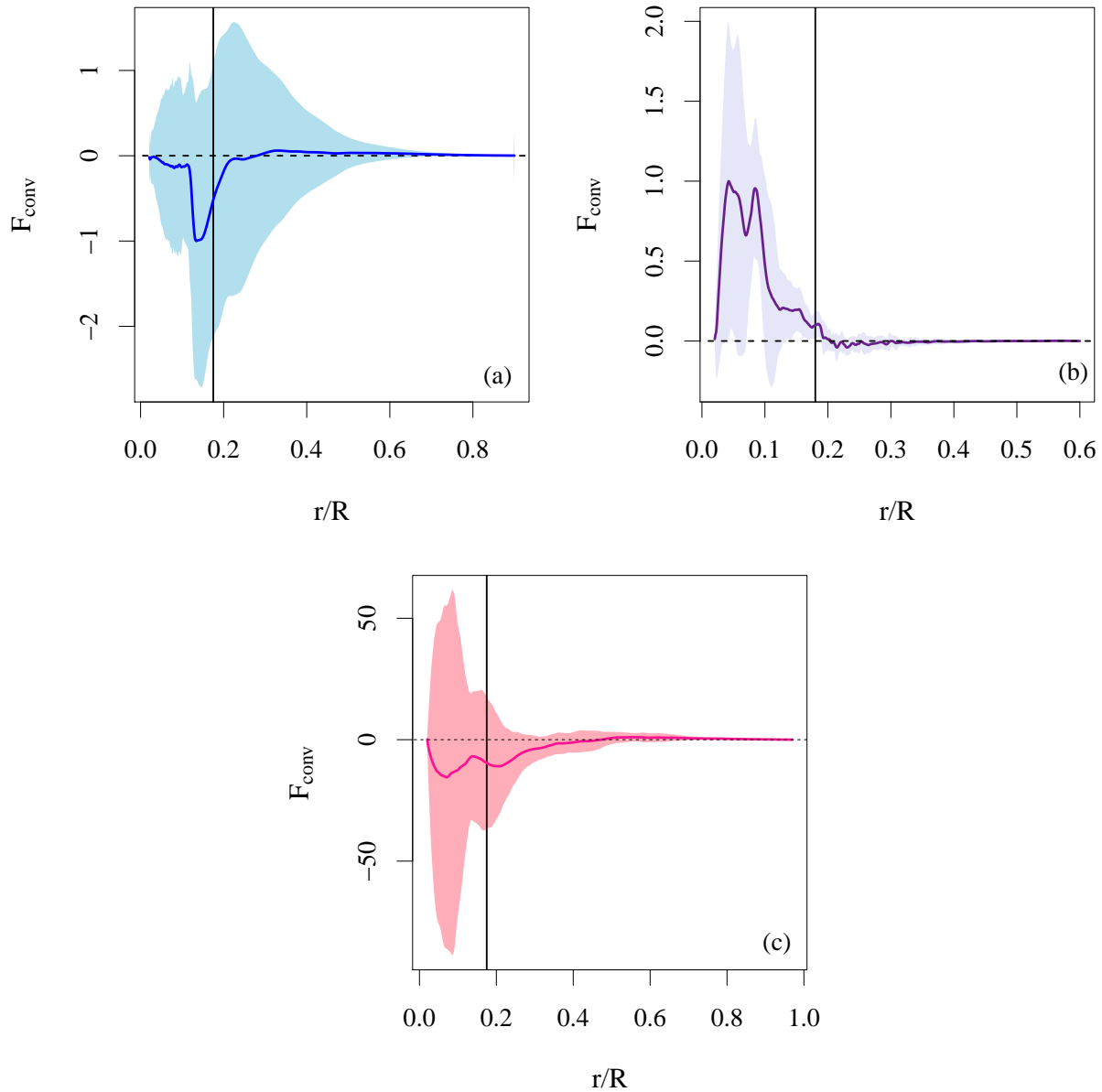


Figure 4.8 The radial profile of time-averaged convective flux for (a) the  $3 M_{\odot}$  red giant star *bg2D*, (b) the  $6 M_{\odot}$  main sequence star with a convective core *ccmod2D*, and (c) a  $4 M_{\odot}$  pre-main sequence star *pms4m2D*, normalized to its maximum magnitude value. The shaded region represents one standard deviation in time, above and below the time-averaged line. The radial position of the convective boundary determined by the Schwarzschild criterion is indicated by a vertical black line.

In their derivation of a filling factor based on the convective flux, Zahn (1991) defines two functions that are “horizontal structures” of the fluid  $h_1(\theta, t)$  and  $h_2(\theta, t)$  such that

$$u_r(r, \theta, t) = u_{r,\text{RMS}}^{\text{in}}(r, t)h_1(\theta, t) , \quad (4.6)$$

$$T_1(r, \theta, t) = T_{1,\text{RMS}}^{\text{in}}(r, t)h_2(\theta, t) . \quad (4.7)$$

Here  $T_1^{\text{in}}$  and  $u_r^{\text{in}}$  are the temperature fluctuations and radial velocity only in the volume where the fluid is moving radially inward. We will derive the convective-flux filling factor for the inflows; the corresponding equations for outflows are fully analogous. The RMS operation takes the average in the horizontal direction, i.e., over  $\theta$  if the simulation is 2D, and over both  $\theta$  and  $\phi$  if the simulation is 3D. Zahn (1991) assumes that  $h_1 = h_2 \equiv h$ . To satisfy this assumption requires that the temperature fluctuation and radial velocity are strongly correlated for inflows, or

$$\frac{u_r(r, \theta, t)}{u_{r,\text{RMS}}^{\text{in}}(r, t)} = \frac{T_1(r, \theta, t)}{T_{1,\text{RMS}}^{\text{in}}(r, t)} . \quad (4.8)$$

If an average over a sufficiently long time period is taken, then the numerators on both sides of this equation will be zero. However, it is unclear how well this assumption is satisfied at any point in time. As the width of a plume changes with the radius, the ratios in eq. (4.8) could change as well; this could happen if the inflows are less coherent, or if a convective boundary layer alters the flow near the bottom of the convection zone. The degree to which eq. (4.8) is satisfied could also be different for different stars.

Zahn (1991) then defines the convective-flux filling factor  $f_z$  as a horizontally averaged function from these horizontal structures

$$f_z(r, t) \equiv \overline{h_1(r, \theta, t)h_2(r, \theta, t)} \equiv \overline{h^2(r, \theta, t)} . \quad (4.9)$$

Solving eqs. (4.6) and (4.7) for  $h_1(\theta, t)$  and  $h_2(\theta, t)$ , we express eq. (4.9) as

$$f_z(r, t) = \frac{\overline{u_r(r, \theta, t)T_1(r, \theta, t)}}{u_{r,\text{RMS}}^{\text{in}}(r, t)T_{1,\text{RMS}}^{\text{in}}(r, t)} . \quad (4.10)$$

This expression clarifies that the filling factor defined by Zahn (1991) is essentially a horizontal average of the convective flux, normalized by a proxy for the convective flux in the inflows. The formula in eq. (4.10) is in a convenient form for direct calculations. Combining this expression for  $f_z$  with Zahn's expression for incompressible convective flux in eq. (4.5), we represent the convective flux in terms of the convective flux filling factor

$$\overline{F}_{\text{conv}}(r, t) = -c_p(r, t)\rho(r, t)u_{r,\text{RMS}}^{\text{in}}(r, t)T_{1,\text{RMS}}^{\text{in}}(r, t)f_z(t) . \quad (4.11)$$

We find that  $f_z(t)$  is highly variable in time and that a long-time average is required to produce a smooth profile; this is unsurprising because this filling factor is related to  $F_{\text{conv}}$ , which also requires a long-time average to converge. Our formulation of the convective-flux filling factor is dependent on radius, a departure from the formula written by Zahn (1991), where the horizontal structure functions are not radially dependent.

A characteristic result for the time-averaged radial profile of the convective-flux filling factor is shown in Figure 4.9. Far from the convective boundary, this filling factor is larger and positive. However, approaching the convective boundary, the convective-flux filling factor becomes small and/or negative. This appears to be related to the negative peak in the convective flux at the convective boundary. The implication is that the complex flow patterns, and thus complex fluxes that occur around this boundary contaminate the convective-flux filling factor. A full description of those flows is beyond the scope of the present work but will be pursued in the future. For a filling factor, which is conceptualized as a percentage of the flow moving inward, a negative number makes little sense. Nevertheless, we have also documented the time-averaged value of  $f_z$  at the Schwarzschild boundary for convective instability for all of the simulations examined in this work in Table 4.3.

#### 4.6 Eliminating compressibility as a source of error for the convective flux filling factor

One possible source of error in the convective-flux filling factor formulated by Zahn (1991) is that the assumption of incompressibility could be unphysical around the convective boundary of a star; we therefore expand on Zahn’s incompressible definition of a filling factor. A definition of the horizontally-averaged convective flux that includes compressibility is

$$\overline{F}_{\text{conv}}(r, t) = -\overline{c_p(r, \theta, t)\rho(r, \theta, t)u_r(r, \theta, t)T_1(r, \theta, t)} . \quad (4.12)$$

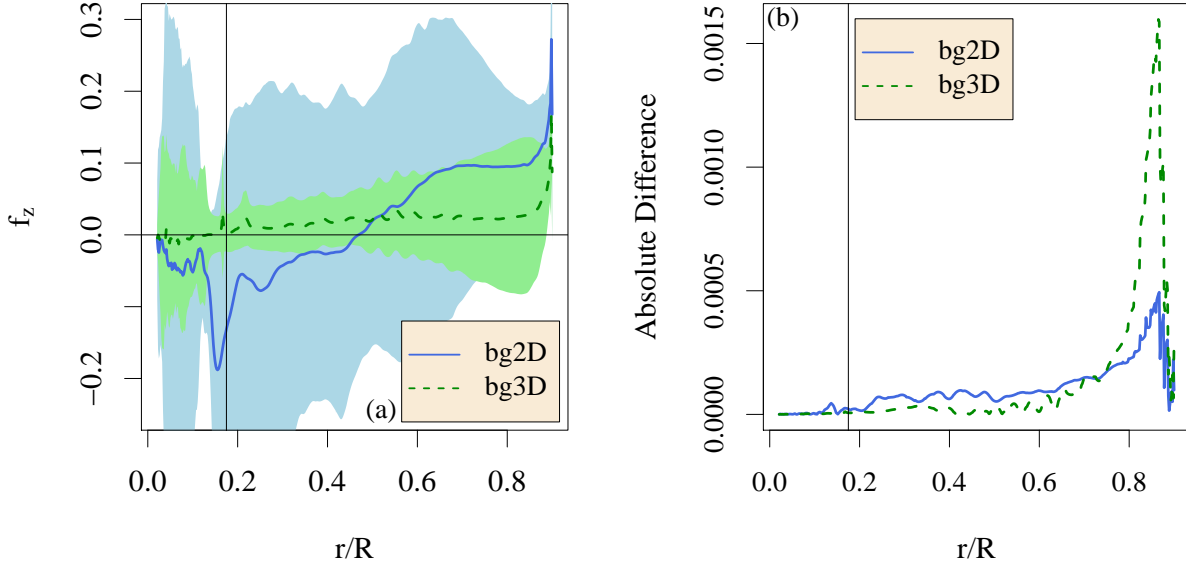


Figure 4.9 Left: The radial profile of the time-averaged filling factor  $f_z$  as defined in eq. (4.10) for 2D and 3D simulations of the  $3M_{\odot}$  red giant star. The lines indicate a time average, taken over the entire simulation time, of the horizontally averaged radial profile. The shaded regions represent one standard deviation above and below the time-averaged line. The radial position of the convective boundary determined by the Schwarzschild criterion is indicated by a vertical black line. Right: Radial profile of the absolute difference  $|f_z - f_{\text{comp}}|$  between the incompressible convective-flux filling factor and the compressible convective-flux filling factor for 2D and 3D simulations of the  $3M_{\odot}$  red giant star. The radial position of the convective boundary determined by the Schwarzschild criterion is indicated by a vertical black line.

We note that Käpylä et al. (2017) use a similar definition of this flux where the horizontal average does not include the specific heat. In this case, we define four horizontal structures

such that

$$u_r(r, \theta, t) = u_{r,\text{RMS}}^{\text{in}}(r, t)h_1(\theta, t) , \quad (4.13)$$

$$T_1(r, \theta, t) = T_{1,\text{RMS}}^{\text{in}}(r, t)h_2(\theta, t) , \quad (4.14)$$

$$\rho(r, \theta, t) = \rho_{\text{RMS}}^{\text{in}}(r, t)h_3(\theta, t) , \quad (4.15)$$

$$c_p(r, \theta, t) = c_{p,\text{RMS}}^{\text{in}}(r, t)h_4(\theta, t) . \quad (4.16)$$

As in the incompressible case, the superscript indicates that the RMS only includes contributions where the fluid is moving radially inward, the RMS operation takes the average in the horizontal direction, and we will derive the filling factor for inward plumes. We then define a compressible-convective-flux filling factor

$$f_{\text{comp}}(t) = \overline{h_1(\theta, t)h_2(\theta, t)h_3(\theta, t)h_4(\theta, t)} , \quad (4.17)$$

$$= \frac{\overline{c_p(r, \theta, t)\rho(r, \theta, t)u_r(r, \theta, t)T_1(r, \theta, t)}}{c_{p,\text{RMS}}^{\text{in}}(r, t)\rho_{\text{RMS}}^{\text{in}}(r, t)u_{r,\text{RMS}}^{\text{in}}(r, t)T_{1,\text{RMS}}^{\text{in}}(r, t)} . \quad (4.18)$$

We calculate  $f_{\text{comp}}$  for all of the simulations studied in this work. The absolute difference between  $f_z$  and  $f_{\text{comp}}$  is small near the convective boundary in all of our simulations (see Figure 4.9). The compressible filling factor  $f_{\text{comp}}$  is slightly larger near the surface in both 2D and 3D, where compressible effects, e.g., Mach numbers, are expected to be slightly larger; this is typical of all of our simulations. Including the effect of compressibility does not resolve the problematic aspects of the convective-flux filling factor near convective boundaries.

## 4.7 Conclusions

Because 2D simulations have higher radial velocities than 3D simulations, it has generally been assumed that 2D simulations have a larger overshooting depth. Examining convection in four different models of stars, we find that the overshooting depth is often similar in 2D and 3D simulations. Because 2D and 3D convective flows are visibly different, one possible explanation has been that a filling factor could explain these results.

Our calculations of a filling factor based on the volume percentage or based on mass flux result in characteristic profiles. These profiles reveal that, for stars with outer convective envelopes, the inward and outward flows are highly asymmetrical near the stellar surface with a value of about one-third (for the volume-percentage filling factor) or two-thirds (for the mass-flux filling factor). However, at the bottom of the convection zone, the filling factor is about one-half, and the convection is nearly perfectly symmetrical. For the convective core simulations *ccmod2D* and *cc2D/3D*, these profiles are similar to those of a convective envelope; at the convective boundary, there is symmetry between inflows and outflows. This is a significant new result for understanding stellar convection because it indicates that a filling factor calculated either using a volume percentage or the mass flux does not distinguish between 2D and 3D simulations or between cores and envelopes. As a result, these filling factors, along with arguments based on asymmetrical convection, are unable to predict the overshooting depth for different stars.

We study a filling factor based on the convective flux, as suggested by Zahn (1991). This calculation reveals that boundary-layer-like flows (Kupka & Muthsam 2017) are significant in

realistic global simulations of stars. These flows contaminate the convective flux, distorting the signal near the convective boundary, where it might be used to predict an overshooting length. We find that a one-point diagnostic does not encapsulate the shape of convection in stellar interiors for the four stars presented in the 2D and 3D study.

Based on the calculations of volume-percentage, mass-flux, and convective-flux filling factors, we find no correlation between the filling factor and convective overshooting depth. The filling factor can only indicate the asymmetry of flow with a one-dimensional description. To understand how the distribution of inflows at any radial point influences this mixing requires higher-order statistics. To identify a diagnostic that is useful in predicting the overshooting depth, we expand our search from one-point to two-point diagnostics.

## CHAPTER 5

### Two-point diagnostics for stellar convection

We found no correlation between the filling factor and convective overshooting depth, and no clear differences between filling factors calculated in 2D and 3D simulations, or between cores and envelopes. Our goal is to identify a filling factor-like diagnostic that correlates with convective overshooting depths: few alternatives have been proposed. One quantity that is similar to a filling factor is the “penetration parameter” proposed by Anders et al. (2022). This penetration parameter is a scalar, a single number calculated from the change in the convective flux between the convection zone and the overshooting layer. Anders et al. (2022) develop and evaluate the utility of this penetration parameter in box-in-a-star-type simulations, which use an ideal gas equation of state and solve the incompressible Boussinesq equations for convection. They do not use a density stratification in the simulation, but rather a background value of  $\rho_0$  with fluctuations  $\rho_1$  about the mean. Our global compressible hydrodynamics simulations use a realistic stratification in each star we study, where the density changes from the photosphere to the bottom of the convection zone by a factor of  $10^5$  in our young sun simulations. Therefore, our stellar simulations provide a new application space for the Anders penetration parameter.

A second alternative is not a diagnostic, but a concept. Other studies have attributed convective boundary mixing to the shape of stellar convection, meaning that convection can exhibit a “tree-like” structure, where the flow depends on depth, or a “forest-like” structure, where the flow is depth-independent (Käpylä et al. 2017; Brandenburg 2016; Spruit 1997).

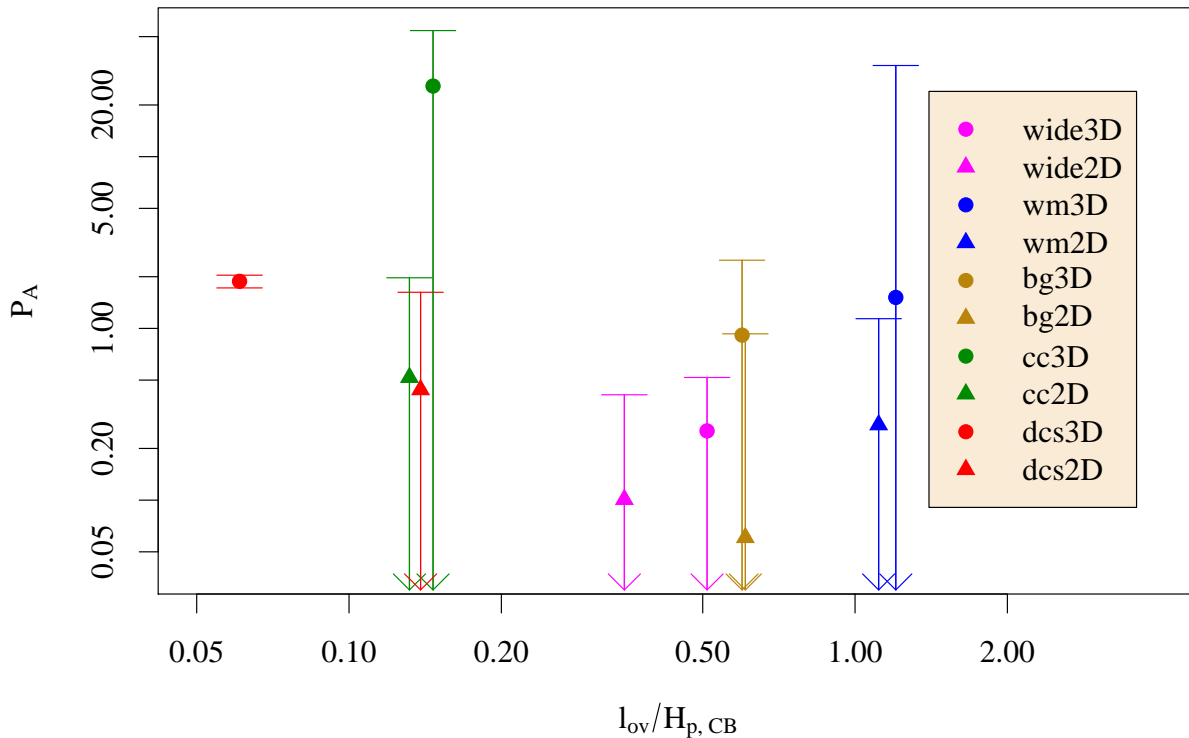


Figure 5.1 The Anders penetration parameter  $P_A$  vs the overshooting depth in units of the pressure scale height at the convective boundary determined by the Schwarzschild criterion  $l_{ov}/H_{p,CB}$  for all 2D and 3D simulations described in Table 4.1. Error bars consider one standard deviation of the convective flux at each of the two radial points that contribute to this number. A logarithmic scale is applied to the vertical axis because this parameter, as formulated, can be larger than one.

The shape of convection in these works is characterized by the number of inflows as a function of depth. After exploring these alternatives, we present two new parameters motivated by our simulation results,  $\sigma_{int}$  and  $\sigma_{merge}$  that could be predictive of convective overshooting.

### 5.1 The Anders penetration parameter

Similar to Zahn (1991), the motivation of Anders et al. (2022) is to predict convective overshooting and penetration using a ratio of convective fluxes. It is therefore fitting to examine the Anders et al. (2022) penetration parameter as a comparison to the filling factor in our realistic global simulations of stars. The Anders penetration parameter  $P_A$  is defined as the ratio of the time-averaged convective flux on either side of the convective boundary, namely

$$P_A = -\frac{\hat{F}_{\text{conv}}|_{\text{CZ}}}{\hat{F}_{\text{conv}}|_{\text{OL}}} . \quad (5.1)$$

In Anders et al. (2022),  $\hat{F}_{\text{conv}}|_{\text{CZ}}$  is described as the time-averaged convective flux evaluated “slightly” inside the convection zone where both outflows and inflows exist, and  $\hat{F}_{\text{conv}}|_{\text{OL}}$  is the time-averaged convective flux located “slightly” inside the radiative zone, in a layer where only inflows exist. In global simulations of stars, this language is not specific enough to determine where the convective flux should be evaluated. In addition, there is the complication of the complex boundary-layer-like flows that we find inside the convective boundary. To calculate the Anders penetration parameter across global simulations of different stars, we define  $\hat{F}_{\text{conv}}|_{\text{CZ}}$  as the maximum time-averaged value of  $F_{\text{conv}}(r)$  in the convective zone, a point that is unaffected by boundary layer flows. Similarly, we define  $\hat{F}_{\text{conv}}|_{\text{OL}}$  as the minimum time-averaged value of  $F_{\text{conv}}(r)$ , which can be found near the convective boundary, in the overshooting layer. This is a significant re-interpretation of the Anders penetration

Table 5.1 This table includes several quantities evaluated above or below the convective boundary, as well as two-point diagnostics related to the filling factor for convection. It includes for convective envelopes (convective cores) the average number of inflows (outflows) in the overshooting layer  $N_{\text{OL}}$  and in the convection zone  $N_{\text{CZ}}$ , and the average width of inflows (outflows) in the overshooting layer  $W_{\text{OL}}$  and in the convection zone  $W_{\text{CZ}}$ . The average widths are displayed in units of the percentage of the simulation volume at the given radius. Two-point diagnostics include the Anders penetration parameter  $P_{\text{A}}$ , the plume merging parameter  $\sigma_{\text{merge}}$ , and the plume interaction parameter  $\sigma_{\text{int}}$ .

	$\ell_{\text{ov,k}}/H_{\text{p,CB}}$	$P_{\text{A}}$	$N_{\text{OL}}$	$N_{\text{CZ}}$	$W_{\text{OL}}$	$W_{\text{CZ}}$	$\sigma_{\text{int}}$	$\sigma_{\text{merge}}$
wide3D	0.51	0.25	16.0	7.6	2.8	5.3	0.53	0.48
wide2D	0.35	0.10	14.3	6.4	3.4	7.5	0.45	0.45
wm3D	1.20	1.52	31.3	19.9	1.6	2.0	0.79	0.64
wm2D	1.11	0.27	26.0	12.9	1.9	3.8	0.50	0.50
bg3D	0.60	0.91	14.9	10.5	3.4	4.7	0.72	0.71
bg2D	0.61	0.06	12.8	3.3	3.8	16.7	0.23	0.26
cc3D	0.15	25.8	17.7	8.7	2.6	5.0	0.51	0.49
cc2D	0.13	0.52	21.7	5.3	2.1	8.7	0.25	0.24
dcs3D	0.06	1.88	28.4	16.0	1.5	2.3	0.67	0.56
dcs2D	0.14	0.44	23.2	8.1	2.1	6.0	0.36	0.35
ccmod2D	0.07	24.6	30.8	1.9	1.6	29.8	0.05	0.06
pms4m2D	0.24	0.09	12.7	7.0	3.8	7.0	0.54	0.55

parameter for the new context of realistic global stellar simulations.

Using the simulations described in Section 4.1, we calculate the Anders et al. (2022) penetration parameter. Values of  $P_{\text{A}}$  for each of our simulations, calculated in this way, are shown in Table 5.1. The Anders penetration parameter has the useful characteristic of producing larger average values in 2D than in 3D for all of our simulation pairs (see Figure 5.1). We use the standard deviation in time of  $\hat{F}_{\text{conv}}|_{\text{CZ}}$  and  $\hat{F}_{\text{conv}}|_{\text{OL}}$  to calculate uncertainties for the penetration parameter; the error bars are large, in most cases overlapping data points from both 2D and 3D simulations. Whether the differences between 2D and 3D simulations that we observe in the Anders penetration parameter can explain differences in the overshooting depth in 2D and 3D, however, remains unclear. A longer time period of data may also be required to successfully evaluate  $P_{\text{A}}$ .

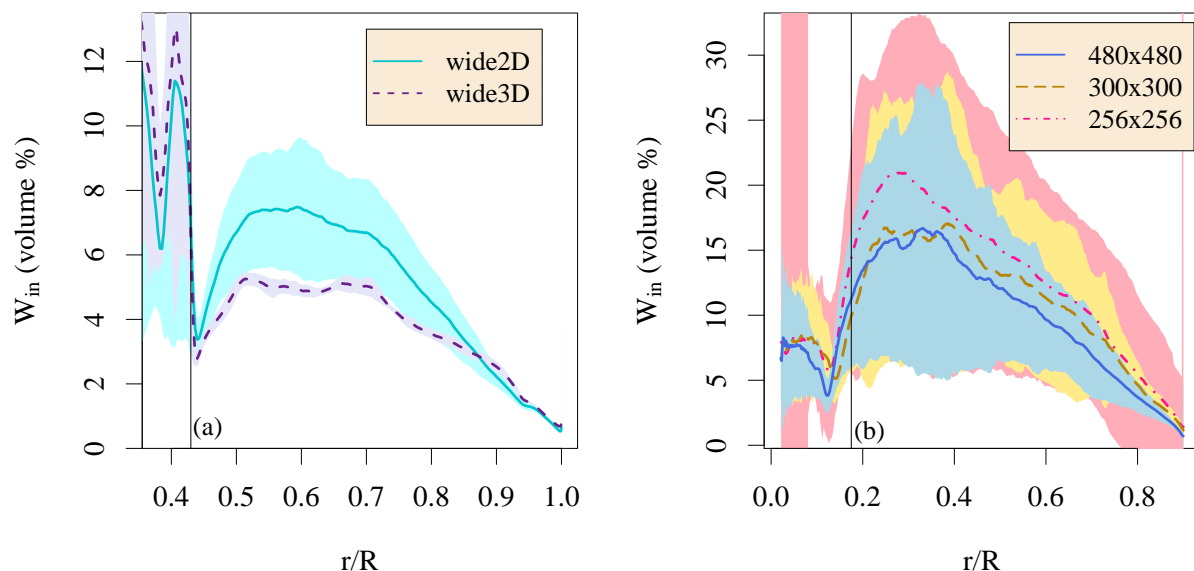


Figure 5.2 Time-averaged profiles of the width of inflows for the young sun simulations (a) in *wide2D/3D*, and (b) in three versions of *bg2D*, each with a different grid size. The radial position of the convective boundary determined by the Schwarzschild criterion is indicated by a vertical black line.

Another useful result is that the Anders penetration parameter produces different values for different stellar models. For the simulation pair *cc2D/cc3D*, which has small overshooting lengths, the minimum of the convective flux in the overshooting layer is also a small value; consequently, the value of  $P_A$  becomes large, exceeding 20 for the 3D simulation. This large value, in addition to the large error bars shown in Figure 5.1, is a result of how the ratio is formulated. Using  $1/P_A$  would tend to produce values less than one, as the formulations of filling factors did.

## 5.2 The width of inflows

As with the volume-percentage filling factor, we define a single inflow as a continuous set of cells in the  $\theta$  direction, at a given radius, that all have a negative radial velocity; similarly, we define an outflow based on positive radial velocity. For our 3D simulations, we perform the same calculation for each angle  $\phi$  in our grid. This allows for the 2D and 3D calculations to be directly compared; otherwise to define a two-dimensional parameter for a convective plume would require a more involved calculation (e.g. Haller 2015; Balasuriya et al. 2018; Rempel et al. 2023). For each of our simulations, a characteristic profile is produced for the average widths of plumes as a function of radius (see Figure 5.2). Two important features emerge in each profile: a maximum average width occurs approximately in the middle of the convection zone, which we call  $W_{\text{CZ}}$ , and a minimum average width occurs near the bottom of the overshooting layer, which we call  $W_{\text{OL}}$ . In our 2D red giant simulation, we find that the difference in the width of plumes between these two points is more than 10%. Figure 5.2 also demonstrates that this characteristic profile is present for simulations with a sufficient resolution; as the grid spacing is decreased, the average width is naturally smaller. We find that there is a wider distribution of average widths in the convection zones in each of the 2D simulations that we study than in their 3D counterparts, which may be due to the larger amount of data generated in 2D.

The distribution of plume widths in the convection zone is a fundamental diagnostic pointing toward the multi-scale nature of stellar convection, i.e. plumes of different widths can exist within the same convection zone. In comparison, the controlled situation of Rayleigh-

Bénard convection produces convection rolls that have roughly the same size, dictated by the size of the experiment. In some thin stellar convection zones, this can also be the case; however, in a large convection zone that is defined by a significant density stratification, inflows can have a range of sizes at any given radius. The stellar simulations we examine in this work have convection zones that represent a wide range of stratifications. Our  $20 M_{\odot}$  convective core simulation has a density ratio of  $\sim 2$  from the top to the bottom of the convection zone, the current sun simulations have a density ratio of  $\sim 55$  across the convection zone, the red giant simulations include a density ratio of  $\sim 200$  across the convection zone, and the density ratio in the young sun simulations is greater than  $10^5$  across the convection zone. Particularly for the young sun, the convection becomes a truly multi-scale flow, with plumes and convection rolls of different sizes frequently interacting with each other. This is evidenced by the examination of higher-order statistics for plume widths. The time-averaged radial profile of the skewness of inflow width is generally positive throughout the convection zone in our simulations (see for example Figs. 5.3 and 5.4), only dipping briefly into the negative for the 3D simulations, where there is a smaller time-series of data available to average. A normal distribution is defined by a skewness of zero; a positive skewness indicates that the distribution of inflowing plume widths is not symmetrical about the mean value, such that inflowing plumes larger than the average are more prevalent than smaller ones.

These figures also include the excess kurtosis, which is zero for a normal distribution. In comparison to a Gaussian distribution, a distribution with positive excess kurtosis indicates a greater prevalence of events in the wings of the distribution. Therefore, the excess kurtosis

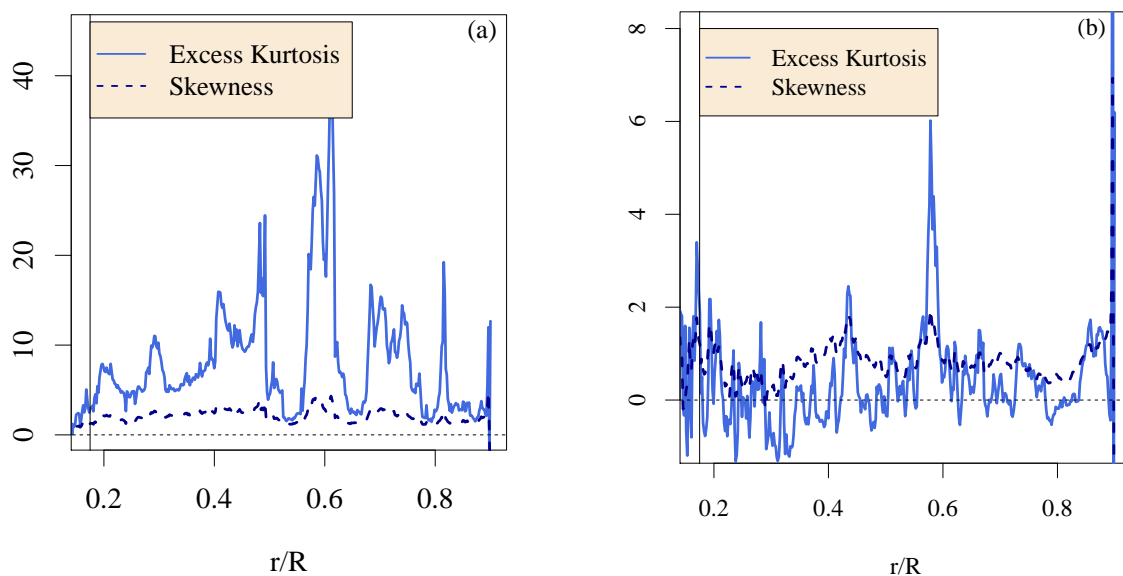


Figure 5.3 Time-averaged profiles of skewness and excess kurtosis of the width of inflows for the red giant simulations (a) in *bg2D*, and (b) *bg3D*. The radial position of the convective boundary determined by the Schwarzschild criterion is indicated by a vertical black line.

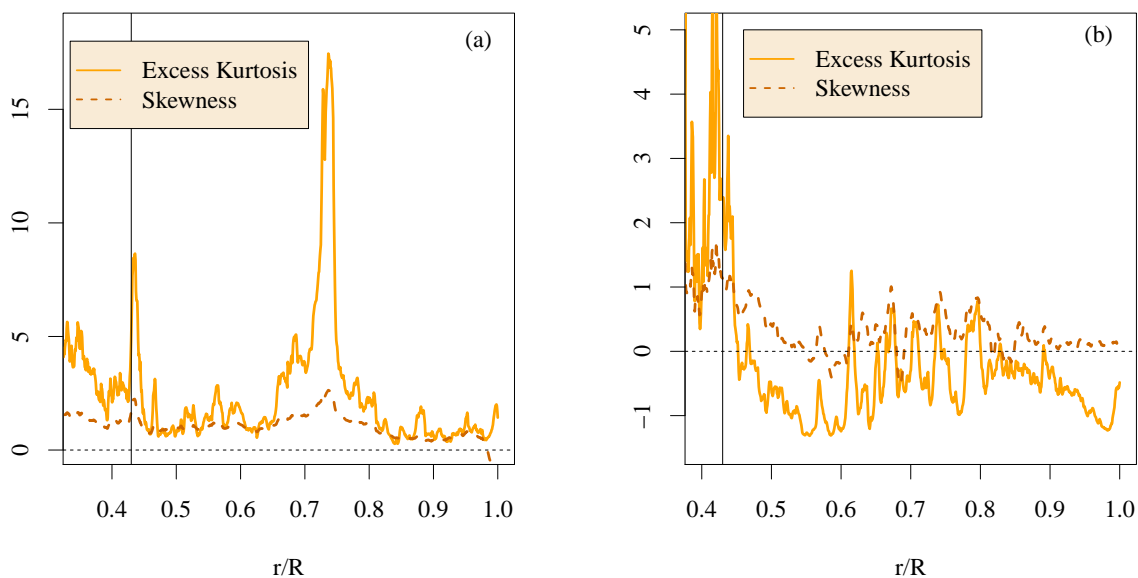


Figure 5.4 Time-averaged profiles of skewness and excess kurtosis of the width of inflows for the young sun simulations (a) in *wm2D*, and (b) *wm3D*. The radial position of the convective boundary determined by the Schwarzschild criterion is indicated by a vertical black line.

could give us an indication of the importance of different scales in a convection zone that involves many length scales. In the 2D red giant simulation *bg2D* shown in Figure 5.3(a), the excess kurtosis is positive throughout. However, the 3D simulation *bg3D* shown in Figure 5.3(b) has an excess kurtosis that is both positive and negative. We find similar results for the young sun pair *wm2D/wm3D*; in Figure 5.4(b), the 3D simulation has negative excess kurtosis. This reinforces the idea that examination of the plume width can expose differences between 2D and 3D simulations.

### 5.3 The number of inflows: missing the forest for the trees

The width of inflows can be directly related to their number. The number of inflows does not capture information on the asymmetry between inflows and outflows; by definition, the number of inflows should be equal to the number of outflows. However, the number of plumes decreases when inflowing plumes are wider and increases when inflowing plumes are thinner. Some theoretical predictions of overshooting have used the number of plumes (Rieutord & Zahn 1995; Pinçon et al. 2016). In addition to this relationship to the plume width, changes in the number of plumes can be related to two possible paradigms for convection in stellar interiors (Käpylä et al. 2017; Brandenburg 2016; Spruit 1997). The first has been described as a “tree-like” structure, where the number of inflows is dependent on depth. The second has been described as a “forest-like” structure where the number of inflows is depth-independent. The picture of tree-like or forest-like convection evokes the question of whether plumes split or merge. To connect these ideas to overshooting, and the differences between 2D and 3D

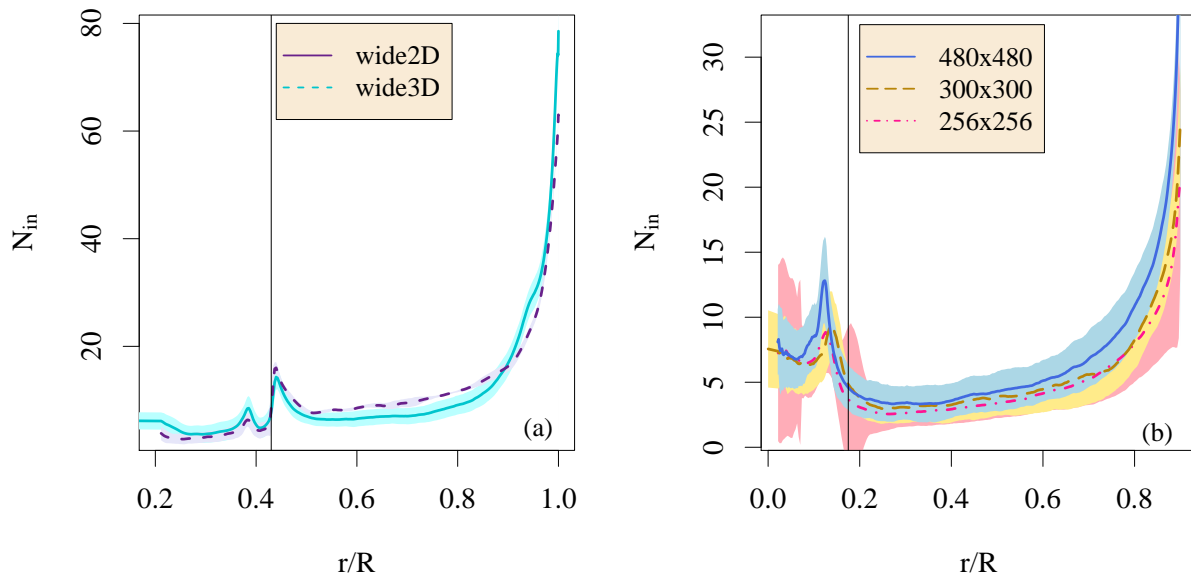


Figure 5.5 Time-averaged profiles of the number of inflows for the current sun simulations (a) in *dcs2D/3D*, and (b) in three versions of *bg2D*, each with a different grid size. The radial position of the convective boundary determined by the Schwarzschild criterion is indicated by a vertical black line.

convection, we examine the numbers of plumes in our simulations.

We calculate the number of inflows,  $N_{\text{in}}$  by counting the continuous regions of inflowing cells at each radius; we then average over time. The number of outflows  $N_{\text{out}}$  is calculated analogously. A large decrease or increase in the number of plumes can indicate the merging or separating of plumes, such that the convection has different properties depending on the radial coordinate in the convection zone. In other words, the convection would be characterized by local conditions.

In each of our simulations with convective envelopes, we find the largest number of inflowing plumes at the surface. As radius decreases, the number of plumes continually decreases until the convective boundary. The average number of inflows increases again as

it approaches the convective boundary (see Figure 5.5), a signature that could indicate the break-up or dissipation of convective flow structures or the interaction between convection and the waves that populate the radiative region.

#### 5.4 Differences between convective cores and envelopes

In stellar structure and evolution codes, the model for convection is different for different types of convection zones, depending on whether the convection is in a core or envelope. In our simulations of convective cores, we find no distinct differences between the filling factor for cores and envelopes. To investigate these different regimes further, we calculate the average widths and number of inflows and outflows.

As shown in Figure 5.6(a), large convective envelopes experience both forest-like and tree-like convection. The number of inflowing plumes increases rapidly for radii above  $r/R = 0.7$ ; this could be described as a tree-like structure, with large plumes dominating at the bottom of this region and much smaller convective flow structures dominating at the top. Below  $r/R = 0.7$ , the number of plumes changes only mildly until the bottom of the convection zone; this region could be described as having a “forest-like” structure, with convective flows of similar size dominating. Following this analogy, a mildly “tree-like” structure exists in the overshooting layer, as the number of inflowing plumes increases with the depth into the overshooting layer; to our knowledge, this has not been observed before.

For shallow envelopes, such as the convection zone in the current sun, we observe “tree-like” convection at the surface because inflows decrease in number with depth, and then a

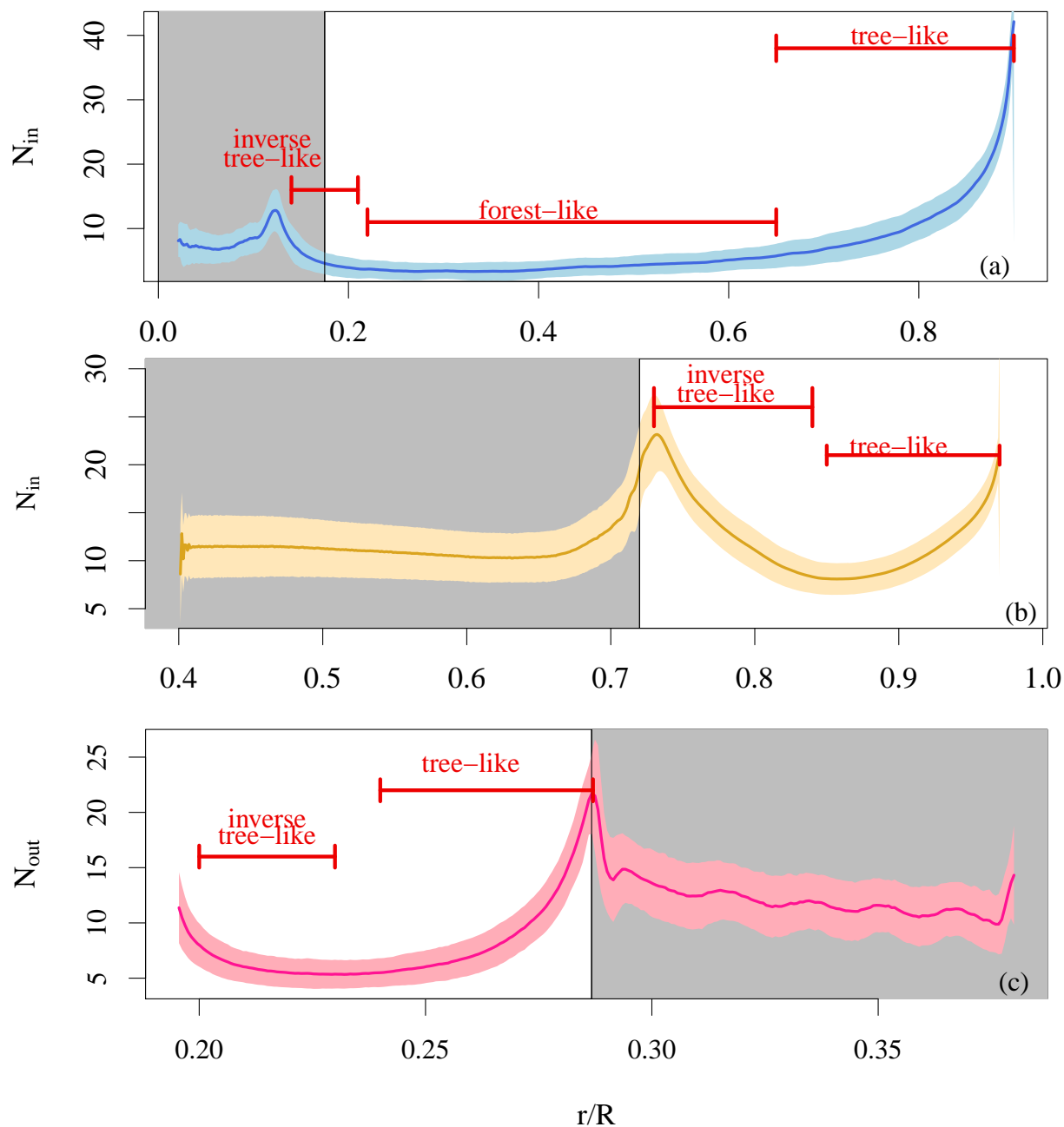


Figure 5.6 Number of inflows vs. internal radius for (a) a star with a large convective envelope *bg2D*, (b) a star with a shallow convective envelope *dcs2D*, and (c) a star with a small convective core *cc2D*. The gray box represents the radiative zone, determined by the Schwarzschild criterion.

sharp increase in number of inflows as it immediately encounters the overshooting layer, as shown in Figure 5.6(b). Therefore, these shallow envelopes exhibit only “tree-like” convection.

In the case of core convection (see Figure 5.6(c)) the largest number of outflows occurs at the convective boundary. Deeper in the convective core, the number of plumes decreases and then increases toward the inner radial boundary of the simulation. The “inverse tree-like” behavior for this star may be caused by the presence of the inner radial boundary placed inside the convection zone. Because the convective core is comparatively small, convection appears to be entirely “tree-like” in this case. This structure in the number of plumes looks highly similar to the structure that we observe in shallow outer convection zones, such as the current sun in Figure 5.6(a). We investigate whether this behavior holds true in higher-resolution simulations *ccmod2D* and *pms4m2D*. Figure 5.7(a) shows that for a high-resolution convective core simulation, we see a purely “tree-like” behavior inside the convection zone. Like *cc2D*, as shown in Figure 5.6(c), the highest number of plumes is at the convective boundary; however, we do not observe “inverse tree-like” convection at the inner radial boundary because the inner radial boundary is much deeper for *ccmod2D*. For the large convective envelope simulation *pms4m2D*, the number of inflows at the surface reaches 200 inflows, demonstrating the multi-scale flow present in large convection zones. Similar to the lower-resolution simulation *bg2D* in Figure 5.6(a), we observe “tree-like” convection until  $r \approx 0.7R$ , and then “forest-like” convection for the rest of the convection zone. Although it is not pronounced due to the large scale of the vertical axis, there is an “inverse tree”

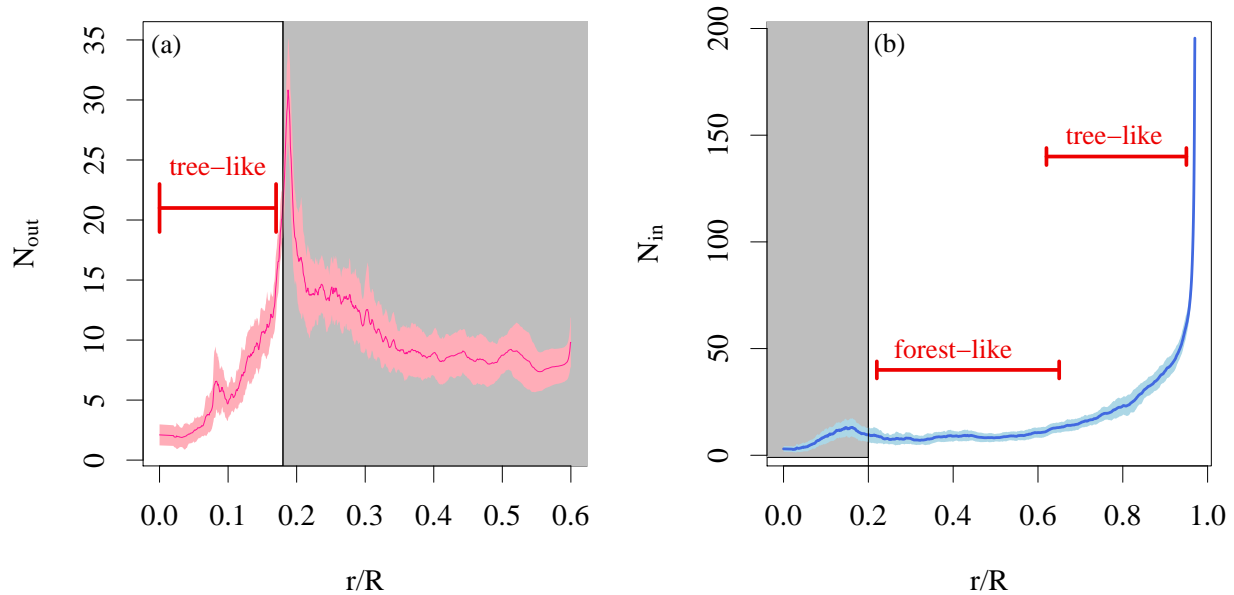


Figure 5.7 (a) The average number of outflows as a radial profile for a high-resolution convective core, *ccmod2D*. (b) The average number of inflows as a radial profile for a high-resolution large convective envelope, *pms4m2D*. The gray boxes represent the radiative zones. The pink and blue shaded regions represent one standard deviation above and below the mean.

effect at the convective boundary. Based on the results of the high-resolution simulations, we find two distinct regions of convection in large envelopes, characterized by “forest-like” convection and “tree-like” convection. We find only one distinct region of convection in convective cores and small convective envelopes, characterized by “tree-like” convection.

### 5.5 The plume interaction parameter

Inspired by our relative success in using the Anders penetration parameter to differentiate between 2D and 3D simulations, we construct a non-dimensional number from widths of inflows, using values at two radial points. The characteristic radial profile of plume widths (see Figure 5.2) indicates that there is a funneling effect on the average width of plumes

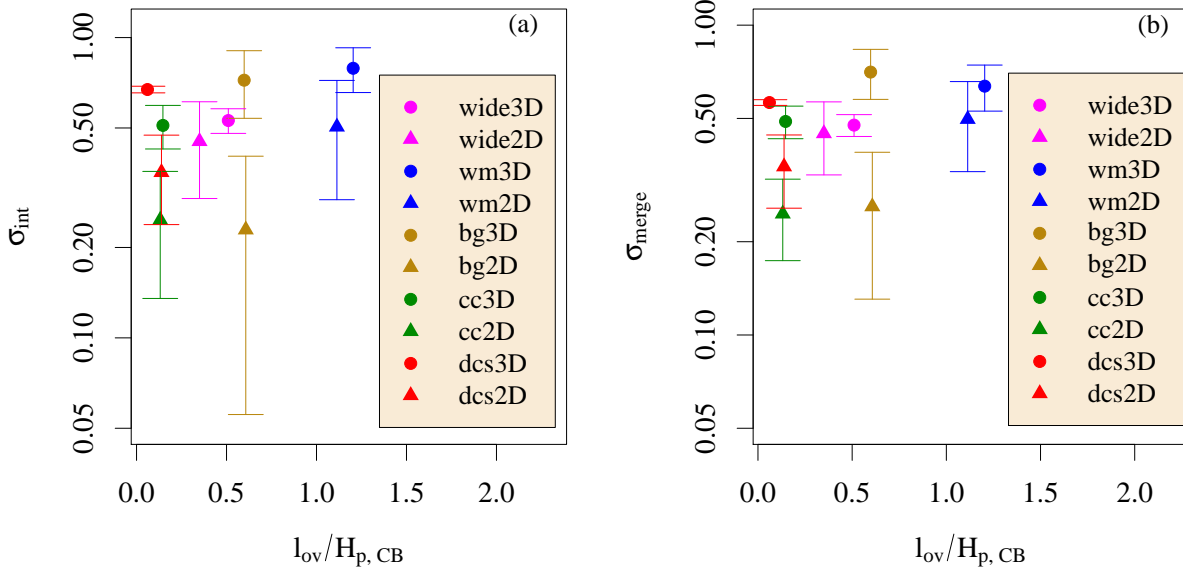


Figure 5.8 Nondimensional ratios (a) the plume interaction parameter, and (b) the ratio of average numbers of plumes  $N_{CZ}/N_{OL}$  vs the overshooting depth in units of the pressure scale height at the convective boundary determined by the Schwarzschild criterion,  $l_{ov}/H_{p,CB}$ , for all simulations studied in this work. A logarithmic scale is applied to the vertical axis, which is identical for (a) and (b). The dots represent 3D simulations, and the triangles represent 2D simulations.

as they interact with the convective boundary. We therefore construct a non-dimensional parameter to indicate the strength of this funneling effect.

Because both the widths and numbers of plumes scale with the number of shear interactions between inflows and outflows, we call this the plume interaction parameter, which we define

$$\sigma_{int} = W_{OL}/W_{CZ} . \quad (5.2)$$

For each of our simulations, the plume interaction parameter is included in Table 5.1; it

is always less than one for our simulations. Because  $W_{\text{CZ}}$  and  $W_{\text{OL}}$  are widths evaluated at two radial points, we generally call the plume interaction parameter  $\sigma_{\text{int}} = W_{\text{OL}}/W_{\text{CZ}}$  a two-point diagnostic. The plume interaction parameter provides a measure of the effective funneling that takes place between the middle and the bottom of the convection zone: the average width of inflows moves from a large number to a smaller number. A smaller plume interaction parameter thus indicates a more “tree-like” structure to the convection. We observe an “inverse tree-like” structure in all of the stars studied here, due to the effects of the boundary layer on the flow. However, in deeper convection zones, there is often an extended region in the middle of the convection zone that is forest-like, which is shown in Figure 5.2.

Resolution of the complex small-scale flows in the overshooting layer can be a challenge for diagnostics. For simulation *wide2D*, we find  $\sigma_{\text{int}} = 0.45$ , while for simulation *wm2D*, where the young sun is resolved about 4 times better,  $\sigma_{\text{int}} = 0.50$ . This gives a clear indication that the plume interaction parameter is sufficiently resolved in our simulations so that it changes only a small amount with increased resolution. The value of  $\sigma_{\text{int}}$  is also always larger for our 3D simulations than our 2D simulations. This suggests that the plume interaction parameter can encapsulate a general difference between 2D and 3D stellar convection. Using the standard deviation of the plume widths to calculate an uncertainty for the average plume interaction parameter, we find that these uncertainties are smaller than the differences between the 2D and 3D values of the plume interaction parameter in about half of our simulation pairs. Because the plume interaction parameter is based solely

on the velocity rather than the convective flux, this measure is also physically distinct from the Anders penetration parameter.

## 5.6 The plume merging parameter

In addition to the widths of plumes, the number of plumes can be combined in a ratio to produce a second nondimensional number, which we call the plume merging parameter,

$\sigma_{\text{merge}}$ :

$$\sigma_{\text{merge}} = N_{\text{CZ}}/N_{\text{OL}} . \quad (5.3)$$

As with the plume interaction parameter, this number is meaningfully different for our 2D and 3D simulation pairs, with the 3D simulation always having a larger value. The plume merging parameter provides information on the merging and splitting of plumes, which can be expressed by the change in plume number with depth. Although a ratio based on the number of plumes does not include information on the asymmetry between inflows and outflows that is found in the widths of inflows, these two parameters produce remarkably similar values.

Figure 5.8 shows how both of our nondimensional ratios relate to the overshooting length in our simulations. We find that the uncertainty, calculated using standard deviations at the two characteristic points in the convective zone and in the overshooting layer, is larger for the plume interaction parameter than the plume merging parameter. No clear trend emerges for these pairs of simulations. However, the stellar models that we selected here are very

different; investigation of a more similar set of stellar models could more easily exhibit a trend between the plume interaction parameter and the overshooting length. Those trends will be described in the next chapters.

## 5.7 Conclusions

Because the three commonly used definitions of a filling factor do not explain the difference visible in convection in 2D and 3D global simulations of stars, we propose alternative ways to predict these differences. We have focused mainly on diagnostics that have the potential to predict overshooting depths.

We begin by re-interpreting the Anders penetration parameter, a quantity connected to the convective flux. This is not a filling factor because it involves two different radial points rather than a separation of inflows and outflows at a single radial point. However, we find that this parameter can distinguish between 2D and 3D stellar convection, so it may be useful in explaining the amount of overshooting in 2D and 3D global simulations of stars, as well as for the box-in-a-star simulations where it was developed. The convective flux in the overshooting layer is particularly intermittent, making this diagnostic converge only slowly.

We examine the time-averaged width of plumes as a function of radius. This can be split into widths of inward-flowing plumes (relevant for overshooting from convective envelopes) and outward-flowing plumes (relevant for overshooting for core convection). We find clear statistical differences between 2D and 3D simulations in the standard deviation and the kurtosis of these widths. We identify a universal shape to the radial profile of the average

plume width. We construct a non-dimensional number from the ratio of the average radial profile of the inward plume widths at two different radial points; we call this the plume interaction parameter. We demonstrate that the plume interaction parameter accounts for the funneling effect, where inflows that have a large average width in the convection zone become narrower at the bottom of the convection zone and in the overshooting layer; this effect captures differences between 2D and 3D simulations.

We investigate the concept of “tree-like” and “forest-like” convection by calculating the number of inflows as a function of depth. For deep convective envelopes, we find that the near-surface layers typically have a high number of inflows, but this number rapidly drops in the upper convection zone; this corresponds to the picture of tree-like convection. In the deeper interior, however, the number of inflows remains nearly flat over a prolonged range in the radius, corresponding to forest-like convection. The tree-like picture of convection also applies to the overshooting layer, where the number of inflows increases rapidly again. For convective cores and shallow convective envelopes, we observe a “tree-like” structure throughout. We construct a plume merging number to describe the changing number of plumes between the convection zone and the overshooting layer. This provides different information than the plume interaction parameter, as it measures the extent to which convection is “forest-like” or “tree-like.”

Although both the Anders penetration parameter and our plume interaction parameter successfully and reliably indicate differences between our 2D and 3D stellar convection, for the set of stars that we examine in this work, they do not clearly correlate with the

overshooting length. However, this set of stars was selected because they are very different from each other: they represent stars of different sizes, with different kinds of convection zones, at different evolutionary phases. A more systematic study of how these parameters change with overshooting depth is described in Chapter 6.

## CHAPTER 6

### The mass dependence of properties of convection

In this chapter, we aim to perform a parameter study to establish how properties of convection, as described by one-point and two-point diagnostics, change for a range of intermediate-mass, pre-main sequence stars with convective envelopes. Using the MESA code, we model 10 stars on the pre-main sequence of their evolutionary track ranging from 1.2 to 6.0  $M_{\odot}$ . The pre-main sequence is an interesting laboratory for a mass study because the location of the convection boundary can be the same for a large range of masses. Pre-main sequence stars are born fully convective and then descend the Hayashi track as they contract, as shown on the right of the HR diagram in Figure 6.1(a). The convection zone recedes to a shallow envelope once the temperature is hot enough from contraction to decrease the value of  $\nabla_{\text{rad}}$  enough to satisfy the Schwarzschild criterion. How shallow the convection zone becomes is mass-dependent (Lamers & Levesque 2017, Section 12.8). We choose the evolutionary point of each model where the Schwarzschild convective boundary first reaches  $r_{\text{CB}}/R = 0.8$  so that each convection zone is the same fractional size of the total radius; this location is indicated for each star with a unique symbol on the HR diagram in Figure 6.1. The mass, age, radius, luminosity, temperature, and effective gravity at the photosphere for each star are provided in Table 6.1. The helium mass fraction is  $y = 0.28$  and the metallicity is  $z = 0.02$  for each star. The youngest star at 6  $M_{\odot}$  has an age of 120,000 years; this type of star is often associated with large rotation, magnetic fields, accretion disks, and other observed physical effects as the star is gravitationally collapsing (Hartmann et al. 2016). In this study, we are

Table 6.1 Parameters of stellar structure models produced with MESA. These models are selected so that the radial position of the convective boundary, as determined by the Schwarzschild criterion, is at  $r_{\text{CB}}/R = 0.8$ , and the radius of the star at the photosphere  $R$  is provided. The stellar mass  $M$  is given in units of the solar mass; the stellar luminosity at the photosphere  $L$  is given in units of the solar luminosity. The age, effective temperature at the photosphere, and log of the acceleration of gravity at the photosphere are also provided in the units used by the MESA code. Each MESA has metallicity  $z = 0.02$  and helium mass fraction  $y = 0.28$ .

Name	$M/M_{\odot}$	Age (yrs)	$R$ ( $10^{12}\text{cm}$ )	$L/L_{\odot}$	$T_{\text{eff}}$ ( $10^3\text{K}$ )	$\log_{10} g_{\text{R}}$
MSTAR1p2	1.2	208.8e5	0.098	2.33	6.02	4.222
MSTAR1p5	1.5	106.8e5	0.142	4.70	5.95	3.993
MSTAR1p7	1.7	75.3e5	0.169	6.45	5.91	3.898
MSTAR2p0	2.0	48.2e5	0.211	9.70	5.86	3.777
MSTAR2p5	2.5	25.6e5	0.282	16.35	5.76	3.619
MSTAR3p0	3.0	15.1e5	0.367	26.45	5.70	3.471
MSTAR3p5	3.5	9.26e5	0.461	39.90	5.64	3.338
MSTAR4p0	4.0	5.87e5	0.575	59.28	5.57	3.205
MSTAR5p0	5.0	2.55e5	0.885	129.06	5.46	2.928
MSTAR6p0	6.0	1.22e5	1.340	269.98	5.33	2.645

only interested in the effect of mass on the behavior of multi-scale convection and convective boundary mixing, so we disregard these other physical effects. Our goal is to determine how the filling factors, Anders penetration parameter, plume interaction parameter, and plume merging parameter change with stellar mass and calculated convective overshooting depths.

Because these stars are otherwise very similar, we consider only how stellar mass impacts convective properties. We first consider the relationship between mass and luminosity. Mass-luminosity relations for main-sequence stars have been estimated for stars of similar masses that we consider here (Torres et al. 1997; Duric 2004; Cuntz & Wang 2018). These relations exist because of the rate of nuclear fusion that is driven by stellar mass. For pre-main sequence stars, it is hard to make such relationships (Stahler et al. 1980); however, we find  $L/L_{\odot} \sim (M/M_{\odot})^{2.8}$  for the pre-main sequence stars in this study (see Figure 6.1(b)). Luminosity is directly related to the amplitudes of convective velocities; this relationship

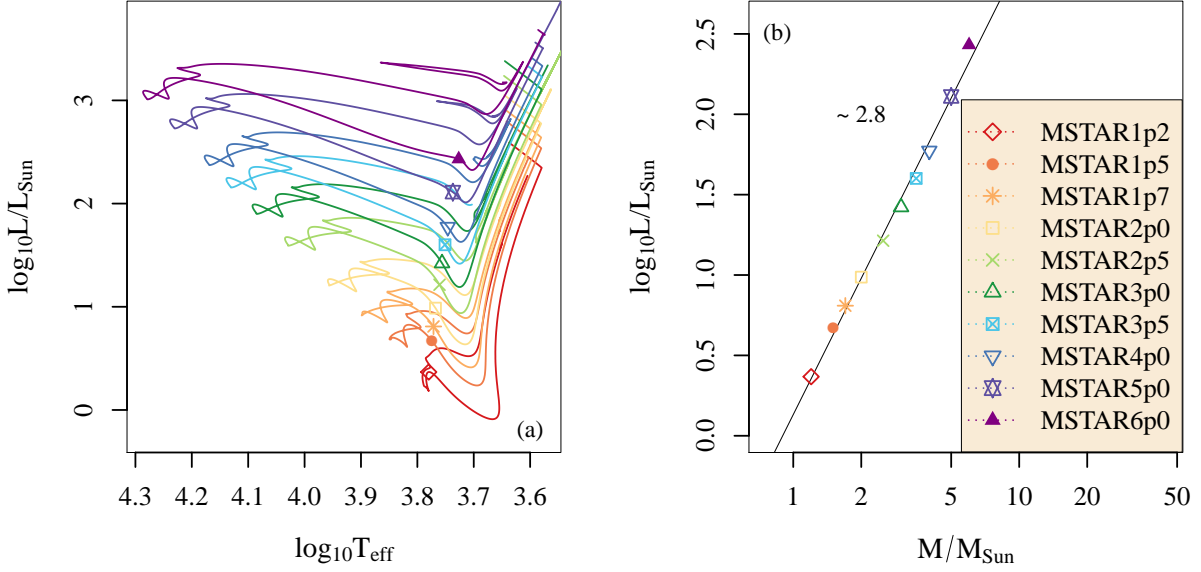


Figure 6.1 (a) Evolutionary tracks for 10 pre-main sequence stars with masses ranging from  $1.2-6 M_{\odot}$  modeled with the MESA code. (b) Mass-luminosity relationship for the pre-main sequence stars in this study, where  $L/L_{\odot} \sim (M/M_{\odot})^{2.8}$ .

can be derived using mixing length theory (Biermann 1932) or by considering that both the kinetic energy and enthalpy flux scale with  $v^3$  (Jones et al. 2016). We demonstrate this relation by scaling the velocity in units of  $(L/L_{\odot})^{1/3}$ , as calculated in MESA and MUSIC (see Figure 6.2(a) and (b)). The MESA 1D velocities are calculated with the mixing length eq. (2.51), and the MUSIC radial velocities are calculated by solving the hydrodynamic equations. The shape of the convective velocity profiles are different, and the value for velocity at the convective boundary is higher for the MUSIC simulations versus the MESA models by a factor of 7 for the highest mass star and a factor of 5 for the lowest mass star. This implies that mixing length theory underestimates the velocity magnitudes. Despite the differences, both MESA and MUSIC velocity profiles scale with luminosity.

We expect the convection to be more vigorous at higher Rayleigh numbers, which may

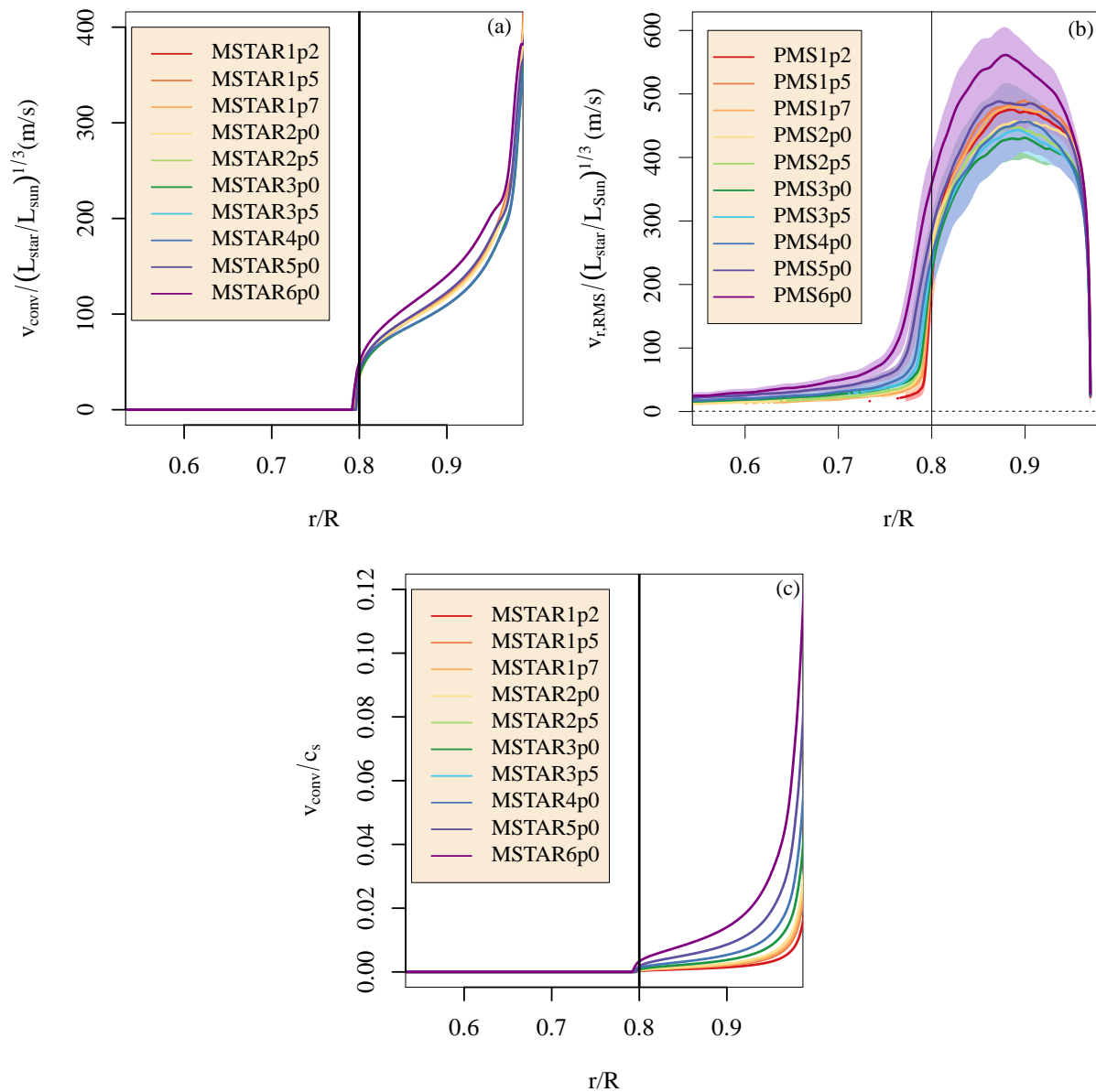


Figure 6.2 Convective velocities for 10 pre-main sequence stars with masses ranging from 1.2-6  $M_{\odot}$  (a) calculated in MESA and (b) calculated in MUSIC simulations. Both (a) and (b) are scaled by the luminosity, such that  $v_{\text{conv}} \sim (L/L_{\odot})^{1/3}$ . (c) The Mach number calculated in MESA approaches 0.1 in the 6  $M_{\odot}$  star.

Table 6.2 MUSIC simulations for 10 stars using the stellar structures from Table 6.1. All simulations span from the inner radial boundary  $R_i/R = 0.4$  to the outer radial boundary  $R_o/R = 0.97$ .

Name	Model	$\tau_{\text{conv}}(10^5\text{s})$	time ( $\tau_{\text{conv}}$ )	$H_{p,\text{CB}}/\Delta r$
PMS1p2	MSTAR1p2	$1.65 \pm 0.14$	59	241
PMS1p5	MSTAR1p5	$1.73 \pm 0.12$	60	243
PMS1p7	MSTAR1p7	$1.91 \pm 0.11$	61	244
PMS2p0	MSTAR2p0	$2.11 \pm 0.15$	190	243
PMS2p5	MSTAR2p5	$2.48 \pm 0.10$	60	245
PMS3p0	MSTAR3p0	$2.67 \pm 0.12$	69	235
PMS3p5	MSTAR3p5	$2.96 \pm 0.24$	60	245
PMS4p0	MSTAR4p0	$3.12 \pm 0.16$	49	247
PMS5p0	MSTAR5p0	$3.25 \pm 0.19$	51	242
PMS6p0	MSTAR6p0	$3.25 \pm 0.21$	34	245

influence these one- and two-point diagnostics. According to the definition for the Rayleigh number (see eq. (1.1)), four stellar properties affect this number: density, temperature, size of the convection zone, and gravity. The equation also takes into account the kinematic viscosity and thermal diffusivity, which change with the temperature of the fluid. While the aspect ratio, or ratio of height to width, is constant for all ten simulations, the physical length scales change as the radius of the star increases with mass. With increasing radius, the gravity of the stars decrease, along with the density and temperature. At the same time, the physical size of the convection zone is increasing. As a result, the Rayleigh number could be comparable between the stars in our study. To calculate this number, we also need to evaluate how the kinematic viscosity and thermal diffusivity change. Because we do not explicitly define viscosity in our ILES simulations, this calculation is difficult.

Each of these stellar models provides the basis for a global hydrodynamic simulation produced by MUSIC. The grid sizes of each star are chosen so that the resolution at the convective boundary  $H_{p,\text{CB}}/\Delta r$  is closely comparable for all ten stars. The constant location of the convective boundary allows the aspect ratio of the simulation to remain constant for

each simulation. The vorticity magnitude and the radial velocity are shown in 2D for an arbitrary time frame in Figure 6.3(a) and (b) for the simulation PMS3p5. These visualizations show that the convective envelope is shallow, and plumes of different sizes exist. The vorticity visualization in Figure 6.3(a) reveals IGWs excited just past the convective boundary at certain angles, the consequence of convective boundary mixing. The data set for each simulation is comprised of only steady-state data, including at least 34 turnover times, as in the case of the  $6 M_{\odot}$ , and up to 190 turnover times, as in the case of the  $2 M_{\odot}$  star. These values are recorded in Table 6.2.

We calculate an overshooting depth  $\ell_{\text{ov}}$  from our MUSIC simulation of each star by fitting the distribution of overshooting plumes calculated using the vertical kinetic energy flux with a generalized extreme value distribution, as described in Pratt et al. (2017). We adopt the location parameter from this fit as the overshooting depth  $\ell_{\text{ov}}$ , and we report the values in Table 6.3 for all of our simulations. These stars exhibit a clear increase in the overshooting depth with mass, similar to the trend seen for convective cores in Baraffe et al. (2023).

## 6.1 One-point diagnostics

We calculate the volume-percentage filling factor  $\sigma_{\text{vp}}$ , the mass-flux filling factor  $\sigma_{\text{mf}}$ , and the convective-flux filling factor  $f_z$  at the convective boundary; for all three definitions, we find that the filling factor does not increase with mass, indicating that the filling factor is independent of mass at the convective boundary. In all ten stars,  $\sigma_{\text{vp,CB}} = 0.48$ ,  $\sigma_{\text{mf,CB}} = 0.52$ , and  $f_{z,\text{CB}}$  is extremely small or negative. We report the convective-flux filling factor for all

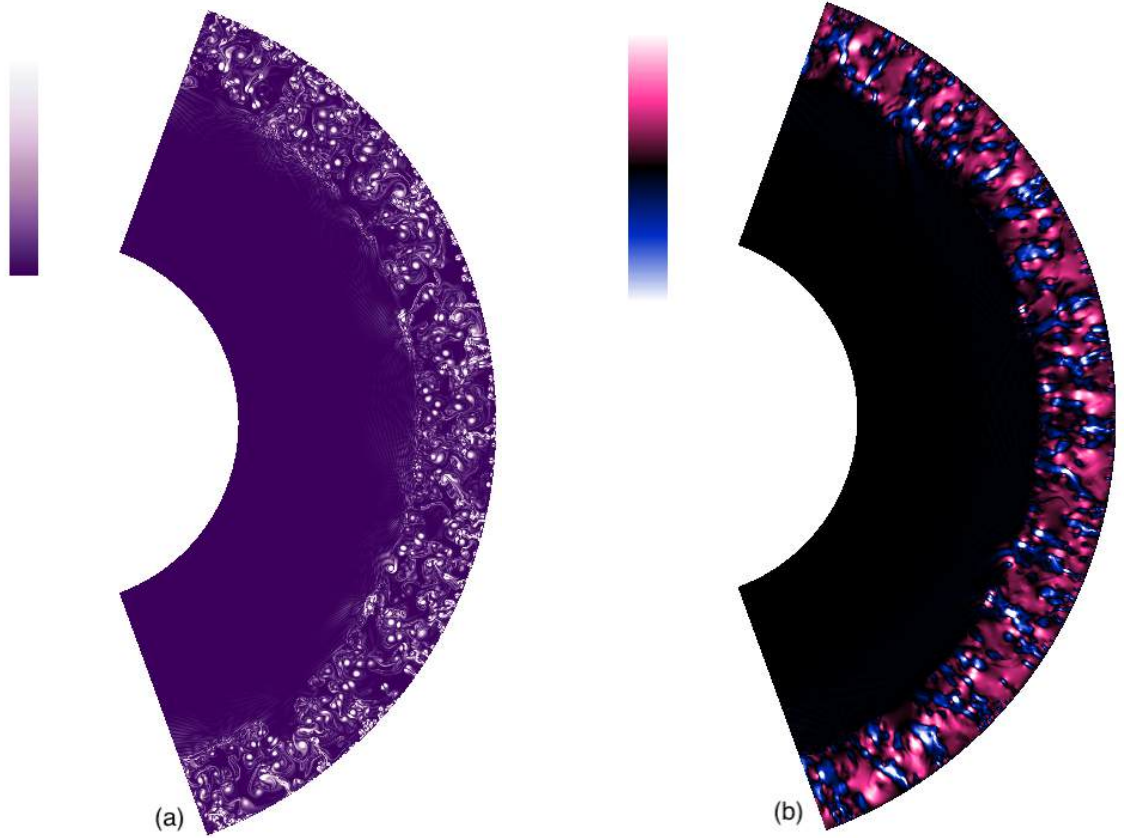


Figure 6.3 2D MUSIC visualizations of (a) vorticity and (b) radial velocity for the  $3.5M_{\odot}$  star, PMS3p5. Dark purple represents zero vorticity, and white represents maximum vorticity. The maximum enstrophy value is  $2.5 \times 10^{-8}$  for this snapshot. For the velocity, pink represents outflows and blue represents inflows, where black is the zero point. The maximum velocity magnitude is  $\pm 2.6$  km/s.

simulations in Table 6.3. The compressible convective-flux filling factor  $f_{\text{comp}}$  is identical to the incompressible definition, which agrees with the results in Dethero et al. (2024).

In addition to evaluating the filling factors at the convective boundary, we calculate horizontally-averaged radial profiles for  $\sigma_{\text{vp}}(r)$  and  $\sigma_{\text{mf}}(r)$  for all ten simulations (see Figure 6.4). For the volume-percentage filling factor,  $\sigma_{\text{vp}}$  is approximately a third at the point in the simulation closest to the photosphere (located at  $r/R = 1$ ). From this point,  $\sigma_{\text{vp}}$  grows smoothly until the bottom of the convection zone, where it reaches a value of one-half.

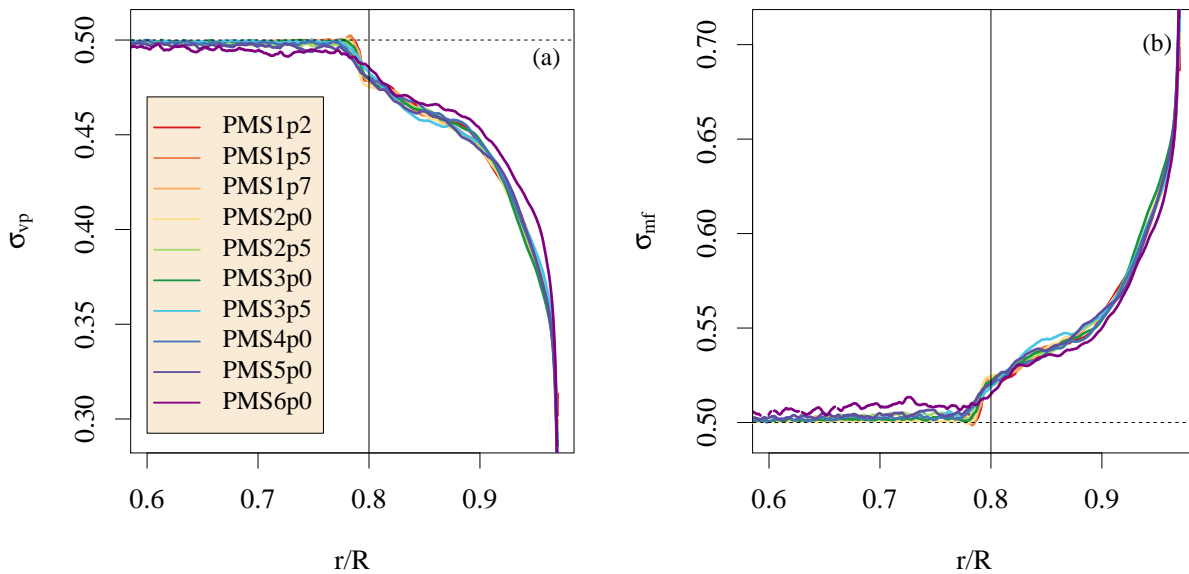


Figure 6.4 Volume-percentage (a) and mass-flux (b) filling factor profiles for ten pre-main sequence stars with shallow convection zones. The convective boundary for each star is located at  $r = 0.8R_*$ , which is represented by a vertical black line. The dashed horizontal line represents a filling factor value of one-half.

Because  $\sigma_{vp}$  reflects the asymmetry between inflows and outflows at a given radius, this indicates that at the photosphere, a large asymmetry exists where inflows are narrower than outflows. For all ten stars, the curvature of the profile of  $\sigma_{vp}$  is remarkably similar between these two points, with the highest mass star, MSTAR6p0 only slightly differing from the rest. This difference may lie in the smaller amount of data that we generated for MSTAR6p0; it may also be related to the fact that the Mach number in the outer layers of this star becomes large, as shown in Figure 6.2(c), where the Mach number calculated in MESA nears 0.1 at  $r/R_* = 0.97$ , the extent of the MUSIC simulation. The fact that  $\sigma_{vp}$  collapses onto a universal trend for all of these stars supports the idea that they are structurally similar, except for the mass of the star. That trend is also complex, with an inflection point located near  $0.85R_*$

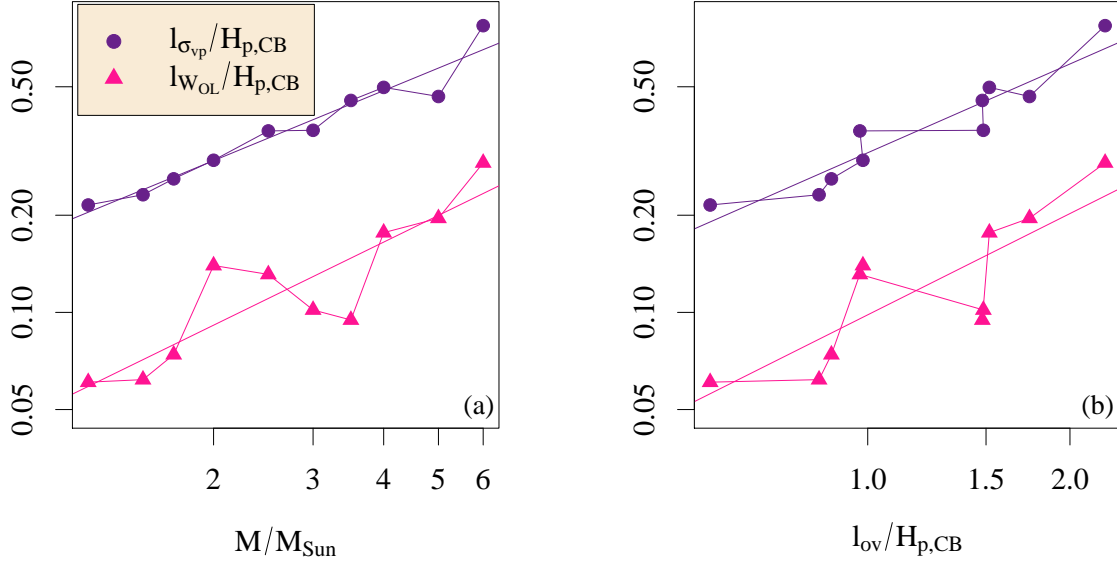


Figure 6.5 Distances  $\ell_{\sigma_{vp}}$  (purple dots) and  $\ell_{W_{OL}}$  (pink triangles) as a function of (a) stellar mass and (b) the overshooting depth. Both plots have a log-log scale.

separating regions of convex and concave curvature. Like the wide variety of stars we have previously studied in Dethero et al. (2024),  $\sigma_{vp}(r)$  and  $1 - \sigma_{mf}(r)$  are highly similar. For these stars, the mass flux and volume-percentage of inflows provide the same information.

In the radial profiles of the filling factors for all ten stars (see Figure 6.4) a uniform distance lies between the convective boundary and the radial point where the filling factor flattens to a constant value of approximately one-half in the radiative zone. We use this distance to define a new length scale  $\ell_{\sigma}$ ; in units of the pressure scale height,  $\ell_{\sigma}$  is larger for stars with higher mass, as shown in Figure 6.5(a). We calculate this new value for both filling factors and find that the distance from the boundary to the flattened value is the same for the volume-percentage and mass-flux definitions, such that  $\ell_{\sigma_{vp}} = \ell_{\sigma_{mf}}$ . We calculate  $\ell_{\sigma_{vp}}$  for all masses and record our results in Table 6.3 in units of the pressure scale height at the

Table 6.3 Calculated quantities related to the filling factor for convection for ten pre-main sequence stars. All stars are identical, other than their mass. The table includes the overshooting depth  $\ell_{\text{ov}}$  in units of the pressure scale height at the convective boundary and the incompressible convective-flux filling factor at the convective boundary  $f_{z,\text{CB}}$ . We include the Anders penetration parameter  $P_A$ , the plume interaction parameter  $\sigma_{\text{int}}$ , and the plume merging parameter  $\sigma_{\text{merge}}$ . It also includes the average number of inflows in the overshooting layer  $N_{\text{OL}}$  and in the convection zone  $N_{\text{CZ}}$ , and the average width of inflows in the overshooting layer  $W_{\text{OL}}$  and in the convection zone  $W_{\text{CZ}}$ . The average widths are displayed in units of the percentage of the simulation volume at the given radius.

$M/M_{\odot}$	$\ell_{\text{ov,k}}/H_{\text{p,CB}}$	$f_{z,\text{CB}}$	$P_A$	$N_{\text{OL}}$	$N_{\text{CZ}}$	$\sigma_{\text{merge}}$	$W_{\text{OL}}$	$W_{\text{CZ}}$	$\sigma_{\text{int}}$	$\ell_{\sigma_{\text{vp}}}/H_{\text{p,CB}}$	$\ell_{W_{\text{OL}}}/H_{\text{p,CB}}$
1.2	0.58	0.00	0.34	102.0	38.3	0.37	0.46	1.19	0.40	0.22	0.061
1.5	0.85	-0.01	0.39	91.8	39.3	0.43	0.53	1.14	0.46	0.23	0.062
1.7	0.88	0.00	0.40	93.5	38.1	0.41	0.52	1.18	0.44	0.26	0.074
2.0	0.98	-0.01	0.38	94.2	38.0	0.40	0.52	1.17	0.44	0.30	0.140
2.5	0.97	-0.05	0.42	93.6	37.0	0.40	0.52	1.22	0.43	0.37	0.131
3.0	1.49	-0.01	0.37	83.2	36.6	0.44	0.59	1.23	0.48	0.37	0.102
3.5	1.48	-0.01	0.44	81.1	37.0	0.46	0.61	1.22	0.50	0.45	0.095
4.0	1.52	-0.01	0.47	83.8	37.1	0.44	0.58	1.22	0.48	0.50	0.177
5.0	1.74	-0.01	0.54	75.3	37.6	0.50	0.65	1.20	0.54	0.63	0.196
6.0	2.25	-0.01	0.62	71.1	34.0	0.48	0.70	1.35	0.52	0.77	0.291

convective boundary. We find  $\ell_{\sigma_{\text{vp}}} \sim M/M_{\odot}^{0.86}$ , as shown in the purple line in Fig 6.5(a). This length scale tells us the radial extent to which inflows and outflows experience asymmetry, so it acts as an indicator for the bottom of the overshooting layer. Because  $\ell_{\sigma_{\text{vp}}}$  correlates with mass, this parameter correlates with overshooting length, as shown in Figure 6.5(b).

## 6.2 Two-point diagnostics

To investigate whether the shape of convection is “tree-like” or “forest-like,” we calculate the widths and numbers of inflows as radial profiles. The filling factor at the convective boundary only indicates asymmetry of the flow in a one-dimensional way; calculating the widths of inflows allows us to quantify the distribution of inflows over all angular coordinates at a given radius. Figure 6.6(a) demonstrates the average width of inflows in units of volume percentage, with the shaded regions representing the spread of different inflow sizes at a

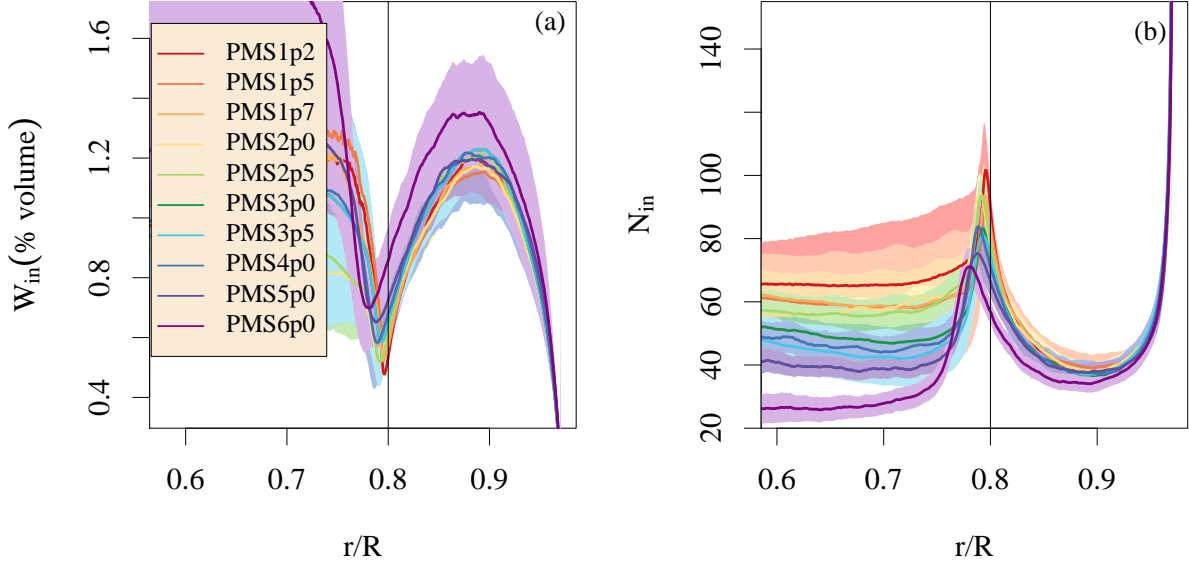


Figure 6.6 Width (a), and number (b) of inflows for 10 pre-main sequence stars ranging from 1.2 to 6  $M_{\odot}$ . The shaded regions represent one standard deviation above and below the time-averaged mean. The vertical line represents the Schwarzschild boundary, where the convection zone is to the right of this boundary.

given radius. The maximum of the average width of inflows in the convection zone,  $W_{CZ}$  and the minimum of the average width of inflows in the overshooting layer,  $W_{OL}$ , are included in Table 6.3. The value of  $W_{CZ}$  is similar for all masses, except the 6  $M_{\odot}$  star, which is slightly larger. The standard deviation of  $W_{CZ}$  shows no correlation with the mass. The radial location of  $W_{OL}$  is deeper into the stable region for higher-mass stars in this study (see Figure 6.5 (a)). We designate the distance between the convective boundary and this radial location as  $\ell_{W_{OL}}$ ; this length scale is larger for larger mass stars, as shown in Figure 6.5(a), where the pink line represents a scaling of  $\sim M/M_{\odot}^{0.72}$ . This trend for  $\ell_{W_{OL}}$  and mass scales similarly to  $\ell_{\sigma_{vp}}$  and mass, but  $\ell_{W_{OL}}$  is consistently lower in value. Therefore,  $\ell_{W_{OL}}$  is not comparable to the bottom of the overshooting layer, but rather some other length scale

inside the overshooting layer. Because  $\ell_{W_{OL}}$  increases with mass, we also observe an increase with the convective overshooting depth, as shown in Figure 6.5(b).

Using the values  $W_{CZ}$  and  $W_{OL}$ , we calculate the plume interaction parameter  $\sigma_{int}$  as discussed in Dethero et al. (2024) to determine how the shape of convection changes in the stars in our study. A higher  $\sigma_{int}$  indicates the average width of plumes throughout the convection zone is less likely to funnel down to narrower inflows at the convective boundary. We find that the plume interaction parameter increases with mass (see Figure 6.7 (a)), so the inflows at the convective boundary are larger than those in lower-mass stars. We calculate the uncertainty for  $\sigma_{int}$  using the standard deviation of the plume widths; this standard deviation exhibits no clear correlation with mass. We also investigate the relationship between the plume interaction parameter and the overshooting depth (see Figure 6.7 (b)). The high-mass stars in our study exhibit a smaller change in plume width from the convection zone to the overshooting layer, and they also exhibit a larger overshooting depth; this means the stars in this study with wider inflows at the convective boundary have larger overshooting depths.

In addition to the widths of inflows, we also calculate the horizontally-averaged number of inflows,  $N_{in}$ , as a radial profile (see Figure 6.6 (b)), where the shaded regions represent the standard deviation. The change in the number of inflows with depth gives a direct indication of whether the shape of convection is “forest-like” or “tree-like.” A flat profile indicates a constant number of plumes throughout the convection zone, which would be comparable to RBC and “forest-like” convection. We calculate the minimum average number of plumes in

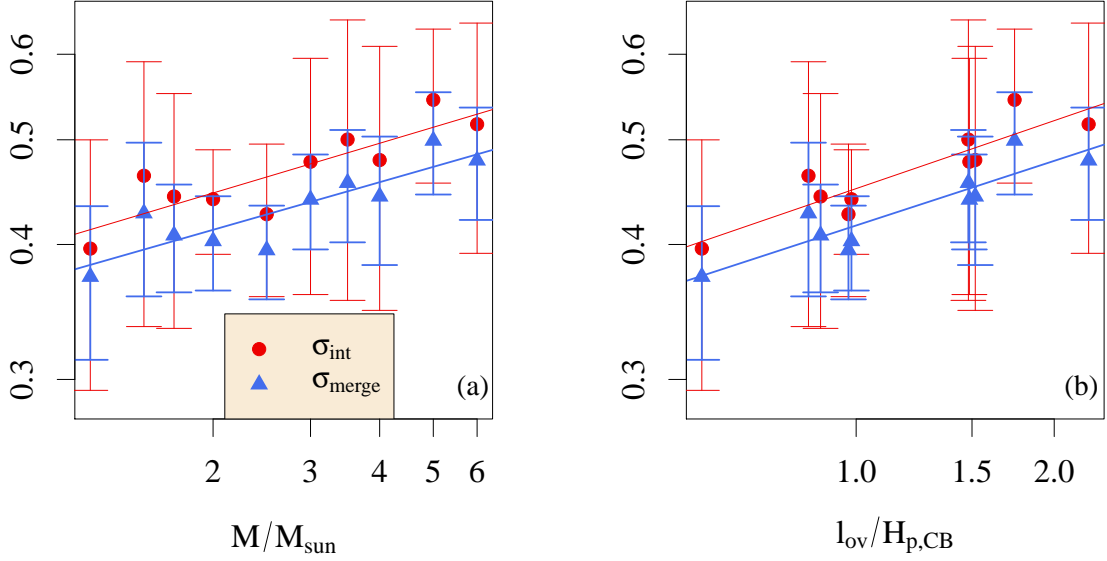


Figure 6.7 Plume interaction parameter  $\sigma_{\text{int}}$  (red dots) and  $\sigma_{\text{merge}}$  (blue triangles) as a function of (a) stellar mass and (b) convective overshooting depth for 10 pre-main sequence stars ranging from 1.2 to 6  $M_{\odot}$ . A logarithmic scale is applied to both axes. The solid lines are linear fits to the data points.

the convection zone ( $N_{\text{CZ}}$ ) and the maximum average number of plumes in the overshooting layer ( $N_{\text{OL}}$ ). We use the ratio of these two points to form a two-point diagnostic for stellar convection,  $\sigma_{\text{merge}}$ . We find  $\sigma_{\text{merge}}$  has a similar relationship with mass as  $\sigma_{\text{int}}$  and mass (see Figure 6.7(a)). The power law relationship for both fits has an exponent of approximately 0.15; in Figure 6.7(b), both scalings with the overshooting depth have a power law exponent of approximately 0.20. For  $\sigma_{\text{merge}}$ , the uncertainty is lower than the uncertainty for the plume interaction parameter for all stars in this study; this is because the number of inflows is constant at each radial point, unlike the widths. The plume merging parameter is consistently lower than the corresponding  $\sigma_{\text{int}}$  value for all ten simulations. The difference between the two diagnostics is smallest for the 1.2  $M_{\odot}$  star, where  $\sigma_{\text{int}}$  is 6% greater than  $\sigma_{\text{merge}}$ , and highest

for the  $3.5 M_{\odot}$  star, where  $\sigma_{\text{int}}$  is 9% greater. The reason for this difference is unclear. One explanation is that the narrow inflows are unresolved; however, the resolution is high, with  $H_{p,\text{CB}}/\Delta r > 240$  for all simulations. An increase in these two diagnostics indicates that a pre-main sequence  $6 M_{\odot}$  star with a few large inflows at the convective boundary exhibits a greater overshooting depth than a lower mass pre-main sequence star with more numerous and narrow plumes, regardless of the filling factor.

The number  $N_{\text{in}}$  and average width  $W_{\text{in}}$  of inflows are related because narrow plumes correspond to more numerous plumes. These diagnostics are not equivalent, but they are correlated in many cases. For example, the different distributions of widths could produce an average width  $W_{\text{in}}$  that corresponds to a different overall number  $N_{\text{in}}$  of inflows. In addition, the average width of the inflows  $W_{\text{in}}$  provides information on the asymmetry of inflows and outflows that is not included in the number of inflows. One could imagine two stars with equal numbers of inflows, but one would have thin inflows while the other would have wide inflows. This additional information is also captured in the standard deviations, which are slightly larger for  $\sigma_{\text{int}}$ , indicating the larger variety of widths compared to the number.

The relationship between  $N_{\text{in}}$  and  $W_{\text{in}}$  is shown in Figure 6.8. The characteristic points in the convection zone ( $N_{\text{CZ}}$  and  $W_{\text{CZ}}$ ) occur at the same radial points, represented by the triangles. The characteristic points in the overshooting layer ( $N_{\text{OL}}$  and  $W_{\text{OL}}$ ) also occur at the same radial points, and are represented by the dots. The three distinct trends in Figure 6.8 occur before and after encountering each set of characteristic points. The average plume width as a function of plume number decreases after encountering the radial point

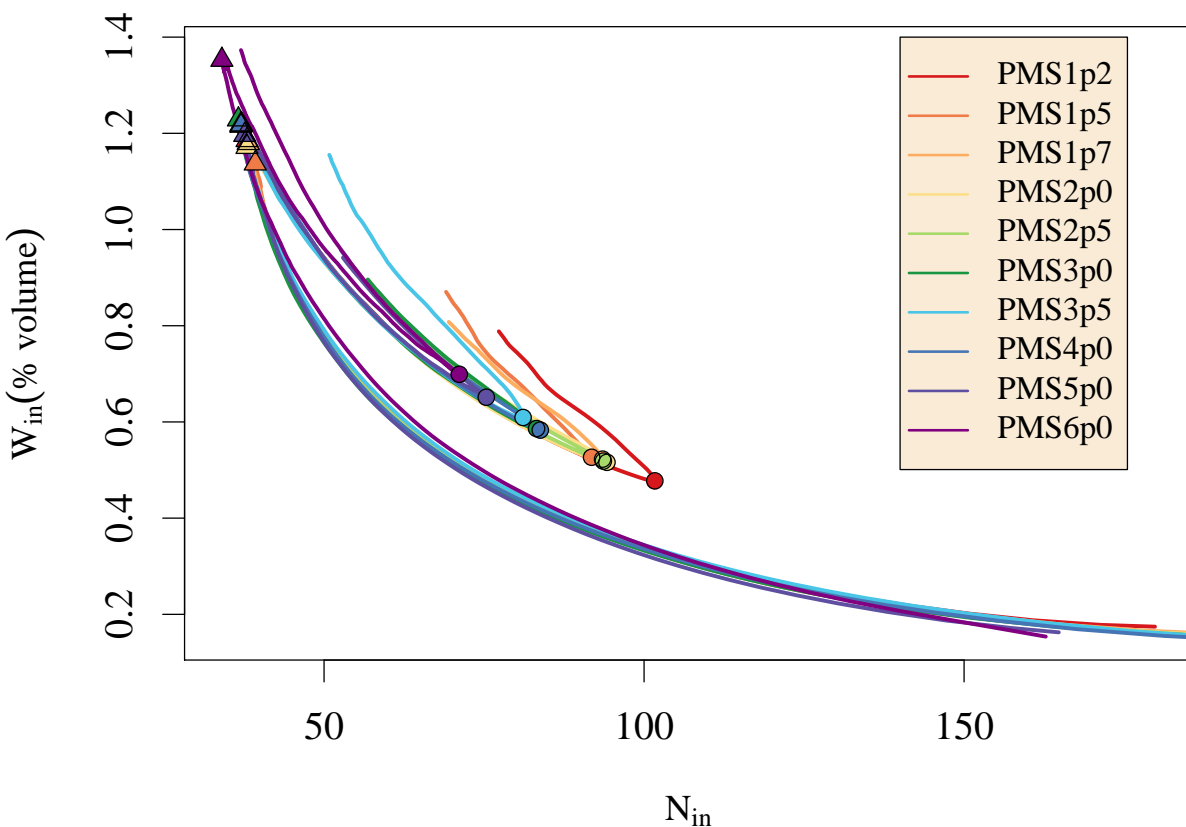


Figure 6.8 The average width of inflows vs. the average number of inflows for all values where the radius is greater than or equal to the radial point where  $r = r_{CB} - \ell_{\sigma_{VP}}$ . The bottom right shows the large number of inflows at the photosphere, and the trend increases up to the peak at the top left of the plot as the convection zone deepens. The peak in the top left corresponds to both  $N_{CZ}$  and  $W_{CZ}$ , which are represented by triangles color-coded to the stellar mass. The width-number relation decreases less steeply as it encounters boundary layer flows, and reaches the final inflection point at the values for  $N_{OL}$  and  $W_{OL}$ , which are represented by the circles.

where  $W_{in} = W_{CZ}$  (represented by the triangles in Figure 6.8). These trends show how the relationship between these two diagnostics changes before and after encountering boundary layer flows. The trend increases again after encountering the radial point where  $W_{in} = W_{OL}$  (represented by the dots in Figure 6.8). The data cease at the point where  $r = r_{CB} - \ell_{\sigma_{VP}}$ .

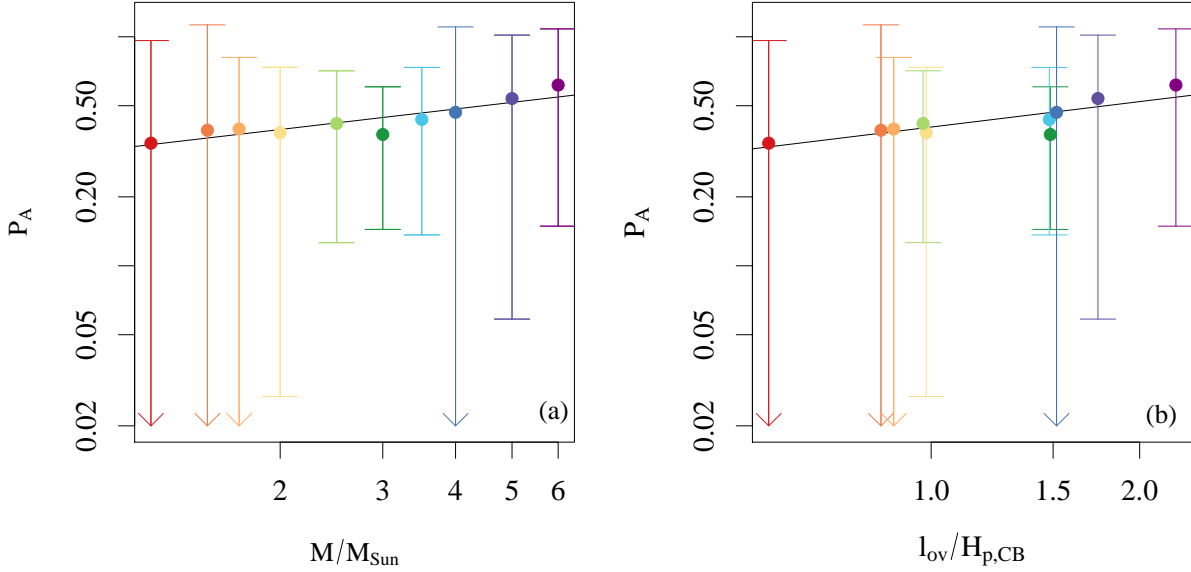


Figure 6.9 The Anders penetration parameter as a function of (a) stellar mass and (b) convective overshooting depth. The uncertainty on each point is calculated using the standard deviations of convective flux for the two points used in the calculation. The simulations PMS1p2, PMS1p5, PMS1p7, PMS2p0, PMS2p5, PMS3p0, PMS3p5, PMS4p0, PMS5p0, and PMS6p0 correspond to the colors red, dark orange, light orange, yellow, lime green, green, light blue, blue, indigo, and violet.

We also calculate the Anders penetration parameter  $P_A$  for the stars in this study, as shown in Figure 6.9; however, the uncertainties on the calculations are large because  $P_A$  is dependent on the convective flux, which requires a large time series of data to converge. Therefore, we do not make any relationships between  $P_A$  and stellar mass or convective overshooting depth.

### 6.3 Discussion

We examine a set of ten pre-main sequence stars with increasing mass, spanning from 1.2-6.0  $M_{\odot}$ . Each star has a convective envelope where the Schwarzschild boundary is  $r_{\text{CB}}/R_{\star} = 0.8$ .

We simulate each star in 2D with **MUSIC**. We calculate the one- and two-point diagnostics presented by Dethero et al. (2024). The filling factors do not increase with mass at any radial point in the stars that we study. The value for the filling factor at the convective boundary is approximately one-half for the volume-percentage and mass-flux definitions, while the convective-flux filling factor is uniformly small and negative in the simulations of these stars.

The horizontally-averaged radial profile for both the volume-percentage and mass-flux filling factors flatten out to a constant value at a distance  $\ell_{\sigma_{vp}}$  from the convective boundary, indicating a radial point corresponding to the bottom of an overshooting layer. This distance is the same for both filling factors and increases with stellar mass. We observe a relationship between the distance of  $W_{OL}$  from the convective boundary, and find that this distance is the same as  $N_{OL}$  from the boundary. These distances are characterized by  $\ell_{W_{OL}}$  and they also increase with stellar mass; however, they are smaller in magnitude than  $\ell_{\sigma_{vp}}$ , indicating an interesting radial point inside the overshooting layer. The ability of these two new diagnostics to indicate the convective overshooting depth or characterize a convective boundary layer will be tested in future studies.

Next, we examine the relationship between the average width of inflows and the average number of inflows. We find that the width-number relationship is nonlinear; the relationship is depth-dependent for the stars in this study with shallow envelopes. We also find that this relationship is different in the upper and lower parts of the convection zone, as well as the overshooting layer, such that one number of inflows could correspond to three different values

for average widths. This relationship reveals that as mass increases, the average width of inflows in the overshooting layer ( $W_{\text{OL}}$ ) increases, such that the profile of the average width of inflows is less steep; this is characteristic of “forest-like” convection.

The plume interaction parameter  $\sigma_{\text{int}}$  and the plume merging parameter  $\sigma_{\text{merge}}$  have a similar relationship with mass, with an experimental scaling law of  $\sim (M/M_{\odot})^{0.15}$ . The difference in magnitude of the two parameters is consistent between the ten simulations, where  $\sigma_{\text{int}}$  is between 5 – 9% higher. We find that as mass increases for the stars in our study, the “tree-like” structure is less extreme at the convective boundary. In the next study, we examine how the shape of convection changes with an increasing convection zone size.

## CHAPTER 7

### Convection in rapidly changing stars along the red giant branch

In laboratory experiments of convection, the aspect ratio of the box – the ratio of the height to the width – determines many characteristics of the convective flow patterns that emerge (Ahlers et al. 2009). Dethero et al. (2024) examined stellar simulations with a variety of evolutionary states, masses, and dimensions, and found that these patterns are different in different stellar structures. In this chapter, we aim to quantify how the shape of convection changes for a study of a single star while the aspect ratio of its convection zone is changing.

As stars evolve along the red giant branch, their convection zones deepen until the first dredge-up point (Salaris et al. 2002). Following the first dredge up, a star’s convection zone then rapidly recedes. This makes the red giant branch an interesting laboratory for studying the effect of the size of the convection zone on stellar convection. Performing hydrodynamic simulations of this star at different points along this evolutionary stage allows us to understand how convection changes throughout the red giant branch when the convection zone size is changing over a relatively short time scale of 10 million years. We simulate each star in MUSIC to calculate the overshooting depth and filling factors and establish how the shape of convection changes with the size of the convection zone.

#### 7.1 The evolution of convection along the RGB

We produce a model for a  $3 M_{\odot}$  star from the pre-main sequence through the red giant branch using the MESA code, version 10398. The inlist for this model uses solar metallicity, and it is provided in Appendix A. The star is evolved from the pre-main sequence through

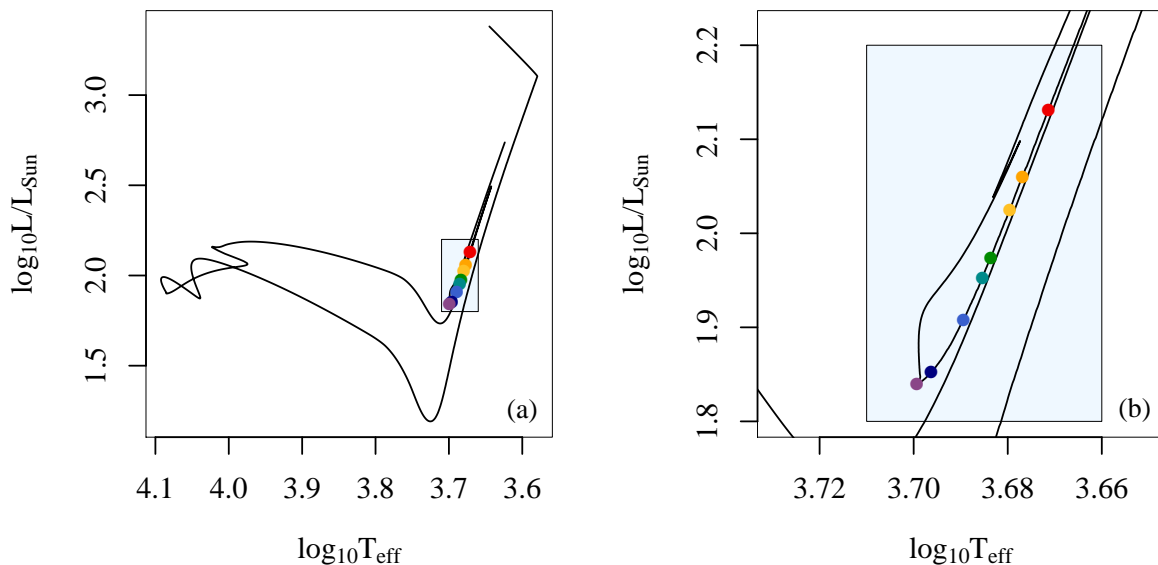


Figure 7.1 (a) HR diagram for a  $3 M_{\odot}$  red giant with solar metallicity. The points represent the structures chosen for the eight MUSIC simulations, which are located on the luminosity bump and Hayashi line of the HR diagram. (b) Luminosity bump in a zoomed-in view of the HR diagram.

the red giant branch, as shown on the HR diagram provided in Figure 7.1(a). To choose the evolutionary points to simulate in MUSIC, we consider the evolution of a  $3 M_{\odot}$  star in the red giant branch, where the convection zone is changing size. Following the first dredge up, the bottom of the convective envelope travels through approximately 40% of the total stellar radius.

When a  $3 M_{\odot}$  star fuses all of the hydrogen in its core into helium, it is left at the terminal age main sequence with a helium core and a hydrogen-burning shell. As the shell produces more helium, the isothermal helium core becomes more massive. Once the core is massive enough to reach a critical mass called the Schonberg-Chandrasekhar limit, the core collapses (Kippenhahn et al. 2013, Section 31.1). A consequence of shell-burning is that if

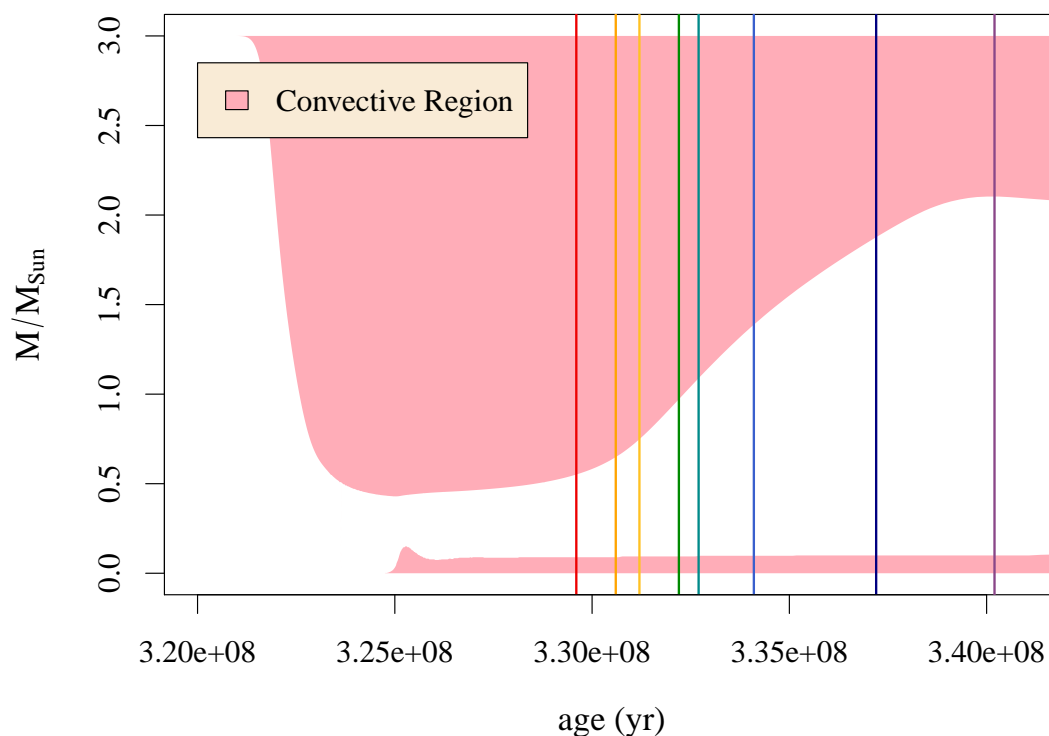


Figure 7.2 A zoomed-in version of Figure 1.3. Eight vertical lines indicate where the stellar structure was used to produce MUSIC simulations. The colors of the vertical lines correspond to the same color-coded points in Figure 7.1.

the core contracts, the outer envelope expands; this is explained by the “mirror principle.” The shell reaches higher temperatures if it follows the contracting core deep into the star, which would increase energy generation; however, to stay in thermal equilibrium, the rate of energy generation must remain constant. To combat the increasing temperature in the shell, the density of the shell must decrease, and therefore the pressure of the envelope on the shell must decrease, so the convective envelope begins to grow, causing the star to expand into a red giant (Lamers & Levesque 2017, Section 14.2).

Table 7.1 Parameters defining model stars produced by MESA. This table describes models along the evolutionary path of a simple 3 solar mass star produced with MESA. Models are along one such evolutionary path that spans a period of 10.61713 million years of evolutionary time. The variable  $r_{\text{CB}}$  indicates the radial position interior to the star of the convective boundary, as determined by the Schwarzschild criterion. The metallicity  $z = 0.02$  and helium mass fraction  $y = 0.2945$ .

Model	age ( $10^8$ yr)	R ( $10^{12}$ cm)	$r_{\text{CB}}/R$	$L/L_{\odot}$	$T_{\text{eff}}(10^3 K)$
RG1	3.296	1.2262	0.13	135.31	4.6917
RG2	3.306	1.1014	0.175	114.88	4.7518
RG3	3.312	1.0445	0.21	105.91	4.7814
RG4	3.322	0.96684	0.275	94.215	4.8265
RG5	3.327	0.93566	0.304	89.676	4.8460
RG6	3.341	0.87263	0.365	80.929	4.8909
RG7	3.372	0.79261	0.45	71.137	4.9690
RG8	3.402	0.77048	0.49	69.157	5.0045

As a result of the outer layers expanding, the star travels across the Hertzsprung-Russel Gap in Figure 7.1(a) and ascends the Hayashi track at the onset of helium burning in the core. The deep convection zone mixes material from the surface deep into the star and vice versa; this is called the first dredge-up event. Products of CNO burning can now be observed at the surface, as a result of mixing throughout the deep convective envelope (Beck et al. 2018; Boothroyd & Sackmann 1999). The star increases in brightness until it eventually reaches the extent of this line, referred to as the luminosity bump, which has been produced in stellar models (Cassisi & Salaris 1997; Christensen-Dalsgaard 2015; Bertolami 2023; Salaris et al. 2002) and observed in luminosity functions of clusters (King et al. 1985; Ferraro et al. 1999). The inflection point at the tip of the luminosity bump corresponds with the hydrogen-burning shell passing through material that was carried down from the surface by the first dredge-up event; as the shell burns this material, the efficiency of energy generation is inhibited, which decreases the luminosity. It is at this stage where the star descends the luminosity bump, and we choose our first model, represented by the red dot in

Figure 7.1, where the envelope is still large and the star has an age of 329.5 million years. As the shell passes through this discontinuity in composition, the convective shell is receding to the surface, as demonstrated in the Kippenhahn diagram produced from the MESA data in Figure 7.2, where the pink-shaded regions indicate areas that are unstable to convection. The second model is chosen a million years later, and the models are continuously chosen with increasing age and decreasing convective envelope sizes. The final model is chosen at an age of 340.2 million years, represented by the violet dot in Figure 7.1. Once the hydrogen burning shell has passed through this discontinuity, normal efficiency returns, and luminosity increases again (Salaris et al. 2002).

The eight evolutionary points we choose to simulate in **MUSIC** are shown on the zoomed-in HR diagram in Figure 7.1(b), where the youngest star has the highest luminosity and is indicated in red, and the oldest star has the lowest luminosity and is indicated in violet. As luminosity decreases, the convective boundary moves outward from  $r_{\text{CB}} = 0.13R_*$  to  $r_{\text{CB}} = 0.5R_*$  and the convection zone shrinks, as shown in the Kippenhahn diagram in Figure 7.2, where the stellar structures simulated with **MUSIC** are represented by color-coded vertical lines. The radial boundary conditions, convective turnover times, and resolution of each simulation are recorded in Table 7.2. Each simulation is run for more than 100 turnover times, indicating sufficient data to produce meaningful statistics.

Our goal in this study is to determine how convection varies with the size of the convection zone. First, we examine the convective velocities in MESA (see Figure 7.3(a)) and the radial root-mean-square velocity in **MUSIC** (see Figure 7.3(b)). Major differences between the two

Table 7.2 Two-dimensional simulations performed with MUSIC. The table includes the MESA model, the inner radial boundary  $r_{\text{in}}/R$ , the outer radial boundary  $r_{\text{out}}/R$ , the time span of the simulation in units of convective turnover times  $\tau_{\text{conv}}$ , and the resolution,  $H_{p,\text{CB}}/\Delta r$ .

Name	Model	$r_{\text{in}}/R$	$r_{\text{out}}/R$	$\tau_{\text{conv}}(10^5\text{s})$	time span ( $\tau_{\text{conv}}$ )	$H_{p,\text{CB}}/\Delta r$
IN1	RG1	0.02	0.90	$9.16 \pm 1.84$	102	54
IN2	RG2	0.02	0.90	$10.20 \pm 2.12$	121	55
IN3	RG3	0.02	0.90	$11.46 \pm 1.36$	101	83
IN4	RG4	0.10	0.90	$9.84 \pm 2.50$	282	56
IN5	RG5	0.10	0.90	$12.23 \pm 1.53$	264	56
IN6	RG6	0.10	0.90	$13.31 \pm 1.45$	263	54
IN7	RG7	0.10	0.90	$14.52 \pm 1.42$	370	55
IN8	RG8	0.10	0.90	$15.55 \pm 1.60$	143	55

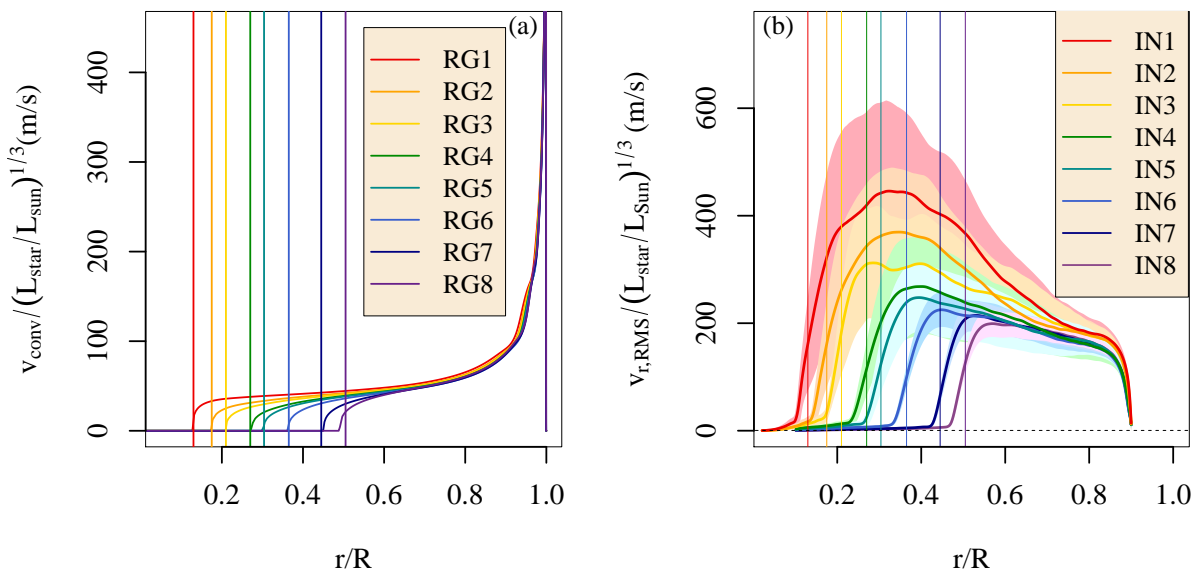


Figure 7.3 (a) The convective velocity for each RG model calculated with the MESA code. (b) The radial root-mean-squared velocity profile for each IN red giant simulation, calculated with MUSIC.

calculations of velocity include the shape of the profile, the magnitude, and the change in convection zone size. MESA uses the mixing length to calculate the velocity, which does not incorporate the convection zone size; as a result, velocities appear similar in the convection zone despite the location of the convective boundary. For the MUSIC simulation, we find that the convective velocities grow with convection zone size, such that the star with the largest

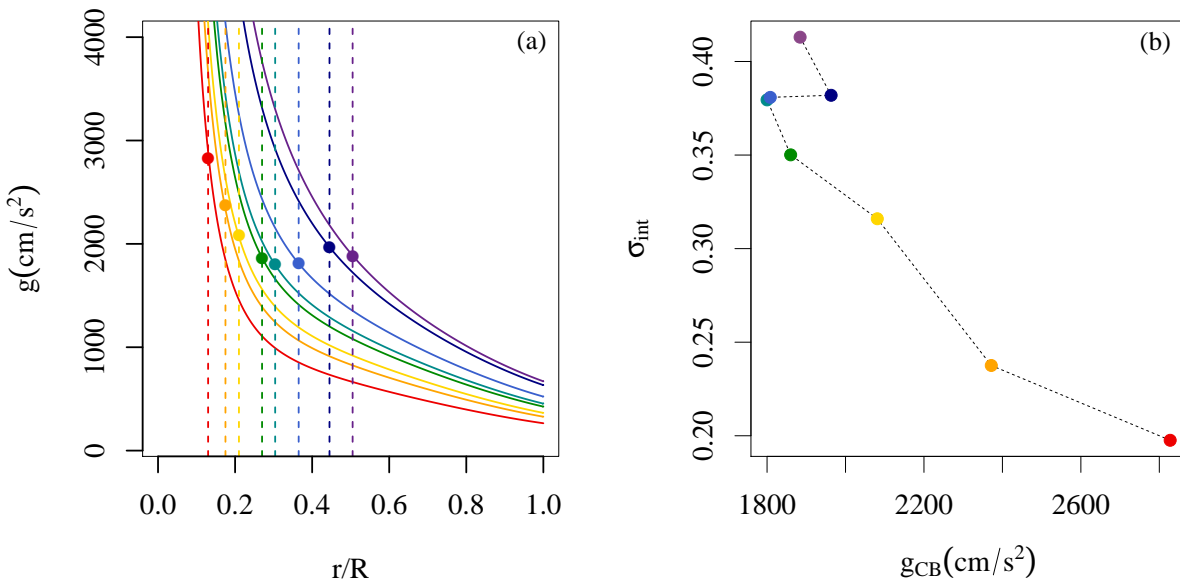


Figure 7.4 (a) Gravity profiles for eight red giant stars. The vertical dashed lines represent the convective boundary, and the dots represent the value for gravity at the convective boundary. (b) Plume interaction parameter calculated with *MUSIC* scales with the value for gravity at the convective boundary. The models RG1, RG2, RG3, RG4, RG5, RG6, RG7, and RG8 correspond to red, orange, yellow, green, light blue, dark blue, indigo, and violet.

convection zone reaches magnitudes three times larger than the simulation with the smallest convection zone. The shaded regions represent one standard deviation above and below the mean, demonstrating that different velocity magnitudes exist at the same radial point. The differences between Figures 7.3(a) and 7.3(b) emphasize the importance of the size of convection zone on multi-scale convection, as well as the limits of mixing length theory.

Another fundamental stellar parameter that influences convection is effective gravity, which can be directly plotted from the MESA models as a radial profile, shown in Figure 7.4(a). We plot color-coded dots at the value for the effective gravity at the convective boundary. We find that this value decreases as the convective boundary recedes from  $r_{\text{CB}} = 0.13$  to  $r_{\text{CB}} = 0.275$ , and then increases again after  $r_{\text{CB}} = 0.3$ . This kink in the gravity at the

Table 7.3 Calculated quantities related to the filling factor for convection for a red giant star at eight points along the first dredge-up point of the red giant branch. The table includes the volume-percentage filling factor  $\sigma_{\text{vp,CB}}$ , the mass-flux filling factor  $\sigma_{\text{mf,CB}}$ , and the incompressible convective-flux filling factor  $f_{z,\text{CB}}$ . The subscript CB indicates that the quantity is evaluated at the convective boundary (CB), as defined by the Schwarzschild criterion. Several additional quantities that are evaluated above or below this convective boundary are also shown. This includes the Anders penetration parameter  $P_{\text{A}}$ , the plume interaction parameter  $\sigma_{\text{int}}$ , and the plume merging parameter  $\sigma_{\text{merge}}$ . It also includes the average number of inflows in the overshooting layer  $N_{\text{OL}}$  and in the convection zone  $N_{\text{CZ}}$ , and the average width of inflows in the overshooting layer  $W_{\text{OL}}$  and in the convection zone  $W_{\text{CZ}}$ . The average widths are displayed in units of the percentage of the simulation volume at the given radius.

	$\sigma_{\text{vp,CB}}$	$\sigma_{\text{mf,CB}}$	$f_{z,\text{CB}}$	$P_{\text{A}}$	$N_{\text{OL}}$	$N_{\text{CZ}}$	$\sigma_{\text{merge}}$	$W_{\text{OL}}$	$W_{\text{CZ}}$	$\sigma_{\text{int}}$
IN1	0.51	0.49	-0.18	0.021	13.4	2.87	0.22	3.68	18.6	0.20
IN2	0.50	0.50	-0.05	0.040	12.3	3.01	0.25	3.91	16.5	0.24
IN3	0.50	0.51	-0.02	0.038	14.9	4.67	0.31	3.29	10.4	0.32
IN4	0.49	0.51	-0.01	0.107	12.3	4.25	0.35	3.94	11.3	0.35
IN5	0.49	0.51	-0.02	0.110	13.3	4.89	0.37	3.66	9.64	0.38
IN6	0.49	0.52	-0.01	0.159	15.2	5.89	0.39	3.12	8.19	0.38
IN7	0.48	0.52	-0.01	0.232	19.0	7.43	0.39	2.49	6.52	0.38
IN8	0.48	0.53	-0.03	0.246	20.7	8.59	0.42	2.26	5.48	0.41

convective boundary demonstrated by the dots in Figure 7.4(a) could be influential on other convective properties. We investigate the one- and two-point diagnostics to understand what they reveal about the changing properties of convection with a changing convection zone size.

## 7.2 One-point statistics

We calculate the volume-percentage filling factor  $\sigma_{\text{vp}}(r)$ , mass-flux filling factor  $\sigma_{\text{mf}}(r)$ , and the convective-flux filling factor  $f_z(r)$  for all eight red giant stars. The value of the filling factor at the convective boundary  $\sigma_{\text{vp,CB}}$  slightly decreases with age, and  $\sigma_{\text{mf,CB}}(r)$  slightly increases with age, as shown in Table 7.3. This is the first study using MUSIC simulations

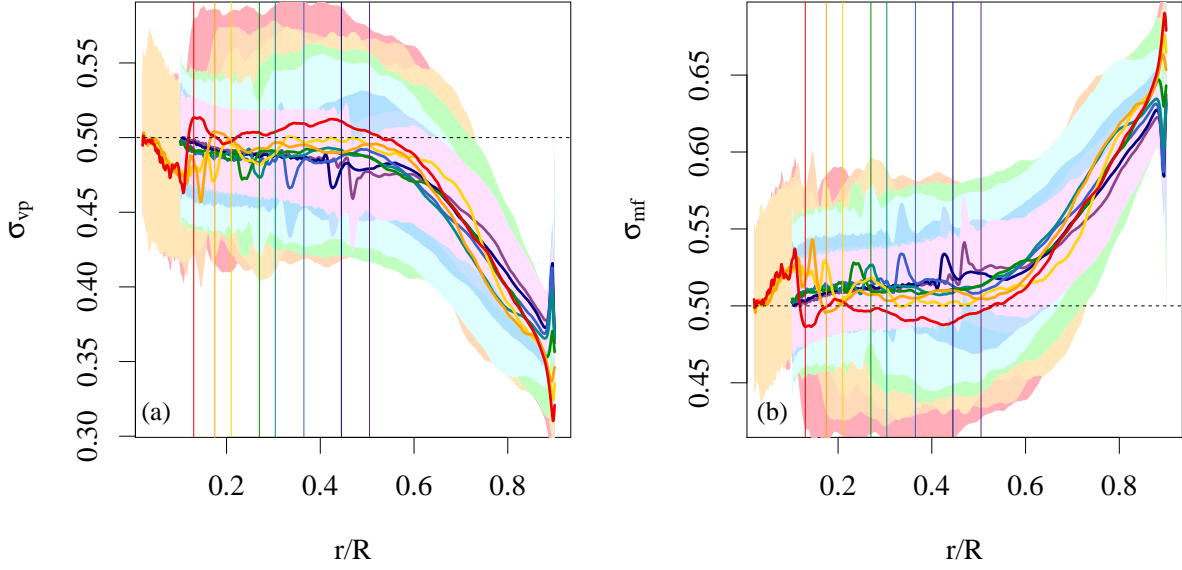


Figure 7.5 Volume-percentage (a) and the mass-flux (b) filling factor profiles for eight  $3M_{\odot}$  red giant stars with different ages. The vertical lines represent the Schwarzschild convective boundary for each simulation. The shaded regions represent one standard deviation above and below the time-averaged mean. The dashed line represents a filling factor value of one-half. The red vertical line represents the Schwarzschild boundary for the youngest red giant with the largest convection zone size. The simulations IN1, IN2, IN3, IN4, IN5, IN6, IN7, and IN8 correspond to the red, orange, yellow, green, light blue, dark blue, indigo, and violet lines.

where the filling factor changes in a significant way; however, the standard deviation for each simulation is larger than the differences in the filling factor for all simulations (see the shaded regions in Figure 7.5). We find the relationship between  $\sigma_{vp}(r)$  and  $1 - \sigma_{mf}(r)$  to increase similarly for all the stars in this study, implying these two filling factors encapsulate the same information. The convective flux filling factor is small and negative for each simulation, similar to the results from Dethero et al. (2024).

The standard deviation of the filling factor increases as the size of the convection zone ( $r_{CZ}$ ) increases (see Figure 7.6(a)). Because each simulation is run for more than 100 turnover

Table 7.4 Calculated quantities related to the convective overshooting depth for a red giant star at eight points along the first dredge-up point of the red giant branch. The table includes the overshooting depth  $\ell_{\text{ov}}$  as well as the characteristic lengths from the filling factor profiles  $\ell_{\sigma_{\text{vp}}}$ , and the width profiles  $\ell_{W_{\text{OL}}}$ , in units of the pressure scale height at the convective boundary.

	$\ell_{\text{ov},k}/H_{\text{p,CB}}$	$\ell_{\sigma_{\text{vp}}}/H_{\text{p,CB}}$	$\ell_{W_{\text{OL}}}/H_{\text{p,CB}}$
IN1	0.29	0.56	0.30
IN2	0.41	0.52	0.28
IN3	0.44	0.80	0.29
IN4	0.48	0.51	0.26
IN5	0.46	0.52	0.25
IN6	0.38	0.42	0.20
IN7	0.32	0.29	0.11
IN8	0.32	0.41	0.26

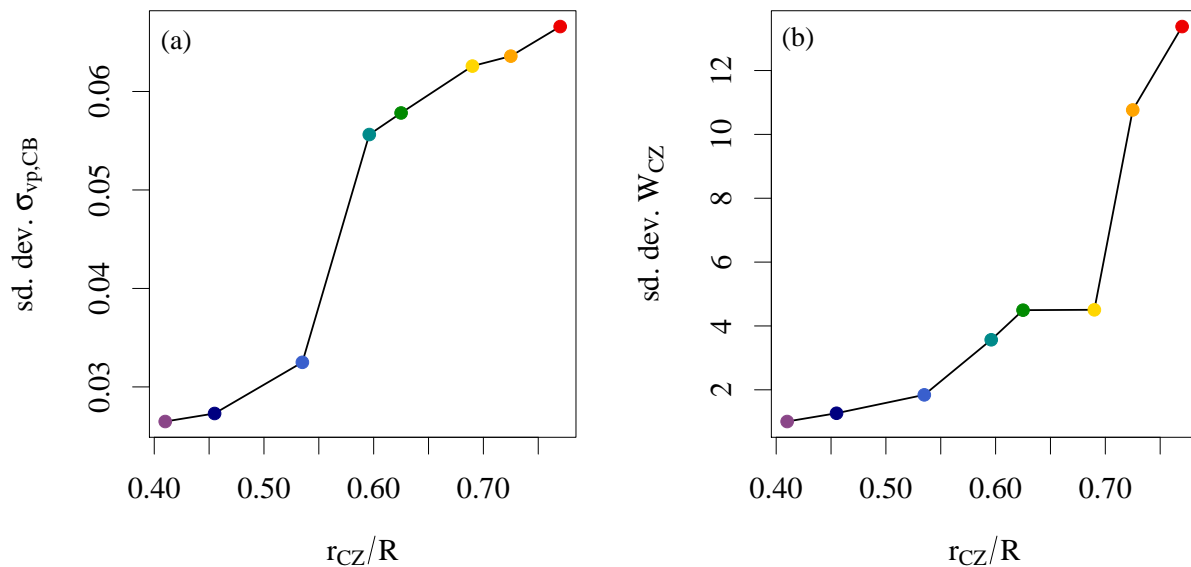


Figure 7.6 (a) The standard deviation in time of the horizontally-averaged volume-percentage filling factor at the convective boundary,  $\sigma_{\text{vp,CB}}$ , as a function of the size of the convection zone in units of the total stellar radius. (b) The standard deviation in time of the maximum value of the average width of inflows in the convection zone,  $W_{\text{CZ}}$ . The simulations IN1, IN2, IN3, IN4, IN5, IN6, IN7, and IN8 correspond to the red, orange, yellow, green, light blue, dark blue, indigo, and violet circles.

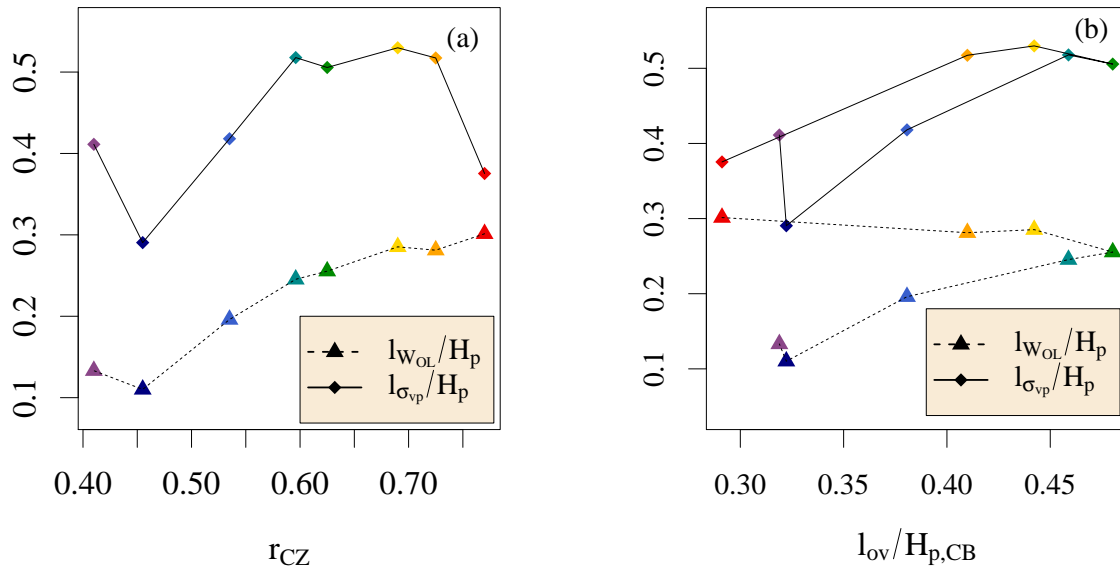


Figure 7.7 The distances  $\ell_{\sigma_{vp}}$  (solid line, diamonds), and  $\ell_{W_{OL}}$  (dashed line, triangles) (a) as a function of the size of the convective boundary and (b) as a function of the convective overshooting depth. The simulations IN1, IN2, IN3, IN4, IN5, IN6, IN7, and IN8 correspond to the red, orange, yellow, green, light blue, dark blue, indigo, and violet symbols.

times, this decrease in the standard deviation of the volume-percentage filling factor is statistically meaningful. The depth of the convection zone provides an upper limit for the largest length scale of the convective flow. Thus as the convection zone increases, the largest length scale of convection also increases, constraining the multi-scale nature of convection. As convection involves more length scales, the variation of plume widths in the flow should also be increased (see Figure 7.6(b)); this is evident even in the simple sum that makes up the volume-percentage filling factor.

An additional feature in the filling factor profiles in this set of stars is a dip just below the convective boundary in the overshooting layer. We conjecture that this feature is the result of stratification in this set of stars. We measure the distance from the convective boundary

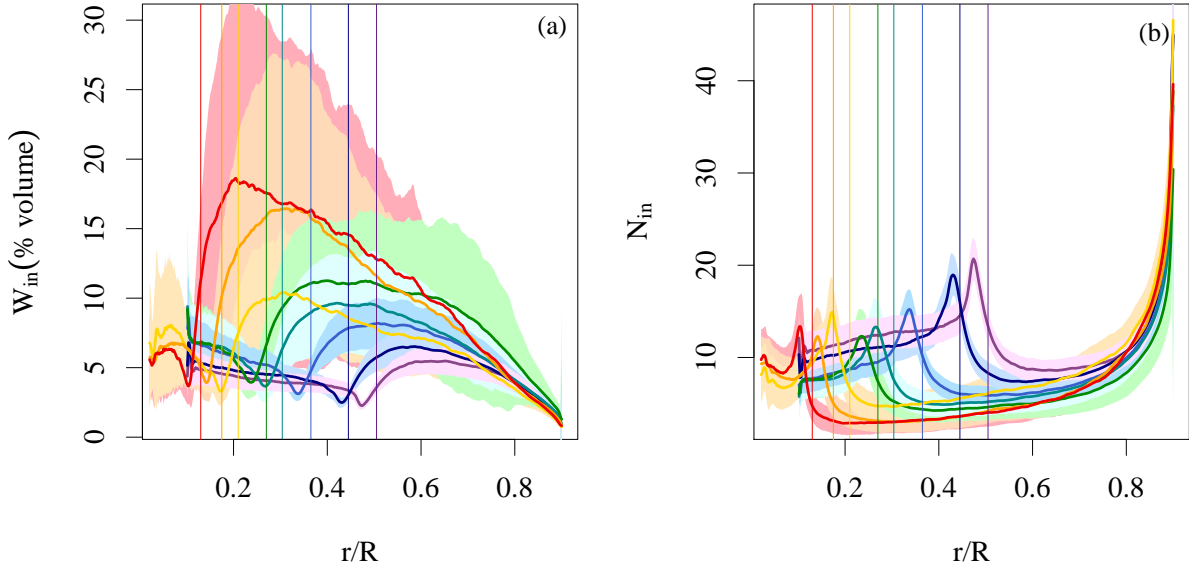


Figure 7.8 The horizontally-averaged (a) width and (b) number of inflows for eight  $3M_{\odot}$  red giant stars along the luminosity bump descent. The vertical lines represent the Schwarzschild convective boundary for each simulation. The shaded regions represent one standard deviation above and below the time-averaged mean. The red vertical line represents the Schwarzschild boundary for the youngest red giant with the largest convection zone size. The simulations IN1, IN2, IN3, IN4, IN5, IN6, IN7, and IN8 correspond to the red, orange, yellow, green, light blue, dark blue, indigo, and violet lines.

to the dip and find the resulting length scale corresponds to  $\ell_{W_{\text{OL}}}$  defined in Section 6.1 as the distance from the convective boundary to  $W_{\text{OL}}$ . We also calculate  $\ell_{\sigma_{\text{vp}}}$  and compare it to the convective overshooting depth calculated with extreme value statistics (Pratt et al. 2017). The values for both of these length scales are recorded in Table 7.4. We find that  $\ell_{\sigma_{\text{vp}}}$  and  $\ell_{W_{\text{OL}}}$  both increase and decrease with the size of the convection zone.

### 7.3 Two-point statistics

The average width of inflows  $W_{\text{in}}(r)$  and the average number of inflows  $N_{\text{in}}(r)$  are shown in Figure 7.8(a) and Figure 7.8(b). As the convection zone becomes smaller with age, in-

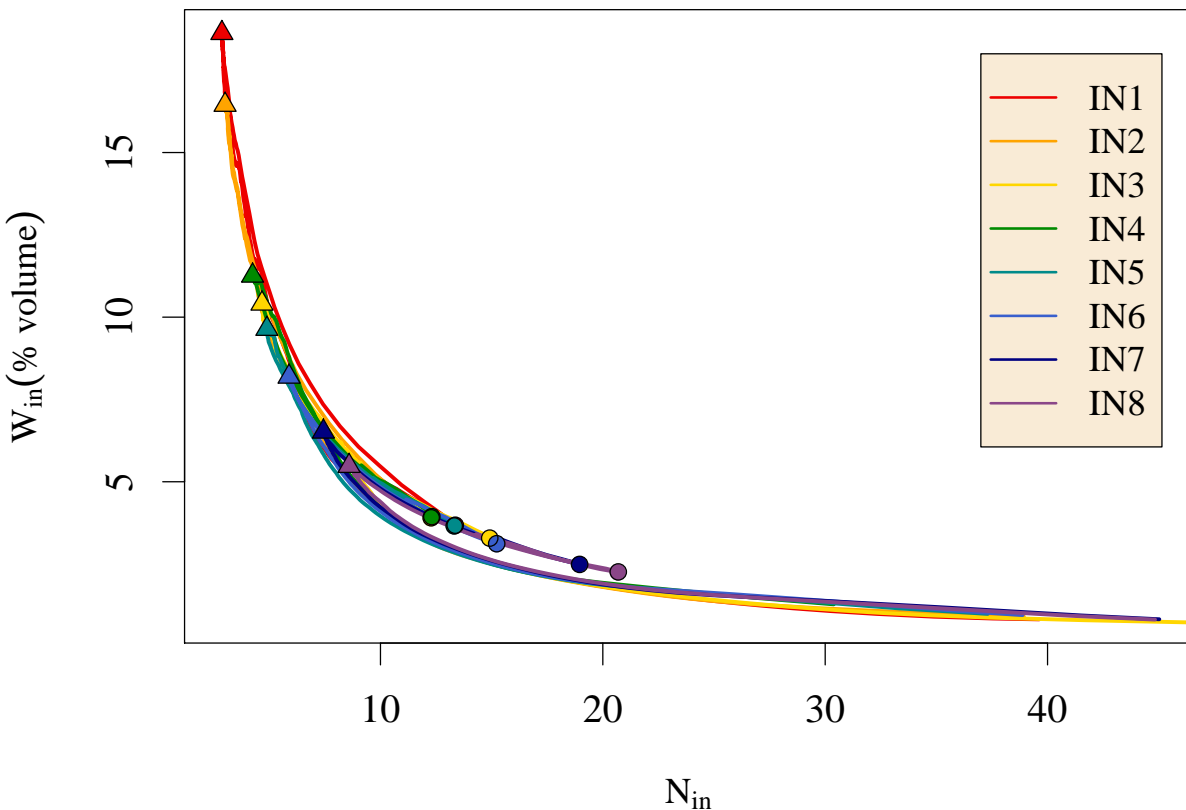


Figure 7.9 The average width of inflows as a function of the average number of inflows. The triangles represent the characteristic values in the convection zone ( $N_{OL}$  vs.  $W_{OL}$ ), and the dots represent the characteristic values in the overshooting layer ( $N_{CZ}$  vs.  $W_{CZ}$ ).

flows become narrower and more numerous. The standard deviation of the average widths throughout the convection zone is decreasing along with convection zone size (see Figure 7.6(b)), indicating that a larger variety of widths exists in deep convection zones versus shallow convection zones. We find that the standard deviation for the number of inflows in 7.8(b) is smaller about the mean than for the widths of inflows in 7.8(a), indicating different information is captured in each diagnostic.

We find a relationship between the width and number of plumes for the red giant stars

in this study that is depth-dependent with a nonlinear relationship. The radial domain included for this relationship is limited to  $r \geq r_{\text{CB}} - \ell_{\sigma_{\text{vp}}}$ , so that the stable region below the overshooting layer is not included. Figure 7.9 demonstrates the relationship between the numbers and widths of plumes can be similar for stars with different convection zone sizes, such that the lines are overlapping. The bottom right of the plot corresponds with the extent of the simulation at  $r = 0.9R$ . The radius decreases toward the top left of the plot until reaching the triangles representing the characteristic points  $W_{\text{CZ}}$  and  $N_{\text{CZ}}$ , and then further decreases until reaching the characteristic points  $W_{\text{OL}}$  and  $N_{\text{OL}}$ , represented by the dots. The relationship between the number and width of inflows is shifted up after encountering the triangles, representing the mid-convection zone, such that the width-number relation can provide two different values for the average width of inflows for the same number of inflows. After encountering the characteristic points in the overshooting layer, represented by the dots, the inflows are dissipating into the stable zone. We find that the widths of the inflows increase along the same trend after encountering the boundary layer.

Figure 7.10 shows  $N_{\text{OL}}$  and  $W_{\text{OL}}$  as a function of the size of the convection zone,  $r_{\text{CZ}}$ , for each simulation. We observe a linear trend between the widths of the inflows until the convective boundary recedes to  $r_{\text{CB}} = 0.275$ , at which point we observe a scattered trend for the deepest convection zones. This result indicates that the width of inflows interacting with the convective boundary is roughly the same among simulations until the convective boundary recedes to  $r_{\text{CB}} = 0.275$ . After this point, the flows at the convective boundary become more numerous and narrower as the convection zone size becomes smaller. We also

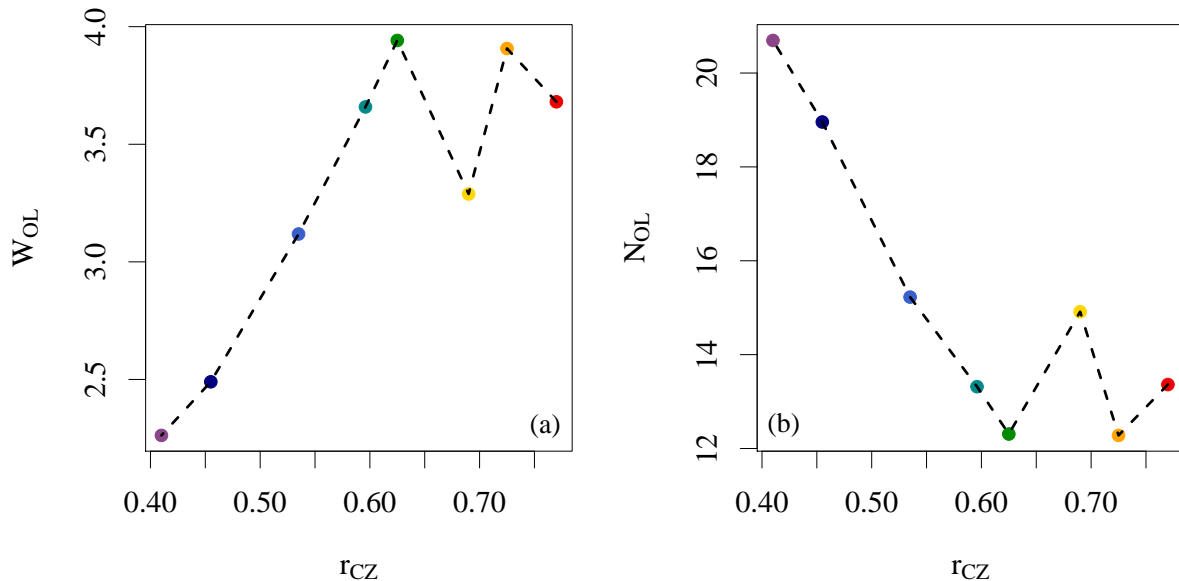


Figure 7.10 The average (a) width and (b) number of inflows as a function of the size of the convection zone,  $r_{CZ}$ . Both  $W_{OL}$  and  $N_{OL}$  exhibit a linear trend until  $r_{CZ} = 0.625$ . The simulations IN1, IN2, IN3, IN4, IN5, IN6, IN7, and IN8 correspond to the red, orange, yellow, green, light blue, dark blue, indigo, and violet circles.

calculate  $\ell_{W_{OL}}$ , the distance from the convective boundary to  $W_{OL}$ , and find it generally increases with the depth of the convection zone,  $r_{CZ}$ , as shown in Figure 7.7(a). However, we find that the trend between this length scale and the overshooting depth has two distinct pieces, one before the green point, representing IN4, and a different piece after this point. These scattered trends indicate how stellar structure can rapidly change, even over the small window of ten million years.

We calculate  $\sigma_{int}$  and  $\sigma_{merge}$  for each simulation, and we find that the values are similar, as recorded in Table 7.3. Figure 7.11(a) demonstrates how both parameters decrease as the convection zone gets bigger. A smaller  $\sigma_{int}$  and  $\sigma_{merge}$  correlate to the deep convection zones with more multi-scale flow and less numerous inflows. The plume interaction parameter,

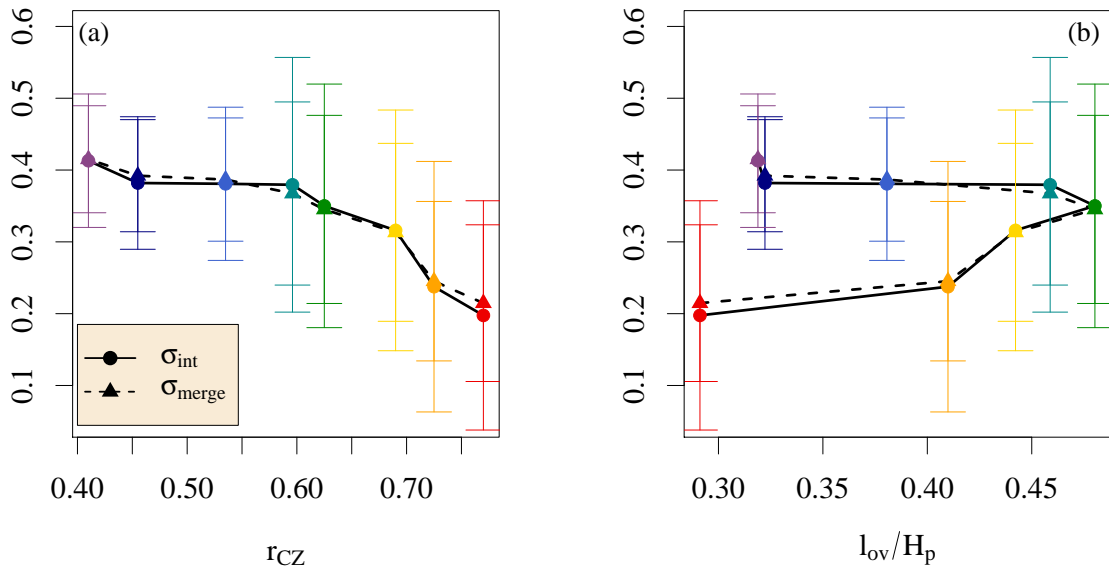


Figure 7.11 Two-point diagnostics  $\sigma_{\text{int}}$  (dots) and  $\sigma_{\text{merge}}$  (triangles) as a function of (a) convective boundary and (b) convective overshooting depth. The simulations IN1, IN2, IN3, IN4, IN5, IN6, IN7, and IN8 correspond to the red, orange, yellow, green, light blue, dark blue, indigo, and violet circles.

$\sigma_{\text{int}}$ , has a larger uncertainty than  $\sigma_{\text{merge}}$  due to the larger standard deviation on the widths compared to the numbers. When comparing these diagnostics to the overshooting depth in Figure 7.11(b), we see two distinct pieces, where the green point, representing simulation IN4, is the inflection point. Characterizing the relationship between these two diagnostics must be pursued in other studies.

## 7.4 Discussion

We have explored convection in a  $3 M_{\odot}$  star at eight distinct evolutionary points as it descends the luminosity bump of the red giant branch. We modeled the star at each point using the MESA code, and simulated the star with the MUSIC code in order to examine the

influence of the size of the convection zone on stellar mixing.

The filling factor at the convective boundary is slightly affected by the size of the convection zone, such that  $\sigma_{\text{vp,CB}}$  decreases from 0.51 to 0.48 as the convection zone gets smaller, and  $\sigma_{\text{mf,CB}}$  increases from 0.49 to 0.53. The differences between these values are not statistically significant given the large standard deviations of the data.

We also calculate the new length scales  $\ell_{\sigma_{\text{vp}}}$  and  $\ell_{W_{\text{OL}}}$ . Both show a correlation with the convection zone size and the convective overshooting depth, although the stellar structure is changing too rapidly to derive a direct relationship. We find  $\ell_{\sigma_{\text{vp}}} > \ell_{W_{\text{OL}}}$ , such that  $\ell_{\sigma_{\text{vp}}}$  marks the extent of the overshooting layer and  $\ell_{W_{\text{OL}}}$  is some characteristic point inside this layer. We observe a characteristic dip slightly past the convective boundary for the filling factor profiles, which corresponds to the length scale  $\ell_{W_{\text{OL}}}$ . The convective-flux filling factor is small and negative with no correlation to the size of the convection zone in all simulations we examine.

We find that the widths are larger on average and have a larger standard deviation for the stars with deeper convection zones. The width-number relation for inflows is nonlinear with two distinct curves, revealing that the number of inflows at a certain radius may correspond to two different average widths. The plume interaction parameter  $\sigma_{\text{int}}$  and the plume merging parameter  $\sigma_{\text{merge}}$  decrease similarly with the size of the convection zone, but do not directly correlate with the overshooting depth. We find  $\sigma_{\text{int}} = \sigma_{\text{merge}}$  for all eight simulations. The larger uncertainty on  $\sigma_{\text{int}}$  versus  $\sigma_{\text{merge}}$  shows that the widths of inflows fluctuate more than the number of inflows for these stars.

As the size of the convection zone increases, the radius of the star at the photosphere is also changing, as well as other aspects of the stellar structure such as luminosity and effective gravity. The trends related to convection and overshooting are non-monotonic over this short window of stellar evolution. We observe these trends changing shape around the time of simulation IN4, where the convective boundary is  $r_{\text{CB}} = 0.275R$ . This inflection point is observed in the gravity at the convective boundary, the convective overshooting depths,  $W_{\text{OL}}$ , and  $N_{\text{OL}}$  and highlights the evolution of stellar structure over a small window that is difficult for astronomers to observe.

## CHAPTER 8

### Summary and Conclusions

One-dimensional stellar evolution codes produce models of stars that can be compared to observations to form relationships between stellar mass, ages, radii, luminosity, and metallicity. However, these models for stellar convection and convective boundary mixing have well-documented limitations. The most widely used model for convection, mixing length theory (MLT), involves several free parameters, limiting its predictive power for observations. MLT models are relevant only in cases of envelope convection, and they do not account for a phenomenon called convective overshooting. Additional models have been implemented into stellar evolution codes to account for mixing due to convective overshooting. These overshooting prescriptions include additional free parameters and can be difficult to physically motivate.

To improve our understanding of overshooting and boundary layer mixing, we turn to global, multidimensional hydrodynamic simulations of compressible convection with realistic stellar structures. For this body of work, we use the Multi-dimensional Stellar Implicit Code (MUSIC) to produce simulations in 2D and 3D for a variety of stars. These simulations provide detailed information about stellar convective velocities and fluxes. Long time series of data allow us to form well-converged statistics based on these quantities, allowing us to determine properties of convection and the depth of convective boundary mixing in stars. In three separate studies, we use MUSIC to calculate diagnostics related to convection and convective boundary mixing to determine how they change with different stellar properties,

dimensions, evolutionary stages, location of the convection zone, such as core or envelope, and size of the convection zone, such as shallow or deep. We calculate diagnostics related to the shape of stellar convection in each star: three filling factors ( $\sigma_{\text{vp}}$ ,  $\sigma_{\text{mf}}$ , and  $f_z$ ), the width of inflows ( $W_{\text{in}}$ ), the number of inflows ( $N_{\text{in}}$ ), the Anders penetration parameter ( $P_{\text{A}}$ ), the plume interaction parameter ( $\sigma_{\text{int}}$ ), and the plume merging parameter ( $\sigma_{\text{merge}}$ ).

## 8.1 Summary of Results

### 8.1.1 *The filling factor*

The convective overshooting depth has been linked to the convective velocity and the filling factor in several theoretical works (Schmitt et al. 1984; Stein & Nordlund 1989; Cattaneo et al. 1989; Toomre et al. 1990; Cattaneo et al. 1991; Zahn 1991; Canuto & Dubovikov 1998; Brummell et al. 2002; Rempel 2004; Browning et al. 2004; Rogers et al. 2006; Käpylä et al. 2017; Cai 2020). The filling factor employs a one-dimensionalization similar to that of MLT; Canuto (1992) described this as “the rather extreme MLT assumption that the full eddy spectrum can be represented by one large eddy.” In a study of five pairs of two- and three-dimensional simulations drawn from a wide range of masses and evolutionary stages, we calculate the overshooting depths as well as the filling factor defined in three ways: the volume-percentage filling factor, the mass-flux filling factor, and the convective flux filling factor. We calculate each filling factor as a radial profile spanning a large portion of the stellar radius. For the volume-percentage and mass-flux definitions, we find a filling factor value of approximately one-third at the surface, and one-half at the convective boundary for

all of the stars in our study. This radial shape of the filling factor for convection has not previously been produced or studied. At the convective boundary, the lowest average value is  $\sigma_{\text{vp,CB}} = 0.45$  for the current sun, and the highest value is  $\sigma_{\text{vp,CB}} = 0.51$  for the young sun; this deviation from the value of one-half is slight, and not statistically significant. This result tells us that convective inflows and outflows are in near-perfect symmetry at the convective boundary, regardless of the depth of that boundary or whether we examine a convective envelope or a convective core. Given that early works referred to a strong asymmetry that continued from the surface to the convective boundary, this result is surprising, and it has far-reaching consequences for theoretical scalings for the depth of convective boundary mixing. We also find no correlation between the filling factor and the dimensionality of a simulation, or indeed with the depth of overshooting for the wide variety of stars in the study. This strongly suggests that a different kind of diagnostic is needed to predict the depth of the overshooting layer. Because the filling factor is conceptually similar to the approximations that underlie MLT, this also implies that MLT models are fundamentally incompatible with overshooting.

To investigate whether the filling factor changes in response to mass, we set up a study of 10 identical stellar structures with the same size convective envelope; the only difference between the models is the stellar mass ranges from 1.2 to 6  $M_{\odot}$ . The convective envelopes in this series of stellar models are moderately more shallow than the current sun. We simulate each star with *MUSIC* and find the filling factor is independent of mass for this study of stars with shallow convective envelopes. The average volume-percentage filling factor is uniformly

$\sigma_{\text{vp,CB}} = 0.48$  and the mass-flux filling factor is  $\sigma_{\text{mf,CB}} = 0.52$ . These deviations of these values from one half are not statistically significant. This reinforces our result that, at the convective boundary, inflows and outflows are symmetric.

To understand the impact of the size of the convection zone on the filling factor, we examine a single red giant star at eight points along its evolutionary track immediately following the first dredge-up point, where the convection zone size decreases from 87% of the stellar radius to 51% of the stellar radius. We find that the volume-percentage filling factor slightly decreases over time from  $\sigma_{\text{vp,CB}} = 0.51$  to  $\sigma_{\text{vp,CB}} = 0.48$  and the mass-flux filling factor slightly increases over time from  $\sigma_{\text{mf,CB}} = 0.49$  to  $\sigma_{\text{mf,CB}} = 0.53$ . Because the standard deviation is much larger than the difference between these average values and one-half, the change in filling factor with depth is not statistically significant. As a star evolves and its structure changes considerably, it maintains the symmetry between inflows and outflows at the convective boundary.

Each of these three studies suggests that the mass-flux filling factor does not provide independent information from the volume-percentage filling factor. For all of the stars studied in this body of work  $\sigma_{\text{vp}}(r) \approx 1 - \sigma_{\text{mf}}(r)$ . This is an interesting result because although it is not obviously a universal law for stars, it appears to hold frequently.

In each of these three studies, we universally find that the convective-flux filling factor is small and negative, as shown in Dethero et al. (2024). This prevents this formulation of a filling factor from predicting the overshooting depth. However, it does reveal that complex flow patterns exist around the convective boundary, both inside the convection zone and in

the overshooting layer. Those flow patterns are not reflected in currently available theoretical works.

### ***8.1.2 Two point diagnostics***

In addition to a filling factor, several works have suggested the number and widths of inflows at a given radial point inside the convection zone could indicate the number of interaction points between inflows and outflows (Käpylä et al. 2017; Brandenburg 2016; Spruit 1997). Because MUSIC solves the compressible hydrodynamic equations in global simulations, we can achieve a large density stratification, reaching  $10^5$  in the *wm2d/wm3d* simulation pair, which allows us to study a truly multi-scale flow throughout the convection zone. In these multi-scale flows, there are a large number of plumes at the stellar surface, which drops monotonically to a small number at the convective boundary; this decrease in plume number would indicate a “tree-like” structure of convection, evoking the difference in number between leaves, branches, and trunks. A constant number of plumes of the same size throughout the convection zone, similar to classic Rayleigh-Bénard convection, indicates a “forest-like” structure of convection, evoking a picture of many trees that are similar in size. We calculate the average number of plumes as a function of radius, as well as the average width of plumes as a function of radius. These diagnostics allow us to identify both “tree-like” and “forest-like” regions in deep convection envelopes. This is in contrast to entirely “tree-like” convection in small convective envelopes or convective cores.

To quantify the shape of convection, we define two new nondimensional parameters, the plume interaction parameter based on the average plume widths,  $\sigma_{\text{int}}$ , and the plume merging

parameter based on the average number of plumes,  $\sigma_{\text{merge}}$ . These parameters are based on two characteristic points: one in the middle of the convection zone (CZ), and one in the overshooting layer (OL). The plume interaction parameter tracks the apparent funneling of the average width, which is large in the convection zone, but narrows considerably as plumes approach a convective boundary. Since the width of plumes also corresponds to the number of points where inflows and outflows interact, this tracks shear interactions between plumes. The plume merging parameter indicates a ratio of the number of inflows in a convection zone as opposed to an overshooting layer; although the fluid dynamics picture is likely to be much more complex, this evokes the question of whether convective plumes can merge or split apart as they traverse a convection zone. Both of these parameters indicate whether the shape of convection is “tree-like” or “forest-like,” such that a  $\sigma_{\text{int}}$  or  $\sigma_{\text{merge}}$  approaching one indicates more “forest-like convection.”

We evaluate both of these nondimensional parameters in Dethero et al. (2024) and find that they are capable of distinguishing convection in 2D and 3D; this indicates that one or both of these parameters could be useful in predicting the convective overshooting depth. We identify such a predictive relationship using our study of 10 stars with increasing mass and identical convection zone aspect ratios. We find experimentally that both  $\sigma_{\text{int}}$  and  $\sigma_{\text{merge}} \sim (M/M_{\odot})^{0.15}$ , and  $\sigma_{\text{int}}$  and  $\sigma_{\text{merge}} \sim (\ell_{\text{ov}}/H_{p,\text{CB}})^{0.2}$ . For stars with higher mass, both of these parameters are larger. Further probing reveals that this is largely due to the properties of convective flows that pass through the convective boundary into the overshooting layer; they are wider and less numerous for higher-mass stars.

Although  $\sigma_{\text{int}}$  and  $\sigma_{\text{merge}}$  have similar trends with mass and overshooting depth, we find  $\sigma_{\text{int}} > \sigma_{\text{merge}}$  for all ten stars, with a difference of 6 – 9%. Because the inflows in these simulations are narrow, it is possible that the inflows are under-resolved. Understanding whether this difference is robust would be required before a theoretical interpretation could be found. However, the resolution of these simulations is high, with over 240 grid cells resolving one pressure scale height. The total grid sizes of these simulations are also large compared to published work in this field; the grids in this study have a size of at least  $r \times \theta = 2224 \times 2224$ . Increasing the size of these simulations significantly is not presently feasible.

In the red giant study, we find that  $\sigma_{\text{int}}$  and  $\sigma_{\text{merge}}$  are similar and decrease with the size of the convection zone. These two-point parameters do not scale with the overshooting depth; there are two distinct trends before and after simulation IN4, where  $r_{\text{CB}} = 0.275R$ . This inflection point corresponds to the change in gravity at the convective boundary over time. Fundamental aspects of the structure of these stars appear to be changing during this short window of stellar evolution, affecting the properties of convection as much as the change in luminosity.

For all of the stars we have studied, we have also calculated the Anders penetration parameter. In general we find that it can distinguish between 2D and 3D convection, but the uncertainty on the parameter is large because it depends on the convective flux, which requires a long time average to converge.

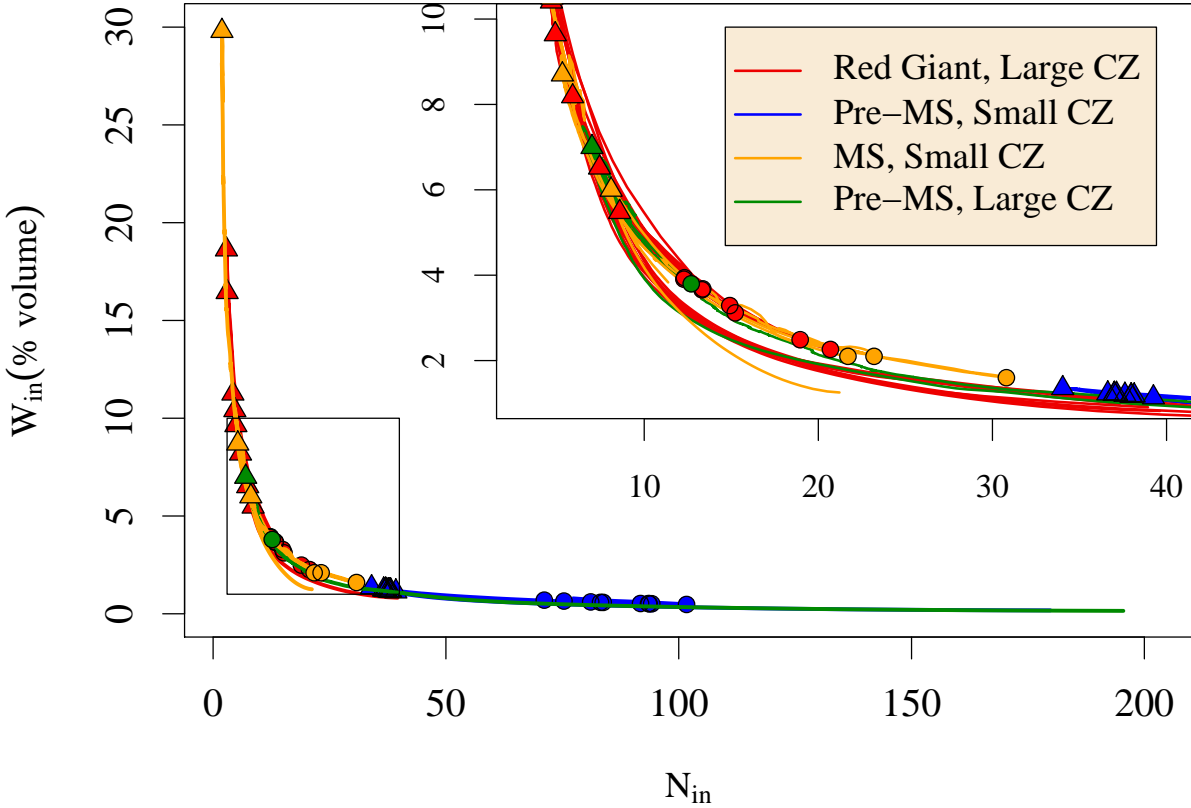


Figure 8.1 The average width of inflows as a function of the average number of inflows for the simulations presented in this work. Two simulations from Dethero et al. (2024), *cc2D* and *dcs2d*, are shown in orange, the pre-main sequence stars introduced in Section 6.1 are shown in blue, and the red giants introduced in Section 7.1 are shown in red. A star with a large envelope on the pre-main sequence, *pms4m*, is shown in green. The triangles represent characteristic points in the convection zone, and the dots represent characteristic points in the overshooting layer. The inset plot is a zoomed-in view of the transition region from numerous, narrow to few, fat inflows, represented by a white square with a black outline.

### 8.1.3 Width-Number Relation

Although we find that  $\sigma_{int}$  and  $\sigma_{merge}$  are similar to each other in three separate studies, it is important to understand that there are differences between these two diagnostics. The number of inflows at a given radius is a single number; the number of inflows by definition

is equal to the number of outflows so this cannot provide information about the symmetry of convection. The number of inflows can conceal the fact that convective plumes exhibit a range of different widths, with a distribution of both narrow and wide inflows at a given radius. This is evident in the red giant study, where the standard deviation at  $r = r_{\text{CB}}$  increases with convection zone size. Because there can be a variety of widths at a given radius, and only one number, the widths encapsulate different information than the number.

The relationship between the widths and numbers can be complex, such that the average number of plumes can correspond to several different average widths at different depths in a star (see Figure 8.1). Included in this figure are the set of pre-main sequence stars with increasing mass, the set of red giant stars with increasing convection zone size, the 2D simulations introduced in Dethero et al. (2024), and the two high-resolution simulations, *ccmod2D* and *pms4m2D*. Due to its deep convection zone and high resolution, the width-number relationship for *pms4m2D* includes both small-scale convection near the photosphere and large-scale convection in the deep interior. Its line on this width-number relation plot overlaps with all three sets of stars. The pre-main sequence stars with small convective envelopes introduced in Chapter 6 have the highest number of inflows at the surface, corresponding to small-scale convection; this is an effect of both high resolution and the fact that these simulations nearly reach the photosphere. The stars with the largest convection zones span the broadest range of the average number of inflows, representing multi-scale convection captured over a large density stratification. An exception to this is the  $6 M_{\odot}$  star *ccmod2D*, which has a small convective core and produces plumes up to 30% of the

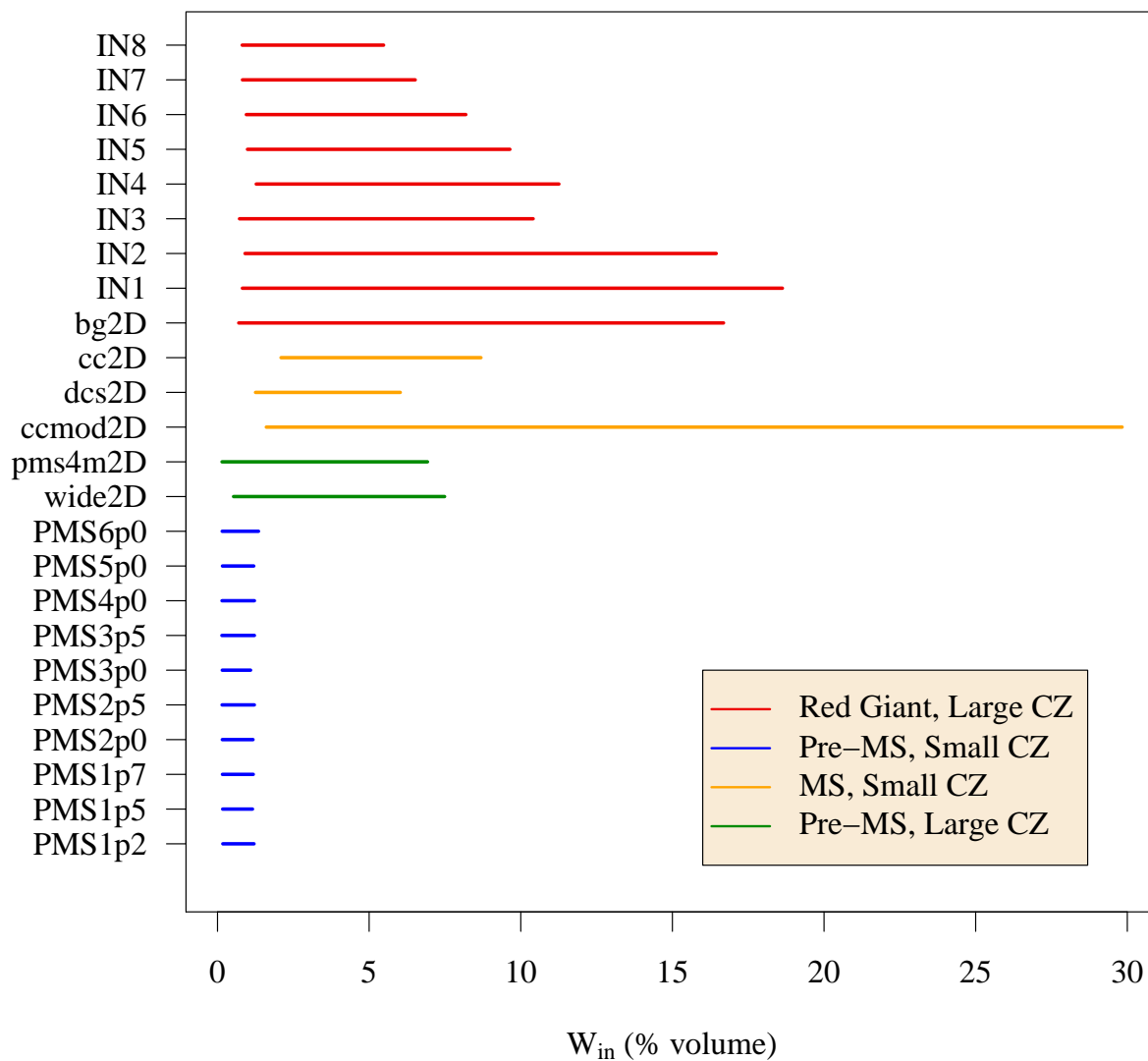


Figure 8.2 The range of average widths of inflows for the simulations presented in this work. Three main sequence simulations with small convection zones, *cc2D*, *dcs2d*, and *ccmod2D*, are shown in orange, the pre-main sequence stars introduced in Section 6.1 are shown in blue, and the red giants introduced in Section 7.1 are shown in red. Two stars with a large envelope on the pre-main sequence, *wide2d* and *pms4m2D*, are shown in green.

total volume near the inner radial boundary, where  $r_i = 0.02$ . The other convective core simulation, *cc2d*, does not reach this depth. Both convective core simulations use data for outflows rather than inflows in Figure 8.1. For all ages, convection zone sizes, and masses that we study, the width-number relation is depth-dependent and nonlinear; it exhibits a marked hysteresis, such that the relationship between width and number in the upper part of the convective envelope is different from that in the lower half approaching the convective boundary (and similarly for convective cores). However, given the large variation that we observe for each single star on this width-number relation plot, it is also surprising that the results for different stars with different stellar structures overlap so strongly.

#### ***8.1.4 Characterizing the overshooting layer***

The filling factor profiles for the 10 pre-main sequence stars with increasing mass reveal an interesting length scale that corresponds to the bottom of the overshooting layer. In this controlled study, we calculate the length  $\ell_{\sigma_v}$  from the convective boundary to the radial point where the filling factor flattens to a constant value in the stable region; we find a correlation with stellar mass and convective overshooting depth. We calculate this length again in our study of red giant stars with convection zones of different sizes, and we find an increase in  $\ell_{\sigma_v}$  with the size of the convection zone, but no clear correlation with the overshooting depth.

We identify an additional length scale in the profile of the average width of inflows. We calculate the length  $\ell_{W_{OL}}$  from the convective boundary to the radial point where  $W_{in}(r) = W_{OL}$ . This length is the same as the length from the convective boundary to the point where

$N_{\text{in}}(r) = N_{\text{OL}}$ . We note that this length corresponds to a point in the overshooting layer, such that  $\ell_{W_{\text{OL}}} < \ell_{\sigma_{\text{vp}}}$ . Another interesting feature of the filling factor profile in the red giant study is a dip in the profile just beyond the convective boundary; this occurs in all of the red giant stars we simulated, but none of the main sequence or pre-main sequence stars. We measure the distance to this dip and find that it corresponds approximately to the position where the average widths are a minimum in the overshooting layer,  $\ell_{W_{\text{OL}}}$ . In addition to the plume interaction parameter and the plume merging parameter,  $\ell_{\sigma_{\text{vp}}}$  and  $\ell_{W_{\text{OL}}}$  may be explored in future studies of convective boundary mixing.

In this body of work, we examined the shape of convection, or pattern of the number and widths of inflows as a function of depth, in different stellar structures to determine their impact on convective boundary mixing. The largest thrust of this work has established the significance of two-point diagnostics in predicting convective overshooting, which we have formulated as nondimensional parameters  $\sigma_{\text{int}}$  and  $\sigma_{\text{merge}}$ . These parameters have allowed us to distinguish between stars in 2D and 3D, stars of different masses, and stars with convective envelopes of different sizes. In the development of these ideas, we have also been able to identify several common properties of stellar convection. We find a mix of “forest-like” and “tree-like” convection in deep convective envelopes, while the shallow convective envelopes and the small convective cores we study exhibit purely “tree-like” convection. In stellar structure and evolution codes, the model for convection is different depending on whether the convection is in a core or envelope; however, clear similarities exist between the shallow envelopes and small convective cores as evidenced by the pattern of asymmetric and

symmetric convection.

## Appendices

## A Inlists

The inlist below was used in the MESA code to produce the pre-main sequence models introduced in Section 6.1.

```
&star_job
```

```
    show_log_description_at_start = .false.
```

```
    create_pre_main_sequence_model = .true.
```

```
    save_model_when_terminate = .true.
```

```
    save_model_filename = 'final.mod'
```

```
    change_initial_net = .true.
```

```
    new_net_name = 'o18_and_ne22.net'
```

```
/ ! end of star_job namelist
```

```
&controls
```

```
    max_num_profile_models = 10000
```

```
    use_gold_tolerances = .true.
```

```
    initial_mass = [see Table 6.1]
```

```
initial_z = 0.02

use_Type2_opacities = .true.

Zbase = 0.02

mixing_length_alpha = 1.9

log_L_upper_limit = 4.3

history_interval = 1

terminal_interval = 10

write_header_frequency = 10

which_atm_option = 'simple_photosphere'

photo_interval = 500

profile_interval = 1

/ ! end of controls namelist
```

The inlist below was used in the MESA code to produce the red giant models introduced in Section 7.1.

```
&star_job

show_log_description_at_start = .false.
```

```
create_pre_main_sequence_model = .true.

save_model_when_terminate = .true.

save_model_filename = 'final.mod'

change_initial_net = .true.

new_net_name = 'o18_and_ne22.net'

/ ! end of star_job namelist

&controls

max_num_profile_models = 10000

use_gold_tolerances = .true.

initial_mass = [see Table 7.1]

initial_z = 0.02

use_Type2_opacities = .true.

Zbase = 0.02

mixing_length_alpha = 1.9
```

```
log_L_upper_limit = 4.3

history_interval = 1

terminal_interval = 10

write_header_frequency = 10

which_atm_option = 'simple_photosphere'

photo_interval = 500

profile_interval = 1

/ ! end of controls namelist
```

## REFERENCES

- Aerts, C. 2021, *Reviews of Modern Physics*, 93, 015001
- Aguirre, V. S. et al. 2020, *Astronomy & Astrophysics*, 635, A164
- Ahlers, G. 2009, *Physics*, 2, 74
- Ahlers, G., Bodenschatz, E., & He, X. 2017, *Physical Review Fluids*, 2, 054603
- Ahlers, G., Grossmann, S., & Lohse, D. 2009, *Reviews of Modern Physics*, 81, 503
- Ahlers, G., & Xu, X. 2001, *Physical Review Letters*, 86, 3320
- Anders, E. H., Jermyn, A. S., Lecoanet, D., & Brown, B. P. 2022, *The Astrophysical Journal*, 926, 169
- Anders, E. H., & Pedersen, M. G. 2023, *Galaxies*, 11, 56
- Andrássy, R. 2015, PhD thesis, Universiteit van Amsterdam
- Andrassy, R. et al. 2022, *Astronomy & Astrophysics*, 659, A193
- Andrassy, R., Leidi, G., Higl, J., Edelmann, P. V. F., Schneider, F. R. N., & Röpke, F. K. 2024, *Astronomy & Astrophysics*, 683, A97
- Angulo, C. et al. 1999, *Nuclear Physics A*, 656, 3
- Anugu, N. et al. 2024, *The Astrophysical Journal*, 974, 113
- Arnett, W. D. et al. 2019, *The Astrophysical Journal*, 882, 18
- Arnett, W. D., Meakin, C., Viallet, M., Campbell, S. W., Lattanzio, J. C., & Mocak, M. 2015, *The Astrophysical Journal*, 809, 30
- Asida, S. 2000, *The Astrophysical Journal*, 528, 896

- Asplund, M., Amarsi, A., & Grevesse, N. 2021, *Astronomy & Astrophysics*, 653, A141
- Augustson, K. C., Brown, B. P., Brun, A. S., Miesch, M. S., & Toomre, J. 2012, *The Astrophysical Journal*, 756, 169
- Baglin, A., Auvergne, M., Barge, P., Deleuil, M., Michel, E., Team, C. E. S., et al. 2008, *Proceedings of the International Astronomical Union*, 4, 71
- Balasuriya, S., Ouellette, N. T., & Rypina, I. I. 2018, *Physica D: Nonlinear Phenomena*, 372, 31
- Balona, L. 2012, *Monthly Notices of the Royal Astronomical Society*, 423, 3420
- Baraffe, I., Chabrier, G., Allard, F., & Hauschildt, P. 1997, *Astronomy & Astrophysics*, 327, 1054
- . 1998, *Astronomy & Astrophysics*, 337, 403
- . 2002, *Astronomy & Astrophysics*, 382, 563
- Baraffe, I. et al. 2023, *Monthly Notices of the Royal Astronomical Society*, 519, 5333
- Baraffe, I., & El Eid, M. F. 1991, *Astronomy & Astrophysics*, 245, 548
- Baraffe, I., Pratt, J., Goffrey, T., Constantino, T., Folini, D., Popov, M., Walder, R., & Viallet, M. 2017, *The Astrophysical Journal Letters*, 845, L6
- Baraffe, I., Pratt, J., Vlaykov, D., Guillet, T., Goffrey, T., Le Saux, A., & Constantino, T. 2021, *Astronomy & Astrophysics*, 654, A126
- Beck, P. et al. 2018, *Astronomy & Astrophysics*, 612, A22
- Beeck, B. et al. 2012, *Astronomy & Astrophysics*, 539, A121
- Berger, T. A., Huber, D., Gaidos, E., van Saders, J. L., & Weiss, L. M. 2020a, *The Astro-*

- nomical Journal, 160, 108
- Berger, T. A., Huber, D., Van Saders, J. L., Gaidos, E., Tayar, J., & Kraus, A. L. 2020b, The Astronomical Journal, 159, 280
- Bertolami, M. M. M. 2023, The Astrophysical Journal, 943, 45
- Biermann, L. 1932, PhD thesis, Göttingen University
- Bildsten, L., Brown, E. F., Matzner, C. D., & Ushomirsky, G. 1997, The Astrophysical Journal, 482, 442
- Binks, A. et al. 2022, Monthly Notices of the Royal Astronomical Society, 513, 5727
- Bohm, K., & Cassinelli, J. 1971, Astronomy and Astrophysics, 12, 21
- Böhm-Vitense, E. 1958, Zeitschrift für Astrophysik, 46, 108
- Boothroyd, A. I., & Sackmann, I.-J. 1999, The Astrophysical Journal, 510, 232
- Brandenburg, A. 2016, The Astrophysical Journal, 832, 6
- Brandenburg, A., & Subramanian, K. 2005, Physics Reports, 417, 1
- Brott, I. et al. 2011, Astronomy & Astrophysics, 530, A115
- Browning, M. K. 2008, The Astrophysical Journal, 676, 1262
- Browning, M. K., Brun, A. S., & Toomre, J. 2004, The Astrophysical Journal, 601, 512
- Brummell, N. H., Clune, T. L., & Toomre, J. 2002, ApJ, 570, 825
- Brun, A. S., Miesch, M. S., & Toomre, J. 2011, The Astrophysical Journal, 742, 79
- Bühler, L., Brinkmann, H.-J., Courtessole, C., Klüber, V., Koehly, C., Lyu, B., Mistrangelo, C., & Roth, J. 2024, Fusion Engineering and Design, 200, 114195
- Burns, K. J., Vasil, G. M., Oishi, J. S., Lecoanet, D., & Brown, B. P. 2020, Physical Review

- Research, 2, 023068
- Busse, F. H. 1978, *Reports on Progress in Physics*, 41, 1929
- . 2005, *Hydrodynamic instabilities and the transition to turbulence*, 97
- Buzulukova, N., & Tsurutani, B. 2022, *Frontiers in Astronomy and Space Sciences*, 9, 1017103
- Cai, T. 2020, *The Astrophysical Journal*, 891, 49
- Calkins, M. A., Julien, K., & Marti, P. 2015, *Proceedings of the Royal Society A: Mathematical, Physical and Engineering Sciences*, 471, 20140689
- Cantat-Gaudin, T. et al. 2020, *Astronomy & Astrophysics*, 640, A1
- Canuto, V. 1992, *Astrophysical Journal*, Part 1 (ISSN 0004-637X), vol. 392, no. 1, June 10, 1992, p. 218-232., 392, 218
- . 2006, *Proceedings of the International Astronomical Union*, 2, 3
- Canuto, V., & Dubovikov, M. 1998, *The Astrophysical Journal*, 493, 834
- Canuto, V., Goldman, I., & Mazzitelli, I. 1996, *The Astrophysical Journal*, 473, 550
- Canuto, V., & Mazzitelli, I. 1991, *The Astrophysical Journal*, 370, 295
- Cassisi, S. 2017, in *EPJ Web of Conferences*, Vol. 160, EDP Sciences, 04002
- Cassisi, S., & Salaris, M. 1997, *Monthly Notices of the Royal Astronomical Society*, 285, 593
- Cattaneo, F., Brummell, N. H., Toomre, J., Malagoli, A., & Hurlburt, N. E. 1991, *The Astrophysical Journal*, 370, 282
- Cattaneo, F., Hurlburt, N. E., & Toomre, J. 1989, *Solar and Stellar Granulation*, 415
- Chabrier, G., Baraffe, I., Leconte, J., Gallardo, J., & Barman, T. 2009, in *American Institute*

- of Physics Conference Series, Vol. 1094, 15th Cambridge Workshop on Cool Stars, Stellar Systems, and the Sun, ed. E. Stempels (AIP), 102–111
- Chabrier, G., Gallardo, J., & Baraffe, I. 2007, *Astronomy & Astrophysics*, 472, L17
- Chabrier, G., & Schatzman, E. 1994, *The equation of state in astrophysics* (Cambridge, UK: Cambridge University Press)
- Chandrasekhar, S. 1957, *Daedalus*, 86, 323
- Chen, G., Chacon, L., Leibs, C. A., Knoll, D. A., & Taitano, W. 2014, *Journal of Computational Physics*, 258, 555
- Chiavassa, A. et al. 2020, *Astronomy & Astrophysics*, 640, A23
- Chillà, F., & Schumacher, J. 2012, *The European Physical Journal E*, 35, 1
- Choudhuri, A. R. 1998, *The physics of fluids and plasmas: an introduction for astrophysicists* (Cambridge, UK: Cambridge University Press)
- Christensen-Dalsgaard, J. 2008, *Astrophysics and Space Science*, 316, 13
- . 2015, *Monthly Notices of the Royal Astronomical Society*, 453, 666
- Cinquegrana, G. C., & Joyce, M. 2022, *Research Notes of the AAS*, 6, 77
- Clarkson, O., Herwig, F., Andrassy, R., Woodward, P., Pignatari, M., & Mao, H. 2019, in *Nuclei in the Cosmos XV*, ed. A. Formicola, M. Junker, L. Gialanella, & G. Imbriani (Cham: Springer International Publishing), 321–325
- Cliver, E. 2006, *Advances in Space Research*, 38, 119
- Clune, T. C., Elliott, J., Miesch, M., Toomre, J., & Glatzmaier, G. A. 1999, *Parallel Computing*, 25, 361

- Colgan, J. et al. 2016, *The Astrophysical Journal*, 817, 116
- Conroy, C. 2013, *Annual Review of Astronomy and Astrophysics*, 51, 393
- Constantino, T., Baraffe, I., Goffrey, T., Pratt, J., Guillet, T., Vlaykov, D., & Amard, L. 2021, *Astronomy & Astrophysics*, 654, A146
- Cox, J. P., & Giuli, R. T. 1968, *Principles of stellar structure* (New York: Gordon and Breach)
- Cukanovaite, E., Tremblay, P., Freytag, B., Ludwig, H., Fontaine, G., Brassard, P., Toloza, O., & Koester, D. 2019, *Monthly Notices of the Royal Astronomical Society*, 490, 1010
- Cuntz, M., & Wang, Z. 2018, *Research Notes of the AAS*, 2, 19
- Demarque, P., Guenther, D., Li, L., Mazumdar, A., & Straka, C. 2008, *Astrophysics and Space Science*, 316, 31
- Dethero, M. G., Hare, J., Airapetian, V. S., Namekata, K., B. Coley, J., Ferrara, E. C., & Gendreau, K. 2023, *Research Notes of the AAS*, 7, 203
- Dethero, M.-G., Pratt, J., Vlaykov, D., Baraffe, I., Guillet, T., Goffrey, T., Le Saux, A., & Morison, A. 2024, *Astronomy & Astrophysics*, 692, A46
- Dotter, A., Chaboyer, B., Jevremović, D., Kostov, V., Baron, E., & Ferguson, J. W. 2008, *The Astrophysical Journal Supplement Series*, 178, 89
- Dumont, T., Palacios, A., Charbonnel, C., Richard, O., Amard, L., Augustson, K., & Mathis, S. 2021, *Astronomy & Astrophysics*, 646, A48
- Duric, N. 2004, *Advanced Astrophysics* (Cambridge, UK: Cambridge University Press)
- Evans, N. R. et al. 2018, *The Astrophysical Journal*, 863, 187

- . 2024, *The Astrophysical Journal*, 971, 190
- Farag, E. et al. 2024, *The Astrophysical Journal*, 968, 56
- Featherstone, N., Edelman, P., Gassmoeller, R., Matilsky, L., Orvedahl, R., & Wilson, C. 2022, *Rayleigh* 1.1.0
- Ferraro, F., Messineo, M., Pecci, F. F., De Palo, M., Straniero, O., Chieffi, A., & Limongi, M. 1999, *The Astronomical Journal*, 118, 1738
- Ferraro, F. R., Valenti, E., Straniero, O., & Origlia, L. 2006, *The Astrophysical Journal*, 642, 225
- Forestini, M., & Charbonnel, C. 1997, *Astronomy and Astrophysics Supplement Series*, 123, 241
- Foteinopoulos, P., Papacharalampopoulos, A., & Stavropoulos, P. 2018, *CIRP Journal of Manufacturing Science and Technology*, 20, 66
- Freytag, B., Ludwig, H.-G., & Steffen, M. 1996, *Astronomy and Astrophysics*, 313, 497
- Freytag, B., Steffen, M., Ludwig, H.-G., Wedemeyer-Böhm, S., Schaffenberger, W., & Steiner, O. 2012, *Journal of Computational Physics*, 231, 919
- Funfschilling, D., Bodenschatz, E., & Ahlers, G. 2009, *Physical Review Letters*, 103, 014503
- Garrido, H. E., Cruz, P., Diaz, M. P., & Aguilar, J. F. 2019, *Monthly Notices of the Royal Astronomical Society*, 482, 5379
- Gilliland, R. L. et al. 2010, *Publications of the Astronomical Society of the Pacific*, 122, 131
- Girardi, L., Bressan, A., Bertelli, G., & Chiosi, C. 2000, *Astronomy and Astrophysics Supplement Series*, 141, 371

- Glatzmaier, G. 2013, *Introduction to Modeling Convection in Planets and Stars: Magnetic Field, Density Stratification, Rotation* (Princeton: Princeton University Press)
- Goffrey, T. et al. 2017, *Astronomy & Astrophysics*, 600, A7
- Grassitelli, L., Fossati, L., Simon-Diaz, S., Langer, N., Castro, N., & Sanyal, D. 2015, *The Astrophysical Journal Letters*, 808, L31
- Grimm-Strele, H., Kupka, F., Löw-Baselli, B., Mundprecht, E., Zaussinger, F., & Schiavsky, P. 2015, *New Astronomy*, 34, 278
- Grinstein, F. F., Margolin, L. G., & Rider, W. J. 2007, *Implicit large eddy simulation*, Vol. 10 (Cambridge: Cambridge University Press)
- Güdel, M. 2020, *Space Science Reviews*, 216, 143
- Guzik, J. A., Jackiewicz, J., & Evans, N. R. 2023, in *Proceedings for the 42nd Annual Conference of the Society for Astronomical Sciences (SAS-2023)* (Society for Astronomical Sciences, Inc.), 74–83
- Guzmán, A. J. A., Madonia, M., Cheng, J. S., Ostilla-Mónico, R., Clercx, H. J., & Kunnen, R. P. 2021, *Journal of Fluid Mechanics*, 928, A16
- Haller, G. 2015, *Annual Review of Fluid Mechanics*, 47, 137
- Hartmann, L., Herczeg, G., & Calvet, N. 2016, *Annual Review of Astronomy and Astrophysics*, 54, 135
- He, X., Funfschilling, D., Nobach, H., Bodenschatz, E., & Ahlers, G. 2012, *Physical Review Letters*, 108, 024502
- Heney, L., Vardya, M. S., & Bodenheimer, P. 1965, *The Astrophysical Journal*, 142, 841

- Herwig, F. 2000, *Astronomy & Astrophysics*, 360, 952
- Herwig, F., Woodward, P. R., Lin, P.-H., Knox, M., & Fryer, C. 2014, *The Astrophysical Journal Letters*, 792, L3
- Hillenbrand, L. A., & White, R. J. 2004, *The Astrophysical Journal*, 604, 741
- Hirzberger, J., Gizon, L., Solanki, S. K., & Duvall, T. L. 2008, *Helioseismology, Asteroseismology, and MHD Connections*, 415
- Holod, I., Hoelzl, M., Verma, P., Huijsmans, G., Nies, R., Team, J., et al. 2021, *Plasma Physics and Controlled Fusion*, 63, 114002
- Hubeny, I., & Mihalas, D. 2014, *Theory of stellar atmospheres: An introduction to astrophysical non-equilibrium quantitative spectroscopic analysis*, Vol. 26 (Princeton: Princeton University Press)
- Hurlburt, N. E., Toomre, J., & Massaguer, J. M. 1984, *The Astrophysical Journal*, 282, 557
- Hurlburt, N. E., Toomre, J., Massaguer, J. M., & Zahn, J.-P. 1994, *Astrophysical Journal*, 421, 245
- Iglesias, C. A., & Rogers, F. J. 1993, *The Astrophysical Journal*, 412, 752
- . 1996, *The Astrophysical Journal*, 464, 943
- Jones, C., Boronski, P., Brun, A., Glatzmaier, G., Gastine, T., Miesch, M., & Wicht, J. 2011, *Icarus*, 216, 120
- Jones, S., Andrassy, R., Sandalski, S., Davis, A., Woodward, P., & Herwig, F. 2016, *Monthly Notices of the Royal Astronomical Society*, stw2783
- Joyce, M., & Chaboyer, B. 2018, *The Astrophysical Journal*, 856, 10

- Joyce, M., & Tayar, J. 2023, *Galaxies*, 11, 75
- Justesen, A. B., & Albrecht, S. 2021, *The Astrophysical Journal*, 912, 123
- Käpylä, P. J. 2011, *Astronomische Nachrichten*, 332, 43
- . 2021, *Astronomy & Astrophysics*, 655, A78
- . 2024, *Astronomy & Astrophysics*, 683, A221
- Käpylä, P. J., Rheinhardt, M., Brandenburg, A., Arlt, R., Käpylä, M. J., Lagg, A., Olsper, N., & Warnecke, J. 2017, *The Astrophysical Journal Letters*, 845, L23
- Kim, T. et al. 2023, *Case Studies in Thermal Engineering*, 49, 103374
- King, C. R., Da Costa, G., & Demarque, P. 1985, *The Astrophysical Journal*, 299, 674
- Kippenhahn, R., Weigert, A., & Weiss, A. 2013, *Stellar Structure and Evolution* (Springer Berlin Heidelberg), 50–72
- Kirk, B. et al. 2016, *The Astronomical Journal*, 151, 68
- Knoll, D. A., & Keyes, D. E. 2004, *Journal of Computational Physics*, 193, 357
- Kraus, A. L., Tucker, R. A., Thompson, M. I., Craine, E. R., & Hillenbrand, L. A. 2011, *The Astrophysical Journal*, 728, 48
- Kupka, F., & Muthsam, H. J. 2017, *Living Reviews in Computational Astrophysics*, 3, 1
- Lacy, C. H. 1977, *Astrophysical Journal, Supplemental Series*, 34, 479
- Lamers, H. J., & Levesque, E. M. 2017, *Understanding Stellar Evolution* (IoP Publishing)
- Langtangen, H. P. 2016, *Center for Biomedical Computing, Simula Research Laboratory and Department of Informatics, University of Oslo*
- Le Saux, A. et al. 2022, *Astronomy & Astrophysics*, 660, A51

- Lecoanet, D. et al. 2019, *The Astrophysical Journal Letters*, 886, L15
- Lester, K. V., & Gies, D. R. 2018, *The Astronomical Journal*, 156, 8
- Lester, K. V., Gies, D. R., Schaefer, G. H., Farrington, C. D., Monnier, J. D., ten Brummelaar, T., Sturmann, J., & Vargas, N. 2019, *The Astronomical Journal*, 157, 140
- LeVeque, R. J., Mihalas, D., Dorfi, E., & Müller, E. 2006, *Saas-Fee Advanced Course 27. Lecture Notes 1997 Swiss Society for Astrophysics and Astronomy, Vol. 27, Computational Methods for Astrophysical Fluid Flow (Springer Science & Business Media)*
- Li, X., Shi, J., Li, Y., Yan, H., & Zhang, J. 2024, *Monthly Notices of the Royal Astronomical Society*
- Lovekin, C. C. 2020, *Frontiers in Astronomy and Space Sciences*, 6, 77
- Maeder, A., & Meynet, G. 1991, *Astronomy and Astrophysics Supplement Series*, 89, 451
- Margolin, L. G. 2019, *Shock Waves*, 29, 27
- Marshall, J., & Schott, F. 1999, *Reviews of Geophysics*, 37, 1
- Matt, S. P., Do Cao, O., Brown, B. P., & Brun, A. S. 2011, *Astronomische Nachrichten*, 332, 897
- Mayeli, P., & Sheard, G. J. 2021, *International Communications in Heat and Mass Transfer*, 125, 105316
- Meakin, C. A., & Arnett, D. 2007a, *The Astrophysical Journal*, 665, 690
- . 2007b, *The Astrophysical Journal*, 667, 448
- Miczek, F., Röpke, F. K., & Edelmann, P. V. 2015, *Astronomy & Astrophysics*, 576, A50
- Miesch, M. et al. 2015, *Space Science Review*, 1

- Milić, I., Smitha, H., & Lagg, A. 2019, *Astronomy & Astrophysics*, 630, A133
- Milone, A. et al. 2011, *The Astrophysical Journal*, 744, 58
- Milone, A. P., & Marino, A. F. 2022, *Universe*, 8, 359
- Morel, P., & Lebreton, Y. 2008, *Astrophysics and Space Science*, 316, 61
- Morrell, S., & Naylor, T. 2019, *Monthly Notices of the Royal Astronomical Society*, 489, 2615
- Moukalled, F., Mangani, L., & Darwish, M. 2015, *The Finite Volume Method in Computational Fluid Dynamics: An Advanced Introduction with OpenFOAM® and Matlab, Fluid Mechanics and Its Applications* (Springer International Publishing)
- Mousseau, V., Knoll, D., & Rider, W. 2000, *Journal of Computational Physics*, 160, 743
- Moutou, C. et al. 2013, *Icarus*, 226, 1625
- Muthsam, H., Göb, W., Kupka, F., Liebich, W., & Zöchling, J. 1995, *Astronomy and Astrophysics*, 293
- Muthsam, H., Kupka, F., Loew-Baselli, B., Obertscheider, C., Langer, M., & Lenz, P. 2010, *New Astronomy*, 15, 460
- Namekata, K. et al. 2022, *Nature Astronomy*, 6, 241
- Newman, C., & Knoll, D. A. 2013, *SIAM Journal on Scientific Computing*, 35, S445
- Nguyen, C. et al. 2022, *Astronomy & Astrophysics*, 665, A126
- Nordlund, Å., Stein, R. F., & Asplund, M. 2009, *Living Reviews in Solar Physics*, 6, 1
- Oertel, M., Hempel, M., Klähn, T., & Typel, S. 2017, *Reviews of Modern Physics*, 89, 015007
- Ogawa, M. 2008, *Fluid Dynamics Research*, 40, 379

- Ossendrijver, M. 2003, *The Astronomy and Astrophysics Review*, 11, 287
- Parker, E. N. 1955, *Astrophysical Journal*, vol. 122, p. 293, 122, 293
- Paxton, B., Bildsten, L., Dotter, A., Herwig, F., Lesaffre, P., & Timmes, F. 2010, *The Astrophysical Journal Supplement Series*, 192, 3
- Paxton, B. et al. 2013, *The Astrophysical Journal Supplement Series*, 208, 4
- Perryman, M. 2005, in *Astrometry in the Age of the Next Generation of Large Telescopes*, Vol. 338 (ASP Conference Series), 3
- Piau, L., & Turck-Chieze, S. 2002, *The Astrophysical Journal*, 566, 419
- Pillitteri, I., Argiroffi, C., Maggio, A., Micela, G., Benatti, S., Reale, F., Colombo, S., & Wolk, S. 2022, *Astronomy & Astrophysics*, 666, A198
- Pinçon, C., Belkacem, K., & Goupil, M. 2016, *Astronomy & Astrophysics*, 588, A122
- Prandtl, L. 1925, *ZAMM-Journal of Applied Mathematics and Mechanics/Zeitschrift für Angewandte Mathematik und Mechanik*, 5, 136
- Pratt, J., Baraffe, I., Goffrey, T., Constantino, T., Viallet, M., Popov, M., Walder, R., & Folini, D. 2017, *Astronomy & Astrophysics*, 604, A125
- Pratt, J., Baraffe, I., Goffrey, T., Geroux, C., Constantino, T., Folini, D., & Walder, R. 2020, *Astronomy & Astrophysics*, 638, A15
- Pratt, J. et al. 2016, *Astronomy & Astrophysics*, 593, A121
- Preibisch, T., & Feigelson, E. D. 2005, *The Astrophysical Journal Supplement Series*, 160, 390
- Press, W. H. 1981, *The Astrophysical Journal*, 245, 286

- Prša, A. et al. 2011, *The Astronomical Journal*, 141, 83
- Rempel, E. L., Chian, A. C.-L., de SA Silva, S., Fedun, V., Verth, G., Miranda, R. A., & Gošić, M. 2023, *Reviews of Modern Plasma Physics*, 7, 32
- Rempel, M. 2004, *The Astrophysical Journal*, 607, 1046
- Renzini, A. 1987, *Astronomy and Astrophysics*, 188, 49
- Ricker, G. R. et al. 2015, *Journal of Astronomical Telescopes, Instruments, and Systems*, 1, 014003
- Rieutord, M., Lara, F. E., & Putigny, B. 2016, *Journal of Computational Physics*, 318, 277
- Rieutord, M., & Zahn, J.-P. 1995, *Astronomy and Astrophysics*, 296, 127
- Rincon, F., & Rieutord, M. 2018, *Living Reviews in Solar Physics*, 15, 1
- Ritos, K., Kokkinakis, I. W., & Drikakis, D. 2018, *Computers & Fluids*, 173, 307
- Roe, P. 1986, *Annual Review in Fluid Mechanics*, 18, 337
- Rogers, F., & Nayfonov, A. 2002, *The Astrophysical Journal*, 576, 1064
- Rogers, T. M., Glatzmaier, G. A., & Jones, C. 2006, *The Astrophysical Journal*, 653, 765
- Röpke, F., Berberich, J., Jones, S., Poala, A. B., Edelmann, P., Michel, A., & Horst, L. 2018, in *NIC Symposium 2018*, Vol. 49, John von Neumann-Institut für Computing, 115–122
- Salaris, M., & Cassisi, S. 2008, *Astronomy & Astrophysics*, 487, 1075
- . 2017, *Royal Society Open Science*, 4, 170192
- Salaris, M., Cassisi, S., & Weiss, A. 2002, *Publications of the Astronomical Society of the Pacific*, 114, 375
- Scheel, J. D., & Schumacher, J. 2014, *Journal of Fluid Mechanics*, 758, 344

- Schmalzl, J., Breuer, M., & Hansen, U. 2002, *Geophysical & Astrophysical Fluid Dynamics*, 96, 381
- Schmitt, J., Rosner, R., & Bohn, H. 1984, *The Astrophysical Journal*, 282, 316
- Schrijver, C. J., & Zwaan, C. 2008, *Solar and stellar magnetic activity*, Vol. 34 (Cambridge University Press)
- Schüssler, M., Bruls, J., Vögler, A., & Vollmöller, P. 2005, *Analysis and Numerics for Conservation Laws*, 107
- Schwenn, R. 2006, *Living Reviews in Solar Physics*, 3, 1
- Shi, N., Emran, M. S., & Schumacher, J. 2012, *Journal of Fluid Mechanics*, 706, 5
- Siess, L., Izzard, R., Davis, P., & Deschamps, R. 2013, *Astronomy & Astrophysics*, 550, A100
- Slawson, R. W. et al. 2011, *The Astronomical Journal*, 142, 160
- Smolentsev, S. 2023, *Fusion Science and Technology*, 79, 251
- Sonoi, T., Ludwig, H.-G., Dupret, M.-A., Montalbán, J., Samadi, R., Belkacem, K., Caffau, E., & Goupil, M.-J. 2019, *Astronomy & Astrophysics*, 621, A84
- Spalart, P. R. 2006, in *IUTAM Symposium on One Hundred Years of Boundary Layer Research: Proceedings of the IUTAM Symposium held at DLR-Göttingen, Germany, August 12-14, 2004*, Springer, 19–28
- Spiegel, E. A. 1971, *Annual Review of Astronomy and Astrophysics*, 9, 323
- Spruit, H. C. 1997, *Memorie della Societa Astronomica Italiana*, 68, 397
- Stahler, S. W., Shu, F. H., & Taam, R. E. 1980, *The Astrophysical Journal*, 241, 637

- Stassun, K. G., Feiden, G. A., & Torres, G. 2014, *New Astronomy Reviews*, 60, 1
- Stein, C., & Hansen, U. 2023, *Journal of Geophysical Research: Solid Earth*, 128
- Stein, R., & Nordlund, Å. 1989, *The Astrophysical Journal*, 342, L95
- Steiner, O., Vigeesh, G., Krieger, L., Wedemeyer-Böhm, S., Schaffenberger, W., & Freytag, B. 2007, *Astronomische Nachrichten: Astronomical Notes*, 328, 323
- Stevens, B. 2005, *Annual Review of Earth and Planetary Sciences*, 33, 605
- Tassoul, M., Fontaine, G., & Winget, D. 1990, *Astrophysical Journal Supplement Series*, 72, 335
- Thornber, B., Mosedale, A., Drikakis, D., Youngs, D., & Williams, R. 2008, *Journal of Computational Physics*, 227, 4873
- Tian, C.-L., Deng, L.-C., & Chan, K.-L. 2009, *Monthly Notices of the Royal Astronomical Society*, 398, 1011
- Toomre, J., Brummell, N., Cattaneo, F., & Hurlburt, N. E. 1990, *Computer Physics Communications*, 59, 105
- Torres, G., & Ribas, I. 2002, *The Astrophysical Journal*, 567, 1140
- Torres, G., Stefanik, R. P., & Latham, D. W. 1997, *The Astrophysical Journal*, 479, 268
- Trompert, R., & Hansen, U. 1998, *Nature*, 395, 686
- Vallenari, A. et al. 2023, *Astronomy & Astrophysics*, 674, A1
- Van Der Poel, E. P., Stevens, R. J., & Lohse, D. 2013, *Journal of Fluid Mechanics*, 736, 177
- Van Horn, H. 1994, *International Astronomical Union Colloquium*, 147, 1
- Van Leer, B. 1974, *Journal of Computational Physics*, 14, 361

- . 1997, *Journal of Computational Physics*, 135, 229
- VandenBerg, D. A., & Stetson, P. 2004, *Publications of the Astronomical Society of the Pacific*, 116, 997
- Ventura, P., D'Antona, F., & Mazzitelli, I. 2008, *Astrophysics and Space Science*, 316, 93
- Ventura, P., Zeppieri, A., Mazzitelli, I., & D'Antona, F. 1998, *Astronomy and Astrophysics*, 334, 953
- Viallet, M., Goffrey, T., Baraffe, I., Folini, D., Geroux, C., Popov, M., Pratt, J., & Walder, R. 2016, *Astronomy & Astrophysics*, 586, A153
- Viani, L. S., Basu, S., JM, J. O., Bonaca, A., & Chaplin, W. J. 2018, *The Astrophysical Journal*, 858, 28
- Vieweg, P. P., Scheel, J. D., & Schumacher, J. 2021, *Physical Review Research*, 3, 013231
- Vlaykov, D., Baraffe, I., Constantino, T., Goffrey, T., Guillet, T., Le Saux, A., Morison, A., & Pratt, J. 2022, *Monthly Notices of the Royal Astronomical Society*, 514, 715
- Vlemmings, W., Khouri, T., Bojnordi Arbab, B., De Beck, E., & Maercker, M. 2024, *Nature*, 633, 323
- Vögler, A., Shelyag, S., Schüssler, M., Cattaneo, F., Emonet, T., & Linde, T. 2005, *Astronomy & Astrophysics*, 429, 335
- Weiss, A., & Schlattl, H. 2008, *Astrophysics and Space Science*, 316, 99
- Woodward, P. R., Herwig, F., & Lin, P.-H. 2014, *The Astrophysical Journal*, 798, 49
- Yan, Z., Liu, W., Tang, Z., Liu, X., Zhang, N., Li, M., & Zhang, H. 2018, *Optics & Laser Technology*, 106, 427

Yang, H. et al. 2017, *The Astrophysical Journal*, 849, 36

Ypma, T. J. 1995, *SIAM review*, 37, 531

Zahn, J.-P. 1991, *Astronomy & Astrophysics*, 252, 179

Zhang, J., Childress, S., & Libchaber, A. 1998, *Physics of Fluids*, 10, 1534